City Research Online

City, University of London Institutional Repository

This is the accepted version of the paper.

This version of the publication may differ from the final published version.

Permanent repository link: https://openaccess.city.ac.uk/id/eprint/29042/

Link to published version:

A UNIFIED APPROACH TO FLUTTER, DYNAMIC STABILITY AND
RESPONSE ANALYSIS OF HIGH ASPECT RATIO AIRCRAFT

by

Anthony Angelo Cal

Thesis submitted for the degree of Doctor of Philosophy

City University
Department of Mechanical Engineering and Aeronautics

February 1992

To my mother, Rita

whose support and faith in me has always been an inspiration

Contents

List of Tables

9

List of Figures

16

Acknowledgements

Declaration

I grant powers of discretion to the University Librarian to allow this thesis to be copied in whole or in part without further reference to me. This permission covers only single copies made for study purposes, subject to normal conditions of acknowledgements.

Anthony Cal

Abstract

A unified method of flutter, dynamic stability and response analysis of deformable aircraft is presented. Normal modes and the generalised coordinate approach are used to develop the equations of motion. Strip theory and Theodorsen's expressions for unsteady lift and moment are utilised to generate the generalised aerodynamic forces. Theodorsen's function C(k) for harmonic motion is employed for the flutter analysis.

A comparison is made between generalised unsteady aerodynamic forces and flutter quantities obtained from lifting line theory and those obtained from conventional strip theory, for both a rigid and elastic wing undergoing binary flutter. This investigation shows good agreement between the two theories particularly at high aspect ratios and suggests that the lower limit of aspect ratio for good flutter prediction, using strip theory, is about 6.

The unified analysis is carried out on three particular aircraft of which two are high aspect ratio sailplanes, the Kestrel 22m, the tailless Ricochet and the Cranfield A1 a moderate aspect ratio aerobatic aircraft. A symmetric flutter analysis, including the effects of rigid body modes is carried out on all three aircraft. The Kestrel is found to suffer from classical wing bending/torsion flutter. The tailplane aerodynamics is seen to have a marginal if not stabilising influence on its flutter behaviour. The Ricochet in the absence of a tailplane is found to suffer from body freedom flutter involving coupling of the short period mode with the first wing bending mode. As the A1 is very stiff and of comparatively low aspect ratio it is found to be virtually flutter free.

Making use of the generalised Theodorsen's function for convergent motion and the current body fixed axis system, the analysis is extended to evaluate the short period mode of an aircraft. Stability derivatives using the normal classical rigid body approach are also used for comparison. The introduction of flexibility and unsteady aerodynamics is seen to have a destabilising influence on the short period mode. Close to the flutter speed, classical rigid body assumptions are found to be inadequate in predicting the short period characteristics of the Kestrel and the Ricochet, but not the relatively stiff A1. An unsteady wing wake is then introduced at the tailplane where this is seen to have a negligible effect on flutter of the Kestrel.

An analysis of the aircraft response to continuous atmospheric turbulence and discrete gusts is carried out using the Power Spectral Density method (PSD) and Statistical Discrete Gust method (SDG) respectively. The introduction of flexibility is seen to substantially increase the overall aircraft response, especially at subcritical speeds. From the analysis carried out on all the three aircraft, an SDG-PSD overlap does appear to be characterised in this investigation not by a 10.4 factor, but rather by a 10.4 plus or minus approximately 17% factor when rigid body modes are considered. For the flexible case this range is found to be plus or minus 31% factor.

21

Notation

a_c non-dimensional distance from mid-chord to local aerodynamic centre (for steady flow) measured perpendicular to elastic axis, positive rearward, fraction of semi-chord b

a_h non-dimensional distance from mid-chord to elastic axis measured perpendicular to elastic axis, positive rearward, fraction of semi-chord

a_0 local wing lift curve slope for a section perpendicular to elastic axis

a_1 local tailplane lift curve slope for a section perpendicular to elastic axis

$\bar{A}$ normalised response quantity defined in Eq.(6.10)

AR   aspect ratio of full wing including fuselage intercept, AR = s/b

$A_r(t)$ indicial admittance to unit step input

b   semi-chord of wing measured in streamwise direction

$\bar{b}$ semi-chord of wing measured perpendicular to elastic axis

c   chord length

$\bar{c}$ standard mean chord (SMC)

$\bar{\bar{c}}$ mean aerodynamic chord (MAC)

$C(k) = F(k) + iG(k)$ Theodorsen's function

EI   flexural rigidity

GJ	torsional rigidity
h	local vertical translational displacement of wing positive downward
$h\bar{\bar{c}}$	distance of centre of gravity aft of leading edge of mean aerodynamic chord of wing
$h_n\bar{\bar{c}}$	distance of aerodynamic centre of aircraft aft of leading edge of mean aerodynamic chord of wing
H	gradient distance
H_n	static margin, stick fixed $= -(\partial C_m/\partial C_L)$
$H_y(i\omega)$	frequency response function of quantity y
$H_1^{(2)}(z)$, $H_0^{(2)}(z)$	complex Hankel functions
$J_0(z)$, $J_1(z)$ $Y_0(z)$, $Y_1(z)$	complex Bessel functions
i	$\sqrt{-1}$
i_y	$I_{yy}/M\bar{\bar{c}}^2$
I_{yy}	aircraft pitching moment of inertia about the Y axis
I_α	mass moment of inertia per unit span about x $= ba_h$
I_p/l	rotational inertia per unit length
Ker( )	Kernel function
k	reduced frequency $\omega b/U$, fractional exponent
k_n	reduced frequency employing velocity component

23

perpendicular to elastic axis $(\omega \overline{b}/U_n)$

k_h heave spring stiffness

k_α pitch spring stiffness

K   gust alleviation factor

l wing length measured along the elastic axis, distance of aerodynamic centre of tailplane aft of aerodynamic centre of aircraft without tail

l_{wt} distance between wing trailing edge and tailplane leading edge

l_T distance of aerodynamic centre of tailplane aft of centre of gravity of aircraft

L   oscillatory lift per unit length of wing, along elastic axis, positive downward, for streamwise sectionsand scale length of turbulence

$\overline{L}$ oscillatory lift per unit length of wing, along elastic axis, positive downward, for sections normal to the elastic axis

m_q $- M_q / i_y$

m_w $- \mu_1 M_w / i_y$

$m_{\dot{w}}$ $- M_{\dot{w}} / i_y$

m_f wing modal mass per unit length

$\overset{\circ}{M}_q, \ \overset{\circ}{M}_w, \ \overset{\circ}{M}_{\dot{w}}$ pitching moment derivatives defined in Eq.(4.20)

M_q non-dimensional pitching moment derivative due to rate of pitch $\overset{\circ}{M}_q / \frac{1}{2}\rho U S_w \overline{\overline{c}}^2$

M_w non-dimensional pitching moment derivative due to velocity increment along OZ $\overset{\circ}{M}_w / \frac{1}{2}\rho U S_w \overline{\overline{c}}$

$M_{\dot{w}}$ non-dimensional pitching moment derivative due to rate of change of w $\overset{\circ}{M}_{\dot{w}} / \frac{1}{2}\rho U S_w \overline{\overline{c}}^2$

M/l mass per unit length,

m mass per unit length, parameter in lifting line theory of Davies, Ref.(11)

M mach number, mass

M_α oscillatory moment about elastic axis per unit length of wing, positive leading edge up for streamwise sections

$\overline{M}_\alpha$ oscillatory moment about elastic axis per unit length of wing, positive leading edge up for sections normal to the elastic axis

n number of modes, parameter in lifting line theory of Davies, Ref.(11)

N number of modes

N_ζ number of strips used to represent one vortex cell defined in Eq.(5.3)

p_i amplitude reduction factor of ith gust defined in Eq.(6.14)

q Dynamic pressure $\frac{1}{2}\rho U^2$, paramter in lifting line theory of Davies, Ref.(11)

q_h, q_p, q_f	generalised coordinates of heave, pitch about aircraft c.g. and wing flexure
$\left.\begin{array}{l} q_1(t) \\ u_1(t) \end{array}\right\}$	generalised coordinates
r_α^2	non-dimensional radius of gyration of the typical section (I_α/mb^2)
s	semi-span of wing measured perpendicular to free stream direction
S	area of wing
t	time
$\hat{t}$	non-dimensional time Ut/b
T	torsional moment
T/θ	gradient of torsional moment to rotational deflection
$T_{1/2}$	time to half amplitude
u_f	ratio of quasi-steady to unsteady flutter speed
U	freestream velocity
U_f	flutter velocity
U_n	component of freestream velocity normal to elastic axis $(U\cos \Lambda)$
U_0	gust intensity parameter
V_f/V_R	ratio of flutter velocity to reference velocity

V_h	modal velocity induced at tailplane by wing bending
V_α	modal velocity induced at tailplane by wing torsion
$\overline{V}$	volume ratio $S_T l / S_w \overline{\overline{c}}$
$\overline{V}_T$	tailplane volume ratio $S_T l_T / S_w \overline{\overline{c}}$
w_g	vertical gust velocity
x	distance of aerodynamic centre form aircraft centre of gravity
x_α	non-dimensional distance from mid-chord to inertia axis, negative rearward, fraction of semi-chord chord b
$\overline{x}$	distance of component centre of gravity from overall aircraft centre of gravity
X, Y, Z	Cartesian coordinate system as defined in Fig. 2.2
$\overline{X}, \overline{Y}, \overline{Z}$	Cartesian coordinate system as defined in Fig. 2.2
z	complex reduced frequency, $\omega b/U - i\mu b/U = \rho e^{i\theta}$
z_q	$- Z_q / \mu_1$
z_w	$- Z_w$
$z_{\dot{w}}$	$Z_{\dot{w}} / \mu_1$
$\overset{o}{Z}_q, \quad \overset{o}{Z}_w, \quad \overset{o}{Z}_{\dot{w}}$	Force component derivatives defined in Eq.(4.20)
Z_q	non-dimensional force derivative due to rate

of pitch $\overset{\circ}{Z}_q / \frac{1}{2}\rho US_w \bar{\bar{c}}$

Z_w non-dimensional force derivative due to velocity increment along OZ $\overset{\circ}{Z}_w / \frac{1}{2}\rho US_w$

$Z_{\dot{w}}$ non-dimensional force derivative due to rate of change of w $\overset{\circ}{Z}_{\dot{w}} / \frac{1}{2}\rho S_w \bar{\bar{c}}$

Z_T height of tailplane above fuselage centre line

α local pitching rotation of wing measured about the elastic axis at streamwise sections, positive leading edge up

$\bar{\alpha}$ local pitching rotation of wing measured about the elastic axis at streamwise sections normal to the elastic axis, positive leading edge up

$d\alpha/dt$ rate of aircraft pitch

γ_i individual worst case responses to a combination of i gusts

$\bar{\gamma}$ defined in Eq.(6.13)

γ_w wake vortex strength distribution defined in Eq.(5.1)

Γ_n wing circulation defined in Eq.(5.5)

Γ_h wing circulation induced by heave

Γ_α wing circulation induced by pitching rotation

$\delta x, \ \delta y, \ \delta z$ displacements along respective co-ordinates

δ/θ gradient of deflection to applied force

$\partial C_m/\partial \alpha$ non-dimensional variation of pitching moment with incidence $C_m = M_\alpha / \frac{1}{2}\rho U^2 S_w \bar{\bar{c}}$

28

$\partial C_m / \partial C_L$	non-dimensional variation of pitching moment with lift $C_L = L/\frac{1}{2}\rho U^2 S_w$
Δn	vertical acceleration of aircraft centre of gravity in terms of g
$d\varepsilon/d\alpha$	rate of change of angle of downwash at tailplane with incidence
ζ	mode shape of wing bending taken along the Y axis
ζ^*	ζ/b
ζ_{sp}	short period damping ratio
η	non-dimensional spanwise distance y/s
θ	argument of z, angle of twist
$\theta x, \theta y, \theta z$	rotations about respective co-ordinates
λ	stability roots $\mu + i\omega$
$\bar{\lambda}$	non-dimensionalised stability roots $\tau\lambda$
Λ	elastic axis sweep angle, positive for sweep back
μ	mass ratio $(m/\pi\rho b^2)$, damping
μ_1	longitudinal relative density parameter $M/\frac{1}{2}\rho S_w \bar{\bar{c}}$
μ_{sp}	short period damping
ξ	downstream coordinate along wake measured from mid-chord
ρ	material and fluid density, modulus of z = $\rho e^{i\theta}$

29

σ	local bending slope of elastic axis $\partial h / \partial \bar{y}$
σ'	$\partial \sigma / \partial \bar{y}$
σ_y^2	mean square value of quantity y
τ	magnitude of time unit $M / \frac{1}{2} \rho U S_w$, local rate of change of twist along elastic axis $\partial \bar{\alpha} / \partial \bar{y}$
τ'	$\partial \tau / \partial \bar{y}$
$\Phi_{w_g}(\omega)$	power spectral density of w_g
$\Phi_y(\omega)$	output power spectral density of quantity y
ω	vibration frequency
ω_f	uncoupled wing bending frequency
ω_h, ω_α	heave and pitch uncoupled natural frequencies
ω_{sp}	short period frequency

<u>matrices</u>

$\begin{bmatrix} A \end{bmatrix}$	aerodynamic strip terms relating L and M_α to h and α, Extensional stiffness matrix from classical laminate plate theory
$\begin{bmatrix} AT \end{bmatrix}$	tailplane aerodynamic strip terms relating L_T and $M_{\alpha T}$ to h_T and α_T
$\begin{bmatrix} AD \end{bmatrix}$	tailplane aerodynamic strip terms including wake effects relating L_T and $M_{\alpha T}$ to h_T and α_T defined in Eq.(G.14)
$\begin{bmatrix} D \end{bmatrix}$	laminate bending stiffness matrix from classical laminate plate theory
$\begin{bmatrix} DA \end{bmatrix}$	aerodynamic strip terms relating L and M_α to σ

	and τ defined in Eq.(B.19)
$\begin{bmatrix} DDA \end{bmatrix}$	aerodynamic strip terms relating L and M_α to σ' and τ' defined in Eq.(B.20)
$\begin{bmatrix} DQT \end{bmatrix}$	tailplane generalised aerodynamic matrix including wake effects defined in Eq.(G.19)
$\begin{bmatrix} `K_\diagdown \end{bmatrix}$	generalised stiffness matrix
$\begin{bmatrix} `M_\diagdown \end{bmatrix}$	generalised mass matrix
$\begin{bmatrix} Q \end{bmatrix}$	generalised aerodynamic matrix
$\begin{bmatrix} \Phi \end{bmatrix}$	matrix of normal modes
$\begin{bmatrix} \Psi \end{bmatrix}$	matrix of shape functions

subscripts

g	gust
LLT	lifting line theory
ST	strip theory
T	tailplane
W	wing

31

1.0 INTRODUCTION

1.1 Historical Background

Aeroelasticity is the science which studies the interaction of aerodynamic, elastic and inertia (including gravitational) forces. This interaction of forces is well represented in Collar's[1] famous triangle of forces shown in Figure 1.1. Classical aeroelasticity primarily deals with aircraft flutter, a self sustained excited oscillation, often destructive, wherein energy is absorbed from the air stream. Early investigations into flutter concentrated on component flutter such as wing-aileron and tailplane flutter, such occurrences can be traced back to the early history of flight. These investigations relied on solving the problems empirically. In the 1920's Frazer and Duncan[2] with their comprehensive monograph "The flutter of aeroplane wings", appear to be the first known investigators to solve the flutter problem analytically and who laid down the principles on which flutter investigations have been based ever since.

The 1930's saw the theoretical advancement of the field with the development of unsteady aerodynamic theories by Glauert[3] Wagner[4] and Theodorsen[5]. Glauert was probably the first to point out the dependency of these aerodynamic properties on the frequency parameter or the reduced frequency. These early two-dimensional methods were implemented in the relatively simple use of strip theory for wings of moderately high aspect ratios. Although this method has been readily accepted as a practical means of flutter analysis by the aviation industry for many years, there have been doubts recently expressed as to the validity of this method[6] With the development of lifting line theory[7] and three-dimensional lifting surface theories, in the late 1960's and 70's, such as the vortex lattice method[8] unsteady aerodynamics has been applied to low aspect ratio wings where the effects of finite span are critical. For a thorough systematic breakdown of the development of aeroelasticity, Refs.(9) and (10) provide interesting reading. Three-dimensional unsteady aerodynamic theories have been extended in some cases for tandem lifting surfaces[11] where the strong aerodynamic coupling between the wing and tailplane may be critical. This is particularly true for

variable geometry aircraft where strong wing downwash forces coupled with a torsionally weak fuselage initiate anti-symmetric tailplane flutter.[12] Although conventional strip theory cannot predict instabilities sensitive to wing tailplane aerodynamic interference, it can be modified to a certain extent to incorporate some of these effects with some success.[13]

Classical flutter analysis deals predominantly with the high frequency dynamic interaction of inertial, elastic (structural) and aerodynamic forces, whereas the implementation of rigid body modes is restricted within the scope of low frequency dynamic stability investigations.[14,15] However studies carried out in the early 1980's have again highlighted the critical role these rigid body freedoms play in flutter. A phenomenon known as "body freedom flutter", reported by Gaukroger,[16] in the early fifties was rediscovered by Banerjee[17] in a symmetric flutter analysis on the Ricochet, an aft swept tailless glider. This instability arises from the coupling of the short period pitching oscillation with the fundamental bending mode. The same type of instability was observed around the same time by Weisshaar[18] for a tailed aircraft with forward swept wings. However Weisshaar established also an anti-symmetric flutter involving the roll mode. The advent of aeroelastic tailoring[19] with structural weight always being minimised with new materials like composites and also the advent of statically unstable aircraft, like the forward sweep X29A aircraft, aeroelastic effects will become more significant and the frequency separation between the rigid-body modes and elastic modes will be reduced. This is particularly true for the flexible aircraft such as sailplanes and this has been well demonstrated in recent studies on a man-powered aircraft.[20]

For aircraft of considerable flexibility, it is important to combine the rigid body motions with the elastic modes of distortion. This means combining two major disciplines of aircraft design namely - the stability and control on one side and the flutter and response on the other, as proposed by Taylor and Woodcock.[21] In general the stability characteristics of an aircraft are investigated using aerodynamic derivatives[14,15] and rigid-body assumptions only. However some authors[22,23] have taken partial

33

account of flexibility by using a quasi-static method or modified aerodynamic derivatives. The more refined and accepted programs that provide an integrated approach such as MSC/NASTRAN[®24] utilise lifting surface techniques in addition to strip theory; such programs also encompass the supersonic region.

An integrated approach must also observe the effects of aircraft response to different classes of disturbance. There are generally two different classes of disturbance, i.e. those arising from the control system inputs made by the pilot or by some automatic device, and those arising from essentially unwanted disturbances such as atmospheric turbulence, buffeting and ground contacts. A characteristic of these unwanted disturbances is that they usually contain sufficient energy at the frequencies of the aircraft elastic modes to excite the latter to a significant extent, and increase the internal stresses within the structure. The theoretical treatment of the response to these disturbances must therefore take account of these modes as well as those of the aircraft rigid body motion. In general, response to atmospheric turbulence is carried out using two complementary techniques. The first is the Power Spectral Density (PSD) method[25] which is a statistical approach in modelling continuous turbulence. The second is a discrete gust technique, e.g. developed by Jones[26] known as the Statistical Discrete Gust (SDG) method. Jones claims[27] under certain circumstances SDG and PSD methods produce similar numerical results.

1.2 Aim of Current Analysis and Layout of the Work

The investigation set out in this thesis establishes an integrated approach to aircraft aeroelastic analysis using strip theory. It encompasses classical and non-classical flutter, aircraft dynamic stability and response analysis. The method of analysis is incorporated in a computer program called FLUSTAR (A Unified Method for the prediction of FLUtter, Dynamic STAbility and Response of Deformable Aircraft).

Using the above approach an aeroelastic analysis is carried out on three case aircraft. These are:

1) The T59H Kestrel

34

2) The Ricochet

3) The Cranfield A1.

The Kestrel and the Ricochet are two high aspect ratio sailplanes representative of most classes of deformable aircraft while in contrast the A1 is an aerobatic aircraft of moderate aspect ratio which is relatively much stiffer. The validity of strip theory as an aerodynamic tool in wing flutter analysis and the influence of sweep is initially examined, in the investigation in Chapter 2. In Chapter 3, a modal and then complete flutter analysis is carried out on each aircraft, introducing the effects of tailplane aerodynamics where appropriate, the relative contribution of the flutter modes is then observed. The effects of fuselage flexibility on the flutter of the Kestrel is also investigated in addition to an anti-symmetric analysis. A thorough modal analysis is undertaken on the A1, including a finite element model (FEM) idealisation of the rear fuselage, in an attempt to establish the necessary stiffnesses, prior to any flutter calculations. The influence of quasi-steady and full unsteady aerodynamics on the flutter of the Kestrel and the Ricochet is examined. The method of analysis is also applied to predict the body freedom flutter of a forward swept model. The effects of flexibility and unsteady aerodynamics on the short period oscillation, stick fixed, is investigated and the results are found in Chapter 4. The short period characteristics are re-examined in Chapter 5 by incorporating a simple unsteady wake model and the influence of downwash on the Kestrel flutter is investigated. Using the Power Spectral Density (PSD) method and the Statistical Discrete gust (SDG) method, the response characteristics of each aircraft to continuous turbulence and discrete gusts are also investigated and the results are given in Chapter 6. The response analysis is further expanded to investigate the claimed SDG-PSD overlap. A summary of overall results from this work is presented in Chapter 7 followed by conclusions and suggestions for further work in Chapter 8.

1.3 Development and Scope of Current Analysis

The program FLUSTAR which stems from the current analysis, is the development of an existing family of aeroelastic programs, CFFF and later CALFUN[28] (A program for CALculation of Flutter Speed Using Normal Modes). The CFFF and CALFUN programs are short, compact and completely self-contained and are written in standard FORTRAN. The programs calculate with a minimum amount of data, the flutter speed and the associated modes of high aspect ratio, slender wing aircraft using normal modes and unsteady aerodynamics in two-dimensional flow. The aircraft is represented by linear structural and aerodynamic theories. The structural idealisation includes beam and lumped mass representations of the aircraft whereas strip theory based on Theodorsen expressions for unsteady lift and moment are used in the aerodynamic idealisation.

CALFUN can utilise coupled frequencies and modes but considers only the cantilever wing case, while CFFF deals with uncoupled modes but, can include whole aircraft configurations with rigid body modes for a free flight flutter analysis. Although both programs neglect tailplane aerodynamics, CFFF has been used in the past to investigate the flutter characteristics of a tailless aircraft[17]. Tailplane aerodynamics are subsequently introduced into CFFF as CFFFT, which assumes the aerodynamic forces to be entirely generated by the wing and tailplane. Using CFFFT as the basic program, additional facilities are incorporated and the present investigation initiated the development of a unified method of determining the aeroelastic behaviour and response to turbulence of deformable aircraft.

The existing flutter analysis within CFFFT, is extended to evaluate the longitudinal short period mode, stick fixed, of an aircraft. Although lateral stability can also be considered, longitudinal motion is considered the more pertinent especially with respect to gust response problems. Control surfaces are assumed fixed in all the analyses undertaken in this thesis. The calculation of the unsteady aerodynamics due to general motion is achieved by employing the generalised Theodorsen function $C(k)$ for non-harmonic-convergent motion, as developed by Luke and Dengler[29] (This is explained in depth in Chapter 4). Based on a method

given by Yates,[30] modified spanwise wing and tailplane aerodynamic parameters a_0 and a_1 are added to augment the stability and flutter analyses involving finite span effects. In order to enhance the dynamic stability analysis and investigate the influence of downwash in flutter, an unsteady wake was also included using a simple vortex lattice method employing strip aerodynamics (this is dealt with in depth in Chapter 5). These additional facilities are presented in the program FLUST (A Unified Method of FLUtter and Dynamic STability Analysis of Deformable Aircraft). A summary of the development of the analysis is shown in Figure 1.2.

The power spectral density method of aircraft response analysis is carried out using both the Von Karman and Dryden forms of the power spectra. In this analysis transport lag effects are neglected and the gust is assumed to encounter the wing and tailplane at the same time. Using Bromwich's integral the indicial admittance is first obtained from the mechanical admittance or frequency response function. This method is implemented within FLUST and is fully explained in Chapter 6. A program written by Purcell,[31] which requires the indicial admittance as one of its input parameters is then linked with FLUST. The worst case response to a pair of step gusts is then evaluated, this is equivalent to method 1 of Ref.(32), in the Statistical discrete gust method. Following this procedure the integrated program developed is named FLUSTAR.
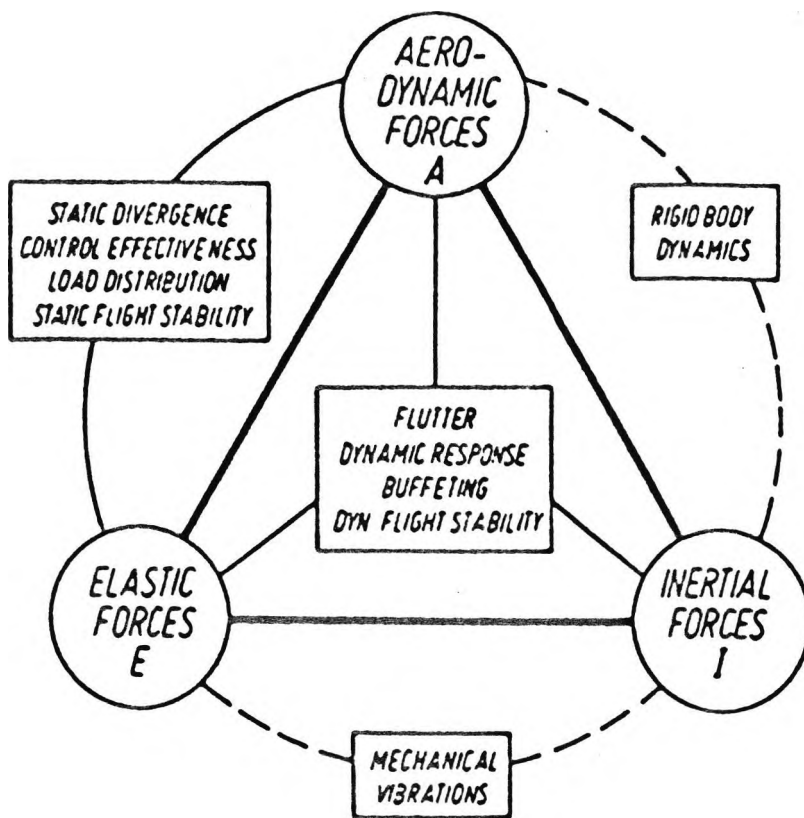
Fig. 1.1   The aeroelastic triangle of forces

```
┌─────────────────────────┐                      ┌─────────────────────────┐
│ CFFF                    │   Coupled            │ CALFUN                  │
│                         ├── Elastic ───────────┤                         │
│ Flutter speed of        │   Modes              │ Flutter speed of        │
│ cantilever/free-flight  │                      │ cantilever wing         │
│ tailless aircraft       │                      │                         │
└────────────┬────────────┘                      └─────────────────────────┘
             │
    Tailplane Aerodynamics
             │
┌────────────┴────────────┐
│ CFFFT                   │
│                         │
│ Flutter speed of        │
│ cantilever/tailed       │
│ aircraft                │
└────────────┬────────────┘
```

Generalised Theodorsen
Function C(k)

Modified Aerodynamic Parameters a_o, a_1 and a_c

Unsteady Downwash at Tailplane

FLUSTAR

FLUST

Types of Analysis

1. Flutter (U_f and ω_f)   } Effects of
2. Dynamic Stability (μ_{sp} and ω_{sp}) } Downwash

3. Response to Atmospheric Turbulence

| Mechanical Admittance | Bromwich's Integral | Indicial Admittance |

PSD

Von Karman and
Dryden Spectra

$\sigma_{\ddot{h}}$, $\sigma_{\ddot{\alpha}}$ or $\sigma_{\dot{\alpha}}$

SDG

PURCELL'S
PROGRAM

$\overline{\gamma}$

Figure 1.2   Development of unified analysis

2.0 WING FLUTTER

2.1 Introduction

Flutter,[33-35] is a dynamic instability. Classically, this is a mechanism involving the coupling of at least two degrees of freedom of the system. Motions in each of the participating degrees of freedom, per se are stable, i.e. they are damped. However when these motions are free to interact, and the fluid flow rate is sufficiently high, the flexible body may, in certain circumstances extract energy from the fluid stream. At this critical flow rate, known as the critical flutter speed, coupled oscillatory motion is sustained. At higher flow rates the oscillatory motion becomes divergent. There may be higher critical flow rates, but in the context of aircraft aeroelasticity, only the lowest of these is of practical importance, since when this is exceeded, the aircraft will (usually) be destroyed. This phenomenon involves the coupling together of three types of forces, displayed in Collar's triangle of forces[1] namely aerodynamic, elastic and inertia forces. In the classical wing flutter[33] problem the two dominant degrees of freedom are provided by the fundamental bending and torsional modes. Wing flutter is perhaps the most common form of flutter. Single degree of flutter can occur, e.g. stall flutter, aileron buzz.[33]

Although there are aircraft components[1] other than wings prone to this phenomenon this chapter deals with mainplane flutter only, in particular, classical bending/torsion flutter. The method of solution involves the use of generalised coordinates and strip theory.

2.1.1 Formulation of the Flutter Determinant

The use of generalised co-ordinates in aeroelastic stability and response calculations is well established.[37-39] In this method the mass, stiffness and the aerodynamic matrices of an aircraft are expressed in terms of the generalised coordinates. Beam and lumped mass elements are used in the finite element idealisation of the aircraft to obtain the mass and stiffness matrices. The flutter matrix is formed by algebraically summing the generalised mass, stiffness and aerodynamic matrices, (see Appendix A for details), and assuming aerofoil oscillatory motion of the form

$e^{i\omega t}$ the following flutter determinant can be obtained

$$\left| \left[\diagdown K_\diagdown \right] - \omega^2 \left[\diagdown M_\diagdown \right] - \left[Q \right] \right| = 0 \qquad (2.1)$$

The solution of the flutter determinant is a complex double eigenvalue problem because the determinant is primarily a complex function of two unknown variables, the airspeed and the frequency. In the solution procedure the real and imaginary parts of the flutter determinant are evaluated for a range of frequencies at a certain airspeed. The process is repeated for a range of airspeeds until both the real and imaginary parts of the flutter determinant and hence the whole flutter determinant vanish completely. The procedure used is shown in Figure 2.1.

2.1.2 Strip Theory

Strip theory[33-35] is used to represent the two-dimensional, unsteady, aerodynamic force distribution. The theory assumes that the loads of each spanwise station along the wing is dependent only upon the motion of that station at any given time. The theory also assumes that there is no spanwise flow along the wing. The wing is divided into "strips" and the aerodynamic forces upon each "strip" are calculated. The aerodynamic loads are based on the two-dimensional coefficients evaluated at the centreline of each section.

The study of these two-dimensional unsteady aerodynamic models has progressed in two directions. The first is the calculation of the indicial loading due to impulsive motion. This was first investigated by Wagner[4] for incompressible flow. Later R.T. Jones[40] and Lomax et al[41] continued this line of investigation. The second approach is the current unsteady aerodynamic theory employed in this investigation, and is based on the calculation of the loads due to simple harmonic oscillations of the wing or section and was first given by Theodorsen[5] The unsteady aerodynamic theory employed in this investigation, are the explicit expressions for lift and moment as provided by Theodorsen. The Theodorsen's function C(k) which appears in the

expressions for lift and moment is a complex "Circulation function", which accounts for the effect of the oscillatory motion on the magnitude and phase angle of the lift vector.

A representative wing section is shown in Figure 2.2, and in this analysis, aerodynamic parameters are taken in streamwise directions. Using a method proposed by Yates[30] the Theodorsen theory has been modified to take into account the variable section lift curve slope and aerodynamic centre, which takes partial account of finite span and compressibility effects. The effect of drag is considered to be small and is neglected in the analysis. The details of the method is given in Appendix B.

2.1.3 Lifting Surface and Lifting Line Theory

Methods for calculating generalised airforce coefficients on a harmonically oscillating flat plate wing in subsonic flow based on linearised theory have been in existence for some years.[42,43] The linearised theory is used to set up an integral equation relating the unknown loading distribution to the known upwash distribution of the wing

$$
W_\alpha \ (x,y) = \frac{1}{4\pi\rho} \iint_S L(\zeta,\eta) \ \text{Ker}(\ x - \zeta, \ y - \eta) \ d\zeta d\eta \qquad (2.2)
$$

where $L(\zeta,\eta)$ is the loading to be determined over the planform S, $w_\alpha(x,y)e^{i\omega t}$ is the harmonic downwash and Ker, the known Kernel of this integral equation, is like an aerodynamic influence function giving the induced normal velocity at the surface field point x,y due to isolated unit loading at ζ and η. Ker contains the frequency and Mach number as parameters and has been expressed in various explicit forms for different speed regimes.

There are various methods for solving the integral equation, (2.2) numerically. In the one the loading distribution is replaced by a distribution of concentrated loads on certain lines and is known as the doublet lattice method,[8,42] whereas in the other the loading distribution is replaced by an approximation which is continuous over the wing except in the neighbourhood of its leading edge and is known as the lifting line theory.[42,43] In this work the lifting line theory as presented by Davies[7,44] is

40

primarily used. The method of solution is an extension of the steady flow lifting line theory of Multhopp[45] to general-frequency harmonic oscillation. (The details are explained in Appendix B).

2.2 Re-validation of Strip Theory as an Aerodynamic Tool
2.2.1 Binary Flutter of a Typical Section

Strip theory because of its simple form and easy adaptation to computer programming is often considered to be a good aerodynamic tool in flutter analysis especially when it is applied to high aspect ratio, low speed aircraft[33,39,46] and also when applied to helicopter blades.[47] However, a controversy arose recently[6,48] when the validity of strip theory was seriously called in question. The exchanges between Rodden[6] and Lottati[48] have cast doubts in some quarters as to the validity of strip theory and its limitation in oscillatory aerodynamics and flutter analysis. Quite surprisingly, there seem to be no details of reported work wherein a direct comparison of results obtained from the strip theory and those obtained from a more accurate theory such as the lifting line theory has been made. Against the above background, we set out to examine critically the validity of strip theory in the calculation of oscillatory unsteady aerodynamics and the consequent limitation it imposes on flutter analysis. The method used is based on the well-established technique which implements generalised coordinates in the flutter analysis.

The investigation was carried out in two parts. Firstly, the generalised aerodynamic forces obtained from the strip theory based on Theodorsen[5] expressions for unsteady lift and moment were compared with those obtained from a comparable lifting line theory[7,44] of Multhopp type. Secondly, the generalised aerodynamic forces obtained from the above two theories were respectively utilised in the binary flutter analysis of a rectangular straight (unswept) wing, for a direct comparison of the flutter speeds. The aspect ratio of the wing was varied between 4 to 16 and the investigation was carried out within the lower ranges of the airspeed. The severity of all assumptions made was within the limits of the Theodorsen theory of unsteady aerodynamics.

41

2.2.1.1 Method of Analysis

The evaluation of the generalised aerodynamic matrix (usually denoted by $Q(i,j)$ in the literature) using strip theory and Theodorsen expressions for lift and moment is fully described and explained in Appendix B, which also explains the evaluation of the same matrix by using lifting line theory of Multhopp type. Note that the generalised aerodynamic matrix $Q(i,j)$ is a complex matrix with each element having a real part and an imaginary part. The generalised aerodynamic force coefficients evaluated using either of these theories can then be used in the flutter analysis. Here attention is confined to binary flutter only, so that the wing can be given two degrees of freedom only, namely the heave (or plunge) and the pitch, to describe its flutter motion. It is assumed that the wing is resting on two springs; one translational with spring stiffness k_h (giving rise to heave or plunge motion) and the other rotational with spring stiffness k_α (giving rise to pitching or torsional motion). Note that the flutter exhibited by such a model is analagous to the binary flutter of a two dimensional rigid aerofoil[33] rather than to the classical bending-torsional flutter of an elastic cantilever wing (which is also covered later for comparison of results).

The dimensionless flutter speed ($U_f/(b\omega_\alpha)$) can be defined for a detailed parametric investigation of the binary flutter problem of a wing. Bisplinghoff, Ashley and Halfman[33] have produced legendary graphs for binary flutter showing variation of $U_f/(b\omega_\alpha)$ against ω_h/ω_α for a range of x_α values. Non-dimensional quantities shuch as those of Bisplinghoff are defined in the usual notation in obtaining the flutter results.

2.2.1.2 Discussion of Results

The details of the computed results indicate that the most sensitive parameter in the analysis when evaluating the strip theory for oscillatory aerodynamics and flutter analysis is, as expected, the aspect ratio (AR) of the wing. So results are obtained for a wide range of aspect ratios for both the oscillatory unsteady aerodynamic forces as well as for the flutter speeds. Representative results for AR = 16, 6 and 4 for the non-dimensionalised generalised aerodynamic forces using both the

42

Strip Theory (ST) and the Lifting Line Theory (LLT) are shown in Figures 2.3 to 2.5 respectively for wings with $\mu = 20$, $a_h = -0.2$, $\omega_h/\omega_\alpha = 0.2$, $b = 0.5m$ and $r_\alpha^2 = 0.25$ for $M = 0.4$.

The parameters used in the generation of the generalised aerodynamic forces, using lifting line theory, (Ref.(44)) are shown in Table 2.1. As a means of testing convergence of the results, selected values of generalised forces for the aspect ratios considered were obtained using larger values of m, n and q, (defined in Appendix B) as suggested by Davies[7]. However q was found to be the most sensitive parameter in the analysis. Table 2.2 outlines the values used and the maximum discrepancy in the real and imaginary part was found to be in the term Q(1,2), (considered to be the important term here), compared with those obtained using the above parameters. Although the discrepancy in the imaginary term Q(1,2) for AR = 16 is large, the original values of imaginary part of Q(1,2) were subsequently multiplied by 1.7 in an ad hoc manner to observe the resulting change in flutter speed. However the original flutter speed did not change. This leads to the conclusion that the flutter speed is not very sensitive to the imaginary part of Q(1,2). Using the appropriate generalised aerodynamic terms from both strip theory and lifting line theory, the flutter speeds and the corresponding frequencies at flutter were obtained and are given in Table 2.3 for comparison.

The real and imaginary parts of the non dimensionalised generalised aerodynamic forces given by $Q(i,j)/\rho U^2$ obtained from the two theories are plotted against the reduced frequency parameter k ($= \omega b/U$). (Note that since heave and pitch motions only are considered, the generalised aerodynamic matrix Q(i,j) will be a 2X2 complex matrix).

Variation of Q_{LLT} and Q_{ST} with reduced frequency k for AR = 16 is shown in Figure 2.3. There is generally good agreement between the two methods. In binary flutter of this type, it is the real part of $Q(1,2)/\rho U^2$ which is usually a dominant term. Referring to this term, the figure indicates the difference between the methods decreases as the frequency is increased, which is generally expected. At k=0 the steady lift state the

43

discrepancy is 10.6%. However within the practical frequency range (i.e. 0.1 < k < 0.5) the discrepancy varies between 4.2% to -2.5% with a corresponding variation of 30% to 7.3% for the imaginary component which plays a relatively minor role in this flutter compared to the real part. The discrepancy arises as a result of the imaginary term being very small, for small values of k, hence comparisons involving this term will be omitted for lower frequencies. Table 2.3 indicates the resulting difference in flutter speeds as -1.8% , validating strip theory at this aspect ratio.

As Figure 2.4 indicates even at AR = 6 the agreement is still reasonable. Considering the circulatory term $Q(1,2)/\rho U^2$ again, there is an initial zero frequency discrepancy of 28.7% but this decreases with increasing frequency. In the practical reduced frequency range under consideration the difference decreases from 20% to 6.3% with a corresponding value of 0.25% for the imaginary part, at the limit of the frequency range considered. Table 2.3 indicates that the difference in flutter speed is -5.1% , still within engineering accuracy at this aspect ratio.

At AR = 4 in Figure 2.5 the influence of finite span effects become more apparent. The initial difference at zero frequency is 39.5% and decreases from 30% to 15% between 0.1 < k < 0.5 with a corresponding percentage error of -4% for the imaginary part. However as Table 2.3 suggests the differences in flutter speeds obtained from the two theories of -9.5% is still reasonable.

The closeness of the results demonstrates the accuracy of the strip theory when compared to the lifting line theory particularly, at high aspect ratios.

2.2.2 Inclusion of Elastic Modes in Flutter Analysis

The example of binary flutter above using a representative section[33] provides a quick and useful means of comparison. However to gain a more realistic insight, it is useful to incorporate the elastic degrees of freedom, at least the two predominant modes in classical bending/torsion flutter, namely the first (fundamental) bending and first (fundamental) torsional modes. Two examples provided respectively by Goland[49,50] and Loring[37] are used in the current investigation. As before the real and imaginary parts of

44

$Q(i,j)/\rho U^2$ from both aerodynamic theories are plotted against the reduced frequency k, for the Goland example only, as this wing has the lower aspect ratio of the two. The flutter speeds for the Goland and Loring wings were calculated from the two methods and were compared with experimental results, wherever appropriate. These quantities were obtained in the same manner as outlined in Appendix B, For these two wings it was necessary to take into account the effects of inertial coupling. Also instead of considering the rigid body modes in heave and pitch, the first bending and first torsional modes of the wing were only introduced assuming cantilever boundary conditions so that the resulting generalised aerodynamic matrix Q(i,j) became complex 2X2 again.

For both wings the following parameters were used in the generation of the generalised aerodynamic forces, when using Davies' program: m = 28, n = 4 and q = 4, 2, 2, 4. These parameters were suggested by Benton (Ref.(48)) in a private communication. The flutter speed and flutter frequency using strip theory were found using the program CALFUN.[28]

2.2.2.1 Goland Wing

This example was taken from an early work on flutter analysis of a uniform cantilever wing of AR = 6.6, carried out by Goland[50] Characteristics of the wing properties needed for calculation are shown in table 2.4.

Variation of Q_{LLT} and Q_{ST} against k for M= 0.4 as a result of the two analysis are shown in Figure 2.6. There is generally good agreement between the two theories, which improves with increasing reduced frequency as expected, which was also noted before when dealing with the rigid binary flutter, (see section 2.2.1). Referring to Figure 2.6 and the dominant term Q(1,2), there is an initial zero frequency discrepancy of 48.9% between strip theory and lifting line theory. However this decreases with increasing k. Considering the practical range of k being 0.1 < k < 0.5 the difference is 42.4% and 30.5% respectively for the real part and 17% for the imaginary part. Again the imaginary term at k = 0.1 is omitted as this term is small and as expected will not contribute much to the overall motion, unlike the dominant real term.

Considering the term Q(1,1) the difference at k = 0 is 49.6%.

However over the range $0.1 < k < 0.5$ the corresponding differences are 46.6% and 77.9% for the real part and 20.5% for the imaginary part.

For Q(2,1), the difference at $k = 0$ is 40%. The subsequent percentage differences in the real term, over the same range is 32.3% and 19.9%. For the imaginary term this is 27% at $k = 0.5$.

Finally the difference for Q(2,2) at k=0, is 39.3%. Over the range of k considered the resulting difference is 32.0% and 17.2% for the real part and 0.38% for the imaginary part.

The overall good agreement between the two aerodynamic theories is borne out from the established flutter speed and flutter frequency presented in Table 2.5, where the percentage difference is between -15.3% and 5.2% respectively. Also noted incidentally is the close agreement of the flutter speed of 137.2 m/s and flutter frequency of 70.68 rad/s as obtained from Goland's corrected flutter result.[50]

2.2.2.2 Loring's Wing

This is a wing flutter model taken from Loring's[37] classical paper on the use of generalised coordinates in flutter analysis. It is a uniform cantilever wing of AR = 13.52, its properties are given in Table 2.6. Loring's experimental results are also presented in Table 2.7 along with those obtained from a flutter analysis using strip theory and lifting line theory. As the results in the table suggest, it takes at least an analysis using 4 modes before the flutter speed obtained using lifting line is close to that obtained from experiment. The reason for this could be the value of m used in the analysis, as the wing has a large aspect ratio and hence a larger value of m is needed to model accurately the reduction in loading distribution close to the wing tips. On the contrary the difference, considering strip theory, is only 0.55% and -11% for the flutter speed and flutter frequency respectively, using the same number of modes. It is interesting to note that Loring's flutter analysis produced a flutter speed of 90.7m/s and a flutter frequency of 57.7 rad/s, using 3 modes only.

2.3 Sensitivity Analysis

A sensitivity analysis was carried out on the Goland[50] and Loring[37] wings in addition to that of the Kestrel wing, with possible applications for optimisation. The percentage variation in flutter speed against percentage variation of four parameters, EI, GJ, M/l and I_p/l was investigated using CALFUN[28] and the results are shown in Figure 2.7. It is noted that raising the torsional frequency has the same effect as lowering the bending frequency. It is because the frequency margin between these modes increase resulting in later coupling and an increase in flutter speed. The most sensitive parameter for these wings appears to be the torsional rigidity. Noting that the Kestrel wing has an aspect ratio of 31.35 it is seen that for a given change in either stiffness or inertia parameter the percentage variation in flutter speed increases with decreasing aspect ratios.

2.4 Effect of Sweep on Flutter
2.4.1 Introduction

Strip theory can be extended to large-aspect ratio swept wings. In doing so, it is observed that some swept wing structures have their ribs oriented in the flight direction, while others have ribs nearly perpendicular to the midchord line or elastic axis.[33] In the first case it is reasonable to assume that streamwise sections remain undeformed during bending or torsion, so that the strip method discussed already is very suitable. Thus it will suffice to take strips parallel to the flight direction as shown in Figure 2.2 and multiply the aerodynamic quantities such as lift L and moment M_α by cos Λ (this is outlined in detail in Appendix B).

Wing structures with ribs perpendicular to the midchord line twist more like a surface developed out of straight lines normal to the elastic axis, (since perpendicular sections are the ones which do not bend). Therefore there are simple harmonic camber changes in planes parallel to U, the amount of camber being proportional to the product sin Λ $(\partial\alpha/\partial y)$. This leads to the alternative method for applying two-dimensional aerodynamics to a finite swept wing as outlined in Appendix B based on velocity

47

components.

Prior investigations into the behaviour of sweep have involved the use of classical solutions using aerodynamic derivatives.[33,52-56] However the velocity component theory[33,57,58] will be discussed as this theory uses the Theodorsen function and lends its self to a normal modes approach. It has been used to calculate the flutter speed of forward swept wings and in its quasi-steady form has predicted divergence speeds.[59,60] This theory has been extensively modified by Yates[30] and successfully employed in flutter calculations for a range of subsonic and supersonic speeds. Notably the theory has also been applied in the transonic domain.[61]

However Bisplinghoff et al[33] has highlighted some short falls in the velocity component theory over its streamwise counterparts, by considering some examples of swept wings at different sweep angles.[57] The results obtained in Ref.(57) were obtained, using the first uncoupled bending and torsional modes. It is in the light of having the facility to utilise coupled modes in the computer program and to also gain an insight into the two theories, the present investigation, in a similar manner to Bisplinghoff, is initiated.

2.4.2 Cosine Theory

The cosine theory[33] takes parameters normal to the flight direction as shown in Fig 2.2 and simply multiplies the unsteady lift (L) and moment (M_α) at $\Lambda = 0^0$ by $\cos \Lambda$. The coupled elastic modes are taken normal to the flight direction. For this case the mass and stiffness matrices in the existing code CALFUN were modified to take into account the structural effect of sweep. Results for eigenvalues i.e. natural frequencies, were checked against Ref.(62).

The case studies considered here compliment the work already carried out by Bisplinghoff et al[33] and Barmby et al[57] very substantially. Swept wings of aspect ratio 4 were dealt with as before to provide an insight into the possible limitations of strip theory when applied to low aspect ratio swept wings.

2.4.3 Velocity-Component theory

Here aerodynamic and structural parameters are taken normal

to the elastic axis[33] as shown in Figure 2.2, the modes are defined along the spar.

As modes are required along the spar the original structural analysis of CALFUN need not be changed and the modes obtained for a straight wing implemented. However the aerodynamic subroutine is adapted to incorporate the changed aerodynamics as outlined in Appendix B. (This new code is called CPSWPG). Although second order terms are generally neglected, these were kept to facilitate checking with Ref.(63). As a check, the case of single degree of freedom flutter for a highly swept wing was chosen. If a swept wing is swept large enough and has a large enough mass parameter the wing can theoretically flutter[63] in pure bending only. The results were found to agree completely with those given in Fig.7 of Ref.(63).

Table 2.8 and 2.9 display the frequencies obtained and the corresponding flutter speeds using the first bending and torsional modes for both the cosine theory and velocity component theory and compares those provided by Ref.(57).

2.4.4 Comparison of Flutter Speeds and Frequencies and Generalised Aerodynamic Forces

2.4.4.1 Flutter Speeds and Frequencies

Referring to Table 2.8 the coupled frequencies obtained from the two methods are identical as expected. The agreement with those obtained in Ref.(57) is within engineering accuracy, with the exception of the bending frequencies at sweep angles 0^0 and 30^0. However there is no indication of mode shapes which is perhaps more relevant.

Referring to Table 2.9 it can be seen both methods maintain their conservatism in predicting flutter speeds when compared with the experimental results. Agreement is seen to improve as the sweep increases beyond 30^0 with differences falling within engineering accuracy, although the agreement is not as good as for the straight planform. The present cosine theory is found to be marginally more accurate. The close agreement between these two methods was also demonstrated in recent studies on swept composite plates, carried out at the City University and discussed in Appendix C. The discrepancies may arise from inaccurate

determination of the wing modes. Without any indication of experimental mode shapes, it is difficult to draw a comprehensive reason to the current discrepancies with experiment. As a note the experimental results are also compared with Ref.(57) own theoretical analysis, and this is shown also in Table 2.9. This approach includes coupling only within the inertial terms. Below a sweep angle of 30° it is found to yield flutter speeds and frequencies, comparable with the current analysis, involving the full effects of coupling. However at higher angles of sweep this agreement is lost and at 60° sweep it no longer maintains its conservatism.

The experimental results and the results from the two theories are then non-dimensionalised with respect to a reference speed V_R. This speed is the flutter speed of the same wing rotated back to the unswept condition. Figure 2.8 shows these ratios plotted against sweep angle. The agreement in the two methods is shown, being within 5% at $\Lambda = 60^{\circ}$. Curves of $1/\cos \Lambda$ and $1/\sqrt{\cos \Lambda}$ are shown in Figure 2.9 for comparison, as carried out in Ref.(57). The two methods also predict the speed decreases slightly for small angles of sweepback and then increases rapidly as sweepback increases as concluded by Molyneux[54,55].

In order to extend this investigation to higher aspect ratios, Figure 2.10 shows V_f/V_R plotted for AR = 6. The methods are in fact in closer agreement, the difference being only 3% at $\Lambda = 60^{\circ}$.

2.4.4.2 Comparison of Unsteady Generalised Aerodynamic Forces

In Figures 2.11 to 2.13 the generalised forces are plotted for sweep angles 10°, 25° and 45° for AR 4 respectively using the first bending and first torsional modes, for the two methods. This is reprinted from work carried out in Ref.(64), partly supervised by the author. As before the generalised forces are represented in terms of their real and imaginary parts with Mach number up to 0.665, verging on the limitations of strip theory[33].

Briefly the worst discrepancies appear to be in the real Q(2,2) and imaginary Q(1,2) terms. The discrepancy between the two theories at Mach number 0.11 to 0.665 for the real Q(2,2) terms are 4.8% to 3.7% respectively for $\Lambda = 10^{\circ}$, 25.8% to 27.5% for $\Lambda =$

25°, 100% to 93% for $\Lambda = 45^{\circ}$.

Similarly the discrepancy noted for the imaginary part of $Q(1,2)$ are 27% to 4.2% for $\Lambda = 10^{\circ}$, 75% to 1.2% for $\Lambda = 25^{\circ}$, 134% to 32% for $\Lambda = 45^{\circ}$. However as mentioned earlier the magnitude of the imaginary terms is negligible at low frequencies. It is observed that although discrepancy is large at 45^{0} there appears to be little difference in the subsequent flutter speeds predicted by the two theories. This perhaps suggests the small contribution the above terms make in this type of flutter.

Aspect Ratio	m	n	q
16	34	4	2
6	8	2	2
4	8	2	2

Table 2.1 Parameters used for generalised aerodynamic forces using lifting line theory for rigid binary flutter

AR	m	n	q	Maximum Percentage (%)	
				$Re(Q_{12})$	$Im(Q_{12})$
16	34	4	32	0.49	65.6
6	12	4	32	6.20	-3.33
4	12	4	32	4.69	2.373

Table 2.2 Variation of Q(1,2) with lifting line parameters

Aspect Ratio	Strip Theory		Lifting Line Theory	
	Flutter Speed (m/s)	Flutter Frequency (rad/s)	Flutter Speed (m/s)	Flutter Frequency (rad/s)
16	87.4	35.0	89.0	34.0
6	138.0	32.0	145.0	33.0
4	167.0	31.0	184.0	32.6

Table 2.3. Flutter speed and flutter frequency using strip theory and lifting line theory.

$b = 0.5m$, $a_h = -0.2$, $r_\alpha^2 = 0.25$, $\mu = 20$.

$$
\begin{array}{ll}
EI = 9.773 \times 10^6 \ Nm^2 & l = 6.096 \ m \\
GJ = 9.876 \times 10^5 \ Nm^2 & b = 0.9144 \ m \\
M/l = 35.717 \ kg/m & a_h = -0.340 \\
I_\alpha/l = 8.642 \ kgm & \rho = 1.225 \ kg/m^3 \\
x_\alpha = -0.183 \ m &
\end{array}
$$

Table 2.4   Structural and aerodynamic properties of the Goland wing

Number of Modes	Strip Theory		Lifting Line Theory	
	Flutter Speed (m/s)	Flutter Frequency (rad/s)	Flutter Speed (m/s)	Flutter Frequency (rad/s)
2	137.5	69.0	158.5	65.4

Table 2.5   Flutter speed and flutter frequency using strip theory and lifting line theory for Goland wing

$$
\begin{array}{ll}
EI = 677.6 \ Nm^2 & l = 2.06 \ m \\
GJ = 1019.6 \ Nm^2 & b = 0.1524 \ m \\
M/l = 8.06 \ kg/m & a_h = -0.4 \\
I_\alpha/l = 0.0585 \ kgm & \rho = 1.112 \ kg/m^3 \\
x_\alpha = -0.038 \ m &
\end{array}
$$

Table 2.6   Structural and aerodynamic properties of the Loring wing

53

Number of Modes	Experimental Result		Strip Theory		Lifting Line Theory	
	Flutter		Flutter		Flutter	
	Speed (m/s)	Frequency (rad/s)	Speed (m/s)	Frequency (rad/s)	Speed (m/s)	Frequency (rad/s)
2	—	—	97.5	49.0	105.0	51.6
3	—	—	91.0	58.0	94.7	63.0
4	—	—	90.5	57.7	94.4	63.3
	90.0	64.0				

Table 2.7   Flutter speed and flutter frequency using strip theory and lifting line theory for Loring wing

Sweep Λ°	Frequencies (Hz)		Percentage difference %
	Experimental	CALFUN	
0°	1B 45.0	36.0	-25.0
	1T 108.0	104.5	-3.0
15°	1B 43.0	49.5	13.1
	1T 103.0	102.5	-0.45
30°	1B 33.0	40.4	18.3
	1T 94.0	91.5	2.8
45°	1B 22.0	24.3	9.6
	1T 93.0	97.2	4.4
60°	1B 12.0	11.7	-2.9
	1T 93.0	85.1	9.2

1B = First bending

1T = First Torsion

Table 2.8   Experimental and theoretical frequencies for the swept wings of Ref.(57)

54

Sweep $\Lambda°$	Flutter speed and Frequency m/s (Hz)				% Difference		
	Exp Ref.57	Theory Ref.57	CPSWPG	CALFUN	Ref.57	CPSWPG	CALFUN
0°	122.48 (66.0)	—— (——)	117.8 (64.0)	117.8 (64.1)	—— (——)	-3.9 (-2.9)	-3.9 (-2.9)
15°	109.5 (62.0)	91.6 (71.0)	86.1 (74.0)	86.7 (72.8)	-19.5 (12.7)	-27.0 (16.0)	-26.0 (14.9)
30°	90.3 61.0)	71.3 (65.0)	69.3 (66.6)	70.6 (65.1)	-26.6 (6.1)	-30.0 (8.4)	-27.9 (6.3)
45°	87.6 54.0)	74.2 (61.0)	79.7 (64.3)	81.4 (61.8)	-18.0 (11.5)	-9.9 (16.0)	-7.6 (12.7)
60°	80.0 37.0)	82.25 (58.0)	74.4 (51.9)	76.0 (49.7)	2.7 (36.3)	-7.5 (28.8)	-5.0 (25.6)

Table 2.9 Experimental and theoretical flutter speed and flutter frequencies for the swept wings of Ref.(57)

```
        ┌─────────────────────────┐
        │  Idealised Aircraft Model│
        │  (i)  Beam and Lumped    │
        │         mass elements    │
        │  (ii) Wing Geometry      │
        └────────────┬────────────┘
                     │
        ┌────────────┴────────────┐
        │    Mass and Stiffness    │
        │         Matrices         │
        └────────────┬────────────┘
                     │
        ┌────────────┴────────────┐
        │   Natural Frequencies    │
        │           and            │
        │       Mode Shapes        │
        └──┬──────────────────┬────┘
           │                  │
┌──────────┴──────┐   ┌───────┴─────────────┐
│ Generalised Mass│   │ Aerodynamic matrix  │
│ and Stiffness   │   │ in modal co-ordinates│
│ Matrices from   │   │ using strip theory  │
│ selected modes  │   │                     │
└──────────┬──────┘   └───────┬─────────────┘
           │                  │
        ┌──┴──────────────────┴────┐
        │     Formulation of       │
        │    Flutter Determinant   │
        └────────────┬────────────┘
                     │
        ┌────────────┴────────────┐
        │   Solution of Complex    │
        │    Flutter Determinant   │
        └────────────┬────────────┘
                     │
        ┌────────────┴────────────┐
        │     Flutter Speed        │
        │     Frequency and        │
        │    Aeroelastic Modes     │
        └─────────────────────────┘
```

Fig. 2.1   Procedure for flutter analysis

X   X̄

U

Y

Λ

2b   2b̄

Ȳ

Elastic axis

1

Aerodynamic centre

Airflow

L

h

α

Mα

bac

bah

Mid-chord

Aerodynamic centre

Inertia axis

Elastic axis

bxα
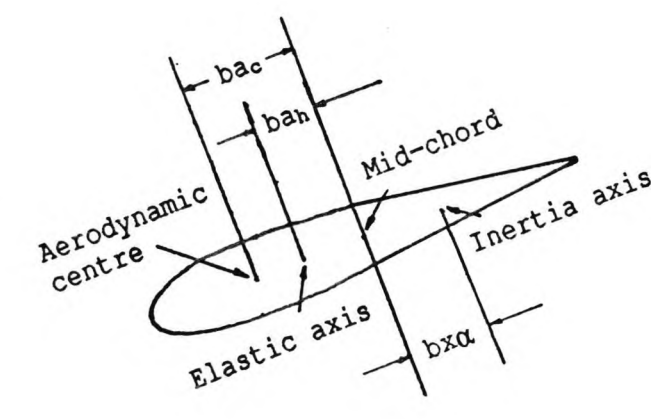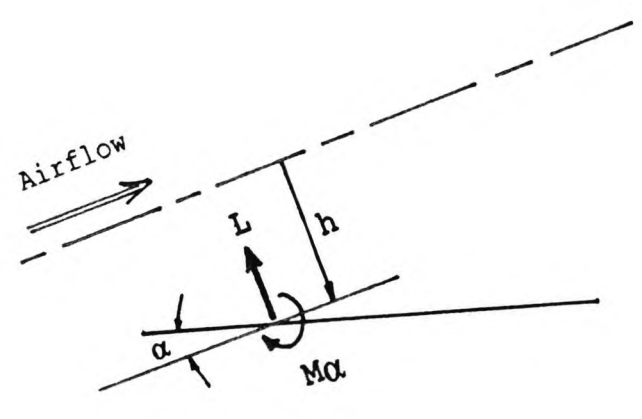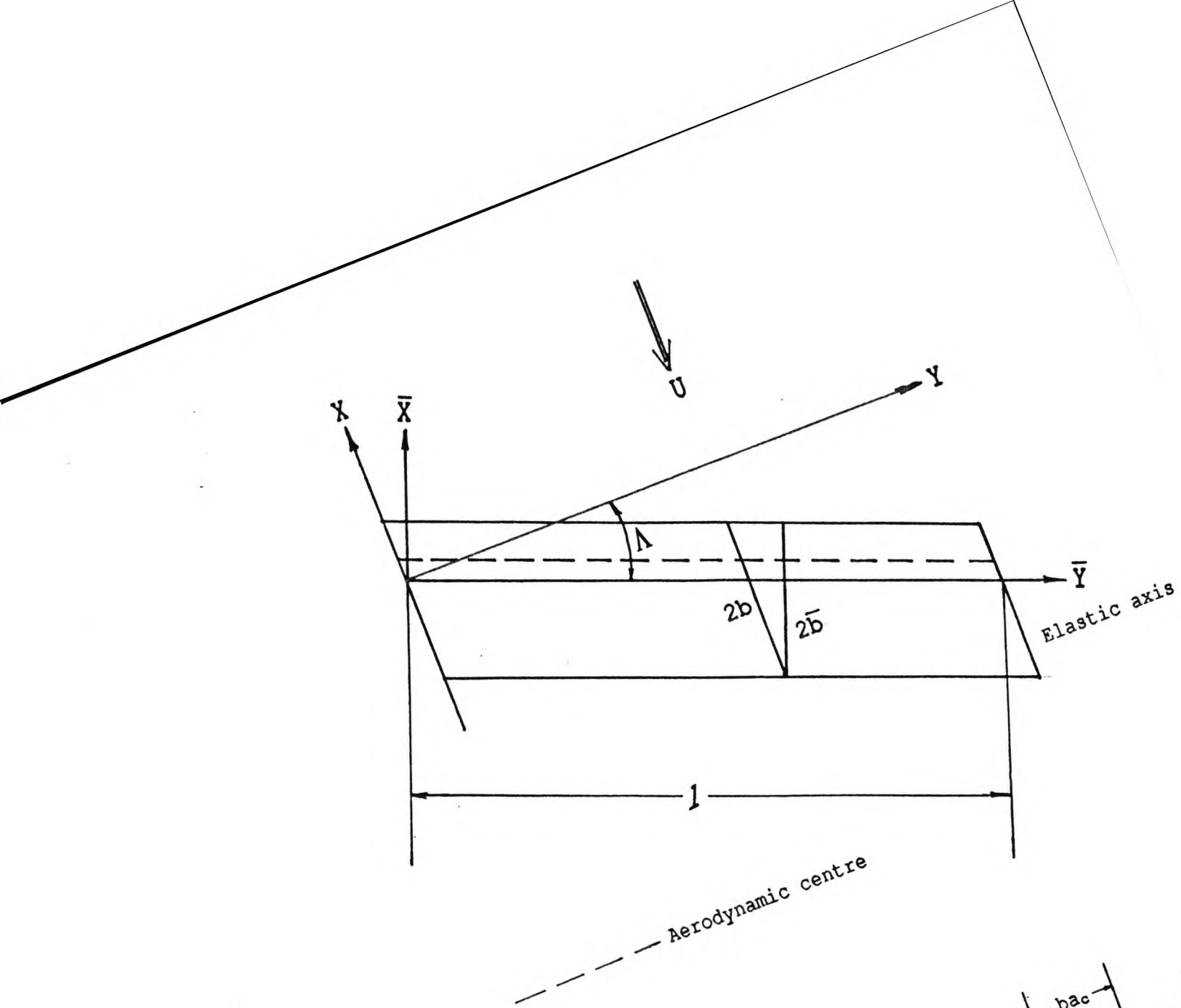
Fig. 2.2 Wing representation
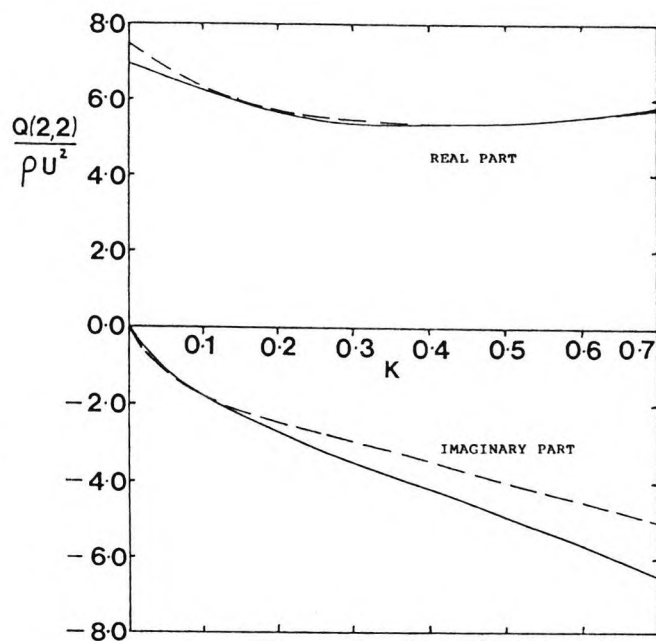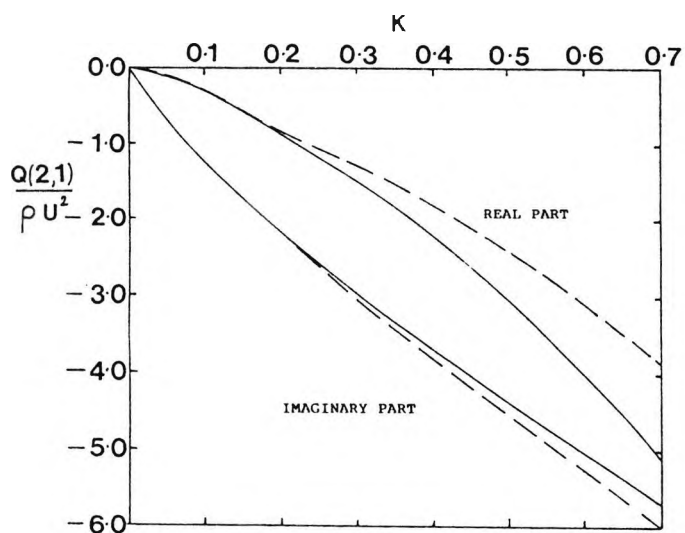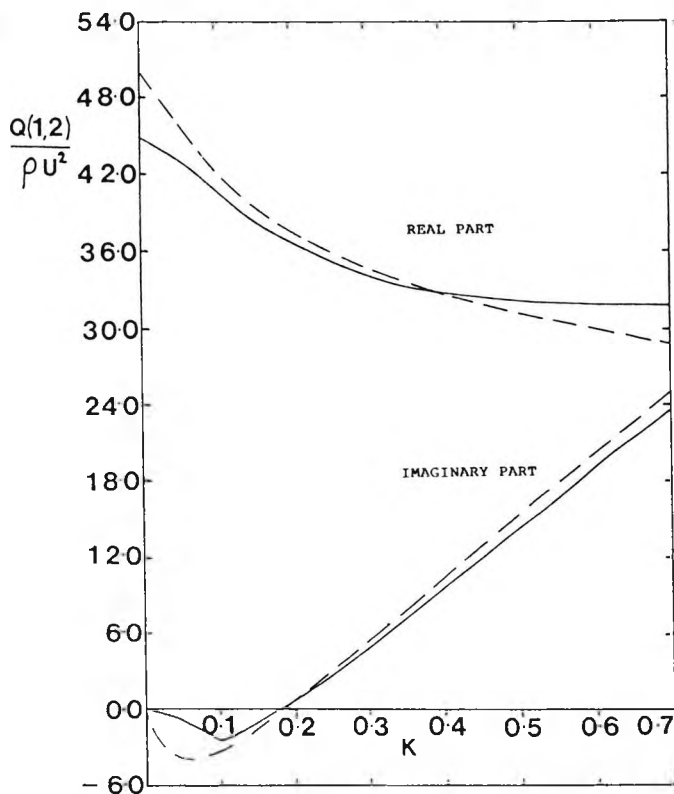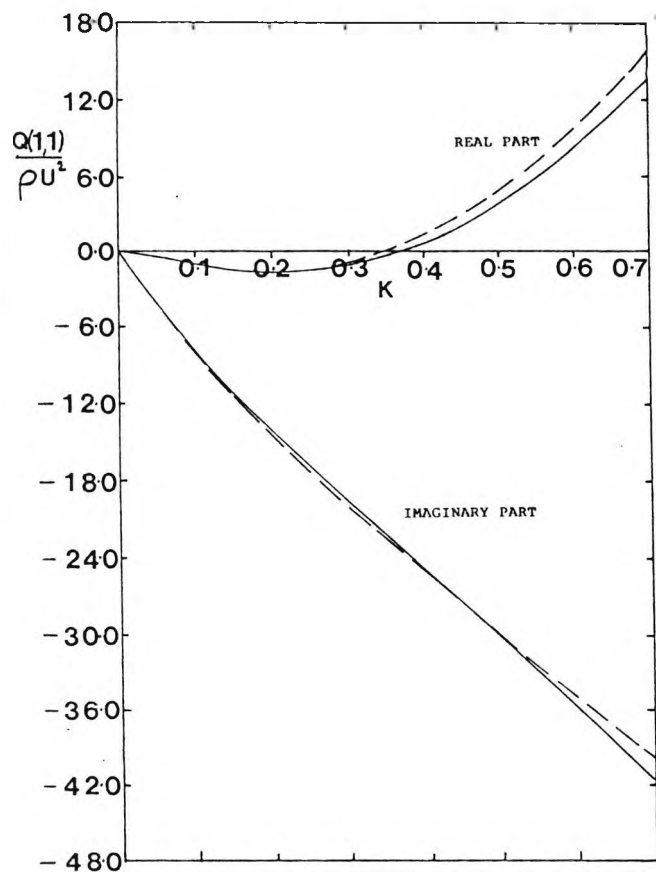
Fig. 2.3   Comparison between lifting line theory and strip theory
for aspect ratio 16 at M=0.4
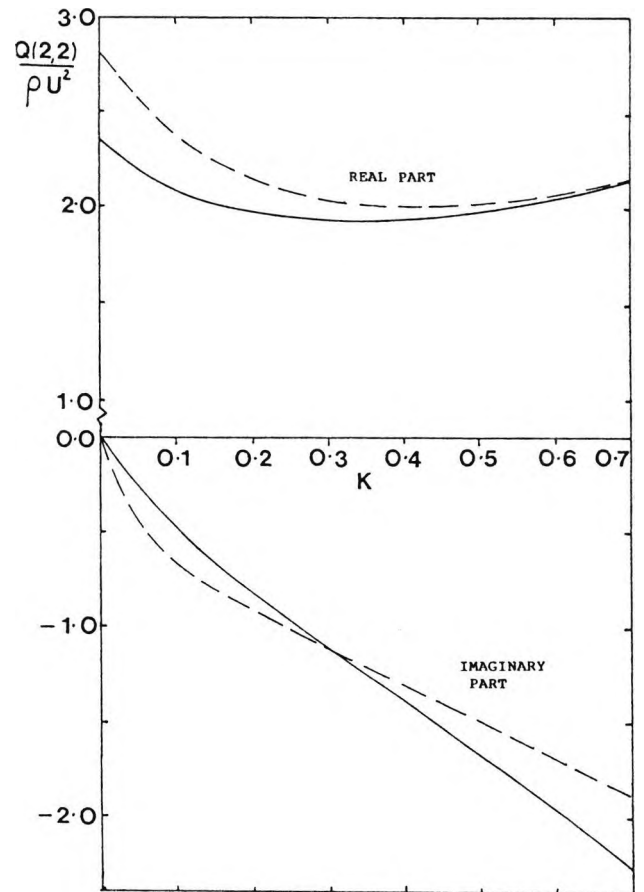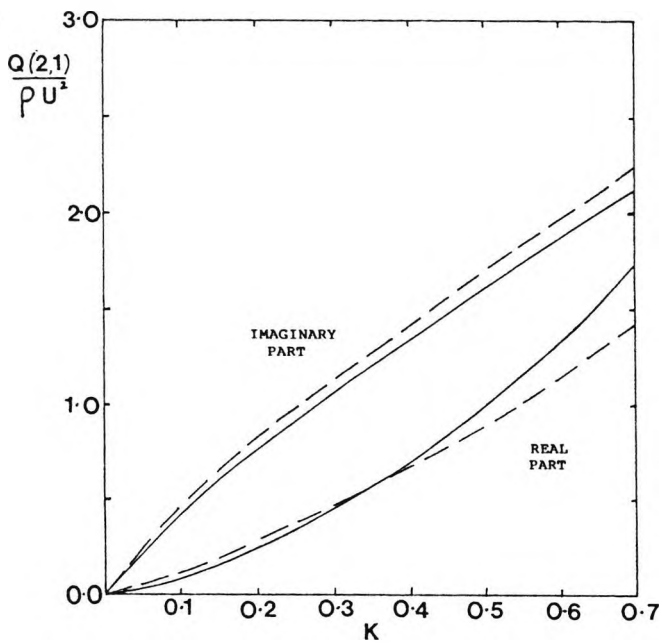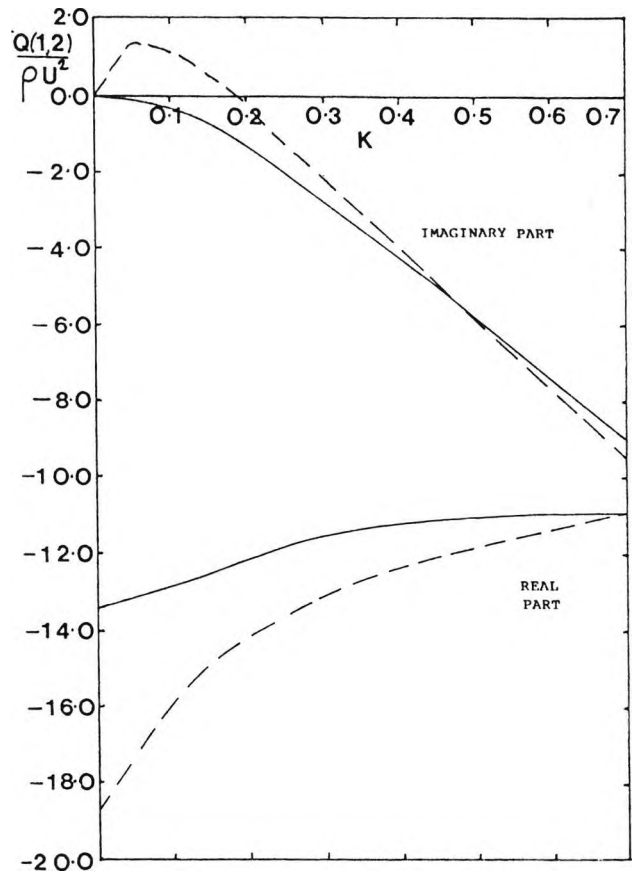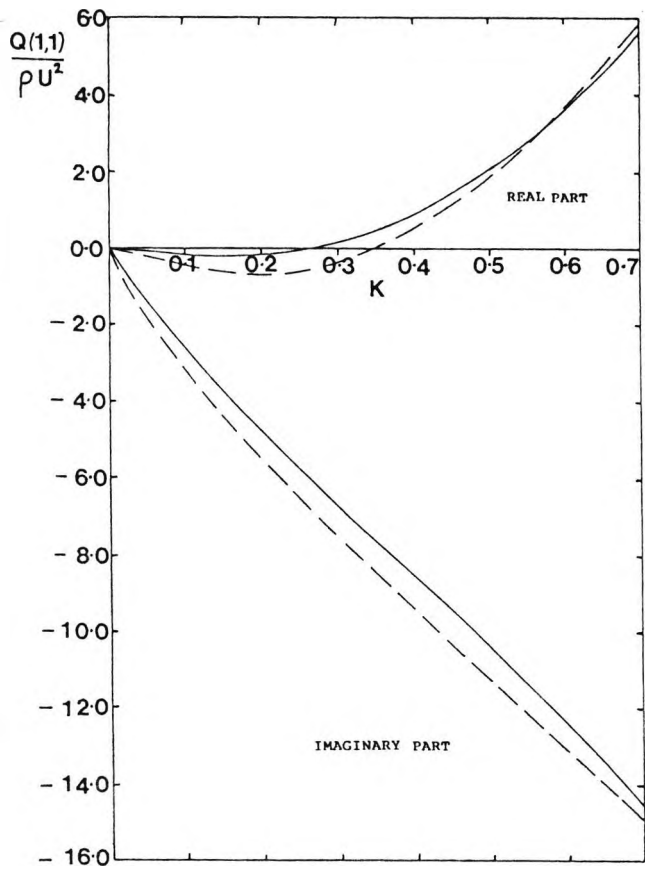
Fig. 2.4   Comparison between lifting line theory and strip theory
for aspect ratio 6 at M=0.4
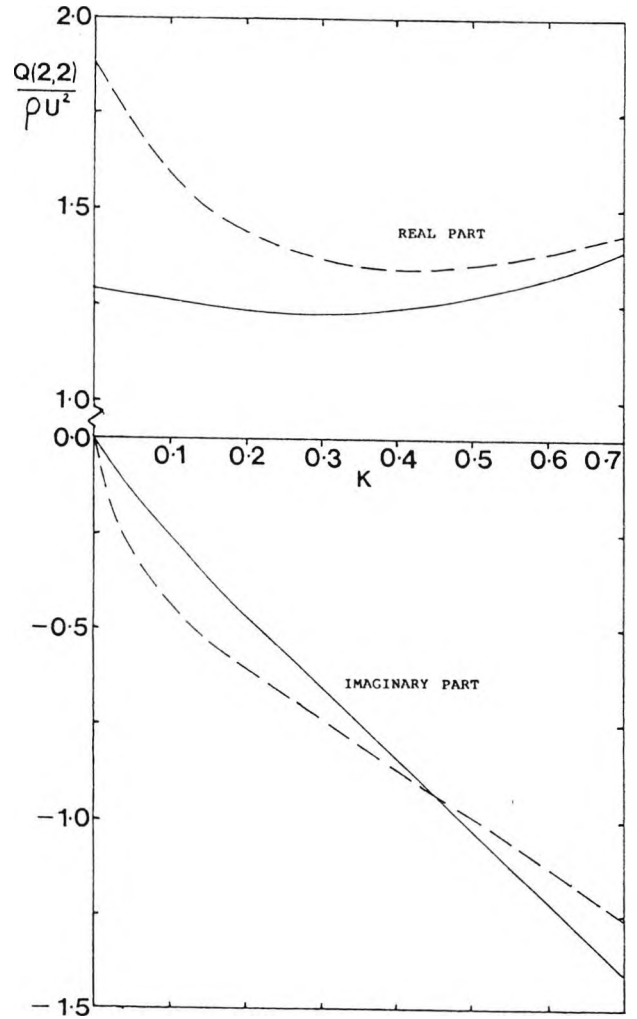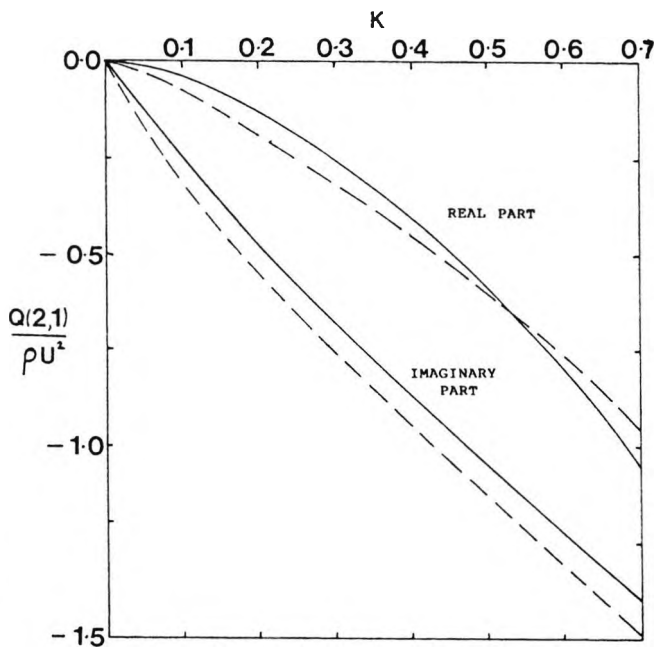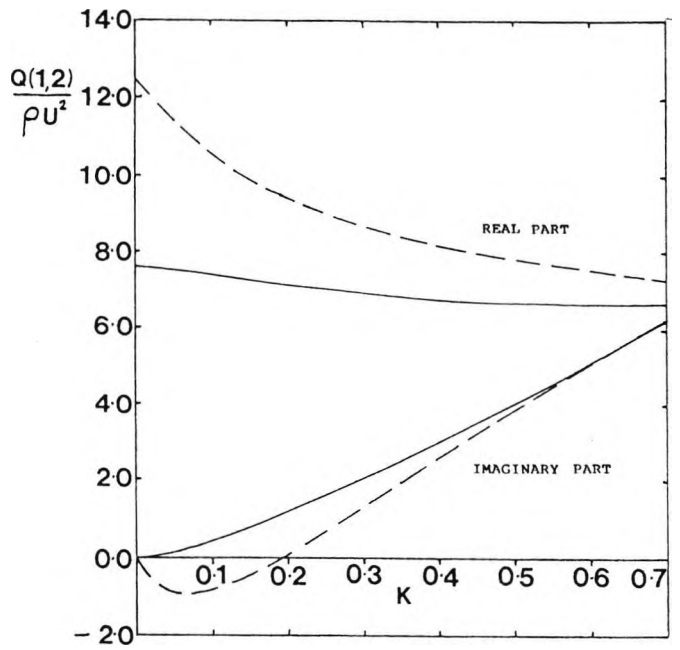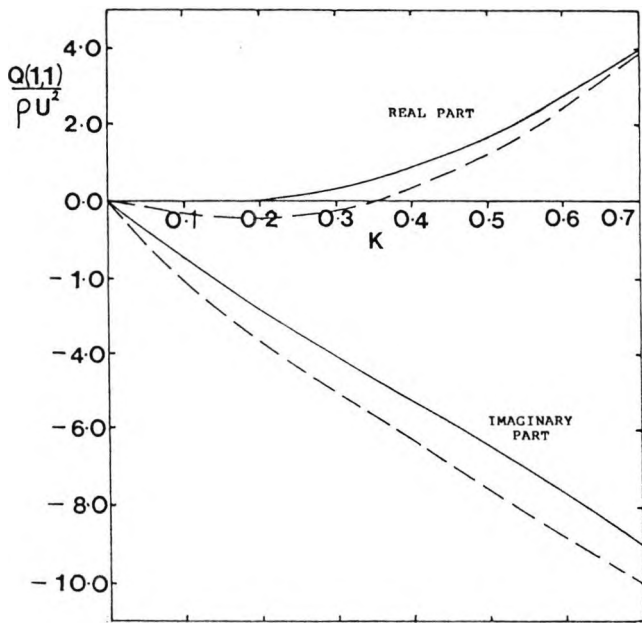
Fig. 2.5   Comparison between lifting line theory and strip theory
          for aspect ratio 4 at M=0.4
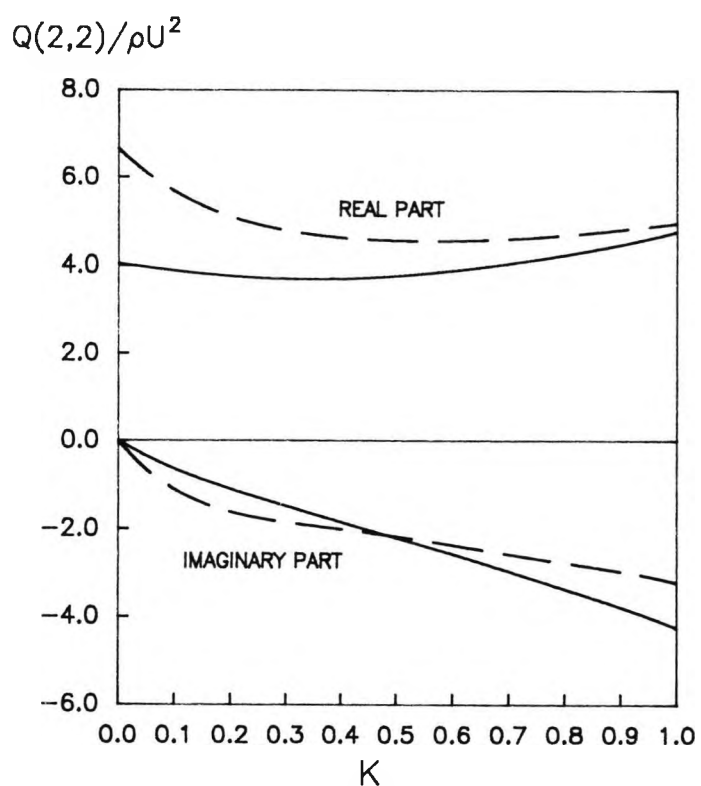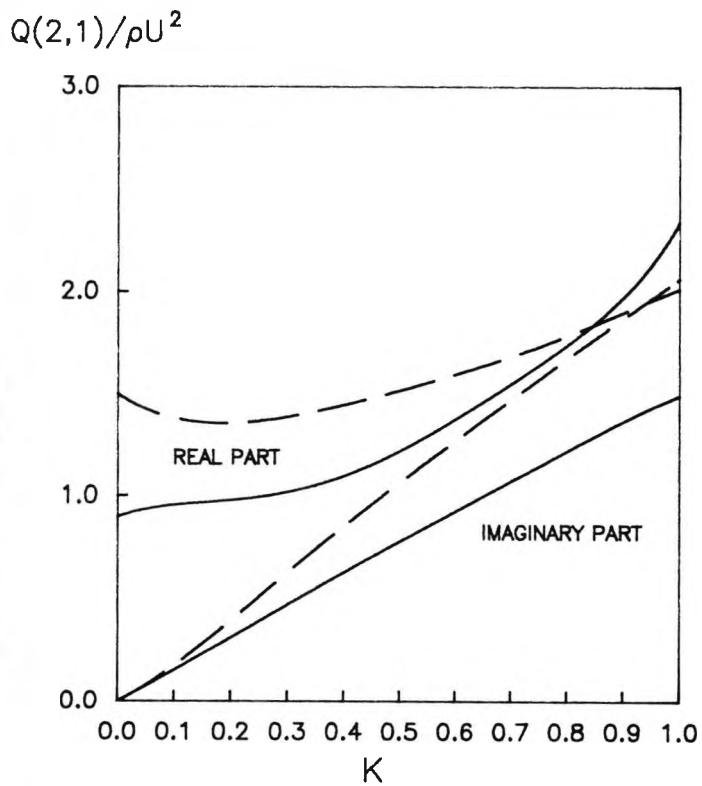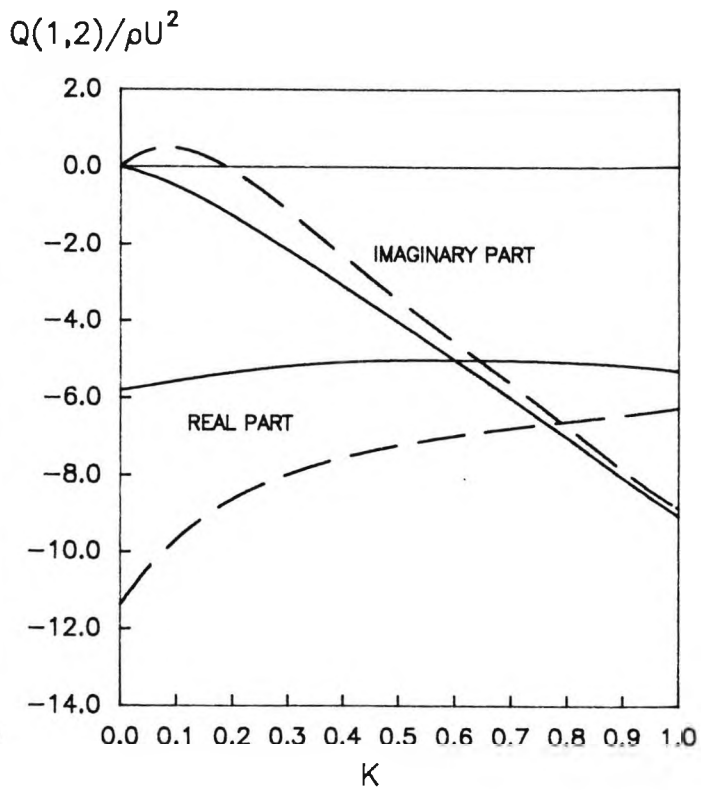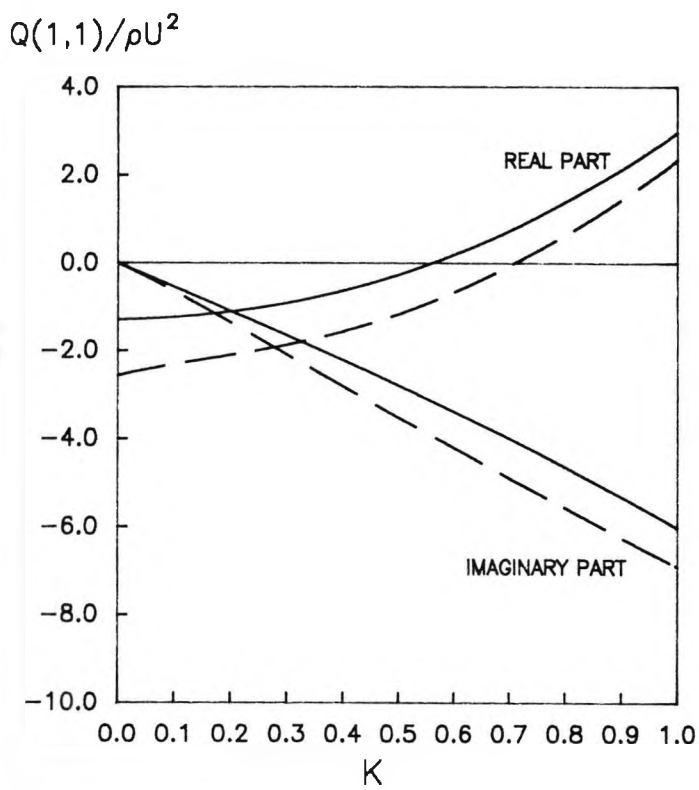
Fig. 2.6   Comparison between lifting line theory and strip theory
for Goland wing at M=0.4
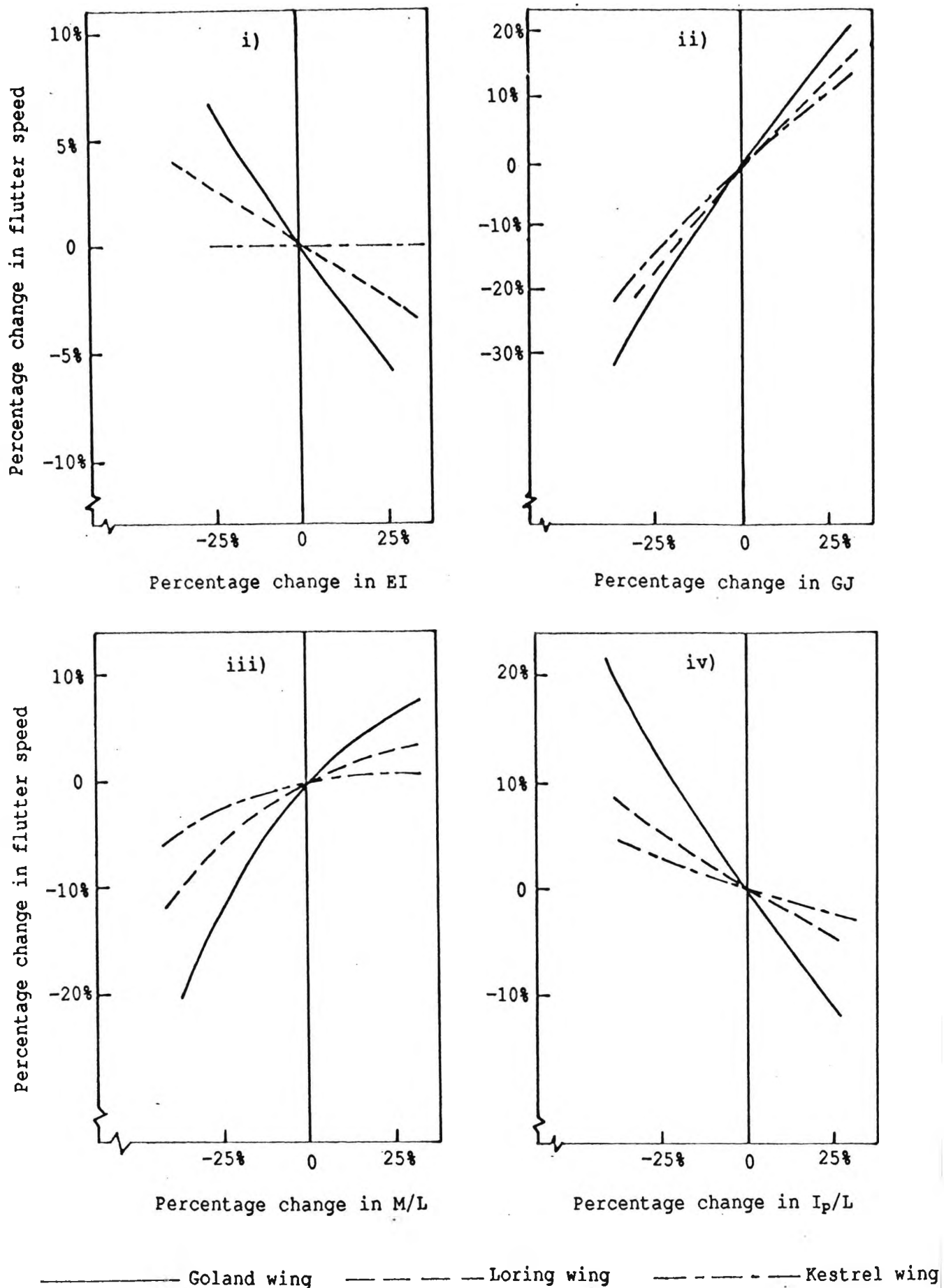
Fig. 2.7 Percentage variation of flutter speed against percentage of
i) Bending rigidity (EI)
ii) Torsional rigidity (GJ)
iii) Mass per unit length (M/L)
iv) Mass moment of inertia per unit length (I_p/L)

FLUTTER SPEED RATIO VF/VR

Legend:
- GARRICK'S THEORY
- COSINE THEORY
- COMPUTED EXPTL VALS

ANGLE OF SWEEP (DEGREES)
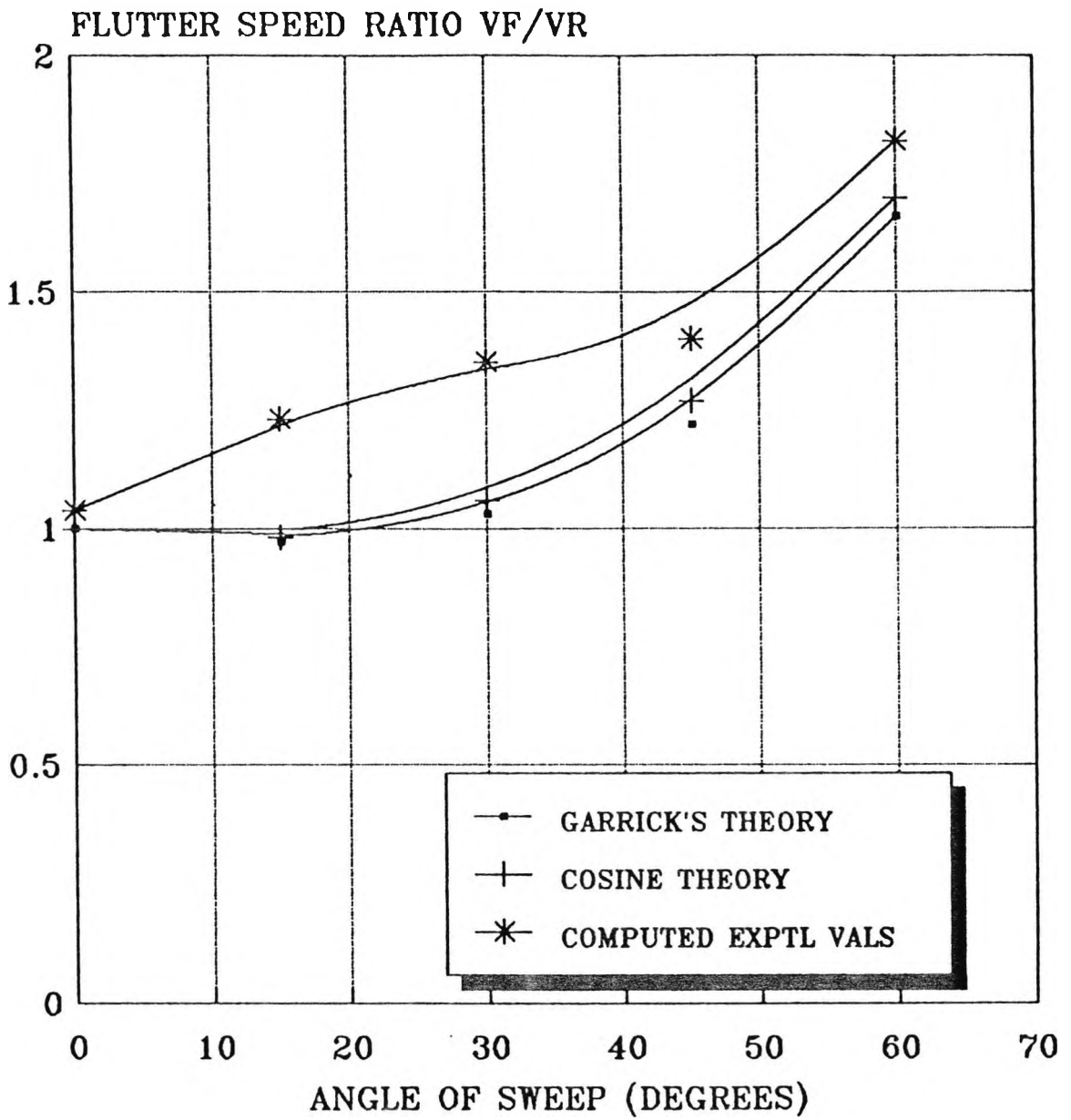
Fig. 2.8 Effect of sweep on flutter comparison between theoretical and experimental results
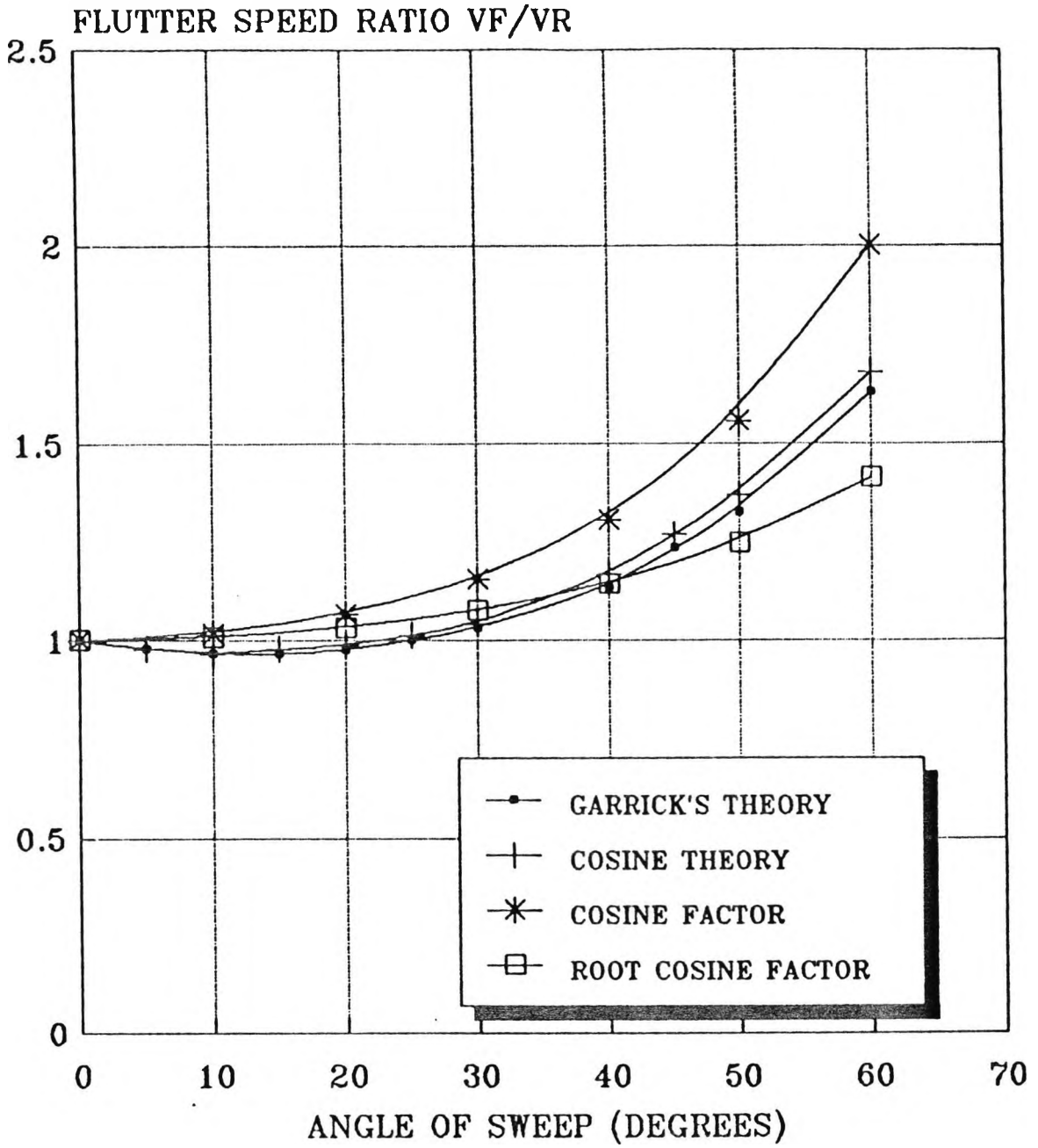
Fig. 2.9 Effect of sweep on flutter for aspect ratio 4
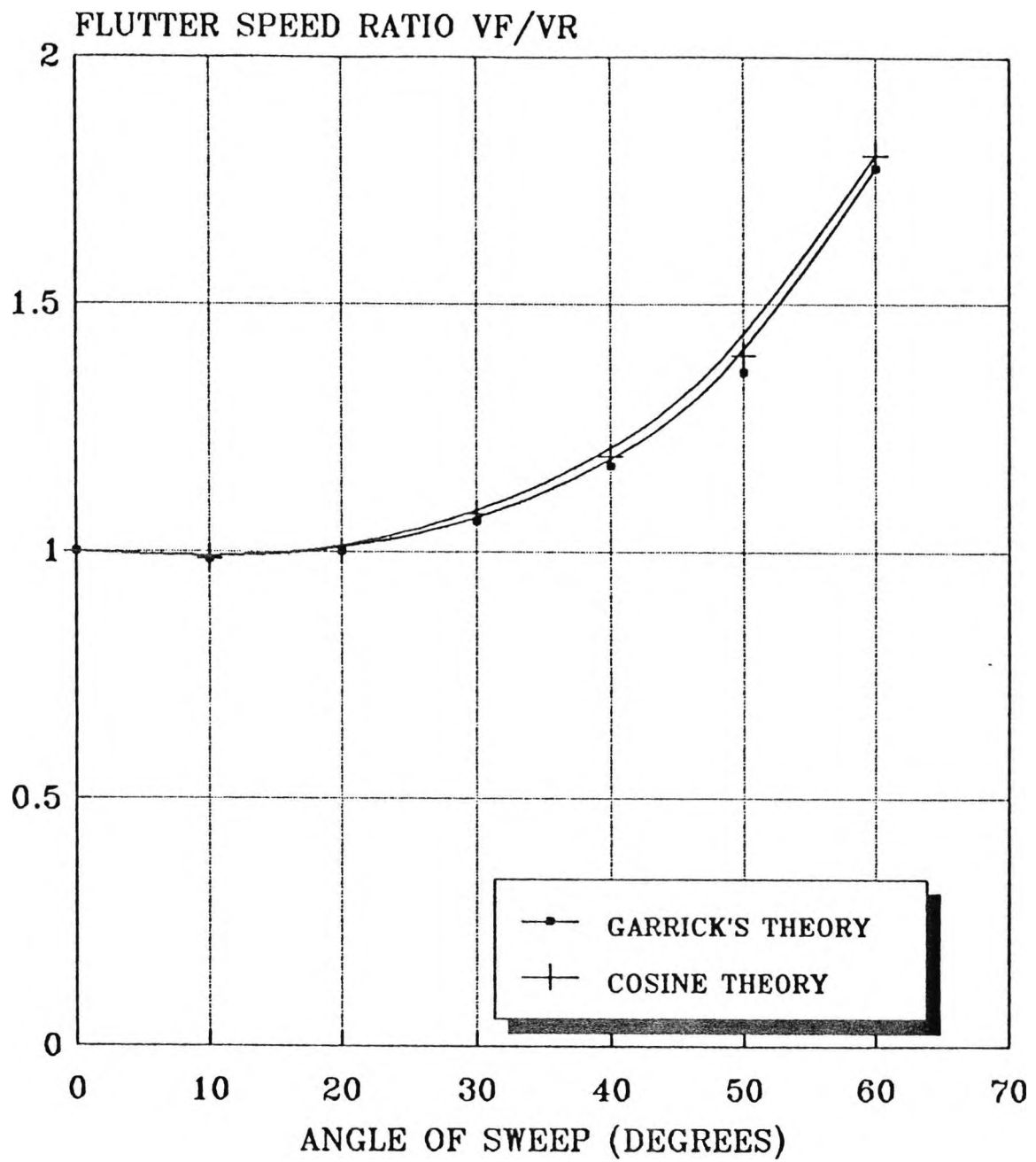
Fig. 2.10 Effect of sweep on flutter for aspect ratio 6
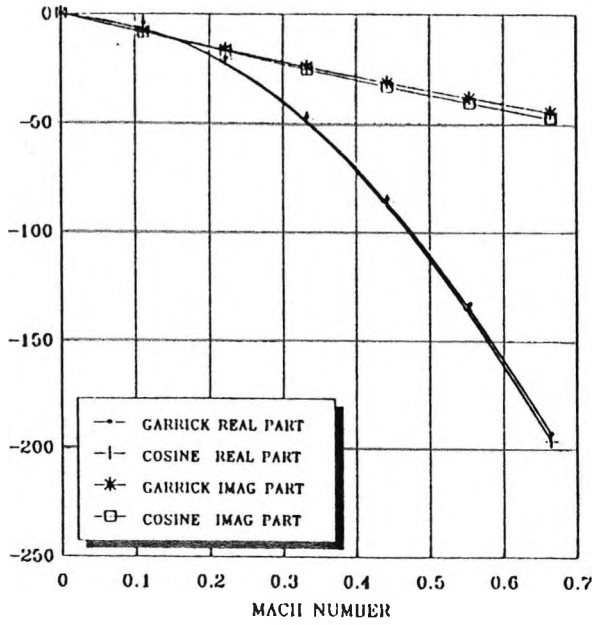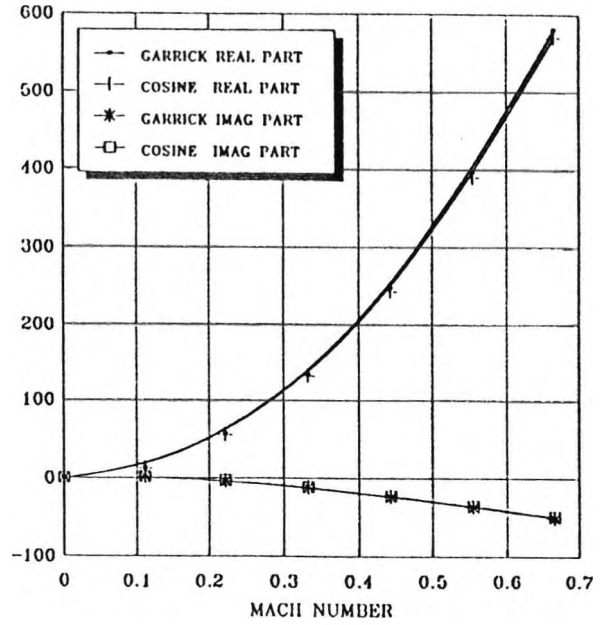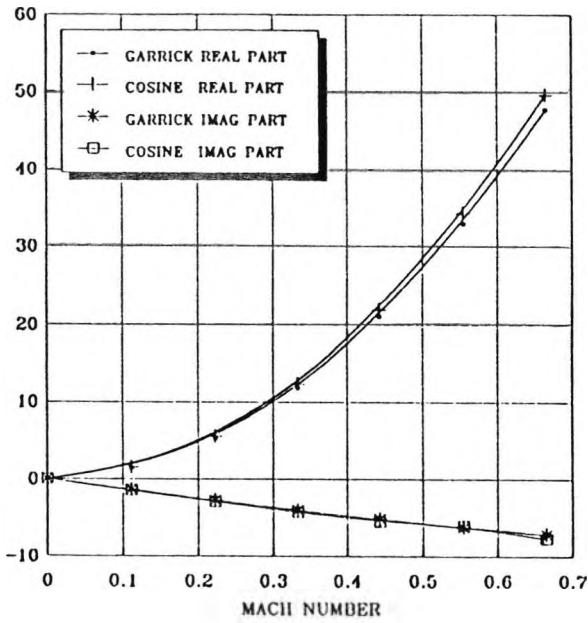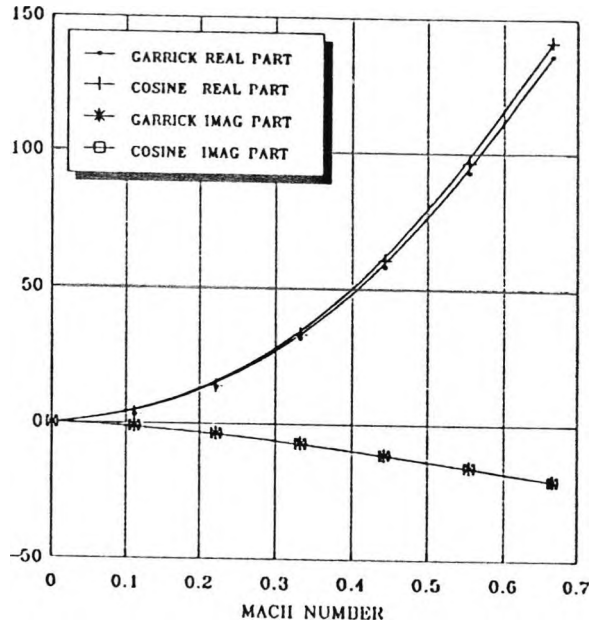
Fig. 2.11   Variation of generalised aerodynamic forces with mach
number at $\Lambda=10^0$
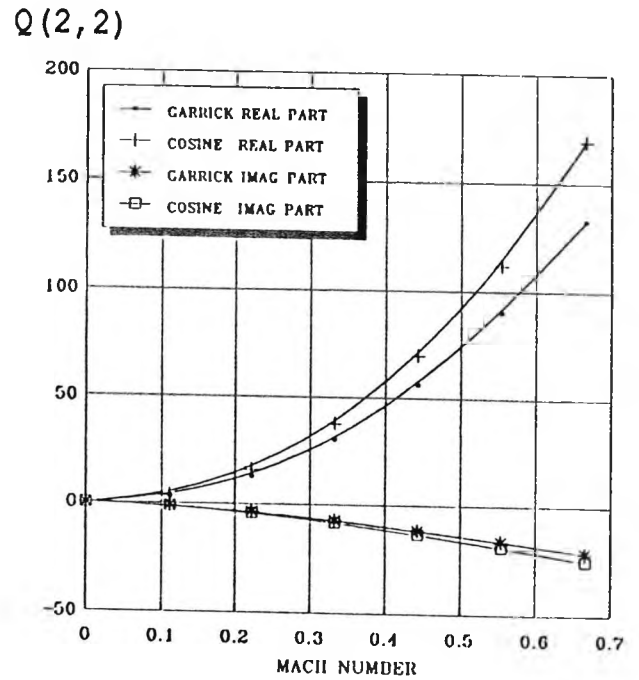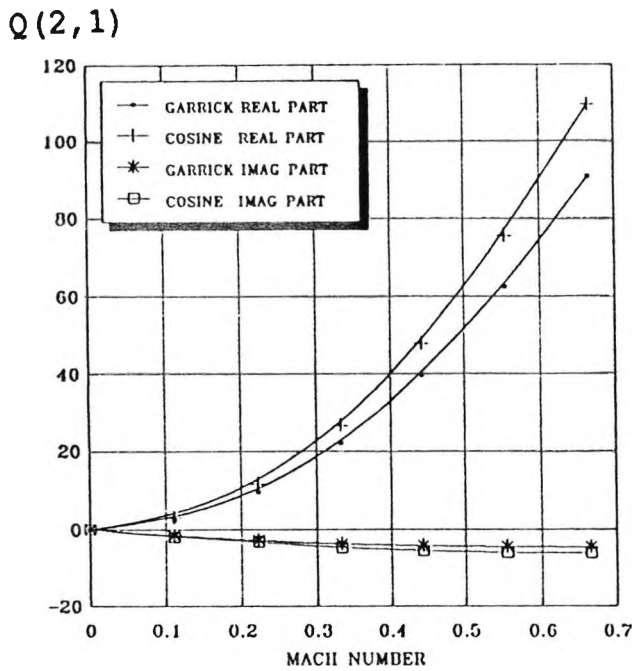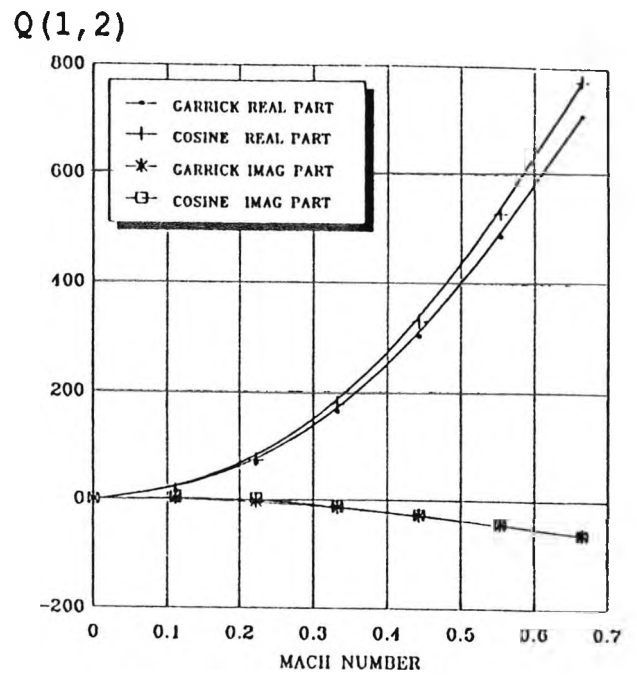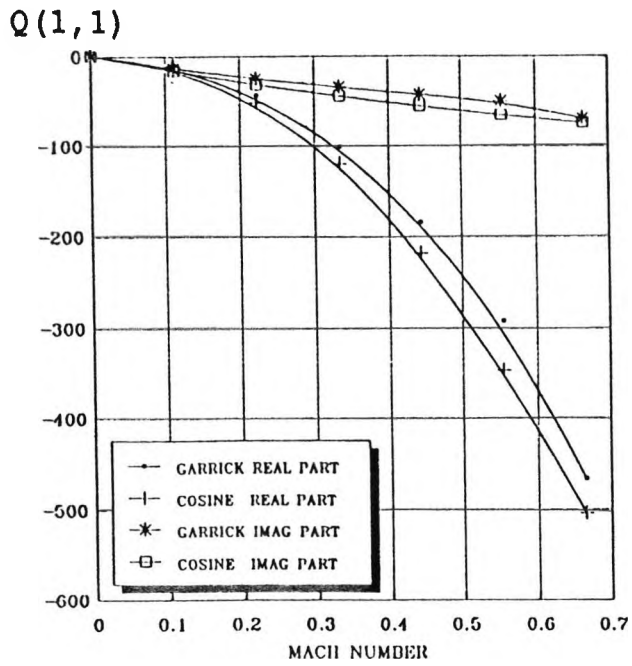
Fig. 2.12 Variation of generalised aerodynamic forces with mach
number at $\Lambda = 25^0$
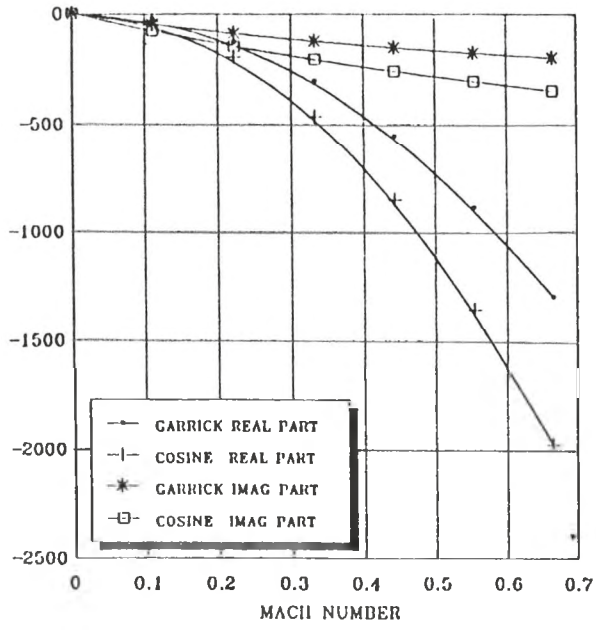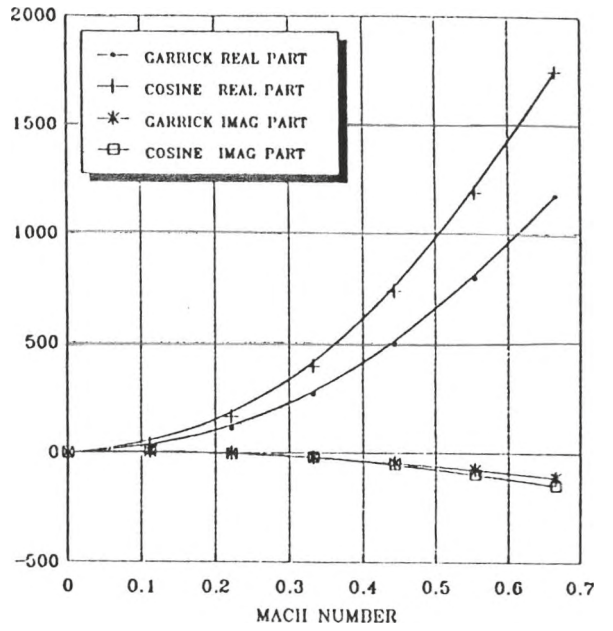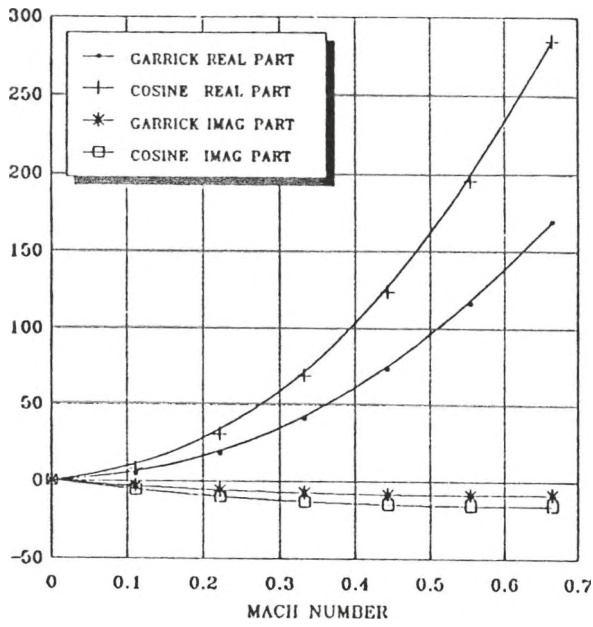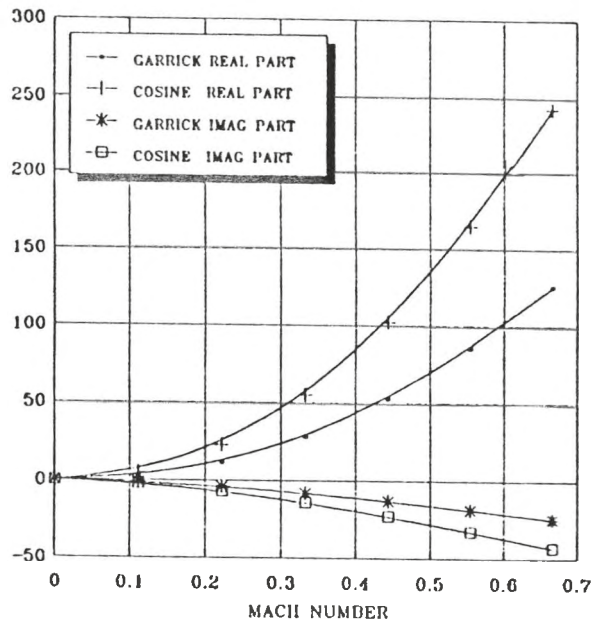
Fig. 2.13   Variation of generalised aerodynamic forces with mach
number at Λ=45⁰

3.0 ROLE OF RIGID BODY MODES IN FLUTTER

3.1 Introduction

Classical flutter analysis has predominantly dealt with the high frequency dynamic interaction of inertial, elastic (structural) and aerodynamic forces as described in Chapter 2. In contrast the implementation of rigid body modes is restricted within the scope of low frequency dynamic stability investigations.[14,15] It is well recognized that one may modify the calculated flutter speed of a cantilevered wing by including the free-free or zero-frequency modes of the aircraft. One of the earliest reports on the subject of the influence of "Body-Freedom" on flutter was due to Frazer and Duncan.[65] However the theme has been re-discovered because the aerodynamic loads caused by the interaction between aircraft rigid body motion and structural flexibility may be particularly important in the correct determination of vehicle instabilities. The interaction between rigid body pitch and plunge modes with the flexible modes of a proposed forward swept wing (FSW) demonstrator aircraft,[66] is of particular significance with the advent of the use of composite materials. Subsequent investigations carried out by Weisshaar et al[18,67] recognized this instability as "Body-Freedom Flutter". A similar instability was discovered by Banerjee[17,38,39] for a tailless aft swept wing (ASW) sailplane.

3.1.1 Body-Freedom Flutter

The first mention of this phenomenon of rigid body/wing bending flutter appears to have been made by Gaukroger[16,68] during tests on a model aircraft with swept back wings. Two distinct types of flutter were observed, which could occur for any angle of sweepback. The pitching moment of inertia of the aircraft primarily determines which type occurs at the lower flutter speed. Thus, i) Symmetric body-freedom flutter. This occurs at the lower values of the pitching moment of inertia and is characterised mainly by body-pitching with wing flexure, and ii) Symmetric disturbed root flutter which occurs with higher values of moment of inertia or the installation of a tailplane and has only small root movement and differs only slightly from fixed flutter mode.

Both the above types of flutter exhibit mainly pitching

56

motion, but the relative amplitude of the body is very much smaller in disturbed root flutter than in body-freedom flutter.

Body-freedom flutter is a type of dynamic instability that involves coupling together the flexible modes with body-freedom modes such as the short period mode or the roll mode.[16,65,67] In this work, symmetric disturbances are considered for the present body-freedom flutter involving the short period mode to be of prime significance. This instability can be observed with either aft swept wing or forward swept wing configurations.[17,67] This phenomenon has been studied analytically, using quasi-steady aerodynamics and fundamental wing bending mode in addition to the required rigid body modes, by Weisshaar et al[67] for the FSW case and by Niblett[69] for the ASW configuration. For FSW aircraft, a close analogy can be drawn between rigid body/wing bending flutter and classical bending/torsion flutter.[66]

Classically, wing divergence, a static aeroelastic phenomenon, has thought to be the primary mode of instability of FSW configurations. This is where, assuming the wing to be a cantilever, the first wing bending mode frequency decreases with increasing dynamic pressure until a zero frequency static divergence instability is encountered. In fact, the wing response is completely different from a cantilever case. The wing is no longer cantilevered in that it is attached to a relatively small mass fuselage which responds to the wing load and significantly modifies the cantilever fixity condition. As dynamic pressure increases the wing first bending mode frequency begins to drop, but the frequency of the aircraft short period mode rises. The short period mode couples with the wing divergence-prone mode resulting in flutter at a speed lower than the static divergence speed. Flutter occurs as a result of the force on the wing bending mode due to the rigid body pitching mode being in phase with the wing bending velocity, when the frequencies of the two modes are close together.

3.2 Application of Current Analysis to the Kestrel, Ricochet and the A1

Analysis using the program FLUST has been applied to two high aspect ratio sailplanes, (which were thought to constitute the best example of deformable aircraft), and one medium aspect ratio aircraft. The first one is the composite built Slingsby T59H Kestrel - 22m, which was built only in limited numbers; its configuration and aerodynamic details are shown in Figure 3.1 and Table 3.1 respectively. Hereafter Kestrel - 22m will be referred to as Kestrel, although there are other versions of the aircraft. The second is the Ricochet,[70] an all metal tailless glider, which was the result of an M.Sc. design study undertaken at Cranfield Institute of Technology, but the aircraft was never built (details are presented in Figure 3.2 and Table 3.2). The third and final example is the Cranfield A1, which is an existing powered aerobatic aircraft of aspect ratio 6.7. The Cranfield A1 is also as a result of a design study carried out at Cranfield, the aircraft having been built and successfully flown. The A1 configuration and aerodynamic details are shown in Figure 3.3 and Table 3.3. CALFUN[28] is used to predict the cantilever flutter speeds and frequencies where appropriate for the above examples. Concerning analyses using FLUST, it is expected that there will not be much inaccuracy in neglecting the inertial coupling, as the distance between the mass and elastic axes is small for all three aircraft and is unlikely to alter the results significantly.

3.3 The Kestrel
3.3.1 Structural Idealisation

A structural analysis was first of all carried out using the finite element program BUNVIS[71] to gain an overall insight into the modes for the whole aircraft. The program FLUST uses a routine based on BUNVIS to obtain the frequencies and modes, assuming that the aerodynamic forces are entirely generated by the wing and tailplane, the program implements only the modes for these components. However it does take into account the dynamics of the whole aircraft. The structural idealisation used is schematically shown in Fig. 3.4. As the aircraft is symmetric about the X-Z

58

plane, only one half of the aircraft needs to be taken into account when preparing the data. Lump masses were used to simulate the inertial properties of the front fuselage (including pilot and equipment) while beam elements, with stiffnesses and inertial properties derived from the cross-sectional details, of the wing, rear fuselage and tailplane respectively, are used (details are given in Appendix D). The Kestrel was idealised using 11 elements for the wing, 4 elements for the fuselage and 4 elements for the tailplane.

Only displacements and rotation within the X-Z plane are considered for symmetric motion. The rigid body modes of heave and pitch needed for the free flight analysis were obtained by putting two very light springs at the aircraft centre of gravity; one translational, the other rotational (as used in Chapter 2). A very light spring was used so that it did not interfere with the subsequent elastic modes that were obtained. For the particular configuration under consideration, the c.g. was located at 57.6% MAC (measured from leading edge fuselage centreline intersection) and this was used throughout the investigation. FLUST considers only longitudinal motion of the aircraft, the aerodynamic forces arising from the fin and fuselage are not included, but are assumed to be generated entirely by the wing and the tailplane. Therefore it was sufficient to locate a lumped mass at the tail to simulate the mass of the fin, to complete the total mass of aircraft. A form of "ill conditioning" arose from the element joining the front fuselage to the wing junction. This was supposed to be a rigid link, but practically it had a stiffness and inertia associated with it that could potentially interact with the elastic modes. As a cross check the frequencies were obtained using BUNVISTC which is an appropriate version of BUNVIS suitable for this problem. (The program BUNVISTC allows the use of "massless" elements and provides a means of adding stiffness to a structure without adding any mass).

The first four natural frequencies and modes of Kestrel obtained from the analysis are shown in Figure 3.5. Note that the frequencies and modes obtained from the line elements correspond to the displacements of the elastic (flexure) axis. The results

59

are compared with those obtained from ground resonance tests conducted on the Kestrel,[72] wherever appropriate. The comparison of results is shown in Table 3.4. It can be seen from the Table 3.4 that the frequencies obtained for the fundamental bending mode is in very close agreement, (the percentage difference is only -2.1%) whereas for the fundamental torsional mode, the difference in result is within 10.87%. The accuracy of these results are reasonable and are within engineering accuracy. However the agreement is not so prevalent for the first overtone bending mode where the difference is 29.2%. The third theoretical mode seems to consist of tailplane bending accompanied by a small amount of wing rotation.

For the flutter analysis however, agreement between fundamental bending and fundamental torsion was considered to be adequate in view of earlier investigations on the Kestrel which exhibited the case of fundamental bending/torsional flutter.[17]

3.3.1.1 Model Ill Conditioning

A severe form of ill conditioning was encountered when trying to simulate rigid links to represent the rigid parts of the aircraft, such as the ones already mentioned above. Rigid massless links were simulated using existing elements set with very high bending and torsional rigidities but with low values of mass and mass moments of inertia. However these pseudo-rigid links introduced local frequencies that were found in general to interfere with the structural rigid body frequencies produced by the artificial springs placed at the c.g. Though the rigid body frequencies were not used in the analysis, they were essential in providing the correct rigid body modes for the free flight investigation.

For a given elemental length, the inertia of the element was dictated by its overall contribution to the structure, so this was deliberately set low. The mass per unit length and the mass moment of inertia per unit length for the present problem were typically set between 0.001 and 0.0001 (kg/m or kgm). Although the rigidities were left to play the dominant role, it was found, as expected, that the shorter the element the more acute this potential ill conditioning problem. From the analysis of a two

degrees of freedom system, the rigid body frequency in heave is $\omega_h = (K_h/M)^{1/2}$ and in pitch $\omega_\alpha = (K_\alpha/I_\alpha)^{1/2}$ where K_h and K_α are the respective spring stiffnesses in heave and pitch, M is the total mass of the aircraft and I_α its pitching moment of inertia. Using ω_h and ω_α as the required frequencies, the element rigidities EI or GJ, depending on the degrees of freedom, were altered until a band of values was obtained within which the rigid body frequencies remained nearly constant and close to ω_h and ω_α. This was done to ensure that the problem was not ill conditioned. Then, by using an acceptable rigidity between this band, the rigid body modes were then obtained. Figure 3.6 shows the type of behaviour of this instability. Later the threshold of ill conditioning was found to be sensitive to machine floating point accuracy and it was found necessary to introduce the rigid body modes artificially into the analysis.

3.3.2 Aeroelastic Analysis

The present investigation is an extension of previous studies, carried out by Banerjee[17,38,39] but with the effects of fuselage flexibility and tailplane aerodynamics accounted for. The flutter analysis was carried out using two rigid body modes and the first four symmetric elastic modes. Considering the large aspect ratio of the Kestrel the wing lift curve slope a_o was assumed to be 2π /rad. A modified tailplane lift curve slope $a_1 = 4.70$ /rad obtained from ESDU[73] was used as part of the aerodynamic details (this was found to give flutter values only marginally lower than the those obtained from assuming $a_1 = 2\pi$ /rad at the tailplane).

The graph showing the locus of the real and imaginary parts of the flutter determinant is given in Fig. 3.7. The flutter speed is found at 72.3 m/s at a frequency of 49.7 rad/s, and this compares favourably with reports of wing flutter incidents occurring in the region of 72.0 m/s. A subsequent flutter analysis was carried out on the Kestrel wing using CALFUN with three elastic modes, neglecting the fuselage and assuming a cantilever condition. This yielded a flutter speed of 73.7 m/s and a flutter frequency of 50.2 rad/s.

3.4 Effects of Tailplane Aerodynamics and Fuselage Flexibility on the Flutter of Kestrel

As already mentioned earlier investigations attempted the flutter problem involving the whole aircraft but took into account only the structural effects and not the aerodynamic effects of the tailplane. However in this particular work tailplane aerodynamics as well as its flexibility have been incorporated. The additional effects of fuselage flexibility are further investigated.

The amount of published literature available on the influence of fuselage flexibility and tailplane aerodynamics on flutter is relatively small and mostly confined to swept aircraft of aspect ratios no greater than six.[12,16,67] To investigate such complex phenomena, reliance is often placed on quasi-steady aerodynamics and strip[67] theory to simplify the problem. In this section we set out to investigate the effects of tailplane aerodynamics and fuselage flexibility on the flutter speed of high aspect ratio, low speed aircraft.

The mass and inertia properties of the Kestrel in this analysis were slightly altered, without affecting the modes significantly. In this new configuration the flutter speed and flutter frequency with the effects of tailplane aerodynamics marginally increases to 72.7 m/s and decreases to 49.6 rad/s respectively. An investigation was carried out, neglecting the tailplane aerodynamics, and the corresponding flutter speed and frequency were 72.3 m/s and 50.0 rad/s respectively. As it can be seen, tailplane aerodynamics do not make any significant difference in the flutter speed or in the flutter frequency. However, the model incorporating the tailplane aerodynamics produces a slightly higher flutter speed and lower flutter frequency, this is to be expected as the tailplane provides aerodynamic damping and hence stability to the aircraft. The marginal difference in results prompted an investigation of the effect of the number of normal modes on flutter. A modal elimination technique was adopted and the number of normal modes included in the analysis was gradually reduced. The results are shown in Table 3.5, where modes 1 and 2 are the rigid-body modes and 3,4,5 and 6 are the elastic modes, as shown in Figure 3.5. As

it can be seen, the flutter speed of the Kestrel can be predicted with reasonable accuracy by including just the fundamental bending and torsional mode of the wing (modes 3 and 6). The flutter of the Kestrel is thus a distinct example of classical bending/torsion flutter and a fixed-root (cantilever) end condition will give sufficiently accurate results.

Further illustration of the effect of these normal modes on the Kestrel flutter is given in Figure 3.8 where only the the real part of the normal mode components of the flutter mode and their resulting values are plotted along the semispan. (The results are plotted for one symmetric half of the aircraft, the fuselage centreline and the flexural intersection is taken to be the origin of the plot). The details relating to the contribution of the flutter modes is shown in Appendix E. When the contributions of normal modes shown by the broken lines are added together, the resulting solid lines are obtained. Small contributions from some of the normal modes are not shown, leaving the predominant modes. In the presentation of the results, all the modes are numbered sequentially, starting from the rigid-body modes and finishing with the elastic modes. It can be seen from Figure 3.8 that the dominant terms in vertical displacement are $q_3 h_3$ and $q_4 h_4$ whereas the dominant terms in pitching rotation are $q_5 \alpha_5$ and $q_6 \alpha_6$. (h_3 and α_6 are respectively the fundamental bending and torsional modes as shown in Fig. 3.5).

Figure 3.9 shows the variation of flutter speed with fuselage stiffness, for both models. For a 30% reduction in fuselage stiffness the flutter speed including tailplane aerodynamics is increased only by about 3%. At this value there is virtually no change in the elastic modes except for a 4% reduction in frequency in the third mode, which is characterised by tailplane bending with small amounts of fuselage bending, with wing and tailplane torsion in antiphase. As fuselage stiffness is increased the flutter speed decreases and at around a 50% increase in fuselage stiffness, appears to level out giving a maximum decrease in flutter speed of 2%. With an increase in fuselage stiffness the elastic modes remain unchanged, except for 2% increase in the frequency in the third mode and a stiffening of the tailplane

mode.

3.5 Anti-Symmetric Flutter Analysis

The anti-symmetric case was dealt with in a similar manner to that of the symmetric case except that motion out of the X-Z plane was considered. The only rigid-body mode in the flutter analysis was the freedom in roll. This was achieved by restricting all degrees of freedom except rotation about the X-axis at the fuselage nodes and inserting a spring at the c.g. to provide the required rigid-body roll about the X-axis.

The anti-symmetric modes for Kestrel are shown in Figure 3.10. Frequencies are compared, where available, with those observed from the ground resonance tests[72] in Table 3.4. For second bending the agreement is poor, where the percentage difference is -30.5%. However anti-symmetric torsion is found close to the value obtained in the corresponding symmetric analysis, the agreement with Ref.(72) is 9.7%. However no fuselage torsion was observed in the analysis.

The above elastic modes, along with rigid-body roll, were used in an anti-symmetric flutter analysis, with tailplane aerodynamics included. The Kestrel appears to suffer from anti-symmetric flutter at 71.3 m/s with a flutter frequency of 47.0 rad/s, very close to the symmetric result. A subsequent investigation was carried out using modal elimination and the results are shown in Table 3.6. It can be seen that this flutter consists of three modes namely rigid-body roll with first elastic bending and first torsional modes, with additional modes not significantly affecting the result.

The dominance of the roll mode[65] is further emphasised in the flutter modes. All the modes are numbered sequentially, starting from the rigid body roll mode at 1 and finishing with the elastic modes. Figure 3.11 illustrates the main contribution of $q_1 h_1$ and $q_2 h_2$ to the vertical displacement of the flutter mode. Pitching rotation consists solely of the torsional mode, $q_5 \alpha_5$.

An analysis was also carried out neglecting tailplane aerodynamics and these results are also shown in Table 3.6 for comparison. It can be seen that tailplane aerodynamics does not

64

play any significant role in this type of flutter.

As to whether this type of flutter is indeed the primary mode of instability of the Kestrel is not certain. As there seems to be closer agreement with the ground resonance tests for the symmetric modes. It is more likely that the flutter of Kestrel is a symmetric form of flutter involving the first bending and first torsional mode.

3.6 The Ricochet
3.6.1 Structural Idealisation

The Ricochet was idealised in a similar manner as to the Kestrel. However as the Ricochet is a tailless aircraft, the idealisation was somewhat simpler. The wing was swept by 13° and was represented by 12 elements, as shown in Figure 3.12. As the fuselage was assumed rigid, it was assumed to be made up of two elements with a lumped mass at the pilot-fuselage centre of gravity to simulate its mass and inertia properties.

As before two light springs one translational the other rotational were located at the aircraft centre of gravity to obtain the rigid body modes in heave and pitch respectively. The first four symmetric elastic modes obtained from BUNVIS are shown in Figure 3.13. These results were cross checked again using BUNVISTC to eliminate possible ill conditioning from the use of a small massless rigid link joining the aircraft and front fuselage centre of gravity.

3.6.2 Aeroelastic Analysis

As the Ricochet has a very large aspect ratio, (AR =22.93) the value of a_0 was left as 2π /rad as was the case in prior investigations.[17,38] However the aircraft centre of gravity was located at the aft c.g. location, with no water ballast assumed. As the program FLUST can not account for the small shift in aerodynamic centre due to wing/body interference, the static margin was adjusted accordingly in the aeroelastic model to accommodate this. However the static margin will be found to be of more significance when dealing with dynamic stability of the aircraft.

The analysis was carried out using the two rigid body modes along with the first four symmetric elastic modes. The flutter

65

speed and frequency were found to be 47.2 m/s and 6.14 rad/s respectively. Modal elimination was also performed, and the resulting flutter quantities are shown in Table 3.7. The graph showing the loci of the real and imaginary parts of the flutter determinant are presented in Figure 3.14. It can be seen that with just the two rigid body modes together with the fundamental bending mode, the flutter speed and frequency are 52.2 m/s and 4.26 rad/s respectively. The flutter speed is far below the design estimate of 150 m/s given in Ref.(70). This type of flutter known as "Body Freedom Flutter",[16,38] is predominantly a coupling between the short period pitching oscillation and the fundamental bending mode, as borne out from prior investigations,[17,38] giving rise to a characteristically low flutter frequency.

As with the Kestrel, (referring to Figure 3.15 for the flutter mode), it can be seen that the predominant modes in vertical displacement are q_1h_1 and q_3h_3. This illustrates the unconventional way the Ricochet flutters, where an upward movement of the fuselage is accompanied by a downward movement of the wing tip. In pitching rotation the dominant contributions are $q_2\alpha_2$ and $q_3\alpha_3$. An inspection of the flutter modes in Fig. 3.15 clearly indicates that the flutter behaviour of the Ricochet is unusual, with large deflections at the wing root, whereas that of the Kestrel is a distinct example of classical wing bending/torsion flutter, with the tip having maximum displacement and the root being almost stationary.

A parametric study of varying c.g. position and pitching moment of inertia is undertaken on the Ricochet, without altering the basic design of the aircraft. Shifting the c.g. of the pilot-fuselage assembly to the forward c.g. position results in a 15.8% reduction in flutter speed using six modes (Weisshaar et al[67] found the opposite effect for a forward swept configuration). The parameter which is found to have the most significant effect on the flutter speed is the pitching moment of inertia of the aircraft. The variation of flutter speed against the pitching moment of inertia of the pilot-fuselage assembly is shown in Figure 3.16 and the results indicate a linear trend.

Instead of using active control technology one possible[69,74]

way of preventing this coupling with the first elastic mode as in the case of the Ricochet, is to make use of aeroelastic tailoring with composite materials as undertaken on a tailless swept back configuration called the SB13,[74] which was successfully test flown.[75]

3.7 The Cranfield A1

3.7.1 Structural Idealisation

The finite element idealisation for one symmetric half of the Cranfield A1 is shown in Figure 3.17. As can be seen, the wing structure was made up of 12 beam elements representing both the elastic/inertia axes, as the coupling between these two axes is assumed small. The root element was made rigid, as it represents the wing/fuselage junction and has only an aerodynamic contribution to the model, and completes the gross area of the wing.

An element with an attached lumped mass was included to simulate the wheel and undercarriage assembly. This unit was necessary because its mass is approximately a third of that of the wing. The front fuselage was assumed to be rigid, so a rigid element with a lumped mass and inertia was used to simulate it (the main mass contribution coming from the engine, oil and Petrol tank). The rear fuselage was represented by two elements. A lumped mass and inertia was located in between these latter elements to simulate the pilot/cockpit combination. A rigid element was interconnected between the wing root elastic axis and the aircraft centre of gravity. The position of the aircraft centre of gravity was taken from flight test data[76] as 26.6% MAC. As with the Kestrel and Ricochet two springs, one allowing heave and the other rotational pitch, were located at the c.g. to provide the required rigid body modes. The fin and rudder were represented as lumped masses and inertias, as they do not contribute to the aerodynamics in this investigation, whereas the tailplane consisted of two beam elements, with its aerodynamics included.

3.7.1.1 Investigation of Fuselage Stiffness

The basic fuselage structure is welded in steel T45 tubes. The general layout of the fuselage is shown in Fig. 3.18. The four

main longeron members are 1.25 in. dia. 17g which are supported by 1 in. dia. 20g and 0.5 in. dia. 17g diagonals and lateral cross bracing. At their forward end the longerons continue as the engine mounting which is also of welded construction in 1.25 in. dia 14g tube. Shear attachments are provided for the wing and tailplane and fin.

An initial evaluation of the stiffness properties of the fuselage was done using the fuselage proof test results provided by Ref.(77). This reference is one of a number of proof tests carried out on certain components of the aircraft at Cranfield, for CAA (Civil Aviation Authority) test certification. Two separate loading cases were simulated. The loads were reacted at the front and rear spar attachment points on the lower surface of the fuselage frame, marked FS and RS respectively (see Fig. 3.18).

i) Test A is concerned with the design proof loading on the front fuselage and spar attachment sections. In particular, vertical nose (N) and tail (T) loads representing the 9g pull-out case are applied in five equal increments. This produces the design proof shear force and bending moment at the front spar section and on the forward fuselage.

ii) Test B is concerned with the design proof loading on the rear fuselage by torsion resulting from the combinations of maximum fin shear force and asymmetric tailplane loading. Therefore from test A and test B it is possible to ascertain the stiffness quantities EI and GJ, for the fuselage, respectively.

3.7.1.2 Fuselage Bending Stiffness

From test A the derived values of $\frac{\delta}{P}$ for both the nose and tail section are shown in Table 3.8, where P is the applied vertical load and δ the corresponding deflection. Referring to Fig. 3.18 it is possible to replace the structure with one forward beam element of EI_1 and two rear elements of the same EI_2 as shown in Fig. 3.18 and using identical loading and support conditions test A was recreated using the finite element program BUNVISRG,[78] which is a program for any pin-jointed or rigid-jointed space frame. Initial estimates of EI_1 and EI_2 could be found by assuming cantilever conditions at FS, because of the nature of the loading it is FS which acts as the main support. Using these initial

estimates as the base, EI_1 and EI_2 were gradually increased until $\frac{\delta}{P}$ for both the nose and tail were close to those values in Table 3.8. The final resulting $\frac{\delta}{P}$ values, and the corresponding percentage differences are also shown in Table 3.8. (The final results were obtained using an iterative procedure). As it can be seen this approach gives good agreement with experimental results.

This bending stiffness was taken for the rear fuselage from the idealisation mentioned above, for the symmetric modal analysis. The resulting elastic modes and mode shapes for the A1 are shown in Figure 3.19, obtained from BUNVISTC. The frequencies are displayed in Table 3.9, along with those where possible are quantities obtained from ground resonance tests conducted at Cranfield[79]. In the theoretical analysis of natural frequencies and mode shapes, three different finite element models of the A1 based on the idealisation of its undercarriage (which constitutes about one-third of the mass of the wing) were used. Model A represents the idealisation of the complete aircraft including the undercarriage which is regarded as an offset mass (and inertia). Model B ignores the offset nature of the undercarriage and represents it just as an equivalent lumped mass and inertia on the wing. In model C the undercarriage is completely ignored.

Referring to Figure 3.19 the first elastic mode has predictably turned out to be the fundamental bending mode of the wing. The agreement between the ground resonance test results and ones obtained from each of the three models mentioned above is found to be good (see Table 3.9). The discrepancy between the theoretical and experimental results for this mode is about 5.8%. Also it can be seen from Fig. 3.19 that the fundamental bending mode of the wing, obtained from the whole aircraft configuration, is very nearly a cantilever mode. For all the three models, the difference in theoretical and experimental results for the second natural frequency is about 10.6%. However the ground resonance test at Cranfield for this particular natural frequency revealed that the mode was dominated by wing bending with some small amount of tailplane bending displacements present. In contrast, the theoretical mode corresponding to this frequency, in Fig. 3.19, indicates that there is some coupling between wing bending and

69

wing-torsion in this mode, but more importantly the mode is dominated by tailplane bending instead, which was not evident in the ground resonance test. The third elastic mode shown in Fig. 3.19 is primarily a wing bending mode, which accords with the observation made in the ground resonance test. Although the modes obtained are similar, the disagreement in frequencies between the theory and the experiment is about 21.3% (see Table 3.9). It may be noted that the effect of the undercarriage is not prevalent in the first three elastic modes. The fourth elastic mode of the aircraft shown in Fig. 3.19 is primarily the fundamental torsional mode of the wing which is clearly confirmed by the ground resonance test results. The disagreement in the frequency between the experiment and theoretical result obtained using model A of the aircraft is about 5.3% (see Table 3.9). However it was noted that in the ground resonance test that this mode was found to be heavily coupled with second wing bending mode, which has not been predicted by the theoretical results (see Fig. 3.19).

It can be seen from the results in Table 3.9 and Fig. 3.19 that the undercarriage does not influence the first three elastic modes involving wing bending but, it has a marked effect on the torsional frequency as expected. It was also noted that the effect of the undercarriage was to increase the amount of coupling between the bending and torsional displacement of the wing particularly in the second and third elastic mode.

3.7.1.3 Fuselage Torsional Stiffness

Using a similar approach to that for the bending stiffness, test B provided a value of $\frac{T}{\theta}$ for the rear fuselage from which GJ could be derived, where T is the torsional moment and θ the corresponding angle of twist. However problems arose in establishing frequencies as it was difficult to correctly estimate the fuselage mass moment of inertia per unit length. Initial calculations were centred on taking sections of the fuselage in its tubular form and estimating the concentration of mass and its effective centroid, from which the polar moment of inertia could be calculated. Ground resonance tests for the anti-symmetric frequencies and modes suggested a low torsional frequency for the fuselage. Therefore as no such frequencies were encountered with

the current models it was decided to model the rear half of the fuselage as a framework using the program BUNVISRG[78] from which the stiffnesses, inertia properties and frequencies could be later derived. The finite element idealisation for this problem is shown in Fig. 3.18.

Figure 3.20 displays the distribution of GJ along the fuselage length. The results were deduced from the finite element analysis above. As the front fuselage was assumed rigid, the fuselage distance was taken from the rear spar attachment point to the tail. A pure torsional moment was applied with two sets of equal and opposite forces, one in the vertical plane, the other in the horizontal. The GJ distributions resulting from these two separate loading conditions yield almost identical values, displaying the symmetry of the framework. As it can be seen the mid section is the stiffest as this has the largest amount of cross bracing. Fig. 3.20 also shows the value derived from test B, as this suggests the value obtained experimentally represents well the overall value of GJ for the rear fuselage.

Using BUNVISRG, the fuselage was first restrained at the front section and the first six fundamental modes are shown in Figure 3.21a. The first two modes are dominated by vertical and horizontal bending respectively. The remaining modes, the first at 69.4 Hz, exhibit coupled bending/torsion motion. The constraints were next removed and Fig. 3.21b shows the free-free analysis. The modes again exhibit coupled bending/torsion motion. However the second mode, at 96.8 Hz displays distinct torsional motion.

Later values of the fuselage mass moment of inertia were furnished by Howe, Ref.(80) in a private communication and along with the values of GJ obtained from the framework idealisation, were incorporated in a BUNVISTC analysis. The subsequent anti-symmetric modes are shown in Figure 3.22. Comparing these results with those obtained from ground resonance tests shown in Table 3.10 it can be seen that the overall agreement is poor. However the low torsional frequency quoted in the ground resonance tests, of 8.18 Hz could be a rigid body mode as the frequencies obtained from the BUNVISRG analysis suggest a higher value. Using the same idealisations as denoted by model B and C, it can be seen

71

from Table 3.11 that the influence of the undercarriage is significant in the anti-symmetric mode, especially with respect to the torsional mode as in the symmetric case.

3.7.1.4 Bending stiffness

Figure 3.20 shows also the vertical bending stiffness obtained from the current analysis, this is compared with that derived from test A. As this figure shows the value of EI suggested experimentally is over twice that obtained from the idealising the fuselage as a framework. The subsequent frequencies obtained from incorporating this reduced stiffness are shown in Table 3.9 , as model D. As the results suggest the effect of fuselage bending stiffness is not significant in the wing modes of A1. It is the modes obtained from using the proof test stiffnesses, that are implemented as the basis for this investigation.

3.7.2 Aeroelastic Analysis

A free flight symmetric flutter analysis was carried out using the four elastic modes presented in Fig. 3.19, in addition to the two required rigid body modes. As the size of the fuselage element between the aircraft c.g. and wing elastic axis is small, severe ill conditioning was encountered and the rigid body modes were introduced artificially, as part of the data. For the flutter analysis, the aerodynamic parameters for both the wing and tailplane were set at 2π /rad. The flutter speed and flutter frequency of the A1 with the effects of tailplane aerodynamics were established as 842 m/s and 221 rad/s respectively. The corresponding values, when neglecting tailplane aerodynamics and considering the wing just as a cantilever, were 1398 m/s and 238 rad/s.

As it can be seen the flutter speeds obtained are well outside the limitations of strip theory, at M = 0.75. Accordingly an anti-symmetric flutter analysis is also carried out using the modes shown in Fig. 3.22: however no flutter of A1 in the anti-symmetric mode is apparent. The flutter free characteristics of the A1 is as a result of the low aspect ratio and overall high stiffness of the A1.

3.8 Quasi-Steady Aerodynamics in Flutter Analysis

The analysis above implements the full effects of unsteady aerodynamics. However, prior investigations[67,69,81] into the mechanics of flutter have made use of quasi-steady aerodynamics, assuming quasi-steady flow (k=0). In this note the non-circulatory terms and the memory effect of the wake, as in low frequency dynamic stability analysis, are neglected. This is achieved in this case by ignoring the non-circulatory terms and setting C(k) = 1.0 within Theodorsen's expressions[5] for lift and moment, and replacing the downwash by $(\dot{h} + U\alpha)$. These expressions are employed within a modified version of FLUST.

Carrying out this analysis on the Ricochet, the flutter speed and frequency obtained using six modes are 46.2 m/s and 6.2 rad/s respectively; this gives u_f = 0.978 (ratio of quasi-steady to unsteady flutter speed). For two rigid body modes and first bending mode the flutter speed and frequency were 50.5 m/s (u_f = 0.986) and 4.4 rad/s. This analysis was also carried out on the Kestrel, and the flutter speed and flutter frequency were established as 41.2 m/s (u_f = 0.569) and 89.6 rad/s respectively using all six modes and 39.0 m/s (u_f = 0.522) and 93.28 rad/s using the first bending and torsional modes. The Ricochet results show good agreement, as the reduced frequency at flutter (k=0.09), and in general body freedom flutter is sufficiently low for quasi-steady aerodynamics to adequately predict the aerodynamic damping. However the reduced frequency in the classical bending/torsion flutter of Kestrel (k=0.48) is high enough for the necessity of the effects of aerodynamic lag and unsteadiness of the wake to be accounted for.[81] The tendency for this type of quasi-steady aerodynamic model, to underestimate the flutter speed is suggested by work done by Lottati[81] on the role of structural and aerodynamic damping on classical bending/torsion flutter.

3.9 Flutter Analysis of a Forward Swept Model

As a part of previous investigations carried into the aeroelastic behaviour of graphite/epoxy cantilever wings,[82,83] a free flight model of a forward swept aircraft was constructed at M.I.T (Massachusetts Institute of Technology) by Chen and

73

Dugundji.[84] This model employed graphite/epoxy wings of various ply layups to investigate the influence material bending/twisting coupling has on body-freedom flutter.

In terms of its appliaction to body-freedom flutter, the present method of analysis has been restricted to the Ricochet, an aft swept aircraft. It was decided to apply the current analysis to the Chen and Dugundji model. Figure 3.23 shows the layout of the aircraft model and Table 3.12 the model and support properties. The flutter analysis carried out by Chen and Dugundji is formulated by the Rayleigh-Ritz approximation, employing the stiffness coupling terms in laminate analysis required for investigation of composite wings involving cross layups. The current idealisation in this work assumes wing construction of isotropic nature. Therefore to avoid possible errors from material cross coupling, the present investigation is restricted to experiments carried out by Chen and Dugundji for a [0_2/ 90]$_s$ layup.

From the material and geometric properties of the wing, it is possible to construct the stiffness and inertia details of the wing. In this case the canard is assumed to be rigid and to contribute only to the aerodynamics. The model is represented in similar fashion to those of Kestrel and Ricochet, i.e. in terms of beam elements: the modes and frequencies checked using BUNVIS. The first three frequencies are shown in Table 3.13 along with those supplied from Ref.(84), obtained from ground resonance tests. As one can see the overall agreement is very good.

Because of the model weight, the preselected wing planform was not able to fly the model completely. Thus the mechanism of support consists of a vertical rod with a linear bearing sliding on the rod and attached to the fuselage through a pitch bearing mount located at the model centre of gravity, a soft helical spring attached to the linear bearing that suspended the model from the top of the vertical rod and a pair of linear springs attached to the pitch gimbals at forward and aft extended arms that provide the support pitching stiffness. Therefore as the rigid body modes are no longer zero frequency, the stiffness in heave and pitch provided by the support system needs to be

introduced into the equations of motion. This is done by inserting one translational and one rotational spring at the aircraft centre of gravity, as before to provide the required rigid body modes but now in addition to include the support frequencies. The support plunge and pitch (support 2) frequencies are shown in Table 3.12.

The subsequent flutter speeds including these rigid body frequencies is shown in Table 3.14 along with the values obtained theoretically and experimentally by Chen and Dugundji[84] The first flutter speed and frequency is obtained assuming a lift curve slope of 2π /rad both on the wing and the canard. Modal elimination shows that the type of flutter encountered is indeed body freedom flutter, involving coupling of the first bending mode of the wing with the rigid body degrees of freedom. Using 5 modes is seen to yield a -55% and 15.2% difference in flutter speed and frequency compared to the quantities obtained experimentally. It must be noted that in the present analysis the lift is assumed to be generated entirely by the canard and wing, unlike in Chen and Dugundji analysis which includes a contribution from the fuselage. Also although the same aerodynamic strip theory is employed using the cosine theory to account for sweep in their theoretical analysis, Ref.(84) uses seven modes and a polynomial to represent the Theodorsen function.

The next step is to use the lift curve slope found experimentally during static tests, to establish the static margin and trim condition. This model was found experimentally to have an overall lift curve slope of 5.33 /rad. To generate this slope for the current idealisation the canard lift curve slope a_1 was taken as 2.75 /rad from Ref.(73) and a_0 deduced as 4.59 /rad, to achieve the overall experimental lift curve slope. The subsequent flutter speed and frequency is also shown in Table 3.14. Using the result obtained using 5 modes it is noted that in this particular case a modified lift curve slope reduces aerodynamic stiffness and damping and predicts a higher flutter speed. This modified approach results in a -38.0% and 9.7% difference in speed and frequency respectively. As with the Ricochet, the dominance of the low rigid body frequencies in this type of flutter is seen from the flutter frequencies.

Geometric Details			
Wing		Tailplane	
Span	22 m	Span	2.85 m
Area	15.44 m^2	Area	1.30 m^2
Aspect Ratio	31.35	Aspect Ratio	6.25
Root Chord	0.90 m	Root Chord	0.557 m
Tip Chord	0.36 m	Tip Chord	0.35 m
Sweep angle	0^0	Sweep angle	0^0
a_0	2π /rad	a_1	4.70 /rad
Inertial Details			
Mass of each Wing	115 kg		
Fuselage mass with Pilot and equipment	278 kg		
Pitching inertia I_{yy}	845 kgm^2		

Table 3.1 Particulars of the Kestrel

Geometric Details	
Span	15 m
Wing Area	10.26 m^2
Aspect Ratio	22.93
Wing Root Chord	0.73 m
Wing Tip Chord	0.50 m
Sweep Angle	13.0^0
Inertial Details	
Mass of each Wing	50 kg
Fuselage Mass with Pilot and equipment	155 kg
Pitching inertia I_{yy}	106 kgm^2

Table 3.2   Particulars of the Ricochet

Geometric Details			
Wing		Tailplane	
Span	10.0 m	Span	3.11 m
Area	15.00 m^2	Area	2.72 m^2
Aspect Ratio	6.7	Aspect Ratio	3.56
Root Chord	2.08 m	Root Chord	1.07 m
Tip Chord	0.91 m	Tip Chord	0.67 m
Sweep angle	9.58^0	Sweep angle	0^0
a_0	4.22 /rad	a_1	3.52 /rad
Inertial Details			
Mass of each Wing	71 kg		
Fuselage mass with Pilot and equipment	734 kg		
Pitching inertia I_{yy}	2637 kgm^2		

Table 3.3   Particulars of the Cranfield A1

Wing Modes	Measured Frequency	
	(Hz)	(rad/s)
Fundamental bending	1.8	11.31
First overtone bending	4.7	29.53
Second overtone bending (anti-symmetric)	8.58	53.91
" " " (symmetric)	11.68	73.39
Fundamental torsion	15.1	94.88
Third overtone bending	Not measured	
First overtone torsion	30.5	191.64
Fuselage Mode		
Fundamental torsion	3.5	21.99

Table 3.4   Symmetric and anti-symmetric natural frequencies for the Kestrel from ground resonance tests

Modes Used	Flutter Speed (m/s) and Frequency (rad/s)	
	Tailplane Aerodynamics accounted for (m/s) (rad/s)	Tailplane Aerodynamics not accounted for (m/s) (rad/s)
1,2,3,4,5,6	72.7 (49.7)	72.3 (50.0)
1,2,3,6	75.3 (54.3)	75.3 (54.3)
3,6	77.1 (41.6)	77.1 (41.0)

Table 3.5   Effect of number of normal modes on flutter speed of the Kestrel

79

| Modes Used | Flutter Speed (m/s) and Frequency (rad/s) | |
	Tailplane Aerodynamics accounted for (m/s) (rad/s)	Tailplane Aerodynamics not accounted for (m/s) (rad/s)
1,2,3,4,5	71.3 (47.2)	71.4 (47.0)
1,2,3,5	71.3 (47.1)	71.3 (47.0)
1,2,5	71.3 (47.2)	71.2 (47.2)

Table 3.6   Effect of number of normal modes on the anti
-symmetric flutter speed of the Kestrel

Modes used	Flutter Speed (m/s)	Flutter Frequency (rad/s)
1,2,3,4,5,6	47.2	6.14
1,2,3,4,5	51.4	5.01
1,2,3,4	51.2	5.05
1,2,3	52.2	4.26

Table 3.7   Effect of normal modes on the flutter of the Ricochet

	TEST A	BUNVISRG	Percentage difference (%)
$\dfrac{\delta_1}{P_1}$ (mm/N x 10^{-3})	0.798	0.798	0.0
$\dfrac{\delta_2}{P_2}$ (mm/N x 10^{-3})	1.693	1.694	0.06

Table 3.8 Comparison of values obtained from beam idealisation and test A

	Frequencies (Hz)			
	1st Bending	1st Tailplane	2nd Bending	1st Torsion
Ground resonance test[78]	11.71	20.93	38.83	64.00
Model A	12.43	23.42	49.37	67.60
Model B	12.42	23.08	49.54	57.64
Model C	12.43	23.49	50.01	71.31
Model D	12.19	17.73	48.71	67.52

Table 3.9 Symmetric natural frequencies of the A1

81

8.18 Hz	Fuselage torsion
13.80 Hz	Wing bending fundamental
27.00 Hz	Wing bending 1st overtone
36.80 Hz	
64.10 Hz	Wing bending 2nd overtone

Table 3.10 Anti-symmetric natural frequencies of the A1 from ground resonance tests

	Frequencies (Hz)			
	1st Bending	Fuselage Torsion	Tailplane Bending	1st Torsion
Model A	23.92	29.07	38.89	65.15
Model B	24.07	29.80	38.89	56.22
Model C	25.31	30.54	38.89	70.42

Table 3.11 Anti-symmetric natural frequencies of the A1

82

Mass	0.956 kg
Pitch inertia	0.0178 kgm^2
Wing mass	0.054 kg
Wing span	0.612 m
Wing swept angle	-30^0
Wing area	0.0538 m^2
Wing aspect ratio	7
Canard area	0.0126 m^2
Fuselage length	0.8 m
Model plunge frequency	0.63 Hz
Model pitch frequency (support 1)	0.20 Hz
Model pitch frequency (support 2)	0.85 Hz

Table 3.12 Aircraft model[84] and support properties

First bending		First Torsion		Second bending	
Calc	Exp	Calc	Exp	Calc	Exp
11.8	11.4	33.3	37.6	72.5	71.8

Table 3.13 Natural frequencies of forward swept model[84]

Modes	Flutter speed and frequency m/s (Hz)		
		$a_0 = a_1$ $(2\pi\ /\mathrm{rad})$	Modified lift curve slopes
1,2,3		16.8 (3.8)	18.9 (3.7)
1,2,3,4		12.9 (3.3)	14.5 (3.1)
1,2,3,4,5		12.9 (3.3)	14.5 (3.1)
Ref.84 (using seven modes)	16.0 (2.3)		
Experimental results	20.0 (2.8)		

Table 3.14   Flutter speed and frequencies for forward swept model[84]
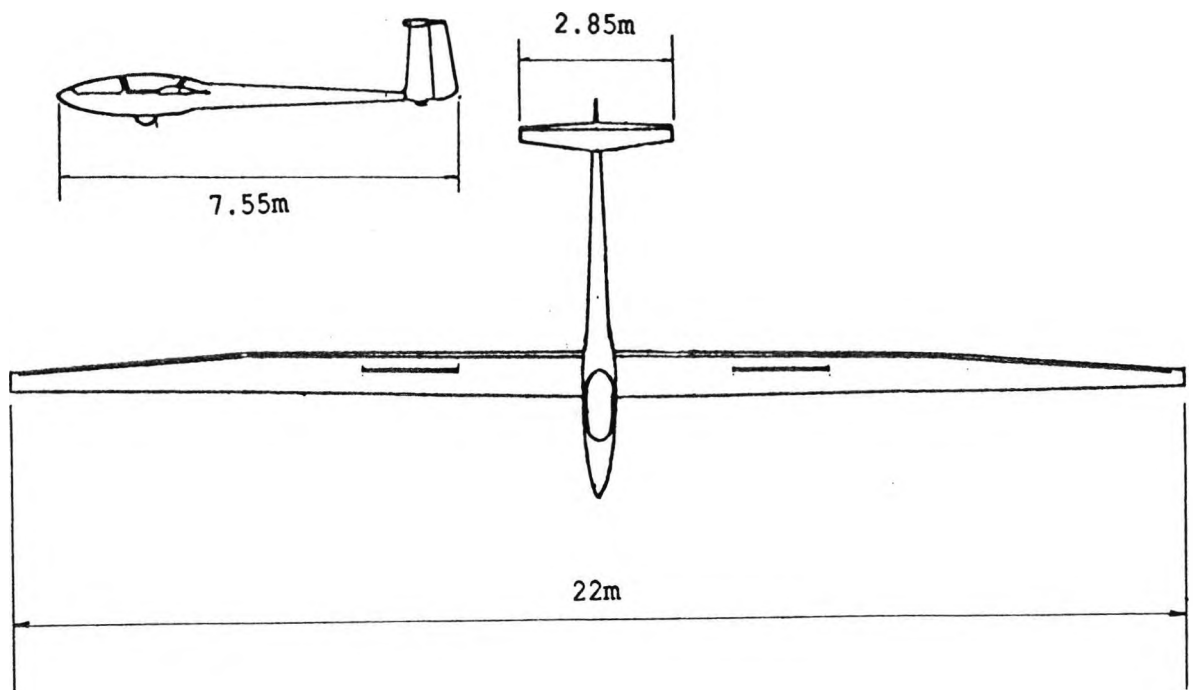
Fig. 3.1 General layout of T59H Kestrel
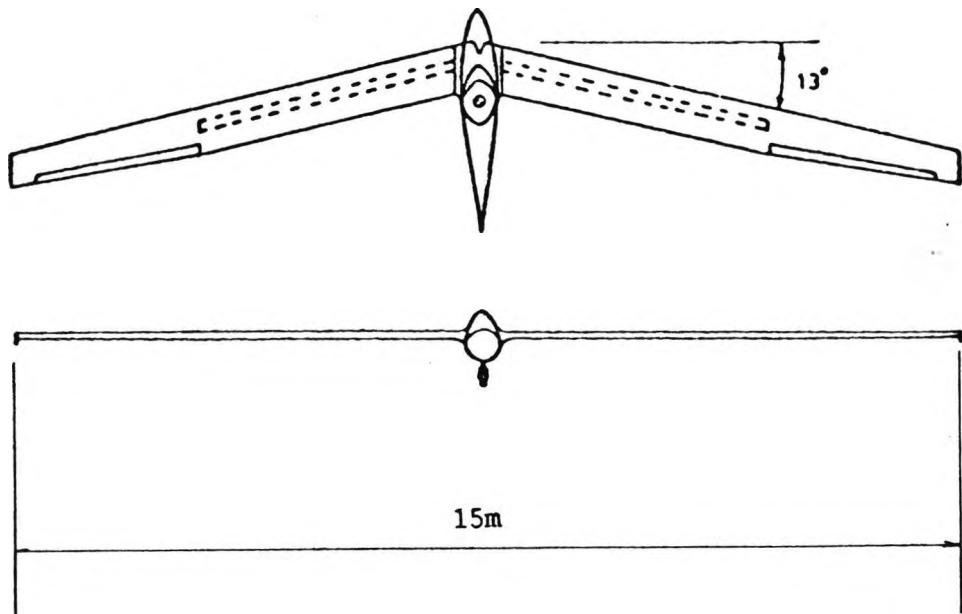
Fig. 3.2 General layout of Ricochet

10m

3.11m

8.14m
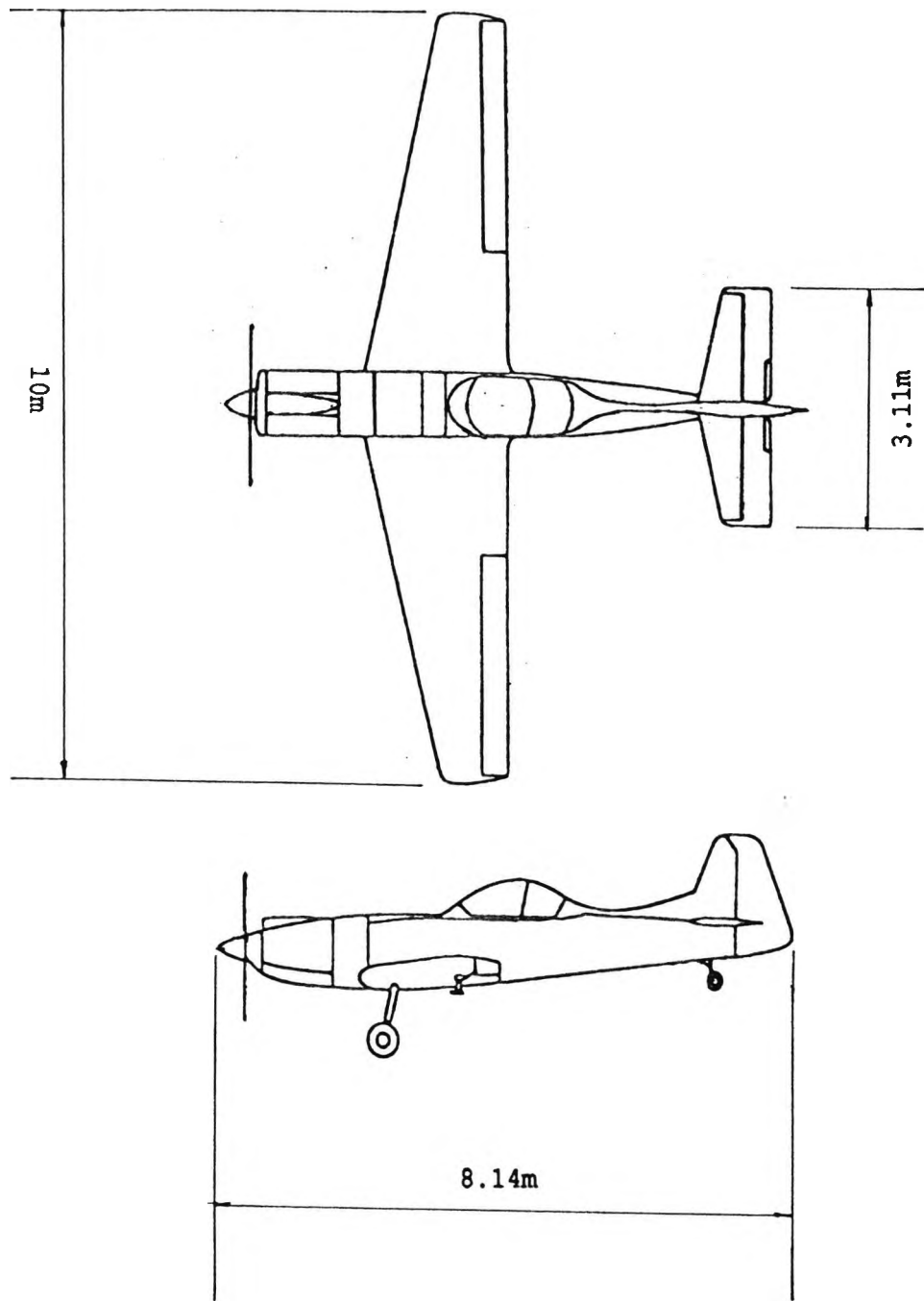
Fig. 3.3 General layout of Cranfield A1

Unmarked elements : Rigid elements

I - XIX : Beam elements
XX : Pilot + front fuselage lumped inertia
XXI : Fin lumped mass

1 - 21 : Node points
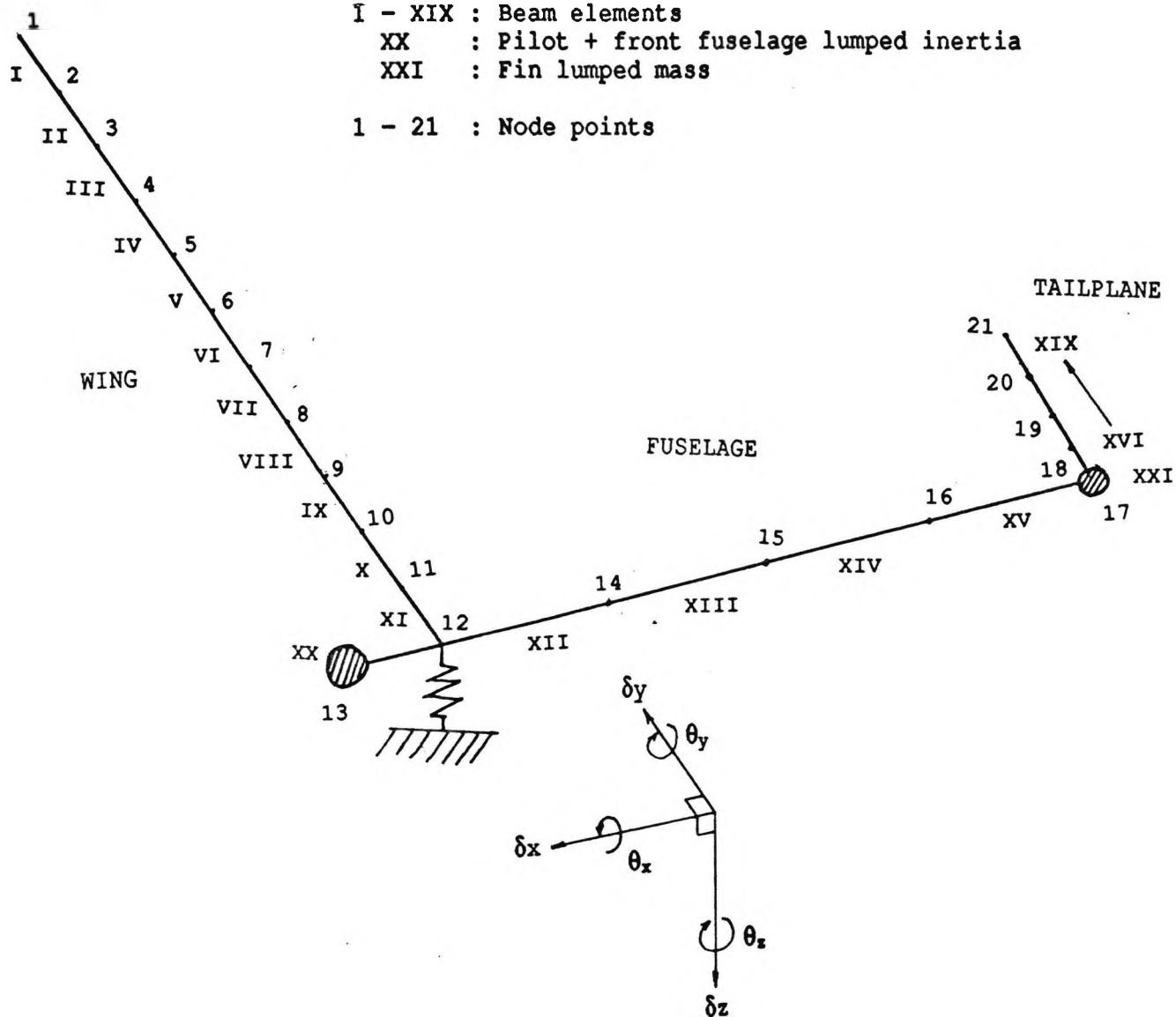
Fig. 3.4 Finite element idealisation of Kestrel

Fig. 3.5 Natural frequencies and mode shapes for Kestrel in symmetric motion

ω_h, ω_α

Flexural or torsional stiffness
of "rigid" element
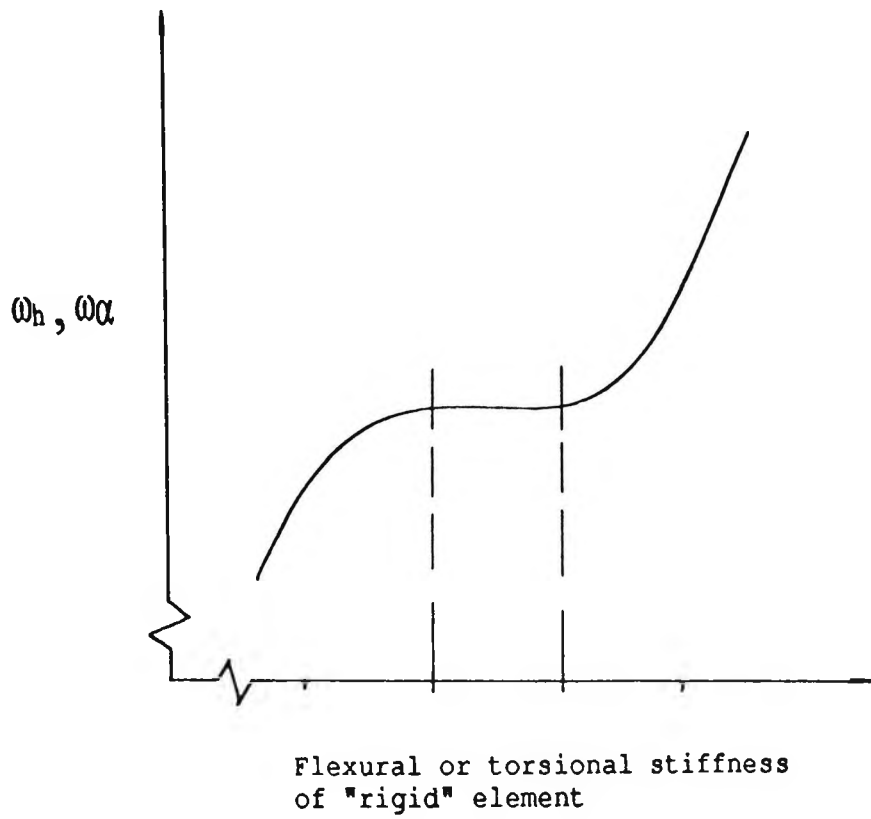
Fig. 3.6   Characteristic trend of instability in model
ill conditioning
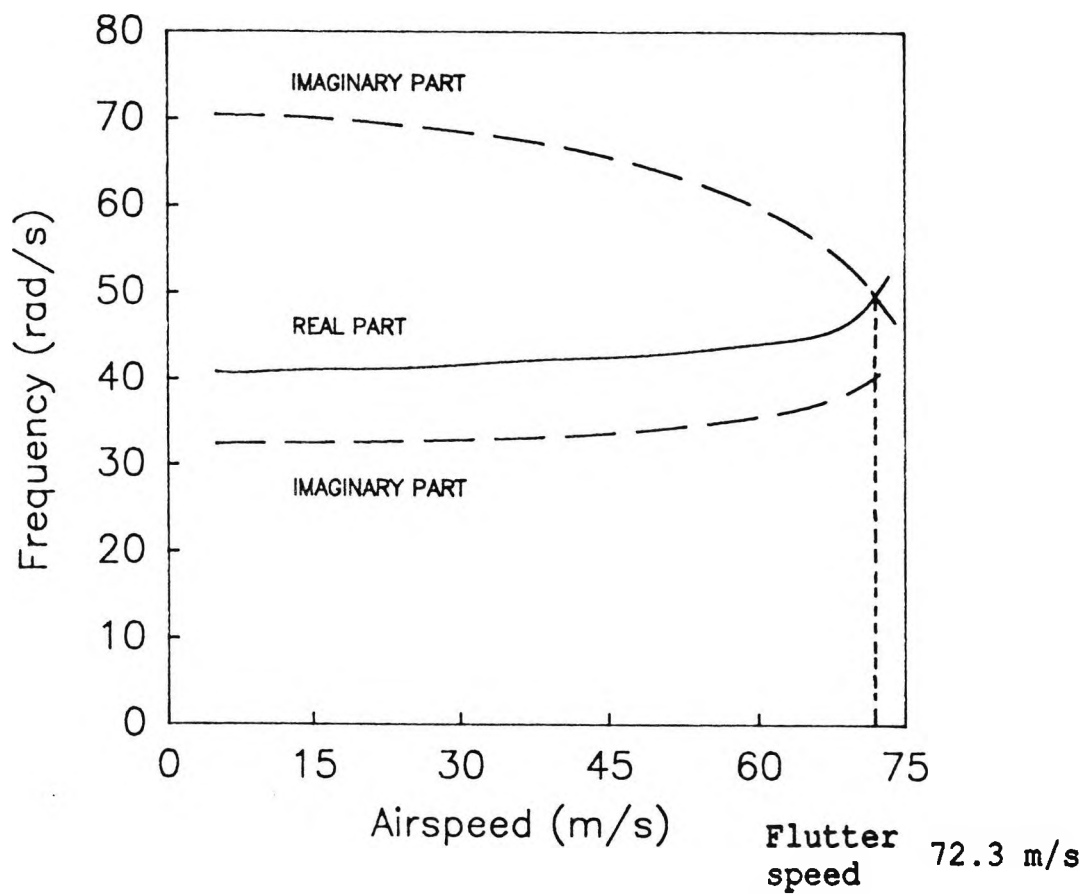
Fig. 3.7 Plot of the complex flutter determinant for Kestrel
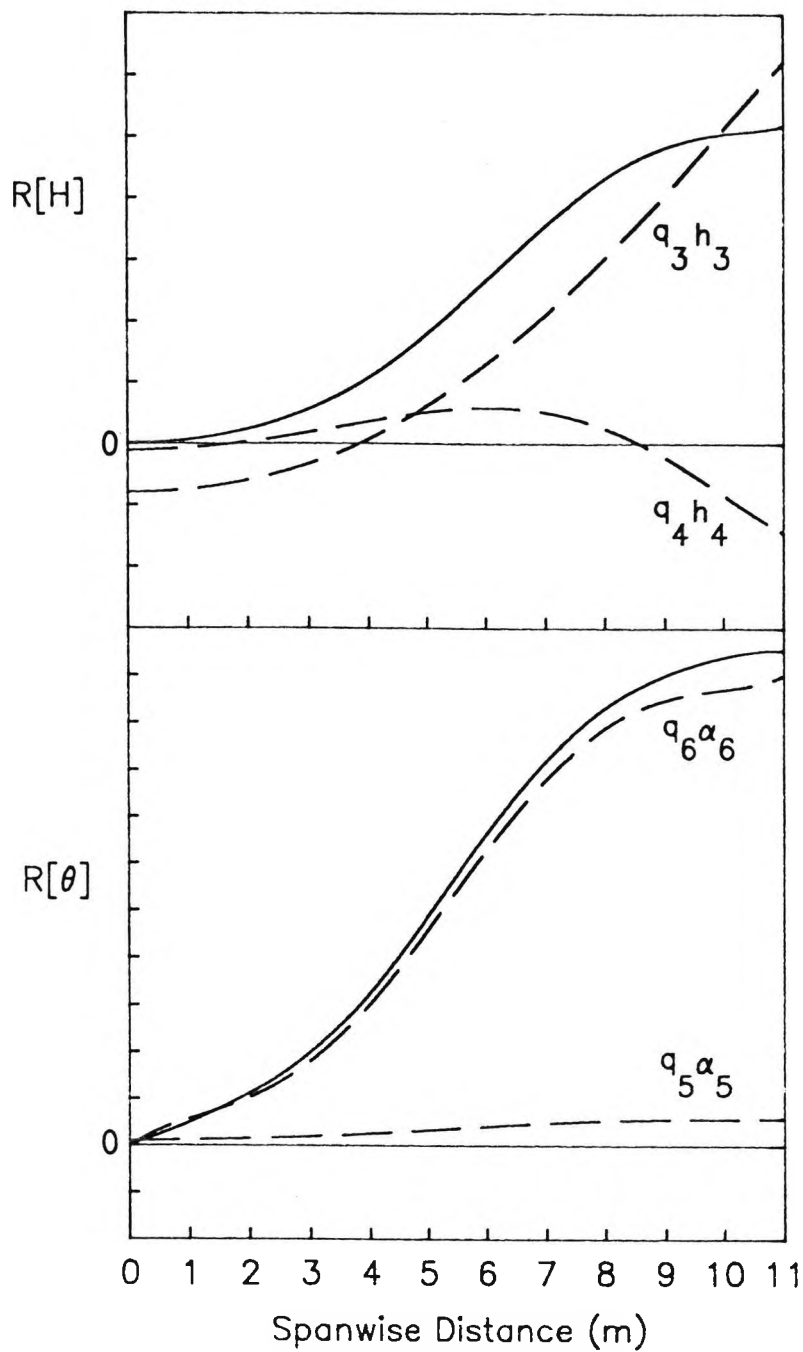
Fig. 3.8 Spanwise variation of real part of vertical displacement
and pitching rotation of Kestrel symmetric flutter mode
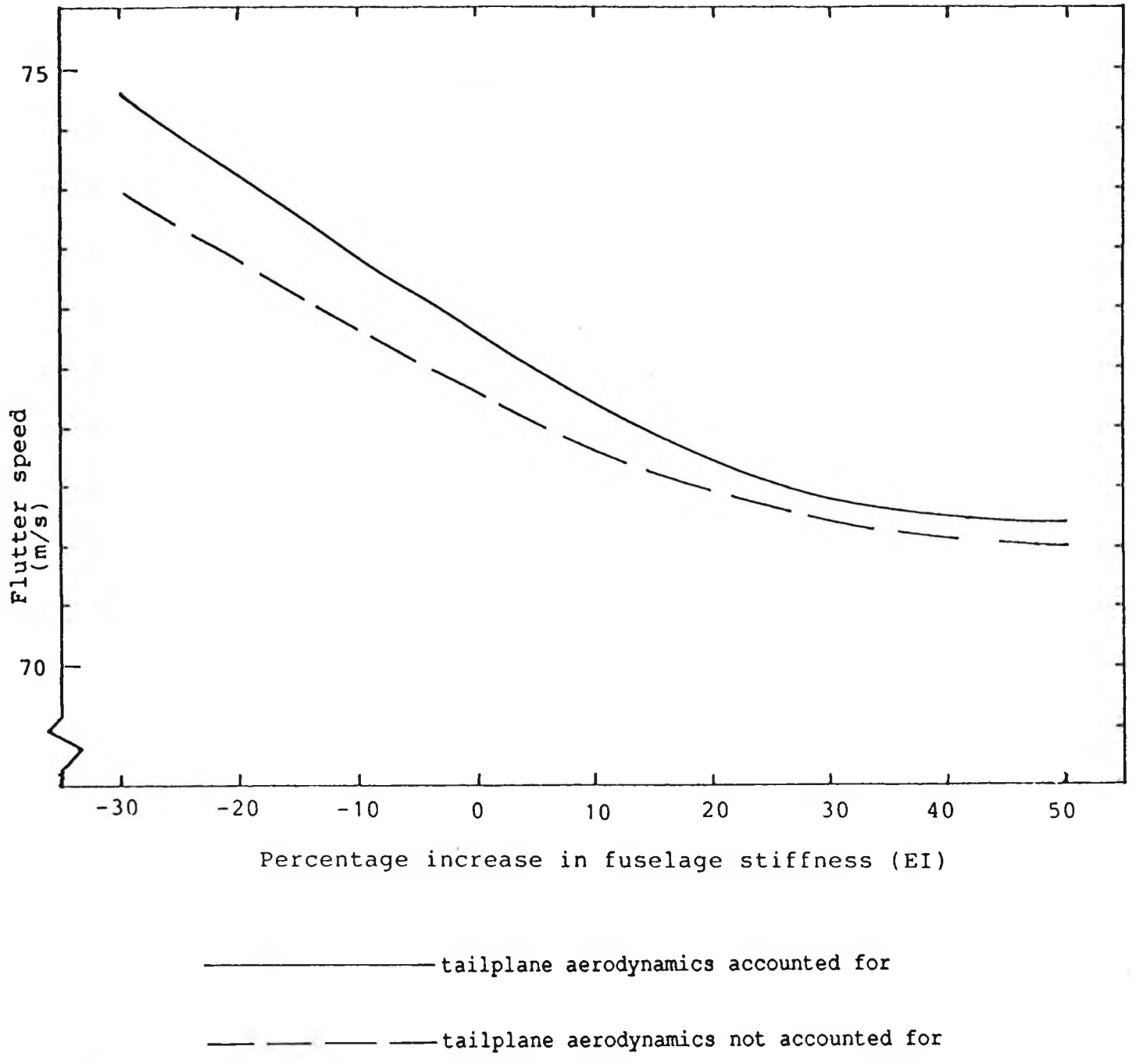
Fig. 3.9   Effect of fuselage bending rigidity on the flutter speed
of Kestrel
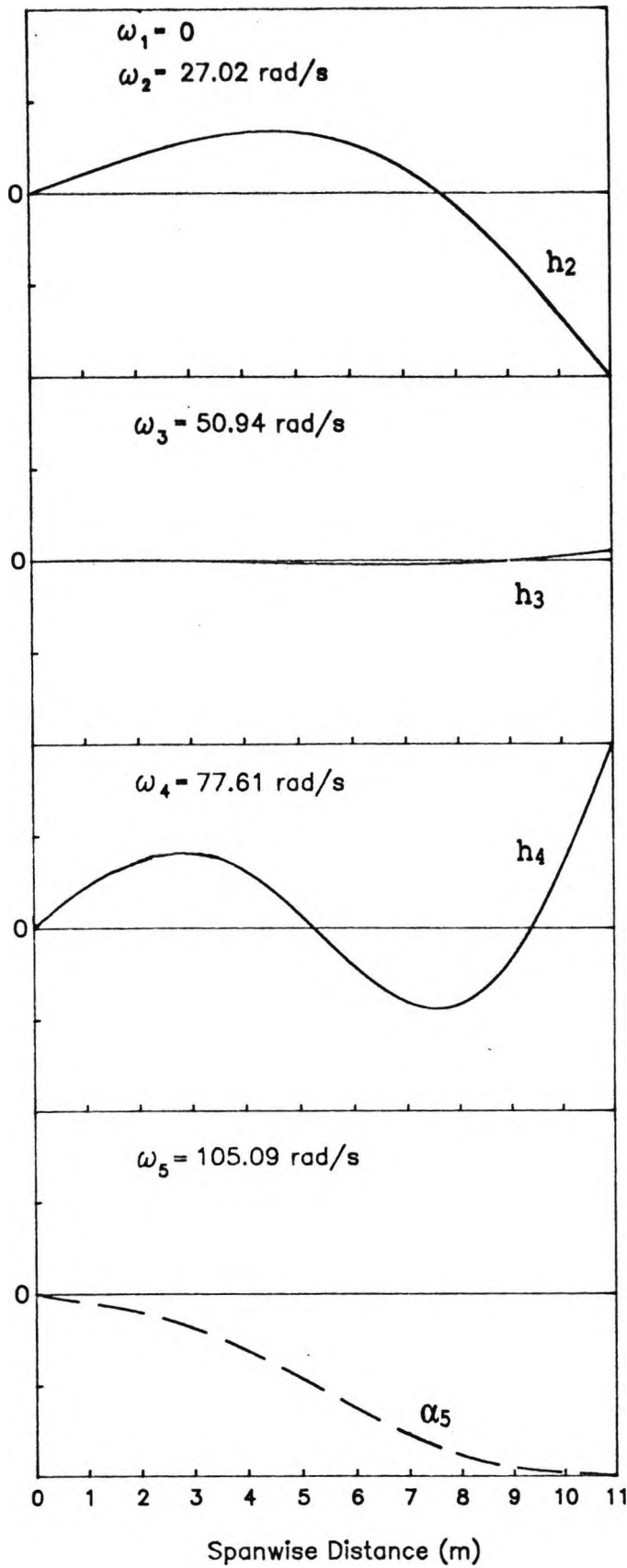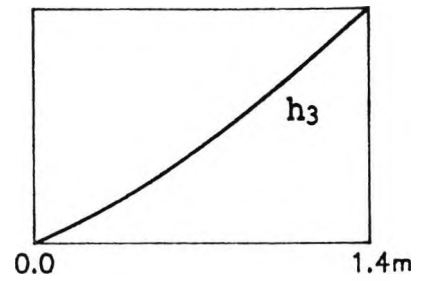
Fig. 3.10 Natural frequencies and mode shapes for Kestrel
          in anti-symmetric motion
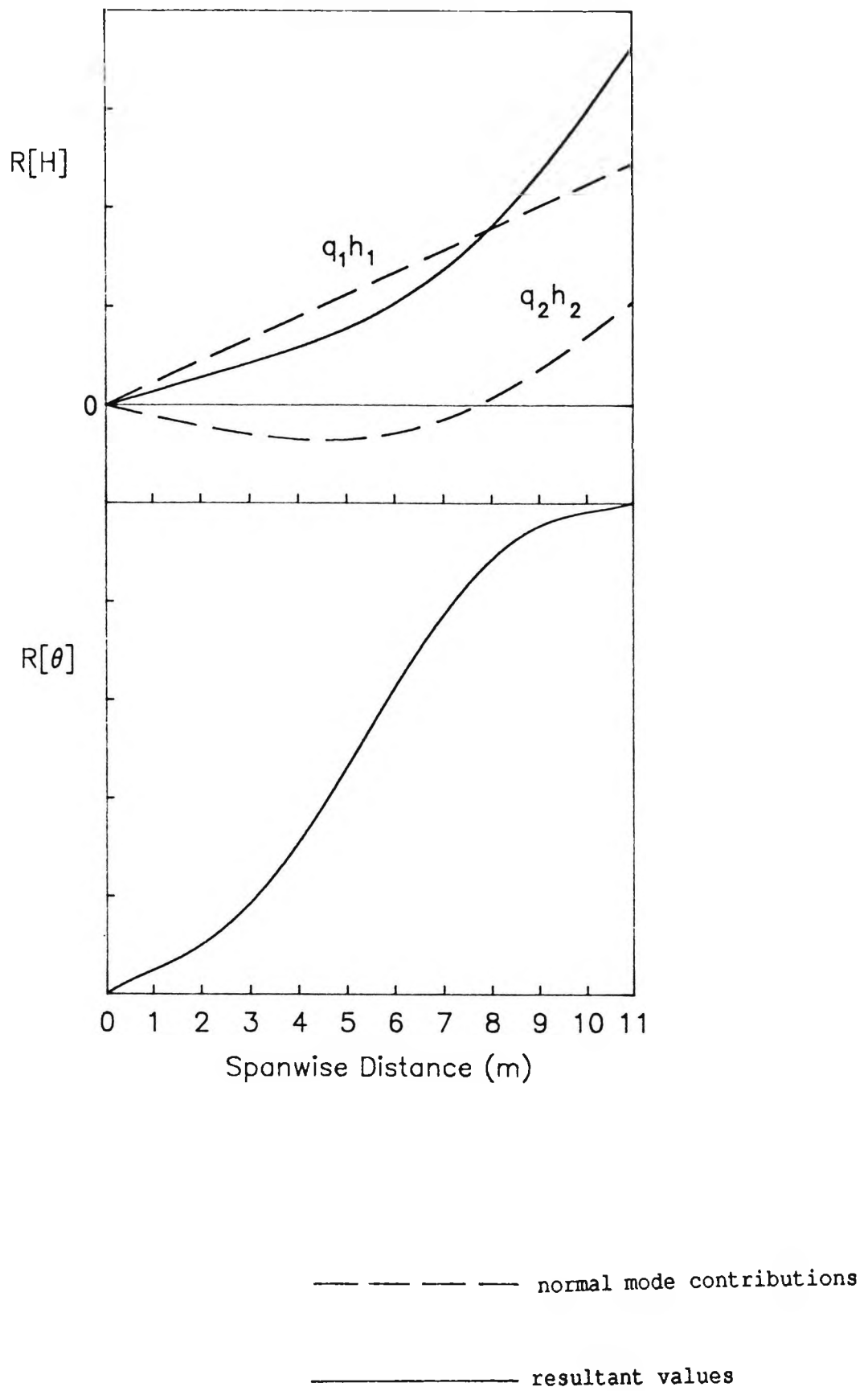
Fig. 3.11   Spanwise variation of real part of vertical displacement
and pitching rotation of Kestrel anti-symmetric flutter
mode
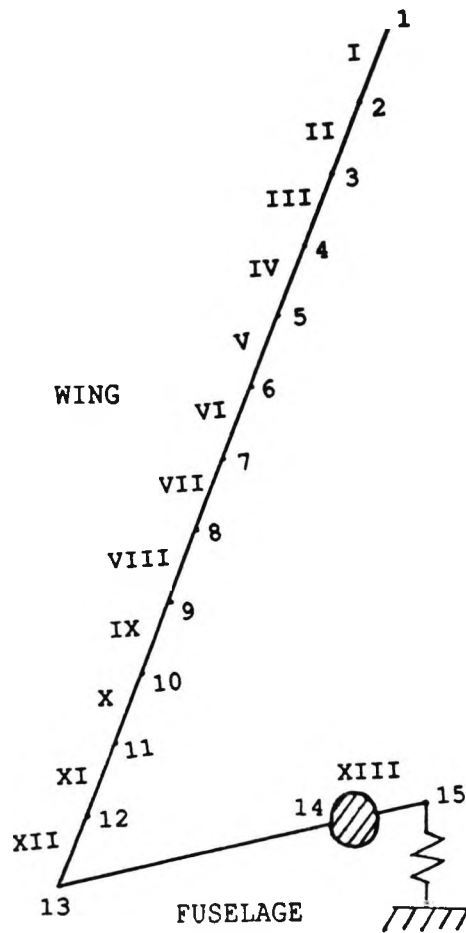
```
1 - XII : Beam elements
   XIII : Pilot + front fuselage lumped inertia

1 - 15 : Node points

Unmarked elements : Rigid elements
```

Fig. 3.12 Finite element idealisation of Ricochet

Wing Modes

$\omega_1 = \omega_2 = 0$
$\omega_3 = 17.72 \, \text{rad/s}$

h_3

0

$\omega_4 = 68.99 \, \text{rad/s}$

h_4

0

$\omega_5 = 169.54 \, \text{rad/s}$

0

$\omega_6 = 283.76 \, \text{rad/s}$

0

α_6

0.0   1.5   3.0   4.5   6.0   7.5
Spanwise Distance (m)

————————— vertical displacement (h)

— —— — —— — pitching rotation (α)
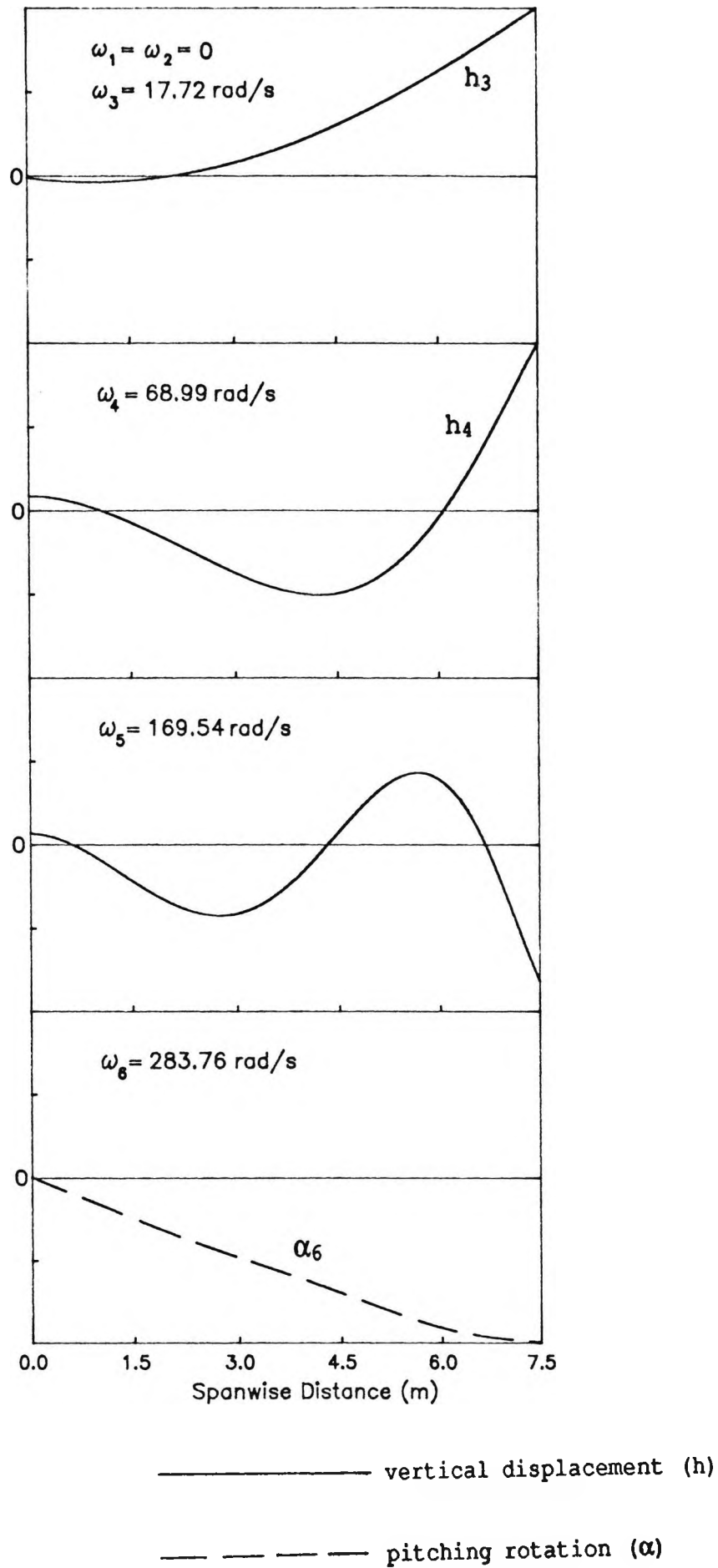
Fig. 3.13 Natural frequencies and mode shapes for Ricochet
in symmetric motion
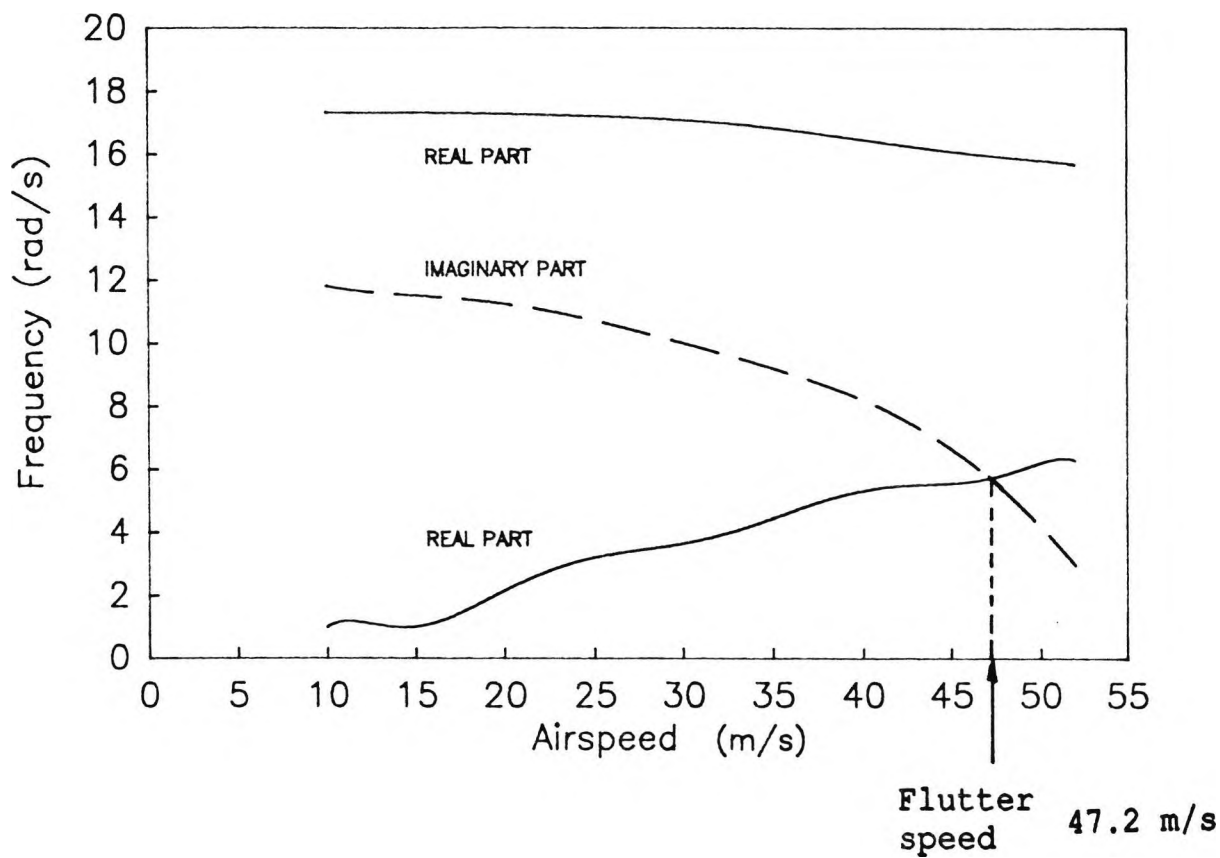
Fig. 3.14 Plot of the complex flutter determinant for Ricochet
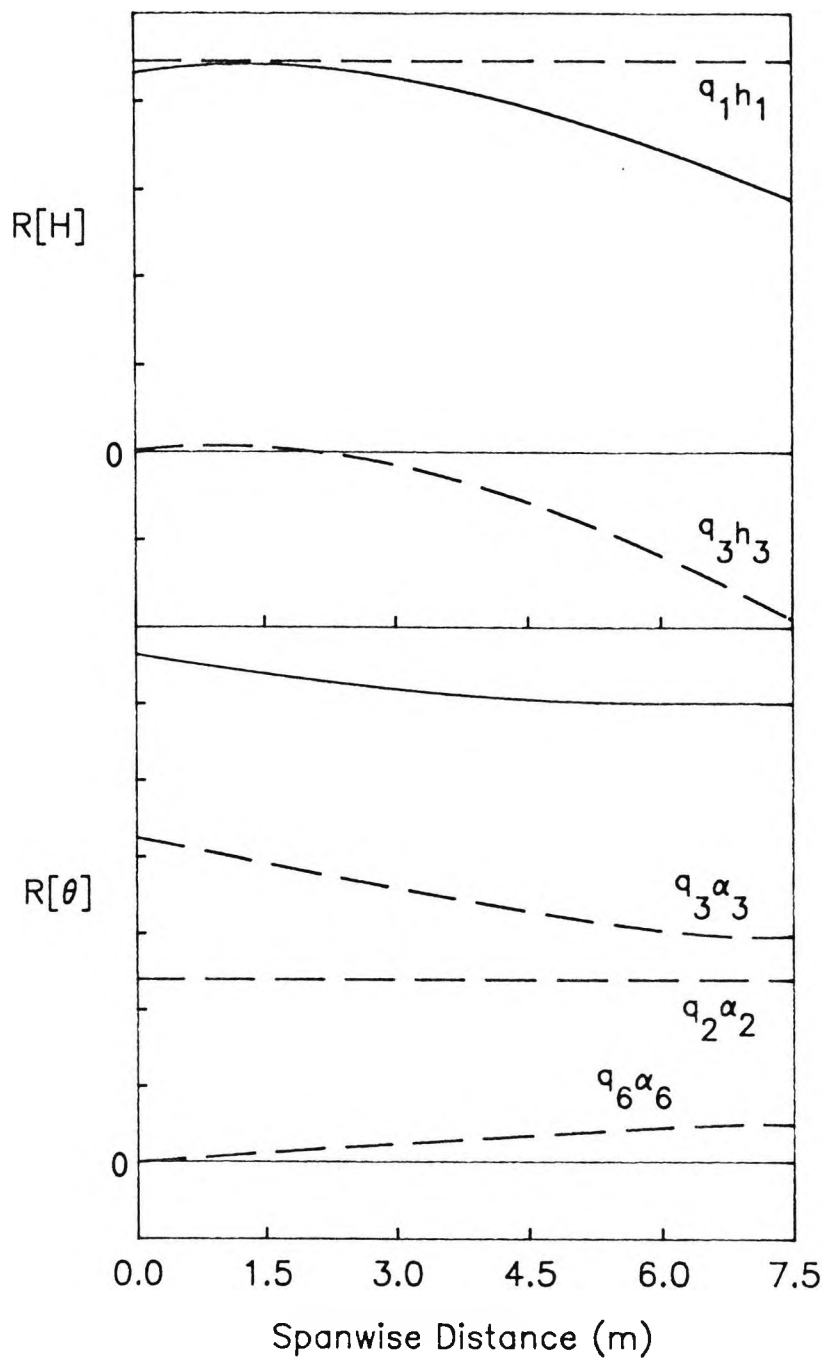
Fig. 3.15 Spanwise variation of real part of vertical displacement
and pitching rotation of Ricochet symmetric flutter mode
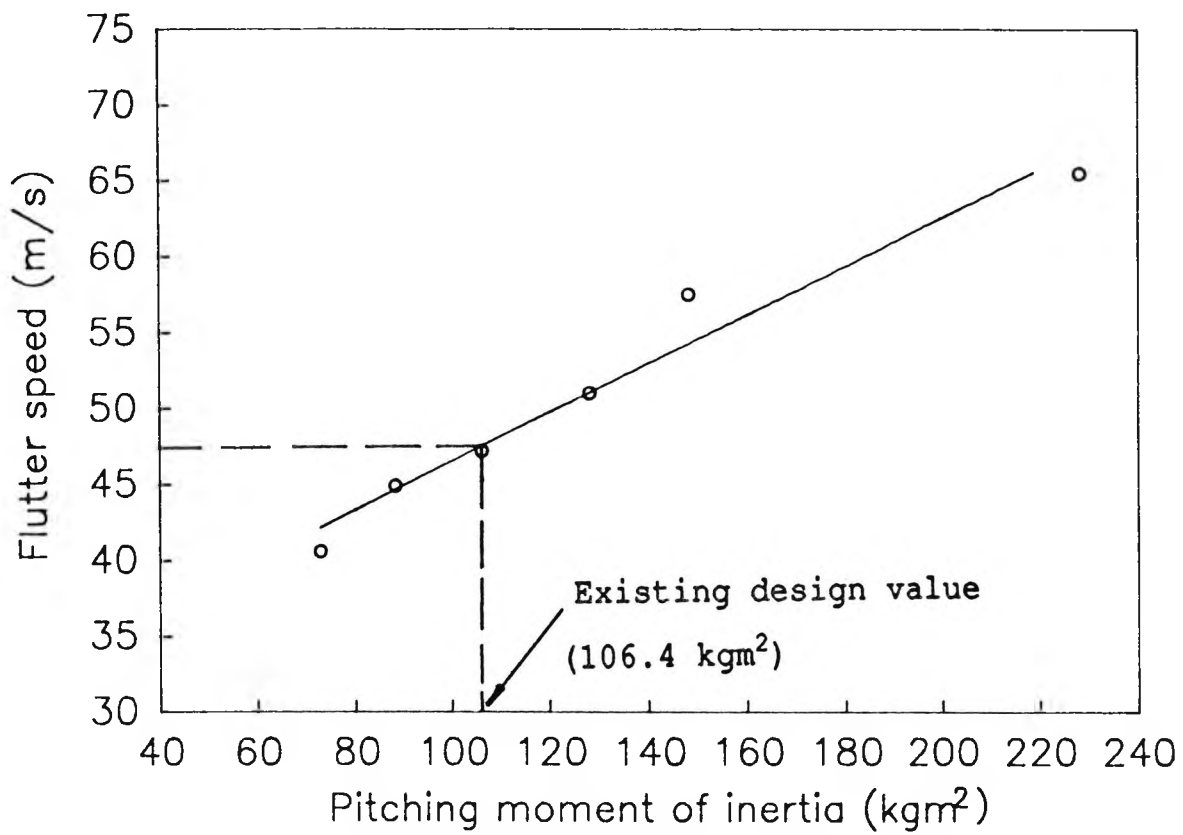
Fig. 3.16 Variation of flutter speed of Ricochet against pitching
moment of inertia of pilot fuselage assembly
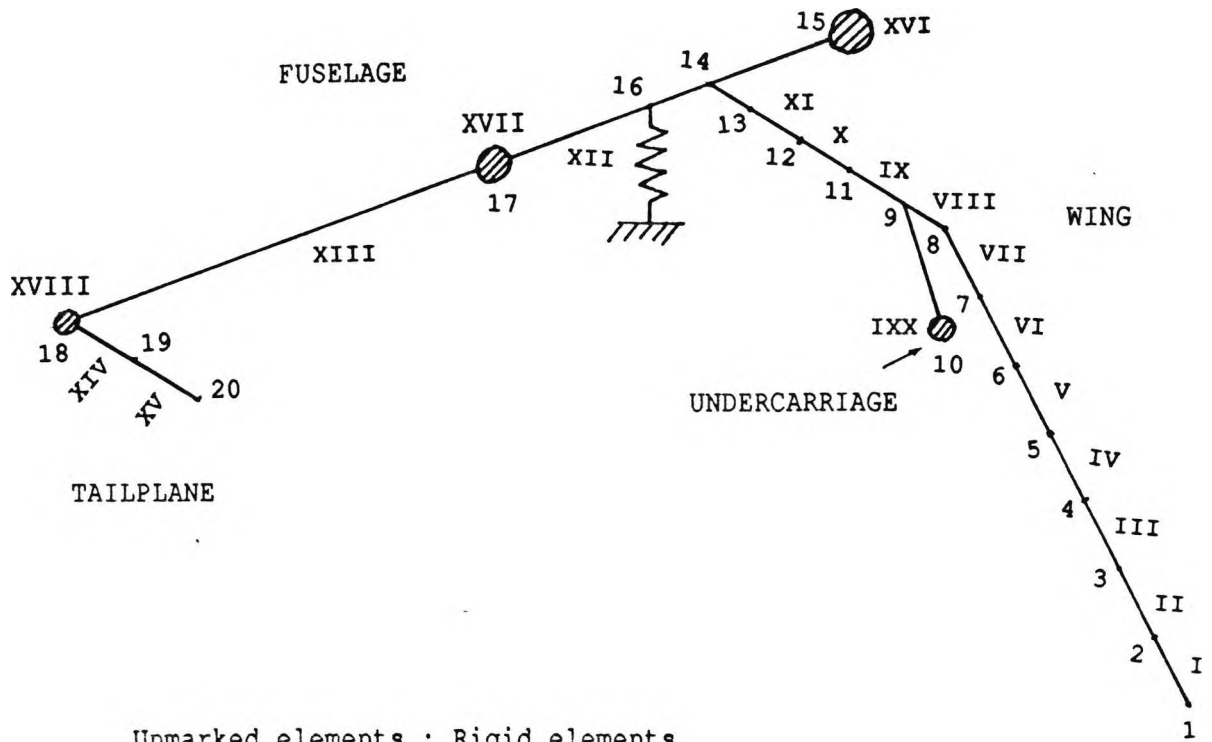
Unmarked elements : Rigid elements

    I - XV : Beam elements
     XVI   : Front fuselage + engine lumped mass
    XVII : Pilot lumped inertia
    XVIII : Fin lumped inertia
     IXX   : Undercarraige lumped inertia

   1 - 20 : Node points

Fig. 3.17 Finite element idealisation of A1

dimensions in mm

side elevation — loading points ∇

Beam element idealisation

Finite element idealisation
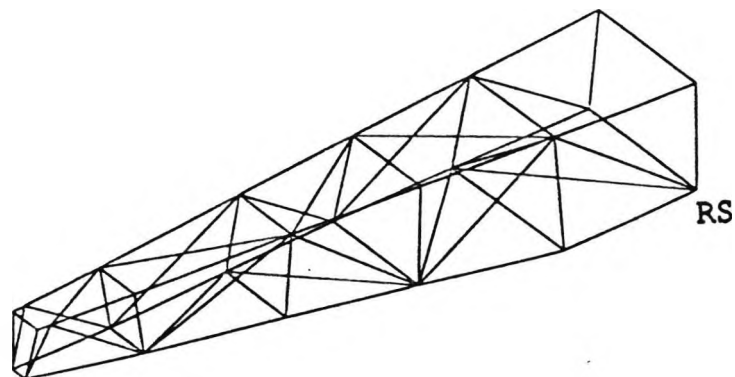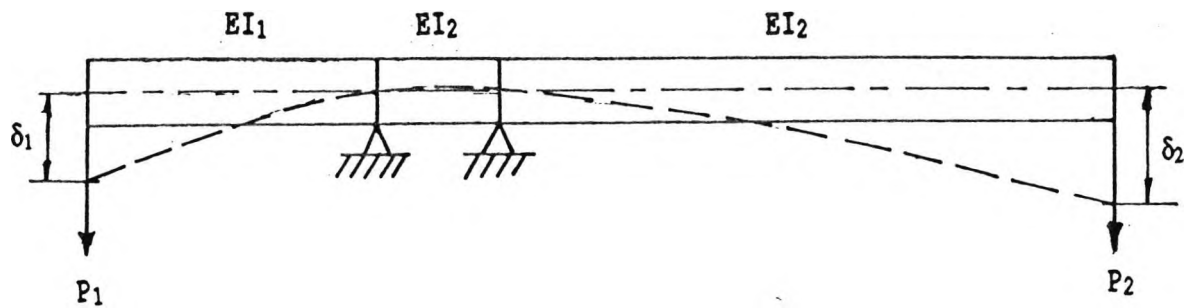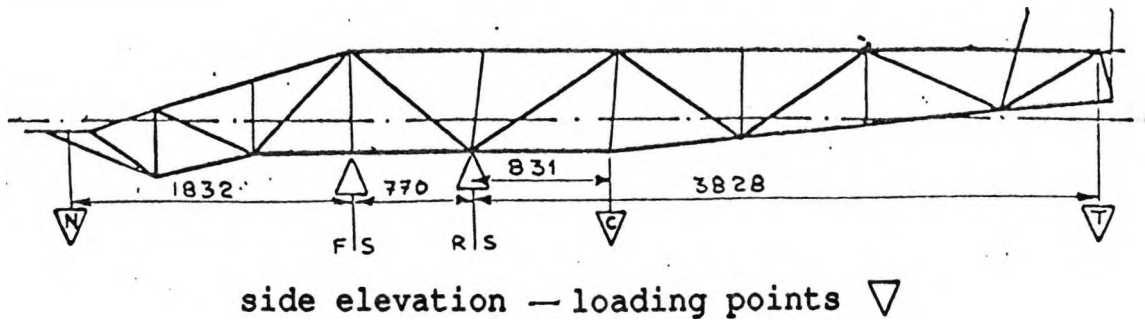
Fig. 3.18 Layout and representation of rear fuselage of A1

Wing Modes

$\omega_1 = \omega_2 = 0$
$\omega_3 = 78.12$ rad/s

h_3

0

$\omega_4 = 147.15$ rad/s

α_4

0

h_4

$\omega_5 = 310.25$ rad/s

α_5

0

h_5

$\omega_6 = 424.77$ rad/s

0

α_6

0.0   1.0   2.0   3.0   4.0   5.0
Spanwise Distance (m)

Tailplane Mode

h_4

0.0   1.6m
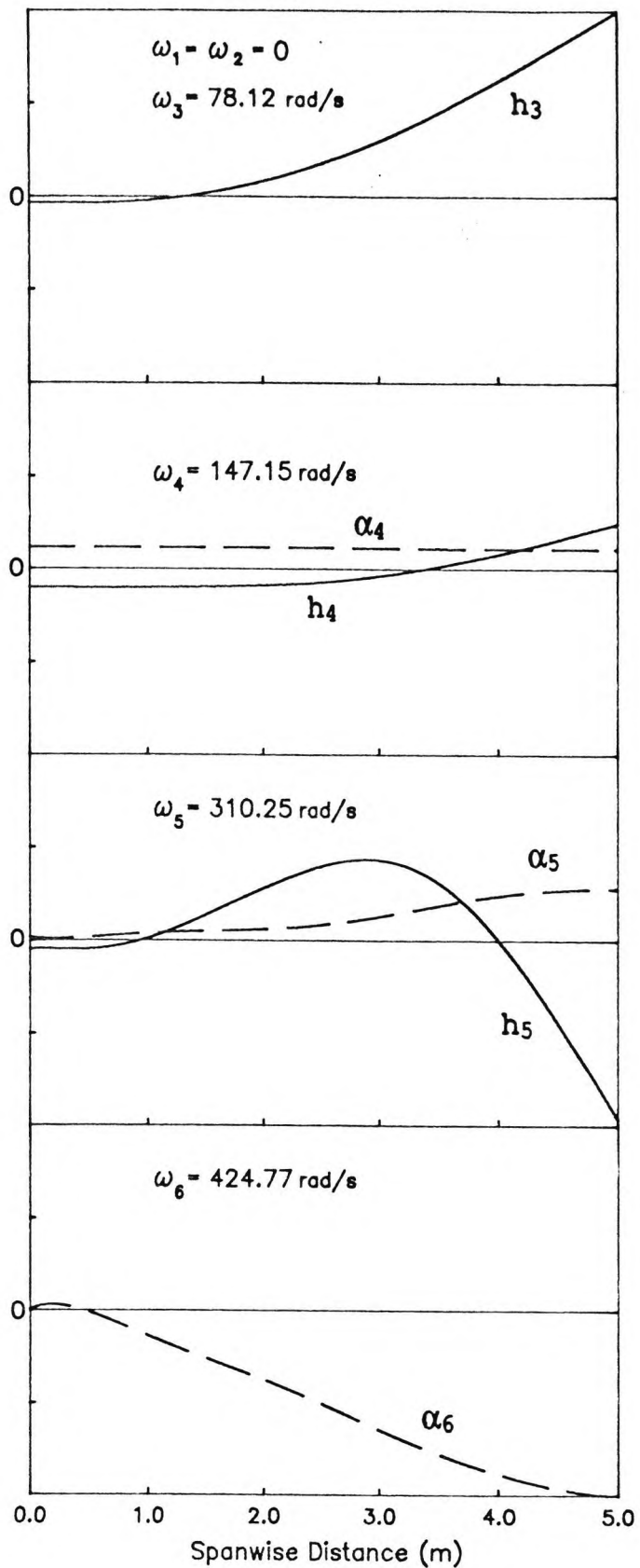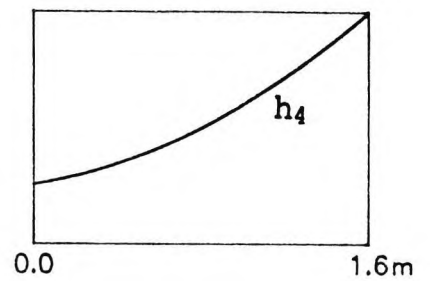
—————————— vertical displacement (h)

— — — — — pitching rotation (α)

Fig. 3.19 Natural frequencies and mode shapes for A1
in symmetric motion
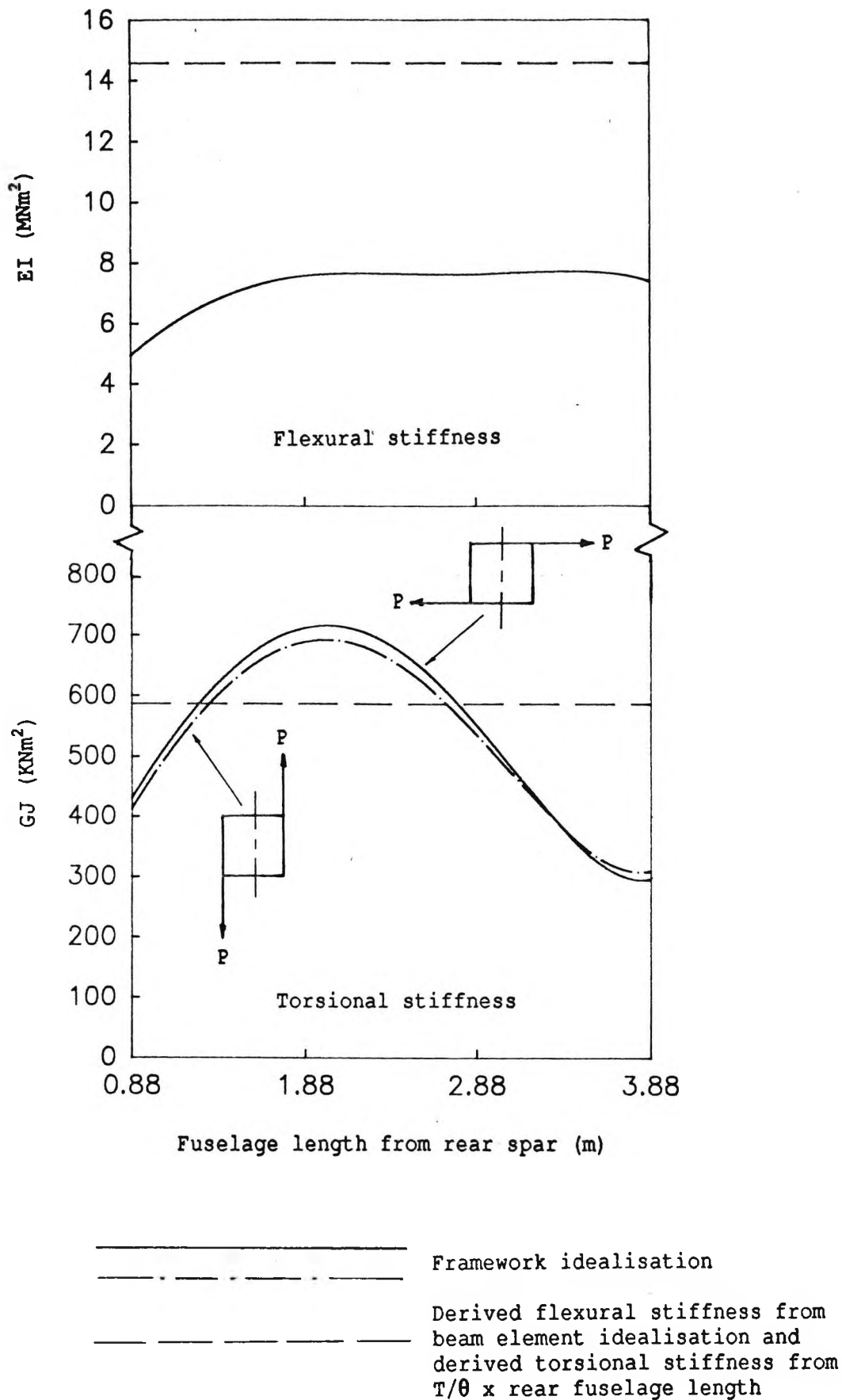
Fig. 3.20 Variation of A1 rear fuselage stiffness with fuselage
          length

$f_3 = 69.4$ Hz
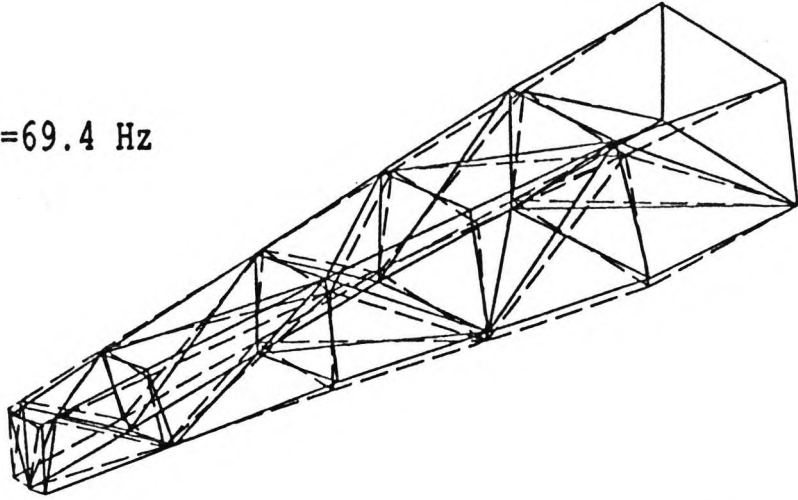
$f_2 = 39.1$ Hz
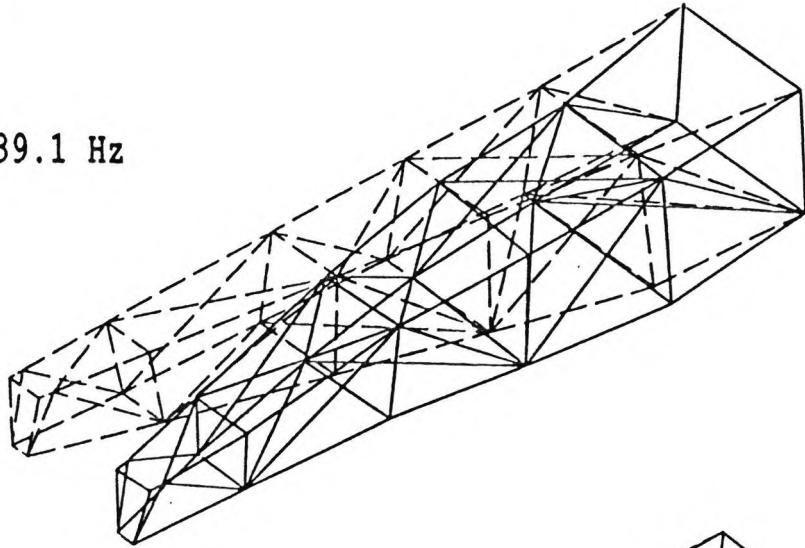
$f_1 = 35.0$ Hz
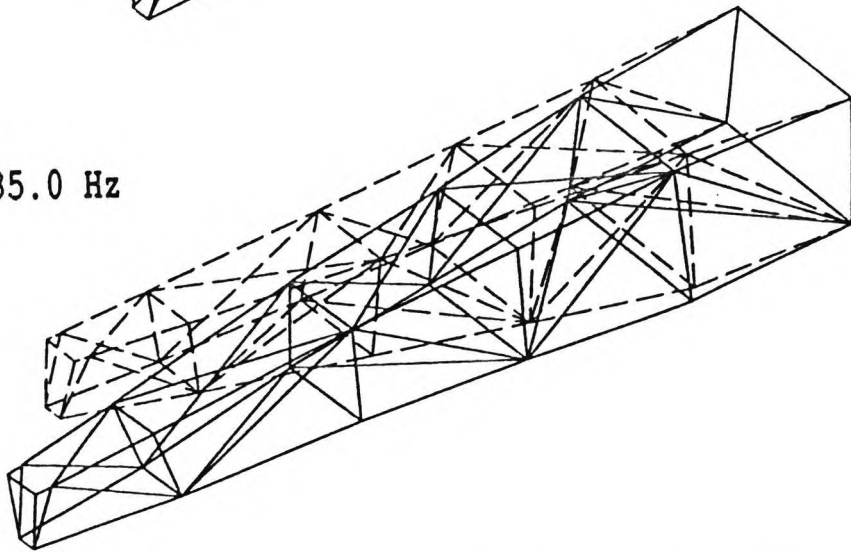
— — — — — undeformed shape

——————— deformed shape

Fig. 3.21a Cantilevered natural frequencies and mode shapes of A1
rear fuselage

$f_6 = 111.8$ Hz
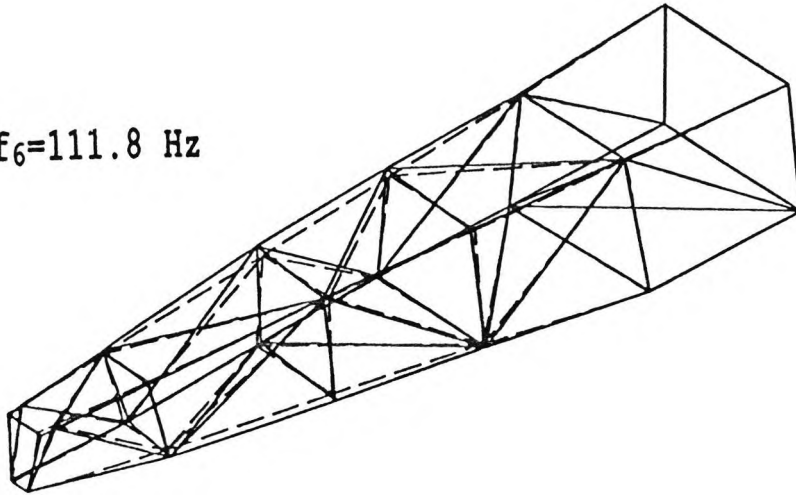
$f_5 = 101.8$ Hz
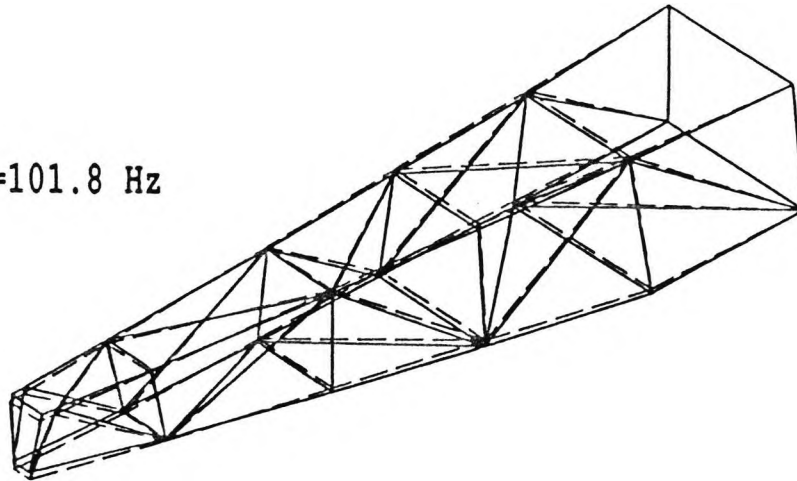
$f_4 = 91.7$ Hz
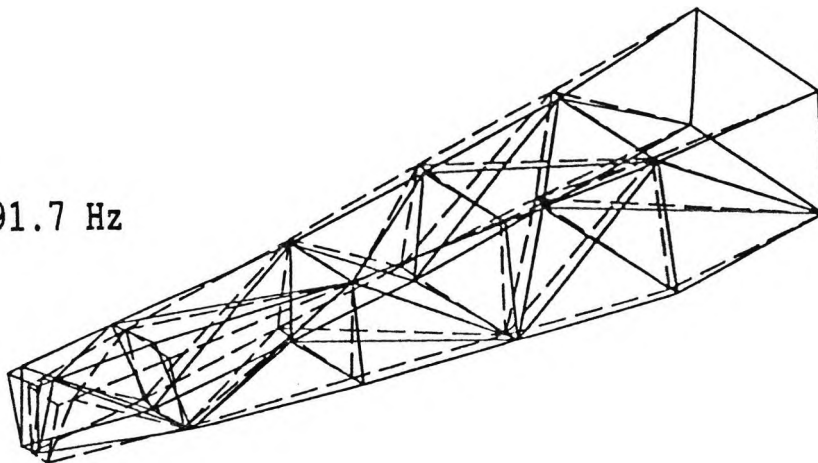
Fig. 3.21a (continued)

$f_9 = 102.2$ Hz
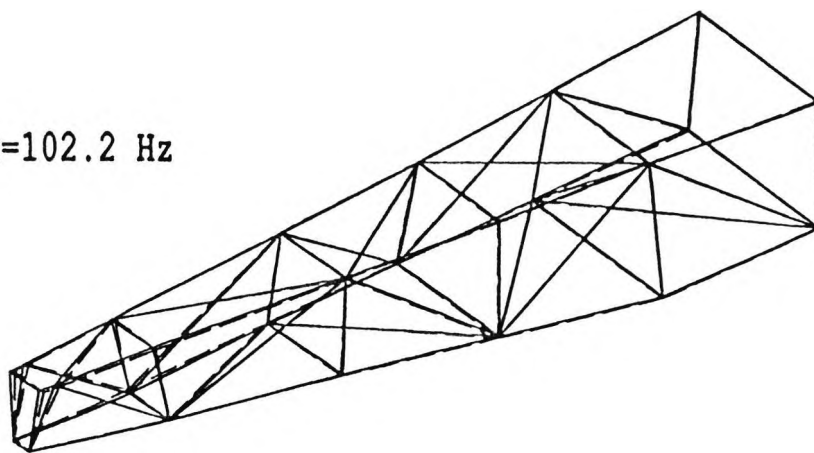
$f_8 = 96.8$ Hz
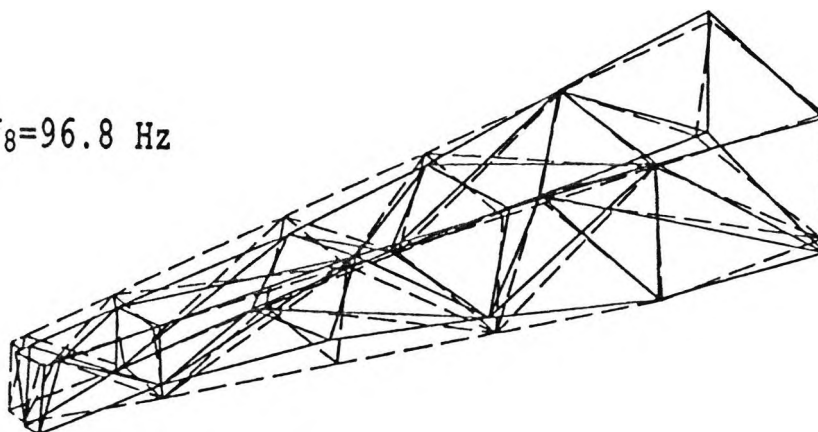
$f_7 = 56.9$ Hz
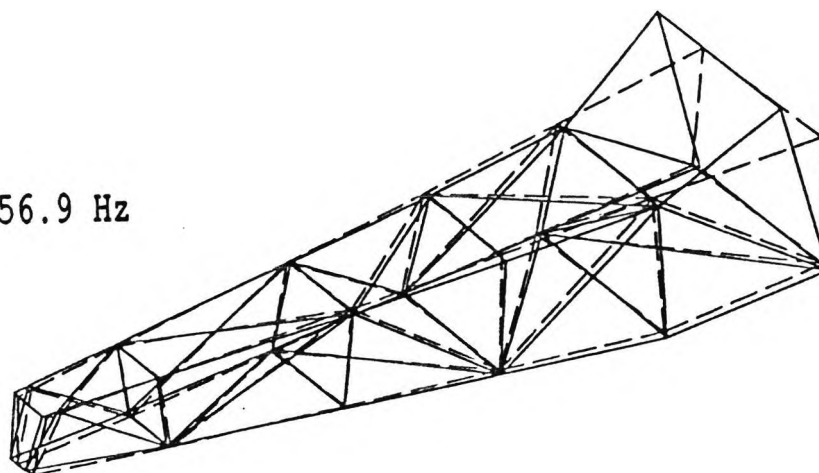
— — — — undeformed shape

——————— deformed shape

Fig. 3.21b Free-Free natural frequencies and mode shapes of A1
            rear fuselage

$f_{12} = 112.1$ Hz
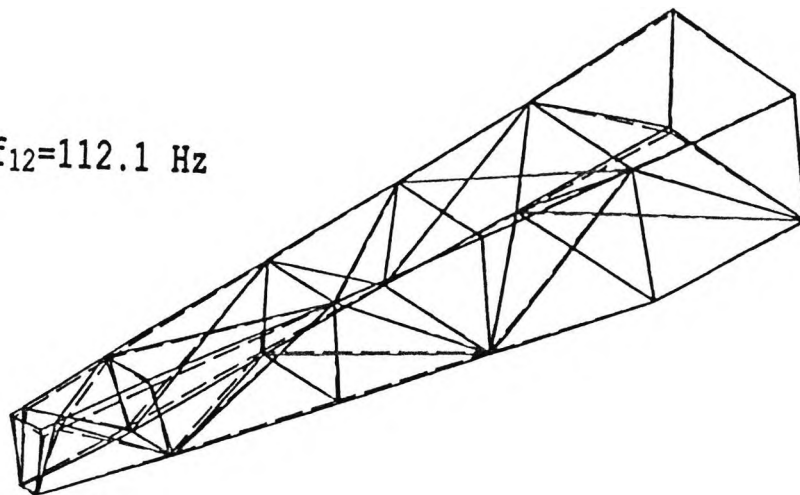
$f_{11} = 109.8$ Hz
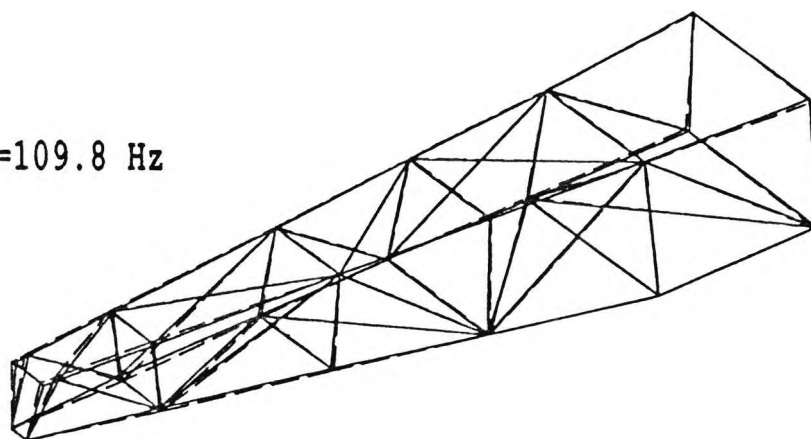
$f_{10} = 104.9$ Hz
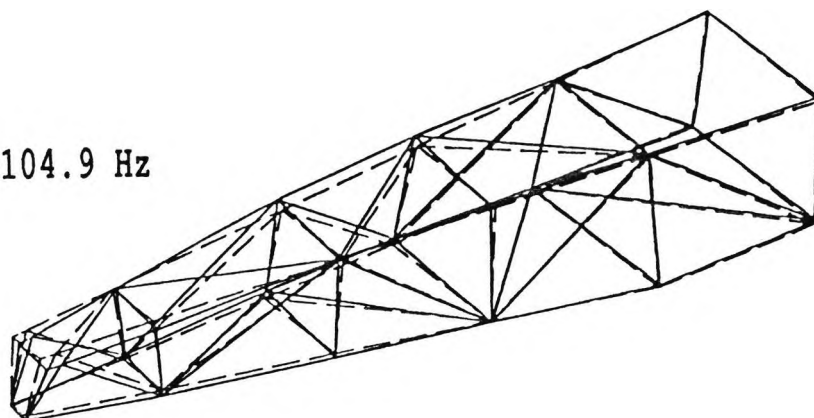
Fig. 3.21b(continued)

Wing Modes

$\omega_1 = 0$

$\omega_2 = 150.28$ rad/s

h_2

0

Fuselage Mode

$\omega_3 = 182.68$ rad/s

h_3

0

$\omega_3 = 182.68$ rad/s

0.0   1.0   2.0   3.0   4.0   5.0   6.0

Fuselage Length (m)

$\omega_4 = 409.07$ rad/s α_4

h_4

0

0.0   1.0   2.0   3.0   4.0   5.0

Spanwise Distance (m)
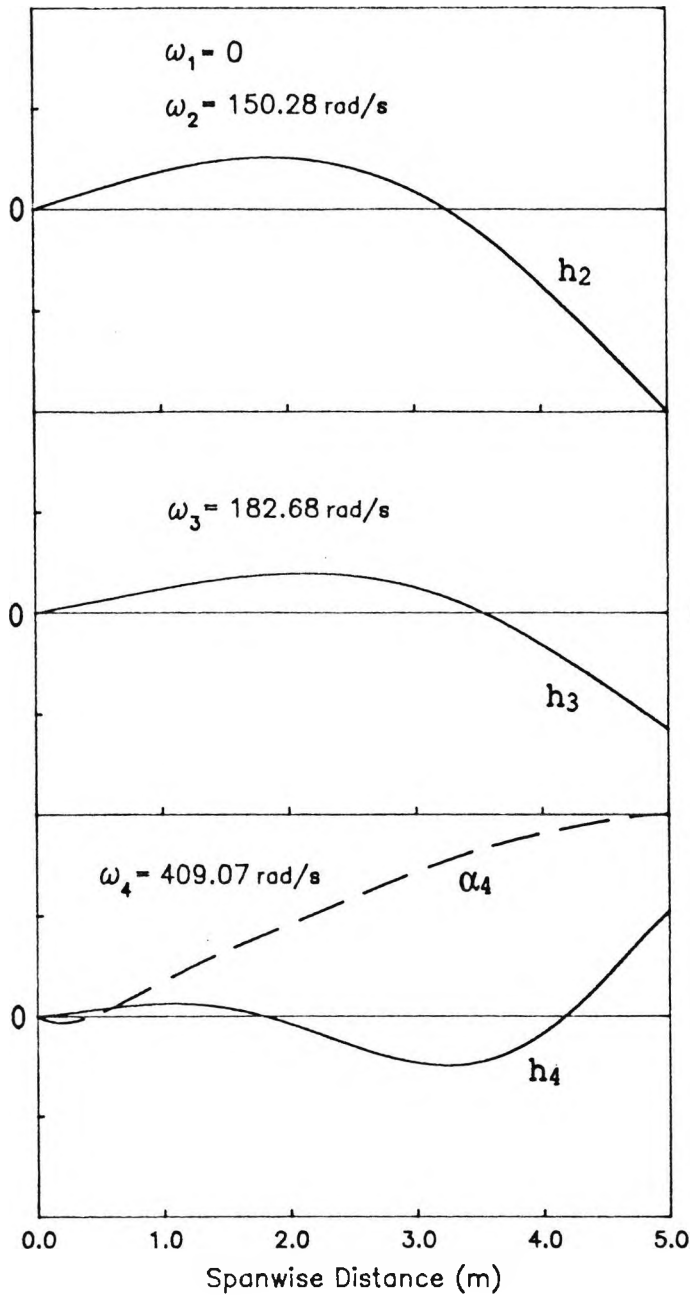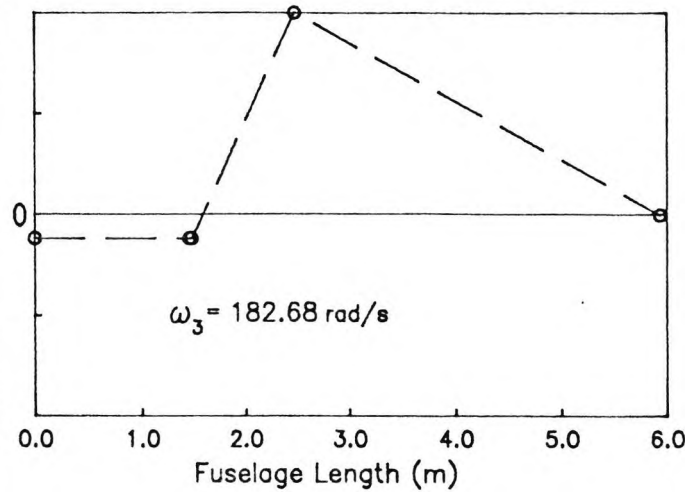
——————— vertical displacement (h)

— — — — — pitching rotation (α)

Fig. 3.22   Natural frequencies and mode shapes for A1
in anti-symmetric motion

UNIT: mm
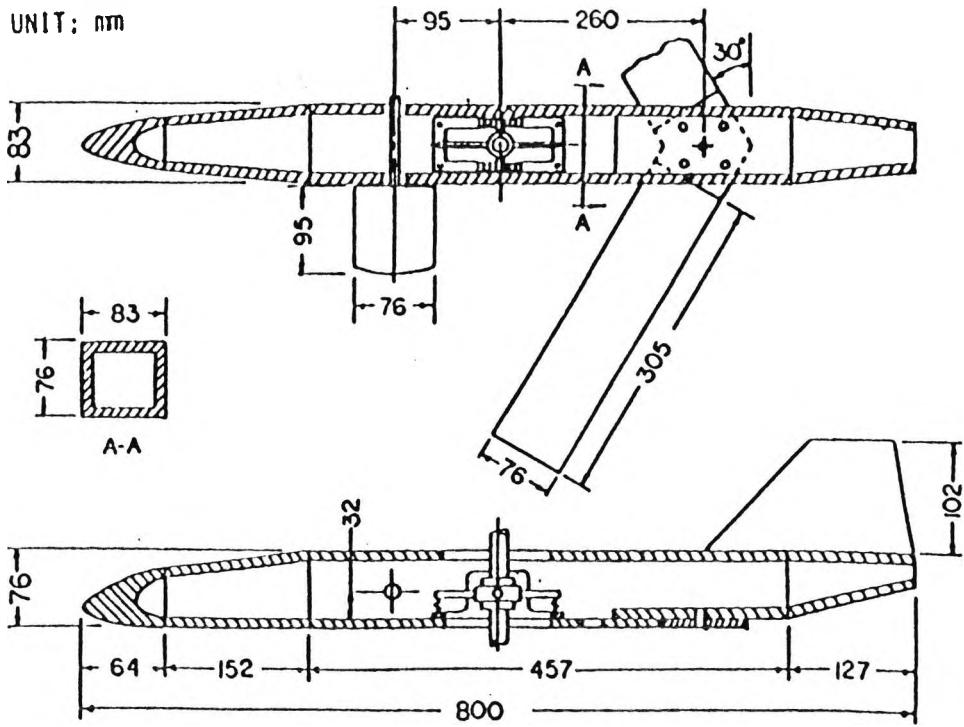
Fig. 3.23 Aircraft model layout

4.0 AIRCRAFT DYNAMIC STABILITY

4.1 Background

In general the stability characteristics of an aircraft are investigated using aerodynamic derivatives[14,15] and with rigid-body assumptions only. This approach, hereafter will be referred to as the classical approach in this investigation. However some authors[22,23,85] have taken partial account of flexibility by using a quasi-static method which employs quasi-steady aerodynamic derivatives (k=0) modified to take into account flexibility on the basis of static deflections only. However these equations are derived on the assumption that all the inertia and damping terms, pertaining to the flexible modes and unsteady aerodynamics are negligible, which is questionable for flexible aircraft at higher frequencies for instance close to the flutter condition.

Other methods introduce the concept of attached, mean and principal axes systems,[86,87] instead of the classical body fixed axes, when introducing flexibility. Warzak et al[88] used a mean axes system, implementing strip theory to represent the quasi-steady aerodynamic forces. Dusto[89] and Rodden et al[90] also made use of mean axes but employed structural and aerodynamic influence coefficients (SIC) and (AIC) to define the structural deformation and the subsequent aerodynamic forces induced. These aerodynamic influence coefficients are generated from lifting surface programs[91] and lend themselves well to aerodynamic factoring. Notably this approach has been implemented within the aeroelastic capabilities of MSC/NASTRAN.[®24]

Woodcock[21] favoured body fixed axes for any integrated approach to aeroelasticity and in this investigation as in the case of the flutter problem, this system is used. Utilising the generalised form of the Theodorsen function, the effects of flexibility and unsteady aerodynamics are examined on the stick fixed short period oscillation of deformable aircraft. Changes in forward speed are omitted so that the current analysis does not predict the phugoid mode. Similar studies have utilised this axis system in the same manner and have used the Theodorsen function

to evaluate the aerodynamic loads.[92,93] However these investigations have restricted themselves to the rigid body modes and low frequency harmonic motion to establish the dynamic stability. Goland[94] used the Wagner function to evaluate the unsteady aerodynamic forces for arbitrary motion but restricted the analysis to rigid body motion. Van Schoor and von Flowtow[20] recently have demonstrated the importance of including unsteady aerodynamic effects, with the use of the generalised Theodorsen function within a dynamic stability analysis on a highly flexible man powered aircraft.

4.1.1 Theodorsen's Generlised Function

In the last section the Theodorsen function $C(k)$ and strip theory were used to evaluate the flutter speed. However for the present investigation a unified method of stability analysis of deformable aircraft is presented. The method involves extending the Theodorsen function to non-harmonic arbitrary motion and again is based on the validity of strip theory.[39]

In the flutter problem, sinusoidal motion is assumed to exist between the transition of stable and unstable oscillatory motion so that above the flutter speed the motion is divergent and below the flutter speed the motion is convergent. The Theodorsen expressions used for lift and moment in the flutter analysis are valid for aerofoil oscillation of the form $e^{i\omega t}$ or $e^{ik\hat{t}}$, where $\hat{t} = Ut/b$. The Theodorsen function used in the flutter analysis is expressed in terms of Hankel functions and shown below.

$$C(k) = \frac{H_1^{(2)}(k)}{H_1^{(2)}(k) + iH_0^{(2)}(k)} = F + iG \qquad (4.1)$$

For non-harmonic oscillation (convergent or otherwise) of an aerofoil, the lift and moment can be obtained if the Theodorsen function $C(k)$ is properly calculated for complex values of k. This involves the solution of Bessel's functions for complex arguments (The details of the derivation in the analysis are in Appendix F). This extension of the Theodorsen function for motion of the form $e^{\lambda t}$ where $\lambda = \mu + i\omega$, can be first found in the work of Luke and

Dengler.[29] However Edwards[95] appears to be the first investigator to practically exploit this function via Laplace transformations to evaluate aerodynamic loads for arbitrary motion of an aerofoil. This technique measures the subcritical and supercritcal stability of aeroelastic systems, for active flutter suppression and gust alleviation modeling.[96] In this investigation this analysis is considered within the frequency domain and includes the aircraft rigid body modes.

To apply this extension of the Theodorsen function, the vertical displacements and pitching rotations at various points on the wing are given appropriate time dependence. The term k in $C(k)$ is regarded as a complex argument so that $k = \dfrac{\omega b}{U} - \dfrac{i\mu b}{U} = \rho e^{i\theta}$. Figure 4.1 shows the real and imaginary parts of $C(k)$ as functions of ρ and θ, where ρ is the modulus of the argument and θ the phase. This figure extends the calculations of Luke and Dengler, to $\theta = + 60^0$ and $\theta = 180^0$. The Theodorsen function is given by the curves for $\theta = 90^0$. However for the current dynamic stability analysis only the convergent plane is considered i.e. $0^0 < \theta < 90^0$.

In the flutter problem the airspeed and the frequency parameter are the primary unknowns and the value of μ, (which is a measure of damping) is zero implying that the motion is simple harmonic. If an airspeed is chosen below the flutter speed, the stability determinant involving ω and hence μ and can be solved for zero's of both the real and imaginary part. In the case of symmetric motion, if the two rigid-body modes, namely heave and pitch are included in the analysis along with the elastic modes, the real part μ gives the short period damping and the imaginary part ω gives the short period frequency of oscillation at the chosen speed.

4.1.2 Formulation of the Stability Determinant

Utilising the flutter equation for the aeroelastic system and assuming aerofoil oscillatory motion of the form $e^{\lambda t}$ the following stability determinant can be obtained

$$\left| \lambda^2 \left[\diagdown M \diagdown \right] + \left[\diagdown K \diagdown \right] - \left[Q \right] \right| = 0 \qquad (4.2)$$

87

where in the mathematical model, the two rigid body modes, heave and pitch are required to define the short period motion associated with elastic modes in the symmetric motion.

The solution of the stability determinant is essentially the same as that of the flutter determinant previous. However since the term k in C(k) is a complex argument $k = \dfrac{\omega b}{U} - \dfrac{i \mu b}{U} = \rho e^{i\theta}$ the determinant becomes primarily a complex function of two unknown variables ρ and θ for a given airspeed. For a chosen airspeed the real and imaginary parts of the stability determinant are evaluated for a range of ρ and θ until both real and imaginary parts vanish and the corresponding entities are obtained.

$$\omega_{sp} = \rho\cos\theta = \text{short period frequency (rad/s)}$$

$$\mu_{sp} = -\rho\sin\theta = \text{short period damping (1/s)}$$

4.2 Extension of Classical Flutter Axes to Dynamic Stability Analysis

4.2.1 Tailed Aircraft

Referring to figure 4.2 we shall consider a rectangular wing aircraft. In addition to the rigid body modes the aircraft is allowed one elastic mode, namely wing bending.

4.2.1.1 Modal Representation

Using a similar approach to that by Bisplinghoff[33] the displacement field of the aircraft is represented with respect to generalised coordinates.

$$w(y,t) = \sum_{i=1}^{\infty} \phi_i(y) q_i(t) \qquad (4.3)$$

where the $\phi_i(y)$ are normalised natural mode shapes of the aircraft under the prescribed boundary conditions, and $q_i(t)$ are normal coordinates. In this transformation, displacement of the aircraft is represented by two rigid body modes of zero frequency plus a superposition of normalised modes of the unrestrained airplane, as

follows:

$$\text{heave} \qquad \phi_1(y) = 1, \qquad \omega_1 = 0,$$

$$\text{pitch} \qquad \phi_2(y) = 1, \qquad \omega_2 = 0,$$

wing bending $\qquad \phi_3(y) = \zeta, \qquad \omega_f \qquad$ taken in the spanwise direction

4.2.1.2 Inertial Representation

The expression for the kinetic energy is written as:

$$T = \frac{1}{2} \int_V \dot{w}(y,t) \; \rho(y) \; dV \tag{4.4}$$

where here ρ is the material density

Assuming for simplicity the mass of the aircraft is concentrated at the wing and tailplane Eq.(4.4)

$$T = \frac{1}{2} \sum (\dot{q}_h - \bar{x}_w \dot{q}_p + \zeta \dot{q}_f)^2_{Wing} \; dm + \frac{1}{2} \sum (\dot{q}_h + \bar{x}_T \dot{q}_p)^2_{Tail} \; dm \tag{4.5}$$

where q_h q_p and q_f are the generalised co-ordinates of heave, pitch about the aircraft c.g. and wing flexure. $\bar{x}_w$ and $\bar{x}_T$ are the respective distances of the wing and tailplane c.g.'s from the c.g. for the complete aircraft.

Since the natural modes are orthogonal, Eq.(4.5) reduces to

$$T = \frac{1}{2} \sum (\dot{q}_h^2 + \bar{x}_w^2 \dot{q}_p^2 + \zeta^2 \dot{q}_f^2)_{Wing} \; dm + \frac{1}{2} \sum (\dot{q}_h^2 + \bar{x}_T^2 \dot{q}_p^2)_{Tail} \; dm$$

$$T = \frac{1}{2} \left(M \dot{q}_h^2 + I_{yy} \dot{q}_p^2 + m_f \dot{q}_f^2 \right) \tag{4.6}$$

where

M Total mass of the aircraft

I_{yy} Total aircraft pitching moment of inertia

89

$$m_f = \int_0^l \zeta^2(y) \ m(y) \ dy \qquad\qquad m(y) \ \text{mass per unit length of one wing}$$

l Spanwise length

The total potential energy for the aircraft contains only the strain energy of the elastic wing i.e.

$$U = \frac{1}{2} \int_0^l EI(y) \left(\frac{\partial^2 w}{\partial^2 y} \right)^2 dy \qquad\qquad (4.7)$$

In terms of normalised natural modes shapes:

$$U = \frac{1}{2} \omega_f^2 \int_0^l \zeta^2(y) \ m(y) \ dy \ q_f^2 \ = \ \frac{1}{2} m_f \omega_f^2 \ q_f^2 \qquad\qquad (4.8)$$

Substituting expressions for the Kinetic and potential energy given by Eq.(4.6) and Eq.(4.8) into Lagrange's equation results in the following equation of motion interms of generalised co-ordinates.

$$\begin{bmatrix} M & 0 & 0 \\ 0 & I_{yy} & 0 \\ 0 & 0 & m_f \end{bmatrix} \begin{bmatrix} \ddot{q}_h \\ \ddot{q}_p \\ \ddot{q}_f \end{bmatrix} - \begin{bmatrix} 0 & 0 & 0 \\ 0 & 0 & 0 \\ 0 & 0 & m_f \omega_f^2 \end{bmatrix} \begin{bmatrix} q_h \\ q_p \\ q_f \end{bmatrix} = \begin{bmatrix} Q_{11} & Q_{12} & Q_{13} \\ Q_{21} & Q_{22} & Q_{23} \\ Q_{31} & Q_{32} & Q_{33} \end{bmatrix}$$

$$(4.9)$$

The generalised force $\begin{bmatrix} Q \end{bmatrix}$ is provided by expressions for the virtual work done by the aerodynamic lifting surfaces.

4.2.1.3 Generalised Aerodynamic Matrix

The work done by the respective lifting surfaces is defined

90

as

$$\delta W = \int_0^{S_W} L_W \delta h_W + M_{\alpha W} \delta \alpha_W \, dy + \int_0^{S_T} L_T \delta h_T + M_{\alpha T} \delta \alpha_T \, dy \qquad (4.10)$$

$$= \int_0^{S_W} \begin{bmatrix} \delta h_W & \delta \alpha_W \end{bmatrix} \begin{bmatrix} L_W \\ M_{\alpha W} \end{bmatrix} dy + \int_0^{S_T} \begin{bmatrix} \delta h_T & \delta \alpha_T \end{bmatrix} \begin{bmatrix} L_T \\ M_{\alpha T} \end{bmatrix} dy$$

$$(4.11)$$

Referring to Figure 4.2 the virtual displacements can be written in terms of the generalised co-ordinates. The transformation which gives the deflection of the aerodynamic axis in terms of the amplitudes of the chosen generalised co-ordinates.

$$\begin{bmatrix} \delta h_W \\ \delta \alpha_W \end{bmatrix} = \begin{bmatrix} 1 & -x_W & \zeta \\ 0 & 1 & 0 \end{bmatrix} \begin{bmatrix} \delta q_h \\ \delta q_p \\ \delta q_f \end{bmatrix} \qquad (4.12)$$

$$\begin{bmatrix} \delta h_T \\ \delta \alpha_T \end{bmatrix} = \begin{bmatrix} 1 & x_T \\ 0 & 1 \end{bmatrix} \begin{bmatrix} \delta q_h \\ \delta q_p \end{bmatrix} \qquad (4.13)$$

where x_W and x_T are the respective distances of the wing and tailplane aerodynamic centres from the aircraft c.g.

The lift and moment $\begin{bmatrix} L \\ M_\alpha \end{bmatrix}$ can also be expressed in terms of the aerofoil displacements.

$$\begin{bmatrix} L \\ M_\alpha \end{bmatrix} = \begin{bmatrix} A_{11} & A_{12} \\ A_{21} & A_{22} \end{bmatrix} \begin{bmatrix} h \\ \alpha \end{bmatrix} \qquad (4.14)$$

91

Substituting the above expressions for the wing and tailplane respectively into Eq.(4.11)

$$
\begin{bmatrix} \dfrac{\delta W}{\delta q_h} \\[2mm] \dfrac{\delta W}{\delta q_p} \\[2mm] \dfrac{\delta W}{\delta q_f} \end{bmatrix}
= \int_0^{s_W} \begin{bmatrix} 1 & 0 \\ -x_W & 1 \\ \zeta & 0 \end{bmatrix}
\begin{bmatrix} A_{11} & A_{12} \\ A_{21} & A_{22} \end{bmatrix}
\begin{bmatrix} 1 & -x_W & \zeta \\ 0 & 1 & 0 \end{bmatrix}
\begin{bmatrix} q_h \\ q_p \\ q_f \end{bmatrix} dy \;\; +
$$

$$
\int_0^{s_T} \begin{bmatrix} 1 & 0 \\ x_T & 1 \\ 0 & 0 \end{bmatrix}
\begin{bmatrix} A_{11T} & A_{12T} \\ A_{21T} & A_{22T} \end{bmatrix}
\begin{bmatrix} 1 & x_T & 0 \\ 0 & 1 & 0 \end{bmatrix}
\begin{bmatrix} q_h \\ q_p \\ q_f \end{bmatrix} dy
$$

$$
= \int_0^{s_W} \begin{bmatrix} AW_{11} & AW_{12} & AW_{13} \\ AW_{21} & AW_{22} & AW_{23} \\ AW_{31} & AW_{32} & AW_{33} \end{bmatrix}
\begin{bmatrix} q_h \\ q_p \\ q_f \end{bmatrix} dy
$$

$$
+ \int_0^{s_T} \begin{bmatrix} AT_{11} & AT_{12} & 0 \\ AT_{21} & AT_{22} & 0 \\ 0 & 0 & 0 \end{bmatrix}
\begin{bmatrix} q_h \\ q_p \\ q_f \end{bmatrix} dy
$$

$$(4.15)$$

92

where for the

Wing	Tailplane

$AW_{11} = A_{11}$

$AT_{11} = A_{11T}$

$AW_{12} = -A_{11}x_W + A_{12}$

$AT_{12} = A_{11T} \ x_T + A_{12T}$

$AW_{13} = A_{11}\zeta$

$AT_{21} = A_{11T} \ x_T + A_{21T}$

$AW_{21} = -A_{11}x_W + A_{21}$

$AT_{22} = A_{11T} \ x_T^2 + A_{12T} \ x_T$

$AW_{22} = A_{11}x_W^2 - A_{12}x_W + A_{22} - A_{21}x_W$

$\qquad\qquad + A_{22T} + A_{21T}x_T$

$AW_{23} = -A_{11}\zeta \ x_W + A_{21}\zeta$

$AW_{31} = A_{11}\zeta$

$AW_{32} = -A_{11}\zeta \ x_W + A_{12}\zeta$

$AW_{33} = A_{11}\zeta^2$ 　　　　　　　　　　　　　　　　　(4.16)

Considering quasi-steady aerodynamics the current expressions for unsteady lift and moment can be re-written, neglecting the non-circulatory terms and setting $C(k) = 1.0$, as

$$\left. \begin{array}{l} L = -2\pi\rho Ub(\dot{h} + U\alpha) \\[2em] M_\alpha = 2\pi\rho Ub^2(\frac{1}{2} + a_h)(\dot{h} + U\alpha) \end{array} \right\} \qquad (4.17)$$

where ρ here is atmospheric density. Assuming aerofoil motion of the form $e^{\lambda t}$ the heave displacement considered can be written as

$$h = h \ e^{\lambda t}$$
$$\dot{h} = \lambda \ h \ e^{\lambda t}$$
$$\ddot{h} = \lambda^2 \ h \ e^{\lambda t}$$

expressions (4.17) are changed to take into account modified aerodynamic parameters.

93

$$A_{11} = -\rho U b a_0 \lambda \qquad\qquad A_{12} = -\rho U^2 b a_0$$

$$A_{21} = \rho U b^2 a_0 \lambda \left(\tfrac{1}{2} + a_h\right) \qquad A_{22} = \rho U^2 b^2 a_0 \left(\tfrac{1}{2} + a_h\right) \qquad (4.18)$$

For simplicity it is assumed that the shear centres of both wing and tailplane are coincident with their respective aerodynamic centres, ie $a_h = -0.5$, therefore $A_{21} = A_{22} = 0$. Integrating Eq.(4.15) with respect to the wing and tailplane spans, the generalised aerodynamic matrix is

$$Q(i,j) = \begin{bmatrix} Q_{11} & Q_{12} & Q_{13} \\ Q_{21} & Q_{22} & Q_{23} \\ Q_{31} & Q_{32} & Q_{33} \end{bmatrix} \begin{bmatrix} q_h \\ q_p \\ q_f \end{bmatrix} \qquad (4.19)$$

The generalised aerodynamic terms $Q(i,j)$ are functions of A_{11} and A_{12} and can be expressed in terms provided by Eq.(4.18)

since $\quad S_W = 2 s_W b_W$

$$\qquad S_T = 2 s_T b_T$$

$$Q_{11} q_h = (s_W A_{11} + s_T A_{11T}) q_h$$

$$= -\rho U (a_0 s_W b_W + a_1 s_T b_T) \dot{q}_h$$

$$= -\tfrac{1}{2}\rho U S_W \left(a_0 + a_1 \frac{S_T}{S_W}\right) \dot{q}_h = \overset{\circ}{Z}_W \dot{q}_h$$

$$Q_{12} q_p = (-s_W A_{11} x_W + s_T A_{11T} x_T + s_W A_{12} + s_T A_{12T}) q_p$$

$$= \rho U (a_0 s_W b_W x_W - a_1 s_T b_T x_T) \dot{q}_p - \rho U^2 (a_0 s_W b_W + a_1 s_T b_T) q_p$$

$$= \tfrac{1}{2}\rho U S_W \left(a_0 x_W - a_1 \frac{S_T}{S_W} x_T\right) \dot{q}_p - \tfrac{1}{2}\rho U^2 S_W \left(a_0 + a_1 \frac{S_T}{S_W}\right) q_p$$

$$= \overset{\circ}{Z}_q \, \dot{q}_p - C_1 \, q_p$$

$$Q_{13}q_f = A_{11}I_\zeta \, q_f \qquad\qquad \text{where } I_\zeta = \int_0^{S_w} \zeta \, (y) \, dy$$

$$= -\rho U a_0 b_w \, I_\zeta \, \dot{q}_f$$

$$Q_{21}q_h = (-s_w \, A_{11} \, x_w + s_T \, A_{11T} \, x_T) q_h$$

$$= \rho U (a_0 s_w \, b_w \, x_w - a_1 s_T \, b_T \, x_T) \dot{q}_h$$

$$= \tfrac{1}{2}\rho U S_w (a_0 x_w - a_1 \, \frac{s_T}{s_w} \, x_T) \dot{q}_h \; = \overset{\circ}{M}_w \, \dot{q}_h$$

$$Q_{22}q_p = (s_w \, A_{11} \, x_w^2 + s_T \, A_{11T} \, x_T^2 - s_w \, A_{12} \, x_w + s_T \, A_{12T} \, x_T) q_p$$

$$= -\rho U (a_0 s_w \, b_w \, x_w^2 + a_1 s_T \, b_T \, x_T^2) \dot{q}_p + \rho U^2 (a_0 s_w \, b_w \, x_w - a_1 s_T \, b_T \, x_T) q_p$$

$$= -\tfrac{1}{2}\rho U S_w (a_0 x_w^2 + a_1 \, \frac{s_T}{s_w} \, x_T^2) \dot{q}_p + \tfrac{1}{2}\rho U^2 S_w (a_0 x_w - a_1 \, \frac{s_T}{s_w} \, x_T) q_p$$

$$= \overset{\circ}{M}_q \, \dot{q}_p + C_2 \, q_p$$

$$Q_{23}q_f = -A_{11}I_\zeta \, x_w \, q_f$$

$$= \rho U a_0 b_w \, I_\zeta \, x_w \, \dot{q}_f$$

$$Q_{31}q_h = A_{11}I_\zeta \, q_h$$

$$= -\rho U a_0 b_w \, I_\zeta \, \dot{q}_h$$

$$Q_{32}q_p = (-A_{11}I_\zeta \, x_w + A_{12}I_\zeta) \, q_p$$

$$= \rho U a_0 b_w \, I_\zeta \, x_w \, \dot{q}_p - \rho U^2 a_0 \, b_w \, I_\zeta \, q_p$$

$$Q_{33}q_f = A_{11}I_{\zeta\zeta} \, q_f$$

$$= -\rho U a_0 b_w \, I_{\zeta\zeta} \, \dot{q}_f \qquad \text{where } I_{\zeta\zeta} = \int_0^{S_w} \zeta^2(y) \, dy$$

(4.20)

From inspection $Q_{32} = UQ_{31}$, $Q_{13} = Q_{31}$

4.2.1.4 Stability Matrix

Referring to the matrix equation (4.9) and considering motion of the form

$$q = q \, e^{\lambda t}$$
$$\dot{q} = \lambda \, q \, e^{\lambda t}$$
$$\ddot{q} = \lambda^2 q \, e^{\lambda t}$$

$$\left| \begin{bmatrix} M & 0 & 0 \\ 0 & I_{yy} & 0 \\ 0 & 0 & m_f \end{bmatrix} \lambda^2 - \begin{bmatrix} 0 & 0 & 0 \\ 0 & 0 & 0 \\ 0 & 0 & m_f\omega_f^2 \end{bmatrix} - \begin{bmatrix} Q_{11} & Q_{12} & Q_{13} \\ Q_{21} & Q_{22} & Q_{23} \\ Q_{31} & Q_{32} & Q_{33} \end{bmatrix} \right| \begin{bmatrix} q_h \\ q_p \\ q_f \end{bmatrix} = 0$$

(4.21)

Matrix (4.21) is identical to that of (4.2) for a system with three degrees of freedom.

To simplify the above equation the distance between the wing aerodynamic centre and the aircraft c.g. is put to zero i.e. $x_w = 0$ therefore the term Q_{23} goes to zero.

96

$$
\begin{bmatrix}
M\lambda^2 - Q_{11} & -Q_{12} & -Q_{13} \\
-Q_{21} & I_{yy}\lambda^2 - Q_{22} & 0 \\
-Q_{31} & -Q_{32} & m_f\lambda^2 + m_f\omega_f^2 - Q_{33}
\end{bmatrix}
\begin{bmatrix}
q_h \\
q_p \\
q_f
\end{bmatrix} = 0
$$

$$(4.22)$$

$$
\begin{bmatrix}
M\lambda^2 - \overset{o}{Z}_w\lambda & -\overset{o}{Z}_q\lambda + C_1 & -Q_{13} \\
-\overset{o}{M}_w\lambda & I_{yy}\lambda^2 - \overset{o}{M}_q\lambda - C_2 & 0 \\
-Q_{31} & -Q_{32} & m_f\lambda^2 + m_f\omega_f^2 - Q_{33}
\end{bmatrix}
\begin{bmatrix}
q_h \\
q_p \\
q_f
\end{bmatrix} = 0
$$

$$(4.23)$$

since $\quad C_1 = -\overset{o}{Z}_w U$

$$C_2 = U\overset{o}{M}_w$$

Expanding the determinant of matrix (4.23) results in the following quartic

$$A\,\lambda^4 + B\,\lambda^3 + C\,\lambda^2 + D\,\lambda + E = 0 \qquad (4.24)$$

where

$$A = 1$$

$$B = \left(-\frac{Q_{33}}{m_f} - \frac{\overset{o}{M}_q}{I_{yy}} - \frac{\overset{o}{Z}_w}{M} \right)$$

$$C = \left(\omega_f^2 + \frac{Q_{33}}{m_f}\left(\frac{\overset{o}{M}_q}{I_{yy}} + \frac{\overset{o}{Z}_w}{M} \right) - \frac{Q_{31}^2}{Mm_f} - \frac{U\overset{o}{M}_w}{I_{yy}} + \frac{\overset{o}{Z}_w\overset{o}{M}_q}{MI_{yy}} - \frac{\overset{o}{Z}_q\overset{o}{M}_w}{MI_{yy}} \right)$$

97

$$D = \left[\omega_f^2 \left(-\frac{\overset{\circ}{M}_q}{I_{yy}} - \frac{\overset{\circ}{Z}_w}{M} \right) + \frac{Q_{33}}{m_f} \left(\frac{U\overset{\circ}{M}_w}{I_{yy}} - \frac{\overset{\circ}{Z}_w \overset{\circ}{M}_q}{MI_{yy}} + \frac{\overset{\circ}{Z}_q \overset{\circ}{M}_w}{MI_{yy}} \right) + \frac{\overset{\circ}{M}_q Q_{13}^2}{MI_{yy} m_f} \right]$$

$$E = \left[\omega_f^2 \left(-\frac{U\overset{\circ}{M}_w}{I_{yy}} + \frac{\overset{\circ}{Z}_w \overset{\circ}{M}_q}{MI_{yy}} - \frac{\overset{\circ}{Z}_q \overset{\circ}{M}_w}{MI_{yy}} \right) \right] \qquad\qquad (4.25)$$

4.2.1.5 Rigid Body Stability

Assuming the wing as rigid the structural frequency dependent terms in the mass and stiffness matrices go to zero and expressions provided by (4.25) are simplified within a quadratic equation.

$$\lambda^2 + \left(\frac{-M\overset{\circ}{M}_q - \overset{\circ}{Z}_w I_{yy}}{MI_{yy}} \right) \lambda + \left(\frac{-U M \overset{\circ}{M}_w + \overset{\circ}{Z}_w \overset{\circ}{M}_q - \overset{\circ}{Z}_q \overset{\circ}{M}_w}{MI_{yy}} \right) = 0$$

$$(4.26)$$

Comparing with quadratic

$$\lambda^2 + B\lambda + C = 0 \qquad\qquad \text{where } \tau = \frac{M}{\frac{1}{2}\rho US_w}$$

$$B = \left(\frac{-M\overset{\circ}{M}_q - \overset{\circ}{Z}_w I_{yy}}{MI_{yy}} \right) = (z_w + m_q)\frac{1}{\tau}$$

$$C = \left(\frac{\overset{\circ}{Z}_q \overset{\circ}{M}_w - (UM + \overset{\circ}{Z}_q)\overset{\circ}{M}_w}{MI_{yy}} \right) = (z_w m_q + (1-z_q)m_w)\frac{1}{\tau^2}$$

$$(4.27)$$

Therefore the short period damping and frequency is

98

$$\mu_{sp} = \frac{B}{2} \qquad\qquad \omega_{sp} = \sqrt{C - \frac{B^2}{4}} \qquad\qquad (4.28)$$

It can be seen the above aerodynamic derivatives are identical to those supplied from more conventional means.[14,15] However unlike these more conventional techniques the current analysis takes into account the damping contribution from the wing as well as the tailplane.

4.2.2 Tailless Aircraft

This configuration is allocated one elastic freedom, namely wing bending and its layout is shown in Figure 4.3. Normal modes and quasi-steady aerodynamic are employed as before in its dynamic representation.

4.2.2.1 Inertial Representation

An expression for the kinetic energy similar to that for the straight wing aircraft can be written as follows:

$$T = \frac{1}{2} \sum (\dot{q}_h - \bar{x}\, \dot{q}_p)^2_{fuselage}\, dm$$

$$+ \frac{1}{2} \sum (\dot{q}_h + (y\tan \Lambda - \bar{x}_w)\dot{q}_p + \zeta\dot{q}_f)^2_{Wing}\, dm$$

$$(4.29)$$

where

$\bar{x}$ is the distance of the fuselage c.g. from the aircraft c.g.

$\bar{x}_w$ is the distance of the wing inertia axis is forward of the aircraft c.g. at the centreline.

y is the spanwise distance

The first term represents the contribution from the rigid body modes and the second the kinetic energy of the wings alone.

$$T = \frac{1}{2} \sum (\dot{q}_h^2 + \bar{x}^2\dot{q}_p^2)_{fuselage}\, dm$$

$$+ \frac{1}{2} \sum (\dot{q}_h^2 + (y\tan \Lambda - \bar{x}_w)^2\dot{q}_p^2 + \zeta^2\dot{q}_f^2)_{Wing}\, dm \qquad (4.30)$$

99

Therefore an expression identical to equation (4.6) is obtained namely

$$T = \frac{1}{2} \left[M \dot{q}_h^2 + I_{yy} \dot{q}_p^2 + m_f \dot{q}_f^2 \right]$$

The above expression for the kinetic energy and that from Eq.(4.8) for the potential energy is substituted into Lagranges equation and the matrix equation of (4.9) is obtained

4.2.2.2 Generalised Aerodynamic Matrix

Considering the virtual work done by just the wing. Equation (4.10) can be re-written as follows, removing the contribution from the tailplane.

$$\delta W = \int_0^S L_w \delta h_w + M_{\alpha w} \delta \alpha_w \, dy \qquad (4.31)$$

$$= \int_0^S \begin{bmatrix} \delta h_w & \delta \alpha_w \end{bmatrix} \begin{bmatrix} L_w \\ M_{\alpha w} \end{bmatrix} dy \qquad (4.32)$$

Referring to Figure 4.3 the virtual displacements can be written in terms of the generalised co-ordinates. The transformation which gives the deflection of the aerodynamic axis in terms of the amplitudes of the chosen generalised co-ordinates. Where x_w is the distance of the wing aerodynamic axis is from the aircraft c.g. at the centreline.

$$\begin{bmatrix} \delta h_w \\ \delta \alpha_w \end{bmatrix} = \begin{bmatrix} 1 & y\tan \Lambda - x_w & \zeta \\ 0 & 1 & 0 \end{bmatrix} \begin{bmatrix} \delta q_h \\ \delta q_p \\ \delta q_f \end{bmatrix} \qquad (4.33)$$

Using expressions (4.33) and those for the lift and moment from

100

(4.14) and substituting into Eq.(4.32)

$$\int_0^{S_w} \begin{bmatrix} 1 & 0 \\ y\tan \Lambda - \bar{x}_w & 1 \\ \zeta & 0 \end{bmatrix} \begin{bmatrix} A_{11} & A_{12} \\ A_{21} & A_{22} \end{bmatrix} \begin{bmatrix} 1 & y\tan \Lambda - x_w & \zeta \\ 0 & 1 & 0 \end{bmatrix} \begin{bmatrix} q_h \\ q_p \\ q_f \end{bmatrix} dy$$

$$\tag{4.34}$$

$$\int_0^{S} \begin{bmatrix} AW_{11} & AW_{12} & AW_{13} \\ AW_{21} & AW_{22} & AW_{23} \\ AW_{31} & AW_{32} & AW_{33} \end{bmatrix} \begin{bmatrix} q_h \\ q_p \\ q_f \end{bmatrix} dy \tag{4.35}$$

where

$$AW_{11} = A_{11}$$

$$AW_{12} = A_{11} y \tan \Lambda - A_{11} x_w + A_{12}$$

$$AW_{13} = A_{11}\zeta$$

$$AW_{21} = A_{11} y \tan \Lambda - A_{11} x_w + A_{21}$$

$$AW_{22} = A_{11} x_w^2 - A_{11} x_w 2y \tan \Lambda + A_{11} y^2 \tan^2 \Lambda - A_{12} x_w +$$
$$A_{12} y \tan \Lambda - A_{21} x_w + A_{21} y \tan \Lambda + A_{22}$$

$$AW_{23} = A_{11}\zeta y \tan \Lambda - A_{11}\zeta x_w + A_{21}\zeta$$

$$AW_{31} = A_{11}\zeta$$

$$AW_{32} = A_{11}\zeta y \tan \Lambda - A_{11}\zeta x_w + A_{12}\zeta$$

$$AW_{33} = A_{11}\zeta^2 \tag{4.36}$$

The aerodynamic expressions provided by Eq.(4.18) are multiplied

by cos Λ to take account the effects of sweep.

$$A_{11} = -\rho U b a_0 \lambda \cos \Lambda \qquad A_{12} = -\rho U^2 b a_0 \cos \Lambda$$

$$A_{21} = \rho U b^2 a_0 \lambda (\tfrac{1}{2} + a_h) \cos \Lambda \qquad A_{22} = \rho U^2 b^2 a_0 (\tfrac{1}{2} + a_h) \cos \Lambda$$

$$\left. \right\} \quad (4.37)$$

Assuming $a_h = -0.5$ Therefore $A_{21} = A_{22} = 0$

After integration of Eq.(4.35) the generlaised aerodynamic matrix is formed as shown in Eq.(4.18)

where $s = s_w$ and $S = S_w$

$$Q_{11} q_h = s A_{11} q_h$$

$$= -\tfrac{1}{2} \rho U S a_0 \cos \Lambda \; \dot{q}_h = \overset{o}{Z}_w \; \dot{q}_h$$

$$Q_{12} q_p = s(- A_{11} x_w + A_{11} \tfrac{1}{2} s \tan \Lambda + A_{12}) q_p$$

$$= \tfrac{1}{2} \rho U S a_0 \cos \Lambda \left[x_w - \tfrac{1}{2} s \tan \Lambda \right] \dot{q}_p - \tfrac{1}{2} \rho U^2 S a_0 \cos \Lambda \; q_p$$

$$= \overset{o}{Z}_q \; \dot{q}_p - C_1 \; q_p$$

$$Q_{13} q_f = A_{11} I_\zeta \; q_f$$

$$= -\rho U a_0 b_w \; I_\zeta \cos \Lambda \; \dot{q}_h$$

$$Q_{21} q_h = s(- A_{11} x_w + A_{11} \tfrac{1}{2} s \tan \Lambda \;) \; q_h$$

$$= \tfrac{1}{2} \rho U S a_0 \cos \Lambda \left[x_w - \tfrac{1}{2} s \tan \Lambda \right] \dot{q}_h = \overset{o}{M}_w \; \dot{q}_h$$

$$Q_{22} q_p = s(A_{11} x_w^2 - A_{11} x_w s \tan \Lambda + A_{11} \tfrac{1}{3} s^2 \tan^2 \Lambda - A_{12} x_w +$$

$$A_{12} \frac{1}{2} s \tan \Lambda \,) \, q_p$$

$$= - \frac{1}{2}\rho U S a_0 \cos \Lambda \left[x_w^2 - s \, x_w \tan \Lambda + \frac{1}{3} s^2 \tan^2 \Lambda \right] \dot{q}_p$$

$$+ \frac{1}{2}\rho U^2 S a_0 \cos \Lambda \left[x_w - \frac{1}{2} s \tan \Lambda \right] q_p = \overset{o}{M}_q \dot{q}_p + C_2 q_p$$

$$Q_{23} q_f = A_{11} I_{\zeta\Lambda} \, q_f \qquad\qquad \text{where } I_{\zeta\Lambda} = \int_0^s \zeta(y\tan \Lambda - x_w) \, dy$$

$$= \rho U a_0 b_w \, I_{\zeta\Lambda} \cos \Lambda \, \dot{q}_f$$

$$Q_{31} q_h = A_{11} I_\zeta \, q_h$$

$$= -\rho U a_0 b_w \, I_\zeta \cos \Lambda \, \dot{q}_h$$

$$Q_{32} q_p = (A_{11} I_{\zeta\Lambda} + A_{12} I_\zeta) q_p$$

$$= -\rho U a_0 b_w I_{\zeta\Lambda} \cos \Lambda \, \dot{q}_p - \rho U^2 a_0 b_w I_\zeta \cos \Lambda \, q_p$$

$$Q_{33} q_f = A_{11} I_{\zeta\zeta} \, q_f$$

$$= -\rho U a_0 b_w \, I_{\zeta\zeta} \, \dot{q}_f \qquad\qquad\qquad\qquad (4.38)$$

On inspection it is seen that $C_1 = -\overset{o}{Z}_w U$ and $C_2 = U\overset{o}{M}_w$

These expressions for the generalised aerodynamic forces are introduced into the equations of motion and the matrix equation of (4.21) is again formed, however in this case the term Q_{23} can not be neglected as this is the function of the static margin for the tailless aircraft. The resulting quartic of equation (4.24) has the new following coefficents.

103

$$A = 1$$

$$B = \left(-\frac{Q_{33}}{m_f} - \frac{\overset{\circ}{M}_q}{I_{yy}} - \frac{\overset{\circ}{Z}_w}{M} \right)$$

$$C = \left(\omega_f^2 + \frac{Q_{33}}{m_f}\left(\frac{\overset{\circ}{M}_q}{I_{yy}} + \frac{\overset{\circ}{Z}_w}{M} \right) - \frac{Q_{31}^2}{Mm_f} - \frac{U\overset{\circ}{M}_w}{I_{yy}} + \frac{\overset{\circ}{Z}_w \overset{\circ}{M}_q}{MI_{yy}} - \frac{\overset{\circ}{Z}_q \overset{\circ}{M}_w}{MI_{yy}} \right.$$

$$\left. - \frac{Q_{23}Q_{32}}{I_{yy}m_f} \right)$$

$$D = \left(\omega_f^2\left(-\frac{\overset{\circ}{M}_q}{I_{yy}} - \frac{\overset{\circ}{Z}_w}{M} \right) + \frac{Q_{33}}{m_f}\left(\frac{U\overset{\circ}{M}_w}{I_{yy}} - \frac{\overset{\circ}{Z}_w \overset{\circ}{M}_q}{MI_{yy}} + \frac{\overset{\circ}{Z}_q \overset{\circ}{M}_w}{MI_{yy}} \right) + \frac{\overset{\circ}{M}_q Q_{13}^2}{MI_{yy}m_f} \right.$$

$$\left. \frac{Q_{31}Q_{23}}{MI_{yy}m_f}\left(\overset{\circ}{Z}_w - \overset{\circ}{Z}_q \right) \right)$$

$$E = \left(\omega_f^2\left(-\frac{U\overset{\circ}{M}_w}{I_{yy}} + \frac{\overset{\circ}{Z}_w \overset{\circ}{M}_q}{MI_{yy}} - \frac{\overset{\circ}{Z}_q \overset{\circ}{M}_w}{MI_{yy}} \right) - \frac{Q_{13}}{MI_{yy}m_f}\left(Q_{23}U\overset{\circ}{Z}_w + (Q_{32} - UQ_{13})\overset{\circ}{M}_w \right) \right)$$

$$(4.39)$$

Neglecting flexibility and retaining the zero frequency terms the expressions above are inserted into the stability matrix and resulting quadratic is identical to Eq.(4.26) and C_1 and C_2 cancel out so that the s.p.p.o (short period pitching oscillation) damping and frequency are obtained by the same expressions as those provided by Eq.(4.28).

4.3 Influence of Quasi-Steady and Unsteady Aerodynamics on Aircraft Dynamic Stability

The analysis above is seen to yield stability derivatives identical to those as established in conventional rigid body dynamic stability analysis,[14,15] neglecting downwash effects. To

104

confirm this agreement, conventional derivatives were obtained using the classical approach[14] and the subsequent s.p.p.o damping and frequency is compared to that obtained using the current code, first with quasi-steady aerodynamics as implemented above followed by the unsteady aerodynamic expressions.

As a simple example, a fictitious aircraft of aspect ratio 20 with a straight rectangular wing and tailplane was created with dimensions similar to most high aspect ratio sailplanes. Its layout and inertia properties are shown in Table 4.1. As elastic modes are not incorporated in this example the wing and tailplane consist of rigid massless beam elements and a lumped mass and inertia located at the the aicraft c.g. to represent these respective quantities. As before, a light spring allowing translational and pitching rotational freedoms provided the required rigid body modes. In this example the c.g. of the aircraft was located at the aerodynamic centre of the wing, i.e. $a_h = -0.5$, to leave out the damping contribution from the wing and make it compatible with the classical approach. Stability roots obtained at U = 90m/s, are non-dimensionalised with respect to τ, (the magnitude of time unit) and are presented in Table 4.2. Referring to this table it is seen that the current analysis employing quasi-steady aerodynamics yields almost identical quantities to that obtained from the classical approach. Different speeds were subsequently investigated using the code and no significant change in the roots was observed, within the accuracy of the program eigenvalue search procedure. Also shown is the effect of moving the c.g. away from the aerodynamic centre, at x_w = 0.4257 m as it can be seen the damping in the s.p.p.o mode increases if the wing contribution is taken into account.

Next, Theodorsen's expressions for unsteady lift and moment were introduced. In addition the Theodorsen function C(k) was extended to cover the case of convergent aerofoil motion of the form $e^{\lambda t}$. These results are also presented in Table 4.2 for comparison. It is seen that the unsteady aerodynamics reduces damping and increases stiffness in the s.p.p.o mode. As the unsteady aerodynamic forces are functions of ρU^2, it is found that these roots too, non-dimensionalised with respect to τ do not vary

with airspeed.

4.4 Unified Aeroelastic Analysis Applied to the Kestrel, Ricochet and the Cranfield A1

This proposed method of stability analysis was demonstrated by applying the theory to the Kestrel, Ricochet and the Cranfield A1, as in the case of flutter. This analysis was first carried out employing quasi-steady aerodynamics and full flexibility. The dynamic stability analysis was completed by incorporating the full effects of unsteady aerodynamics and flexibility. In both cases the damping, frequency and time to half amplitude of the s.p.p.o mode are computed. The corresponding results for the rigid aircraft using stability derivatives are also obtained for comparison. The stability derivatives for each aircraft considered is summarised in Appendix D. In presentation of results, all the modes are numbered sequentially, starting from the rigid body modes and finishing with the elastic modes.

4.4.1 The Kestrel

As the Kestrel is a high aspect ratio aircraft, and flexurally weak it is considered as an ideal example of a deformable aircraft. The effects of flexibility are also expected to be significant within the aspect of dynamic stability. Wing and tailplane aerodynamic parameters were maintained from the flutter study. A technique of modal elimination was carried out for both the quasi-steady and unsteady aerodynamic models, to investigate the dominant modes.

4.4.1.1 Quasi-Steady Aerodynamics

Table 4.3 displays the roots using quasi-steady aerodynamics from which the required quantities shown in Table 4.4 are derived. Table 4.5 and Table 4.6 are the corresponding values for the unsteady case. Referring to Table 4.3 their is good agreement, within engineering accuracy between the roots obtained using the derivative approach and that from the current analysis, assuming only rigid body modes (modes 1 and 2). The agreement is not total as this time the effects of wing and tailplane taper are incorporated in the current analysis. It is also noted that although the angle of structural sweep forward is small, of the

order of 1.4^0, neglecting its effect was subsequently found to double the s.p.p.o frequency. This is because the wing sectional a_h increases the local pitching moment, this inturn increases the overall aircraft $\partial C_m / \partial C_L$ and subsequent static margin. Referring to U = 30 m/s the introduction of flexibility is seen to destabilise the s.p.p.o mode, in particular the fundamental bending and torsional modes (modes 3 and 7). This stems from approximity to the flutter speed of 41.2 m/s predicted from the quasi-steady theory, this is also reflected in the severe drop in damping ratio. From Table 4.4 the ratios of the s.p.p.o damping (μ_{sp}), s.p.p.o period frequency (ω_{sp}) and time to half amplitude for the flexible, using all six modes, and rigid aircraft are 1.20, 5.80, 0.83 for a speed of 30 m/s. The results for 60 m/s suggest convergent motion, however practically flutter is followed by divergent motion, which appears not to be predicted from this particular quasi-steady model.

4.4.1.2 Unsteady Aerodynamics

Comparing in Table 4.5, the roots obtained using the present theory using two rigid body modes, it is seen that the introduction of unsteady aerodynamics has a destabilising influence on the s.p.p.o mode. Introduction of flexibility, as before increases this instability. As both speeds are below the flutter speed for this case, there is not the marked increase in s.p.p.o frequency until at around a speed of 60 m/s the Kestrel is sufficiently close to its predicted flutter speed that the damping ratio substantially decreases. From Table 4.6 The ratios this time are 1.56, 1.19 and 0.65 for a speed of 30 m/s and 0.69, 2.06 and 1.5 for a speed of 60 m/s. It is also seen from the time to half amplitude that, at 30 m/s the ride quality is improved with the introduction of flexibility, except close to the flutter speed.

It is seen from both quasi-steady and unsteady models that the inclusion of just the first bending and first torsion elastic modes is sufficient in predicting the dynamic characteristics of the Kestrel.

The contrast between the quantities obtained assuming a rigid body idealisation and aerodynamic derivatives and the proposed

analysis employing unsteady aerodynamics and flexibility is demonstrated in Figure 4.4 at 30 m/s and 60 m/s. Here the rate of pitch ($d\alpha/dt$) is plotted against time for both the rigid case and the flexible case based on four elastic modes. It is indicated from Table 4.4 and 4.6, that at 60 m/s the classical approach over-estimates the short period damping by 35.2% and underestimates the short period frequency by 60.6%.

4.4.2 The Ricochet

The Ricochet in the absence of a tail is expected to suffer loss of damping in pitch. In prior investigations[17,38] the interaction of rigid-body modes with the elastic modes of distortion was demonstrated in the flutter results.

The Ricochet was given two rigid body and four elastic degrees of freedom in the symmetric motion, as in Chapter 3. The investigation was carried out for two airspeeds below the flutter speed to ensure convergent oscillation, these were 25 m/s and 40 m/s. Although in the prior flutter investigation $a_0 = 2\pi$ /rad the value of $a_0 = 5.68$ /rad is taken from Buchanhan[70] and was used for both the quasi-steady and unsteady analysis. The static margin stick fixed was kept at 1.79% SMC as in the flutter calculations aswell as the mass and inertia quantities.

4.4.2.1 Quasi-Steady Aerodynamics

Table 4.7 displays the roots using quasi-steady aerodynamics from which the required quantities shown in Table 4.8 are derived from. Referring to Table 4.7 it can be seen that there is good agreement (within 12%) between the roots obtained from the current analysis, using the two rigid body modes of heave and pitch and that derived using the classical approach. It appears that the assumption of modifying the lift by cos Λ, for this small angle of sweep, is adequate in predicting the m_q term or the damping contribution in pitch from the swept wing. Referring to Table 4.8 the ratios of the s.p.p.o damping (μ_{sp}), s.p.p.o period frequency (ω_{sp}) and time to half amplitude for the flexible, and rigid aircraft are 0.92, 1.36, 1.08 for a speed of 25 m/s and 0.45, 2.23, 2.23 for a speed of 40 m/s. The effect of flexibility is seen to increase the frequency in the oscillatory mode. It is seen that at 40 m/s the damping has significantly reduced. At this

speed the Ricochet is close to its calculated flutter speed of 46.2 m/s using quasi-steady aerodynamics. Hence if the speed were to be increased, the damping in the resulting motion would reduce and finally become zero at the flutter speed. At this point the flutter mode will be achieved and the motion will become sinousoidal.

4.4.2.2 Unsteady Aerodynamics

Referring to the roots in Table 4.9 it can be seen that the introduction of unsteady aerodynamics does not significantly modify the the s.p.p.o quantities, predicted by the quasi-steady model. The agreement between the quasi-steady and unsteady aerodynmic theories is good as this aircraft's aeroelastic stability is dominated by the low frequency rigid body modes. Unsteady aerodynamics is found to marginally increase both the frequency and damping. From Table 4.10, the ratios this time are 0.85, 1.24, 1.18 for a speed of 25 m/s and 0.43, 1.57, 2.32 for a speed of 40 m/s. As exhibited in the quasi-steady analysis, the damping is significantly reduced at 40 m/s as the Ricochet approaches its flutter speed of 47.2 m/s, using unsteady aerodynamics.

Like the Kestrel the subsequent rate of pitch against time is plotted in Figure 4.5, for the rigid case and flexible case based on four elastic modes, at the two speeds considered. From this it is seen that the effect of flexibility is significant on the short period oscillation characteristics of the Ricochet, in particularly at 40 m/s. Again close to the flutter speed the classical approach is seen to be inadequate in predicting the dynamic characteristics of the Ricochet. At 40 m/s the classical approach overestimates the short period damping by 110.4% and underestimates the frequency by 57.3%. At this speed the introduction of flexibility and unsteady aerodynamics is seen to significantly degrade the ride quality for Ricochet, doubling the time to half amplitude.

4.4.3 The Cranfield A1

The present stability analysis was carried out on the A1 at 41.1 m/s and 61.7 m/s. These speeds were chosen to be compatible with those speeds flown at during flight tests to identify the

longitudinal derivatives.[76] Accordingly the density was also adjusted to account for the altitude in which the tests were conducted at, this was chosen as ρ = 1.055 kg/m^3. A modified wing lift curve slope a_0 = 4.22 /rad and the corresponding tailplane lift curve slope a_1 = 3.52 /rad were obtained using Ref.(73) and used as part of the aerodynamic details. The lift curve slope of the wing and tailplane were adjusted for finite span effects which can especially be significant at this lower aspect ratio. The A1 was given two rigid body modes in addition to the four elastic modes presented in Chapter 3.

4.4.3.1 Quasi-Steady Aerodynamics

The stability roots obtained from both the quasi-steady aerodynamic idealisation and the derivative approach are shown in Table 4.11. Referring to this table it is seen that for a rigid body assumption, for both speeds considered, the agreement between s.p.p.o roots from both methods of analysis is very good. The reason for this close agreement lies again in the accurate determination of the static margin stick fixed and the contribution to m_q, especially at this smaller angle of sweep. It is seen from the introduction of additional elastic modes, that the s.p.p.o mode does not change, this is as a result of the high stiffness of the A1. Also noted is how the damping ratio remains constant for both speeds. These roots are used to generate the s.p.p.o damping, frequency and time to half amplitude for Table 4.12. As shown in this Table these quantities do not change with flexibility. It is seen from the above results that an analysis using rigid body assumptions is satisfactory in determining the stability characteristics of the A1, assuming quasi-steady aerodynamics.

4.4.3.2 Unsteady Aerodynamics

Table 4.13 shows the unsteady aerodynamic case. Here again it is seen that the influence of flexibility for the A1 is marginal as far as the short period frequency is concerned. However the introduction of unsteady aerodynamics is seen to have a destabilising effect on the s.p.p.o mode. Referring again to Table 4.13 it is seen that the damping ratio has also decreased, but is the same magnitude for both speeds. From Table 4.14 the effect of

unsteady aerodynamics and flexibility (based on four elastic modes) is seen to increase the time to half amplitude for the **A1** by over 18% for both speeds and consequently reduce ride comfort.

As the **A1** is very stiff, the classical approach only over-estimates the short period damping by 19.4% and underestimates the frequency by 0.9% at an aircraft speed of 61.7 m/s.

As a means of comparison Table 4.14 also includes the values from the classical approach, and the results from flight data. It is seen that the two methods underestimate the damping quite substantially, leading to an overestimation of the s.p.p.o frequency. The percentage discrepancy in frequencies is 25.6 % and 23.3% for 41.1 m/s and 61.7 m/s respectively employing unsteady aerodynamics and flexibility. Using the quantities quoted in Table 4.14, the rate of pitch ($d\alpha/dt$) is plotted against time for both the rigid and flexible case (based on four elastic modes) with the values from flight data, which are only available for the latter speed of 61.7 m/s. Figure 4.6 shows the plots for these two, speeds. There are a variety of reasons for these discrepancies, perhaps the most important is the effect of downwash at the tailplane which has the effect in general of increasing the damping in the s.p.p.o mode and reducing the frequency.[14] The influence of downwash in this case is perhaps that much more important as the A1 is of moderate aspect ratio and the magnitude of the velocities induced at the tailplane can be expected high.

Geometric Details			
Wing		Tailplane	
Span	20 m	Span	4 m
Area	20 m^2	Area	2 m^2
Aspect ratio	20	Aspect ratio	8
Root chord	1 m	Root chord	0.5 m
Tip chord	1 m	Tip chord	0.5 m
Sweep angle	0^0	Sweep angle	0^0
a_0	2π /rad	a_1	2π /rad
Inertia Details			
Total Mass	600 kg		
Pitching Inertia	800 kgm^2		

Table 4.1   Particulars of representative aircraft of aspect
ratio 20

Method of Analysis	$\bar{\lambda}$	
	$x_w = 0$	$x_w = 0.4257m$
Stability derivative approach (Ref.14)	$-9.65 + i10.17$	$-8.67 + i2.56$
Quasi-steady aerodynamics (i.e C(k) = 1, non-circulatory terms neglected)	$-9.64 + i10.13$	$-9.07 + i2.33$
Unsteady Aerodyanmics (C(k) ≠ 1, non-circulatory terms included)	$-8.09 + i11.14$	$-8.75 + i2.04$

Table 4.2   Stability roots for representative aircraft using quasi-steady and unsteady aerodynamic model

Method of Analysis	U = 30 m/s		U = 60 m/s	
	$\bar{\lambda}$	ζ_{sp}	$\bar{\lambda}$	ζ_{sp}
Stability derivative approach[14]	$-5.86 + i3.43$	0.86	$-5.86 + i3.43$	0.86
Quasi-steady aerodynamics with modes :				
1,2	$-5.60 + i3.02$	0.88	$-5.84 + i3.06$	0.88
1,2,3	$-6.22 + i18.16$	0.32	$-4.43 + i8.34$	0.47
1,2,3,6	$-6.62 + i17.53$	0.35	$-4.47 + i7.91$	0.50
1,2,3,4,6	$-6.74 + i17.66$	0.36	$-4.56 + i7.86$	0.50
1,2,3,4,5,6	$-6.71 + i17.49$	0.36	$-4.52 + i7.89$	0.50

Table 4.3   Stability roots for Kestrel using quasi-steady aerodynamics

Method of Analysis	U = 30 m/s			U = 60 m/s		
	μ_{sp} 1/sec	ω_{sp} rad/s	$T_{1/2}$ sec	μ_{sp} 1/sec	ω_{sp} rad/s	$T_{1/2}$ sec
Stability derivative approach[14]	-3.22	1.89	0.22	-6.45	3.77	0.11
Quasi-steady aerodynamics with modes :						
1,2	-3.08	1.66	0.23	-6.43	3.37	0.11
1,2,3	-3.42	9.99	0.20	-4.88	9.18	0.14
1,2,3,6	-3.64	9.64	0.19	-4.92	8.70	0.14
1,2,3,4,6	-3.71	9.72	0.19	-5.02	8.65	0.14
1,2,3,4,5,6	-3.69	9.62	0.19	-4.97	8.68	0.14

Table 4.4   Time to half amplitude, damping term and frequency for Kestrel using quasi-steady aerodynamics

Present theory with modes :	U = 30 m/s		U = 60 m/s	
	$\bar{\lambda}$	ζ_{sp}	$\bar{\lambda}$	ζ_{sp}
1,2	$-6.25 + i4.05$	0.84	$-6.27 + i4.03$	0.84
1,2,3	$-7.82 + i3.87$	0.90	$-4.38 + i8.84$	0.44
1,2,3,6	$-9.69 + i4.80$	0.90	$-4.26 + i8.34$	0.46
1,2,3,4,6	$-9.45 + i4.69$	0.90	$-4.34 + i8.32$	0.46
1,2,3,4,5,6	$-9.78 + i4.84$	0.90	$-4.34 + i8.30$	0.46

Table 4.5   Stability roots for Kestrel using unsteady aerodynamics

Present theory with modes :	U = 30 m/s			U = 60 m/s		
	μ_{sp} 1/sec	ω_{sp} rad/s	$T_{1/2}$ sec	μ_{sp} 1/sec	ω_{sp} rad/s	$T_{1/2}$ sec
1,2	-3.44	2.23	0.20	-6.90	4.43	0.10
1,2,3	-4.30	2.13	0.16	-4.82	9.72	0.14
1,2,3,6	-5.33	2.64	0.13	-4.69	9.17	0.15
1,2,3,4,6	-5.20	2.58	0.13	-4.77	9.15	0.15
1,2,3,4,5,6	-5.38	2.66	0.13	-4.77	9.13	0.15

Table 4.6   Time to half amplitude, damping and frequency for
Kestrel using unsteady aerodynamics

Method of Analysis	U = 25 m/s		U = 40 m/s	
	$\bar{\lambda}$	ζ_{sp}	$\bar{\lambda}$	ζ_{sp}
Stability derivative approach[14]	-4.52 + i2.29	0.89	-4.52 + i2.29	0.89
Quasi-steady aerodynamics with modes :				
1,2	-4.10 + i2.61	0.84	-4.29 + i2.67	0.85
1,2,3	-3.84 + i3.23	0.77	-2.50 + i4.52	0.49
1,2,3,6	-3.83 + i3.50	0.74	-2.04 + i5.73	0.34
1,2,3,4,6	-3.76 + i3.57	0.73	-1.90 + i5.99	0.30
1,2,3,4,5,6	-3.78 + i3.55	0.73	-1.93 + i5.98	0.31

Table 4.7   Stability roots for Ricochet using quasi-steady
aerodynamics

Method of Analysis	U = 25 m/s			U = 40 m/s		
	μ_{sp} 1/sec	ω_{sp} rad/s	$T_{1/2}$ sec	μ_{sp} 1/sec	ω_{sp} rad/s	$T_{1/2}$ sec
Stability derivative approach[14]	-2.79	1.41	0.25	-4.46	2.26	0.16
Quasi-steady aerodynamic with modes						
1,2	-2.53	1.61	0.27	-4.23	2.64	0.16
1,2,3	-2.37	1.99	0.29	-2.47	4.46	0.28
1,2,3,6	-2.36	2.16	0.29	-2.01	5.65	0.35
1,2,3,4,6	-2.32	2.20	0.29	-1.87	5.91	0.37
1,2,3,4,5,6	-2.33	2.19	0.29	-1.90	5.90	0.37

Table 4.8   Time to half amplitude, damping term and frequency for Ricochet using quasi-steady aerodynamics

Present theory with modes :	U = 25 m/s		U = 40 m/s	
	$\bar{\lambda}$	ζ_{sp}	$\bar{\lambda}$	ζ_{sp}
1,2	-4.64 + i3.28	0.82	-4.97 + i3.43	0.82
1,2,3	-3.97 + i3.58	0.74	-2.73 + i4.28	0.54
1,2,3,6	-3.89 + i3.89	0.71	-2.20 + i5.13	0.39
1,2,3,4,6	-3.83 + i3.97	0.69	-2.13 + i5.37	0.37
1,2,3,4,5,6	-3.93 + i4.06	0.70	-2.15 + i5.36	0.37

Table 4.9   Stability roots for Ricochet using unsteady aerodynamics

Present theory with modes :	U = 25 m/s			U = 40 m/s		
	μ_{sp} 1/sec	ω_{sp} rad/s	$T_{1/2}$ sec	μ_{sp} 1/sec	ω_{sp} rad/s	$T_{1/2}$ sec
1,2	-2.86	2.02	0.24	-4.91	3.38	0.14
1,2,3	-2.45	2.21	0.28	-2.69	4.22	0.26
1,2,3,6	-2.40	2.40	0.29	-2.17	5.06	0.32
1,2,3,4,6	-2.36	2.45	0.29	-2.10	5.30	0.33
1,2,3,4,5,6	-2.42	2.50	0.30	-2.12	5.29	0.33

Table 4.10   Time to half amplitude, damping term and frequency for Ricochet for unsteady aerodynamics

Method of Analysis	U = 41.1 m/s		U = 61.7 m/s	
	$\bar{\lambda}$	ζ_{sp}	$\bar{\lambda}$	ζ_{sp}
Stability derivative approach[14]	$-4.42 + i9.76$	0.41	$-4.42 + i9.76$	0.41
Quasi-steady aerodynamics with modes :				
1,2	$-4.36 + i9.64$	0.41	$-4.38 + i9.66$	0.41
1,2,3	$-4.39 + i9.67$	0.41	$-4.36 + i9.68$	0.41
1,2,3,6	$-4.39 + i9.67$	0.41	$-4.40 + i9.71$	0.41
1,2,3,4,6	$-4.39 + i9.67$	0.41	$-4.36 + i9.68$	0.41
1,2,3,4,5,6	$-4.39 + i9.67$	0.41	$-4.40 + i9.69$	0.41

Table 4.11   Stability roots for A1 using quasi-steady aerodynamics

117

Method of Analysis	U = 41.1 m/s			U = 61.7 m/s		
	μ_{sp} 1/sec	ω_{sp} rad/s	$T_{1/2}$ sec	μ_{sp} 1/sec	ω_{sp} rad/s	$T_{1/2}$ sec
Stability derivative approach[14]	-1.64	3.62	0.42	-2.46	5.44	0.28
Quasi-steady aerodynamic with modes						
1,2	-1.62	3.58	0.43	-2.44	5.38	0.28
1,2,3	-1.63	3.59	0.43	-2.43	5.39	0.29
1,2,3,6	-1.63	3.59	0.43	-2.45	5.41	0.28
1,2,3,4,6	-1.63	3.59	0.43	-2.43	5.39	0.29
1,2,3,4,5,6	-1.63	3.59	0.43	-2.45	5.40	0.28

Table 4.12 Time to half amplitude, damping term and frequency for
A1 with quasi-steady aerodynamics

Present theory with modes :	U = 41.1 m/s		U = 61.7 m/s	
	$\bar{\lambda}$	ζ_{sp}	$\bar{\lambda}$	ζ_{sp}
1,2	-3.69 + i9.78	0.35	-3.72 + i9.84	0.35
1,2,3	-3.69 + i9.78	0.35	-3.70 + i9.85	0.35
1,2,3,6	-3.69 + i9.80	0.35	-3.70 + i9.85	0.35
1,2,3,4,6	-3.61 + i9.59	0.35	-3.70 + i9.85	0.35
1,2,3,4,5,6	-3.69 + i9.78	0.35	-3.70 + i9.85	0.35

Table 4.13 Stability roots for A1 using unsteady aerodynamics

Method of Analysis	U = 41.1 m/s			U = 61.7 m/s		
	μ_{sp} 1/sec (ζ_{sp})	ω_{sp} rad/s (Hz)	$T_{1/2}$ sec	μ_{sp} 1/sec (ζ_{sp})	ω_{sp} rad/s (Hz)	$T_{1/2}$ sec
Stability derivative approach[14]	-1.64	3.62	0.42	-2.46	5.44	0.28
Present theory using modes :						
1,2	-1.37	3.63	0.51	-2.07	5.48	0.34
1,2,3	-1.37	3.63	0.51	-2.06	5.49	0.34
1,2,3,6	-1.37	3.64	0.51	-2.06	5.49	0.34
1,2,3,4,6	-1.34	3.56	0.52	-2.06	5.49	0.34
1,2,3,4,5,6	-1.37	3.63	0.51	-2.06	5.49	0.34
Flight test[76] results	(--)	2.70	(--)	-9.88	4.21	0.07

Table 4.14   Time to half amplitude, damping term and frequency for
A1 with unsteady aerodynamics and comparison with the
classical approach and flight data
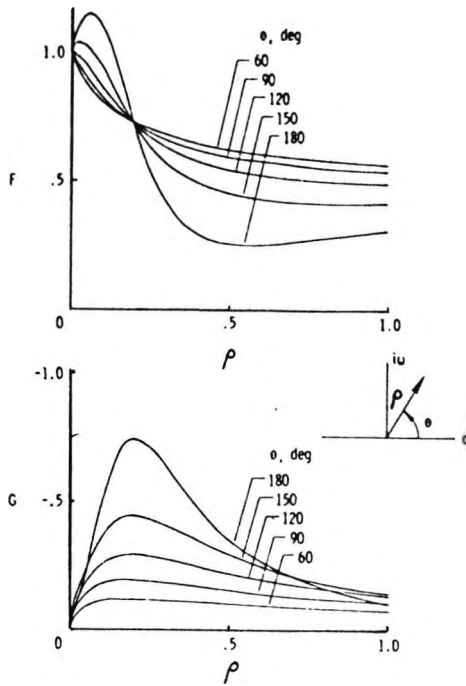
Fig. 4.1 The generalised Theodorsen function

$$C(z)=F+iG \quad z=\rho e^{i\theta}$$
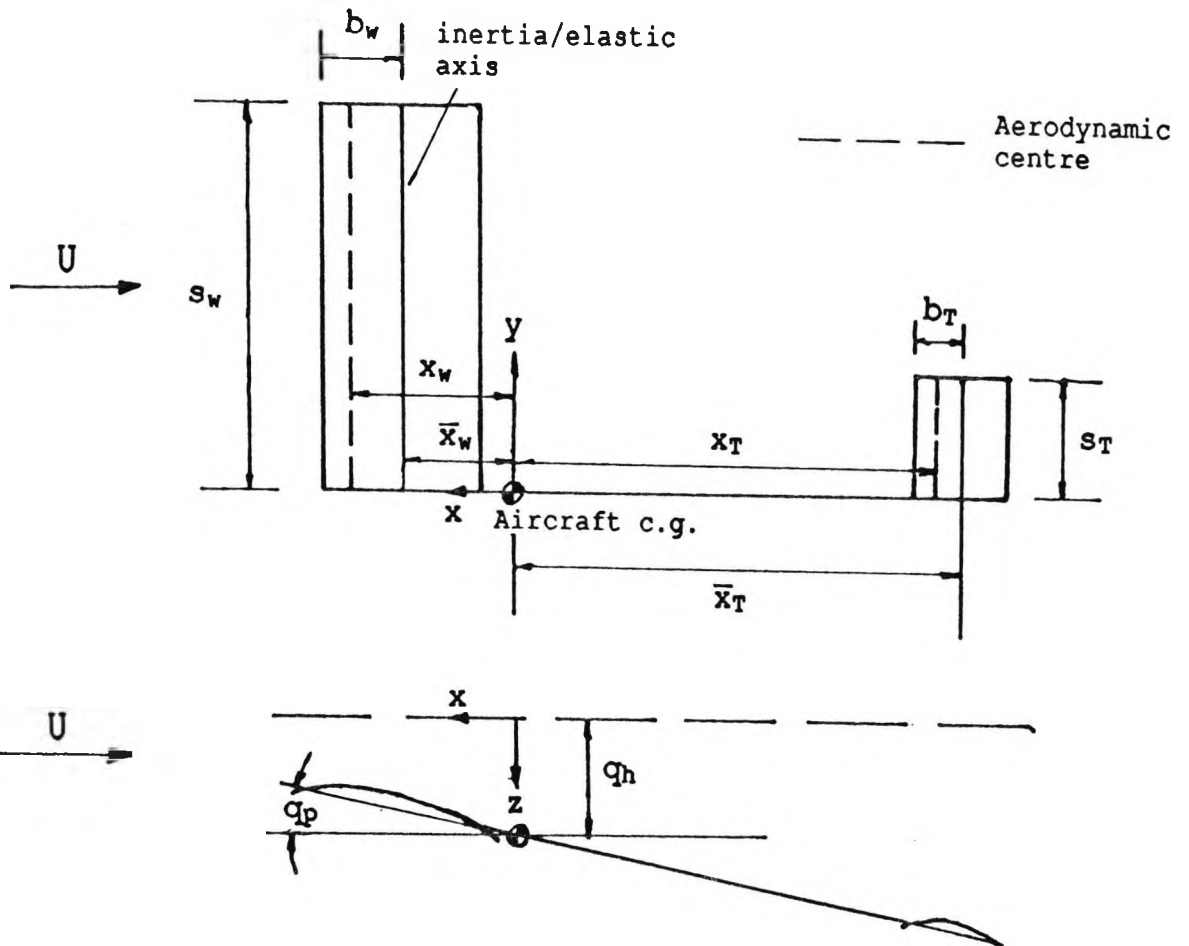
Fig. 4.2 Tailed configuration
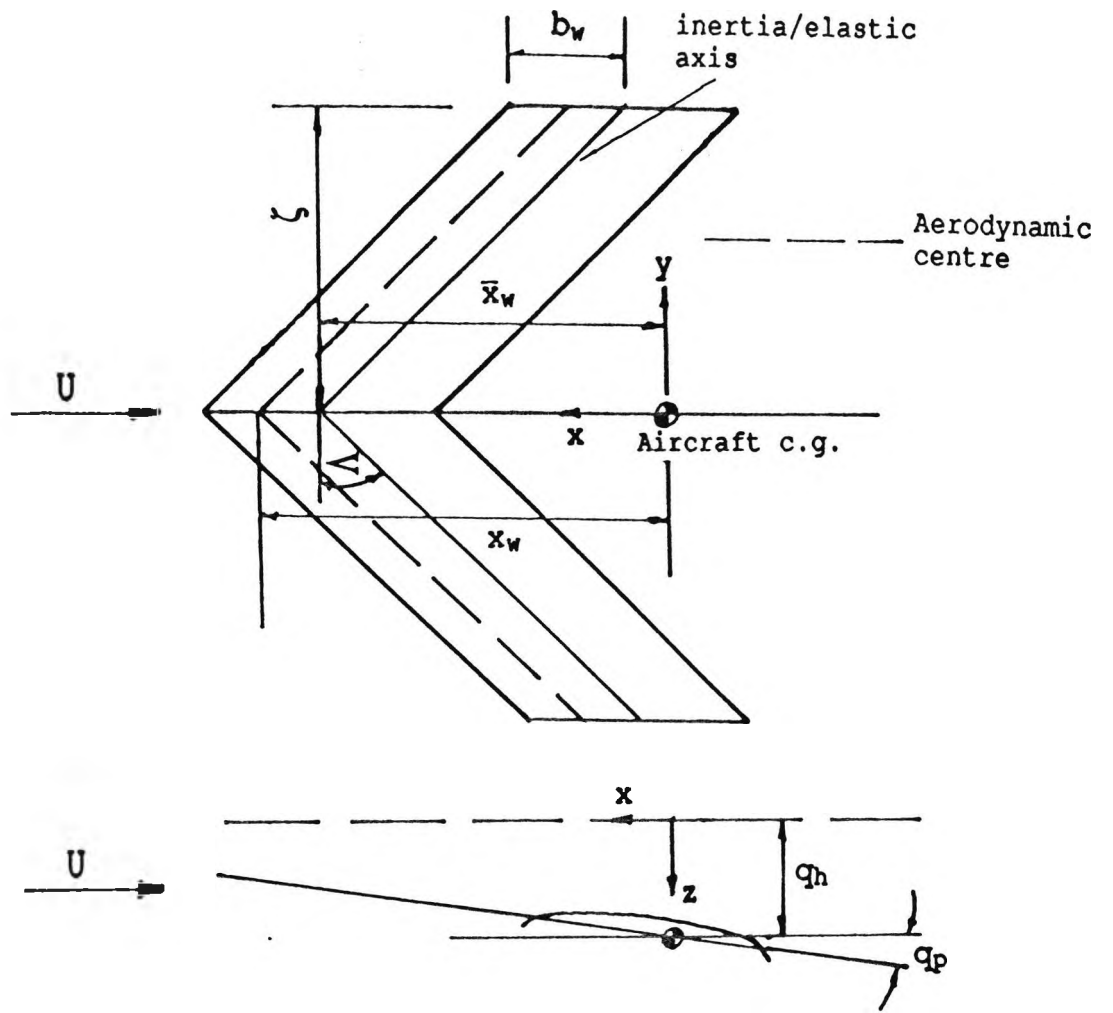
Fig. 4.3 Tailless configuration
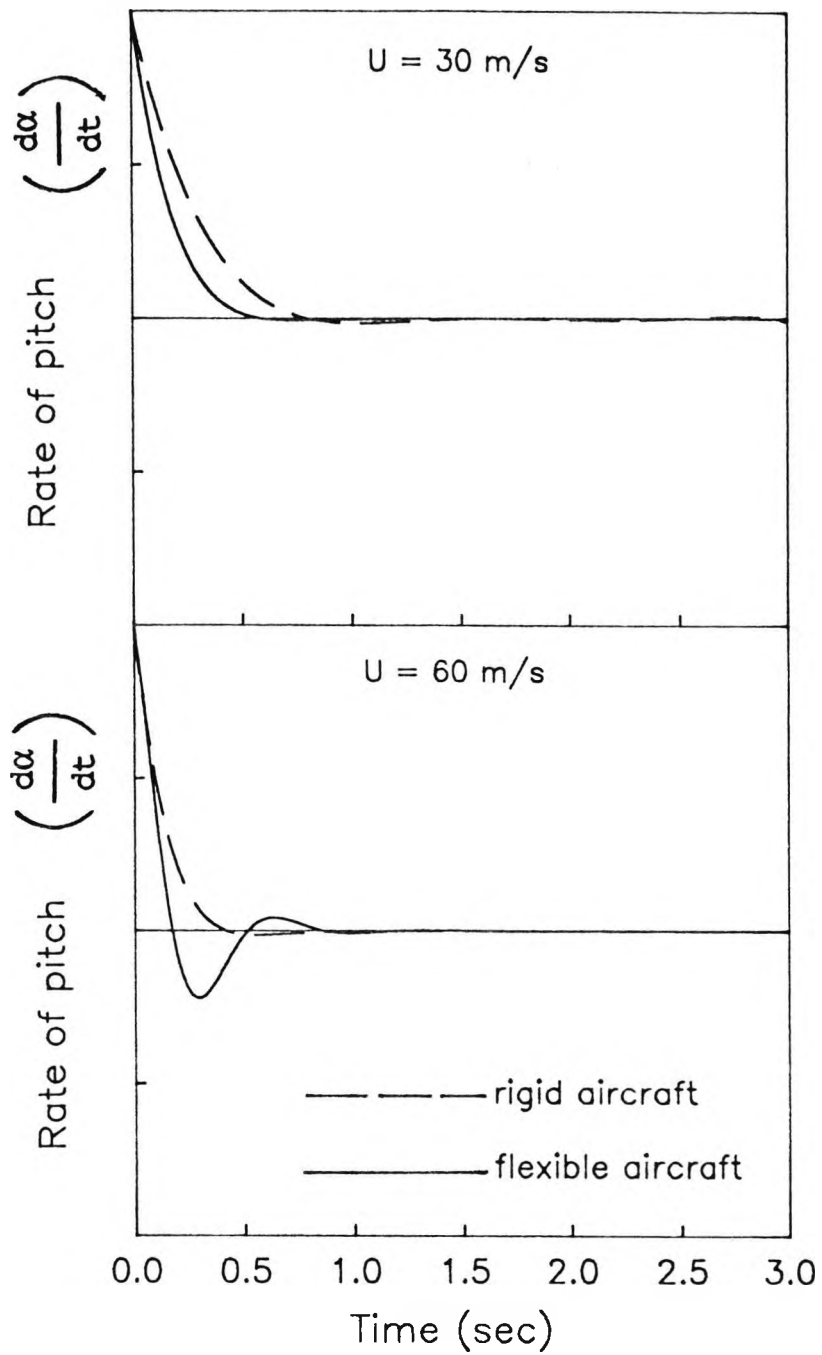
Fig. 4.4   Short period mode for Kestrel for both rigid
and flexible cases
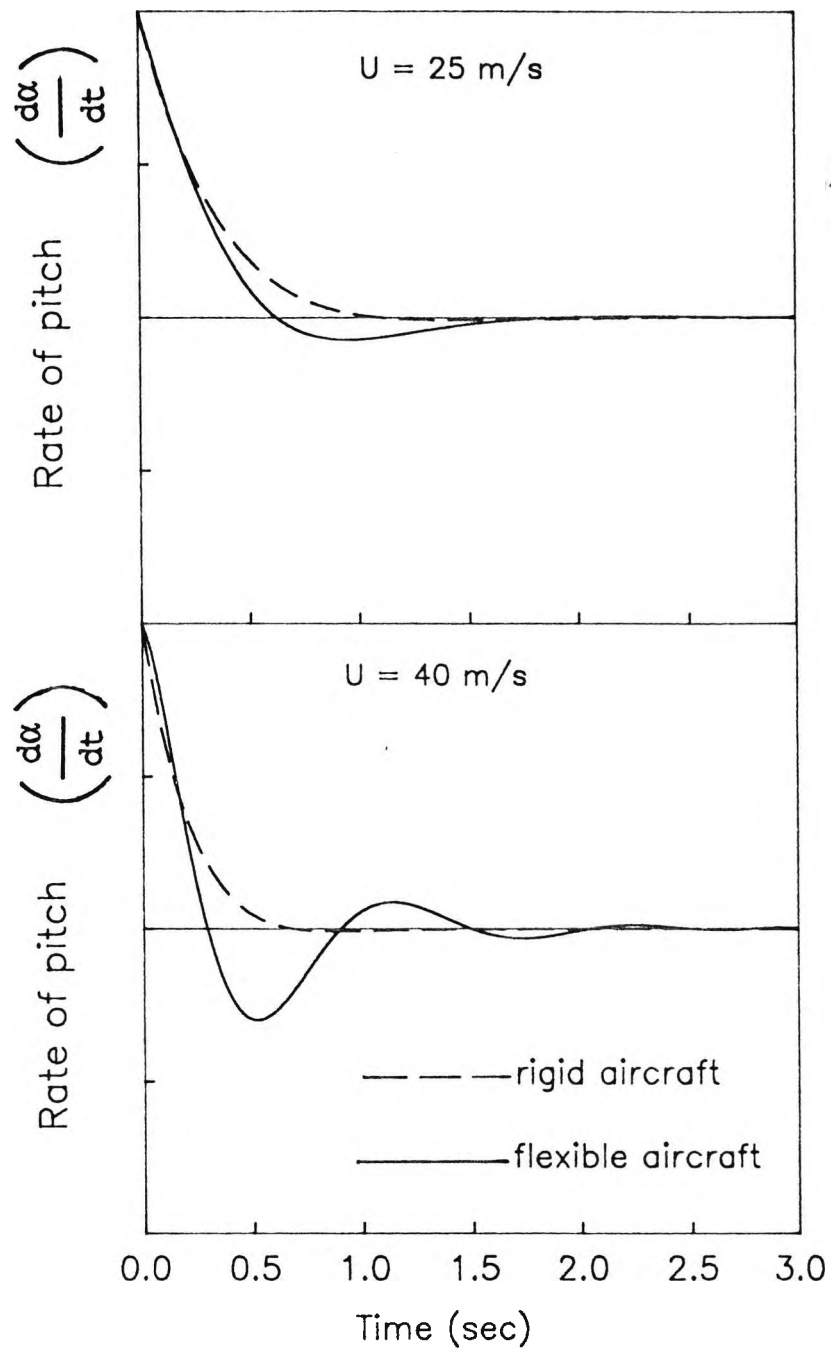
Fig. 4.5 Short period mode for Ricochet for both rigid
and flexible cases
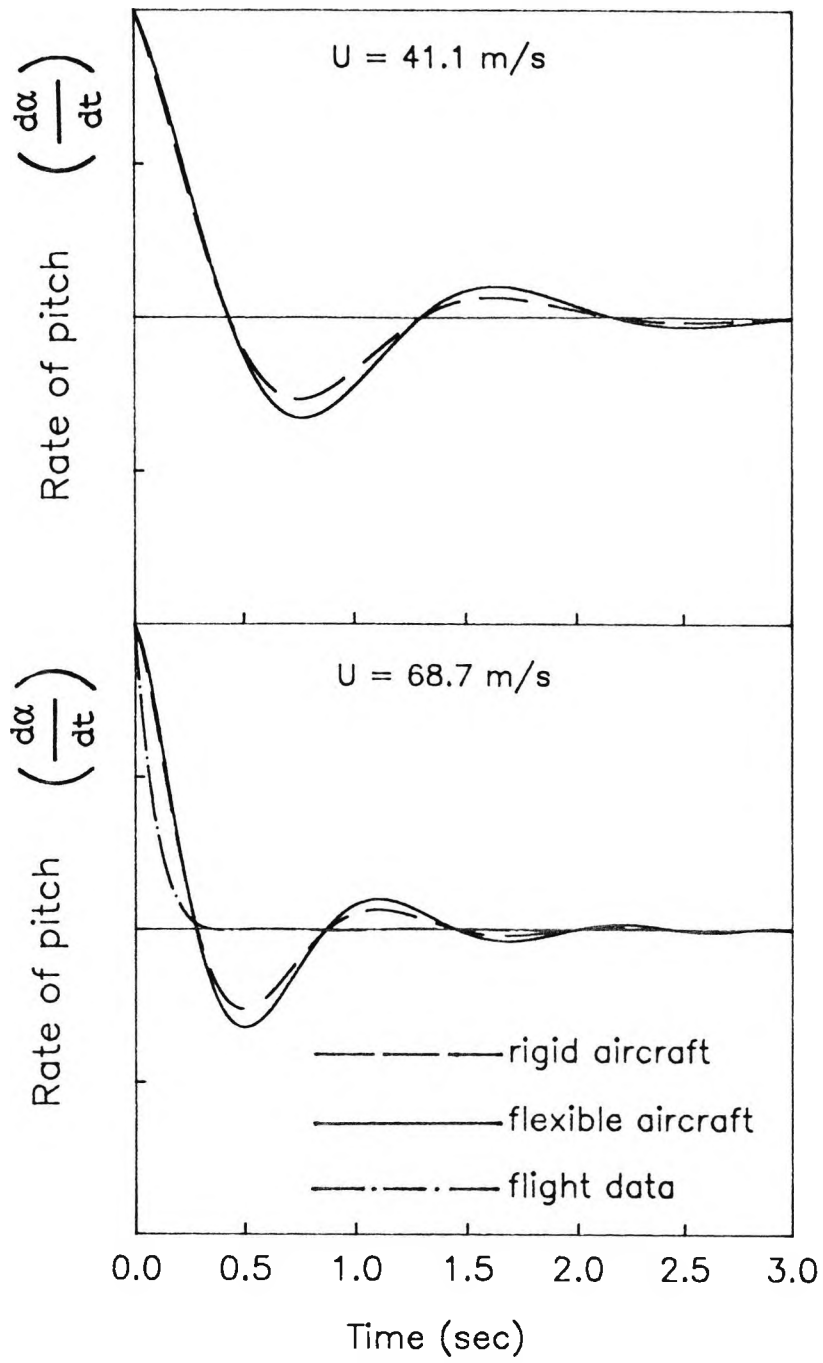
Fig. 4.6 Short period mode for A1 for both rigid and flexible cases

5.0 DOWNWASH EFFECTS IN AIRCRAFT STABILITY AND FLUTTER

5.1 Introduction

Aerodynamic interaction between the wing and tailplane of an aircraft has all along been an important consideration in defining aircraft stability and control characteristics. In particular the angle-of-attack induced on the tail by the wing downwash plays an important role and taken into account when establishing horizontal tail size and location.[14,15] However effects are generally neglected in conventional aircraft flutter investigations. Flutter analysis as outlined in this work so far, sums up the contribution of the unsteady air loads from the wing and tailplane neglecting wing interference effects. To a certain extent this assumption can be assumed valid for moderate to high aspect ratio tandem surfaces. The amplitudes of the wing oscillation are usually small in the region near the body and high near the wing tip. Thus, high induced-velocity components usually can be expected downstream from the wing tip. Consequently, interference in most cases will become important where the span of the tail is not small relative to the wing span.

Configurations with relatively larger tailplanes are found on many modern airplanes especially on those with variable-geometry wings, or canard types, for such configurations the wing/tailplane interference can be very important. For example Topp et al[97] referred to an anti-symmetric flutter case as experienced in a wind-tunnel test of an aircraft with variable wing geometry. For low wing sweep angles, the critical flutter modes were those mainly involving high frequency bending and torsion motions of the lifting surfaces. For wing sweep angles above $58°$, increasing the wing sweep angle produced a rapid drop in the flutter speed in a new flutter mode involving lower frequency modes of the wing, fuselage and tail (see Ref.(97)). This condition could not be determined theoretically by using conventional flutter approaches. After careful consideration of all prevailing influences, the instability was assumed to be due to the aerodynamic interference of wing and tail. This trend was properly predicted by Sensberg and Laschka[98] when taking into account of wing-tail unsteady aerodynamic interference. Further theoretical and flutter model

investigations of such coupled wing-fuselage-tail flutter problems with regard to the aerodynamic idealisation were subsequently carried out, for example in Refs.(13),(99) and (100).

The introduction of aerodynamic theories to take into account wing-tail interaction were late coming, probably because coupling of elastic modes to produce a critical flutter mode involving mechanical interaction of the wing, fuselage and tail is not generally encountered in aircraft with more conventional configurations. An over-view of this development and discussion of various theories can be found in Refs.(12) and (101).

It appears to be difficult to find any references, which give any quantitative account of wing-tail interference in flutter calculations for more conventional configurations considered in the work so far. As a result of a lack of any hard evidence to preclude these interactions for the cases considered in this work and also to improve the stability model, it was decided to incorporate these effects as best as possible.

It has been shown in Chapter 4 that determination of stability of an aircraft using rigid body heave and pitch modes, in conjunction with quasi-steady aerodynamics, is equivalent to methods based on stability derivatives (see Babister[14]). It was from this approach that the first attempt to incorporate downwash was made. However this proved difficult as additional terms not pertinent to the original equations of motion were being introduced. However in retrospect the extension of the average $d\varepsilon/d\alpha$ would not be sufficient for the flutter case as this factor does not take into account the unsteadiness of the wake. Its use also as an accurate means of stability determination has also been questioned by Hancock and Lam.[102]

It was realised at this time that some account of the unsteady wake had to be introduced into the existing representations for unsteady lift and moment. As outlined earlier, existing methods based on subsonic Kernel functions which take proper account of the three-dimensional unsteady aerodynamics and the interaction between wing and tail, are well established.[11,12,101] However these procedures could not be reconciled with the existing simplified strip idealisation

implemented in this project. Another technique introduced by earlier investigators was the vortex-lattice method (VLM) presented by for example Shelton, Tucker and Davis.[99] This method considers the aerodynamic interaction of the wing on the tail but not vice versa, as the more refined techniques do so. However this method was found to give flutter results[13,99] in close agreement to those furnished by the Kernel function approach, which suggests that the effects of tail-to-wing aerodynamic interaction are often practically negligible. Thus a method using a similar approach to that of the VLM, however some what simpler, was introduced into the existing aerodynamic model in this work.

5.2 Unsteady Wake Model

5.2.1 Unsteady Aerodynamic Wake

The unsteady wake is represented by a two-dimensional "field" of ring vortices extending at least up to 12 chord lengths downstream from the wing trailing edge however this distance is dependent upon the frequency and freestream speed of the wake. This was thought adequate distance to cover the main contribution of this field. However in this idealisation there is no rolling up of the trailing vortex and it is assumed to remain in the horizontal plain of the aircraft. The wing is represented by its equivalent straight wing of chord $\bar{c}$ to simplify construction of the wake, the original geometry is taken into account when evaluating the unsteady circulation and ring vortex strengths.

The downstream field behind the wing is composed of the "bound vortex" or circulation about the wing and the "trailing vortex" which arises form the rate of change of wake circulation with respect to the wing span.

5.2.2. Wake Circulation

The running wake circulation at a general point ξ (measured downstream from the mid chord of the aerofoil) of the wake is given by Eq.(5-320b) in Ref.(33) as;

$$\gamma_w(\xi) = - \frac{i\omega}{U} \Gamma_n e^{ik} e^{-i(\omega\xi/U)} \qquad (5.1)$$

where Γ_n is the magnitude of circulation of the aerofoil bound vortex. Referring to Figure 5.1 the trailing vortex sheet is simulated by "vortex cells", which represent one complete cycle of the alternating wake strength.

Therefore to give the net change in the bound circulation between point ξ_A and ξ_B downstream from the wing

$$d\Gamma = \int_{\xi_A}^{\xi_B} \gamma_w(\xi) \; d\xi = - \int_{\xi_A}^{\xi_B} \frac{i\omega}{U} \Gamma_n e^{ik} \; e^{-i(\omega\xi/U)} \; d\xi$$

$$= \Gamma_n e^{ik} \left[\; e^{-i(\omega\xi_B/U)} - e^{-i(\omega\xi_A/U)} \; \right] \qquad (5.2)$$

Referring to Figure 5.2, for a wake element, Eq.(5.2) can be generalised to give the net change in wake circulation over a given element $d\zeta$ as

$$\Gamma_{n-i} - \Gamma_{n-(i-1)} = \Gamma_n e^{ik}\left(e^{-\frac{i\omega\xi_{n-i}}{u}} - e^{-\frac{i\omega\xi_{n-(i-1)}}{u}} \right) \qquad (5.3)$$

For i = 1,2 ...n
where

$\qquad$ n = MN_ζ

$\qquad N_\zeta$ = Number of strips of elemental length $d\zeta$ to cover one vortex cell, where $N_\zeta = \dfrac{2\pi U}{\omega.d\zeta}$

$\qquad$ M = Minimum number of vortex cells to extend downstream 12 chord lengths, M $\geq \dfrac{12k}{\pi}$

As one can see M and N_ζ are both functions of the reduced frequency, where $k = \omega\bar{c}/2U$.

However this gives the net change in circulation for the bound section. To obtain the trailing vortex circulation manipulation of Eq.(5.3) will give.

$$\Gamma_{n-1} = \Gamma_n e^{ik}\left(e^{-\frac{i\omega\xi_{n-1}}{u}} - e^{-\frac{i\omega\xi_{n-(1-1)}}{u}} \right) + \Gamma_{n-(1-1)} \qquad (5.4)$$

5.2.3 Aerofoil Circulation

The unknown original aerofoil circulation Γ_n can be obtained from Eq.(5-334) of Ref.(33).

$$\Gamma_n = \frac{4\, b\, e^{-ik} \displaystyle\int_{-1}^{1} \sqrt{\frac{1+\xi^*}{1-\xi^*}}\; W_a(\xi^*)\, d\xi^*}{\pi i k \left(H_1^{(2)}(k) + i H_0^{(2)}(k) \right)} \qquad (5.5)$$

where $\xi^* = \dfrac{\xi}{b}$

$$W_a(\xi^*) = -i\omega h - U\alpha - i\omega b\alpha(\xi^* - a_h)$$

Considering convergent motion of the form λ, Eq.(5.5) can be re-written as below, (see Appendix G for details).

$$\Gamma_n = 4\, U\, e^{-\lambda} \left[\frac{\lambda h + \alpha b + \lambda b\alpha\,(\tfrac{1}{2} - a_h)}{\lambda\left(H_1^{(2)}(-i\lambda) + i H_0^{(2)}(-i\lambda) \right)} \right] \qquad (5.6)$$

It can be shown that $\Gamma_n = 2\pi U b\alpha$ for the steady case. The induced velocity is found at the mid-point of each vortex ring using the Biot-Savart[103] law taking into account the vertical location of the tailplane. Circulation contributions from the other side of the aircraft are included. The induced velocities at the tailplane integration points (tailplane aerodynamic centre) are then obtained via grid interpolation, including the velocities induced at the other side of the aircraft.

The formulation of the unsteady generalised aerodynamic matrix in this model is approached in a similar manner to that

used in the strip method. The lift and moment are seen to be both functions of the unsteady velocities induced by the heave and pitch modes at the wing. Applying the transformation into normal co-ordinates.

$$V_h(y,t) = \sum_{i=1}^{N} V_{ih}(y) \; q_i(t)$$

$$\text{(5.7)}$$

$$V_\alpha(y,t) = \sum_{i=1}^{N} V_{i\alpha}(y) \; q_i(t)$$

where the first two modes are rigid-body modes and the remaining (N-2) modes are the independent natural vibration modes of the wing.

The velocities induced by these two-degrees of freedom are dealt with independently by considering them as separate cases inducing the wing circulation and subsequent wake field. Re-arranging Eq. (5.6) the circulation induced by these two types of displacement i.e. Γ_h and Γ_α can be separated.

Applying the correct transformation the resulting lift and moment which take proper account of unsteady lag effects can be expressed in terms of these induced velocities as follows.

$$\begin{bmatrix} L_T \\ M_{\alpha T} \end{bmatrix} = \begin{bmatrix} AD_{11} & AD_{12} \\ AD_{21} & AD_{22} \end{bmatrix} \begin{bmatrix} V_h \\ V_\alpha \end{bmatrix}$$

$$\text{(5.8)}$$

Reintroducing these expressions for lift and moment in terms of generalised aerodynamic forces one obtains the following expression for a new modified tailplane generalised aerodynamic matrix with downwash effects included. (Detail derivation for method is given in Appendix G).

$$DQT(i,j) = \int_0^{S_T} AD_{11} V_{jh} h_{iT} + AD_{12} V_{j\alpha} h_{iT} + AD_{21} V_{jh} \alpha_{iT} + AD_{22} V_{j\alpha} \alpha_{iT}$$

$$\text{(5.9)}$$

AD_{ij} are elements given in Appendix G. The procedure above is

125

shown in Figure 5.3.

5.3 Incorporation of a Quasi-Steady Wake in Dynamic Stability

In the derivation that follows, the circulation due to quasi-steady aerodynamics is assumed such that $\Gamma = 2\pi U b \theta$, where $\theta = (\frac{\lambda h}{U} + \alpha)$. The unsteadiness of the wake is neglected and the wing is assumed to be of uniform planform, therefore the wake pattern is made up of a bound vortex on the wing and trailing vortices from the wing tip. The analysis given below is restricted to the rigid body modes and quasi-steady aerodynamics, although this analysis is later extended to incorporate unsteady aerodynamics and wing flexibility.

As the induced velocity at the tailplane is proportional to the wing circulation, these induced velocities may be written in the form, for the rigid body modes of heave and pitch.

$$V_{ind} = \begin{bmatrix} 1 & 1 \end{bmatrix} \begin{bmatrix} V_h \\ V_\alpha \end{bmatrix} e^{\lambda t} \qquad (5.10)$$

This may be written in matrix form as

$$\begin{bmatrix} V_h \\ V_\alpha \end{bmatrix} = \begin{bmatrix} v_h \frac{\lambda}{U} & 0 \\ 0 & v_\alpha \end{bmatrix} \begin{bmatrix} h_w \\ \alpha_w \end{bmatrix} \qquad (5.11)$$

The virtual work done by the induced velocity at the tailplane may be written as

$$\delta W_T = \int_0^{S_T} L_T \delta h_T + M_{\alpha T} \delta \alpha_T \, dy = \int_0^{S_T} \begin{bmatrix} \delta h_T & \delta \alpha_T \end{bmatrix} \begin{bmatrix} L_T \\ M_{\alpha T} \end{bmatrix} dy$$

$$(5.12)$$

where the deflection of the tailplane aerodynamic centre is given as before in Chapter 4 as:

$$
\begin{bmatrix} \delta h_T \\ \delta \alpha_T \end{bmatrix} = \begin{bmatrix} 1 & x_T \\ 0 & 1 \end{bmatrix} \begin{bmatrix} \delta q_h \\ \delta q_p \end{bmatrix}
\tag{5.13}
$$

The lift may be written in terms of the induced velocities given by Eq.(5.10) where

$$
\begin{bmatrix} L_T \\ M_{\alpha T} \end{bmatrix} = \begin{bmatrix} AD_{11} & AD_{12} \\ AD_{21} & AD_{22} \end{bmatrix} \begin{bmatrix} V_h \\ V_\alpha \end{bmatrix}
$$

$$
\begin{bmatrix} L_T \\ M_{\alpha T} \end{bmatrix} = \begin{bmatrix} AD_{11} & AD_{12} \\ AD_{21} & AD_{22} \end{bmatrix} \begin{bmatrix} v_h \dfrac{\lambda}{U} & 0 \\ 0 & v_\alpha \end{bmatrix} \begin{bmatrix} h_w \\ \alpha_w \end{bmatrix}
\tag{5.14}
$$

where considering just quasi-steady aerodynamics

$$
AD_{11} = AD_{12} = -a_1 \rho U b
$$

$$
AD_{21} = AD_{22} = a_1 \rho U b^2 (\tfrac{1}{2} + a_h)
\tag{5.15}
$$

Inserting expressions for the displacement from Eq.(5.13) and the lift and moment from Eq.(5.14), the virtual work done by the downwash given by Eq.(5.12) can be re-written as:

$$
\begin{bmatrix} \dfrac{\delta W}{\delta q_h} \\ \dfrac{\delta W}{\delta q_p} \end{bmatrix} = \int_0^{s_T} \begin{bmatrix} 1 & 0 \\ x_T & 1 \end{bmatrix} \begin{bmatrix} AD_{11} & AD_{12} \\ AD_{21} & AD_{22} \end{bmatrix} \begin{bmatrix} v_h \dfrac{\lambda}{U} & 0 \\ 0 & v_\alpha \end{bmatrix} \begin{bmatrix} q_h \\ q_p \end{bmatrix} dy
\tag{5.16}
$$

$$
\int_0^{s_T} \begin{bmatrix} AD_{11} v_h \lambda/U & AD_{12} v_\alpha \\ AD_{11} v_h \lambda/U \, x_T + AD_{21} v_h \lambda/U & AD_{12} v_\alpha x_T + AD_{22} v_\alpha \end{bmatrix} \begin{bmatrix} q_h \\ q_p \end{bmatrix} dy
$$

127

$$= \begin{bmatrix} s_T AD_{11} v_h \ \lambda/U & s_T AD_{12} v_\alpha \\ s_T AD_{11} v_h \ \lambda/U \ x_T + s_T AD_{21} v_h \ \lambda/U & s_T AD_{12} v_\alpha x_T + s_T AD_{22} v_\alpha \end{bmatrix} \begin{bmatrix} q_h \\ q_p \end{bmatrix}$$

$$DQT(i,j) = \begin{bmatrix} DQT_{11} & DQT_{12} \\ DQT_{21} & DQT_{22} \end{bmatrix} \begin{bmatrix} q_h \\ q_p \end{bmatrix} \qquad (5.17)$$

Expressions for the rigid body generalised forces from the wing and tailplane are added to those obtained in Chapter 4 to give the total generalised aerodynamic matrix.

$$Q(i,j) = \begin{bmatrix} Q_{11} & Q_{12} \\ Q_{21} & Q_{22} \end{bmatrix} \begin{bmatrix} q_h \\ q_p \end{bmatrix} \qquad (5.18)$$

If $a_h = -0.5$ as before. Hence $AD_{21} = AD_{22} = 0$

$$Q_{11} q_h = (s_W A_{11} + s_T A_{11T} + s_T AD_{11} v_h \frac{\lambda}{U}) q_h$$

$$= -\frac{1}{2}\rho U S_W (a_0 + a_1 \frac{S_T}{S_W}(1 + \frac{v_h}{U})) \dot{q}_h$$

since $\quad -\dfrac{d\varepsilon}{d\alpha} = \begin{bmatrix} \dfrac{v_h + v_\alpha}{U} \end{bmatrix} e^{\lambda t}$

$$= -\frac{1}{2}\rho U S_W (a_0 + a_1 \frac{S_T}{S_W}(1 - \frac{d\varepsilon}{d\alpha})) \dot{q}_h = \overset{\circ}{Z}_W \dot{q}_h$$

$$Q_{12} q_p = (-s_W A_{11} x_W + s_T A_{11T} x_T + s_W A_{12} + s_T A_{12T} + s_T AD_{12} v_\alpha) q_p$$

$$= \frac{1}{2}\rho U S_W (a_0 x_W - a_1 \frac{S_T}{S_W} x_T) \dot{q}_p - \frac{1}{2}\rho U^2 S_W (a_0 + a_1 \frac{S_T}{S_W}(1 + \frac{v_\alpha}{U})) q_p$$

128

$$= \frac{1}{2}\rho U S_W (a_0 x_W - a_1 \frac{S_T}{S_W} x_T)\dot{q}_p - \frac{1}{2}\rho U^2 S_W (a_0 + a_1 \frac{S_T}{S_W}(1 - \frac{d\varepsilon}{d\alpha}))q_p$$

$$= \overset{o}{Z}_q \dot{q}_p - C_1 q_p$$

$$Q_{21} q_h = (-s_W A_{11} x_W + s_T A_{11T} x_T + s_T AD_{11} v_h \frac{\lambda}{U} x_T)q_h$$

$$= \frac{1}{2}\rho U S_W (a_0 x_W - a_1 \frac{S_T}{S_W} x_T (1 + \frac{v_h}{U}))\dot{q}_h$$

$$= \frac{1}{2}\rho U S_W (a_0 x_W - a_1 \frac{S_T}{S_W} x_T (1 - \frac{d\varepsilon}{d\alpha}))\dot{q}_h = \overset{o}{M}_W \dot{q}_h$$

$$Q_{22} q_p = (s_W A_{11} x_W^2 + s_T A_{11T} x_T^2 - s_W A_{12} x_W + s_T A_{12T} x_T$$
$$+ s_T AD_{12} v_\alpha x_T)q_p$$

$$= -\frac{1}{2}\rho U S_W (a_0 x_W^2 + a_1 \frac{S_T}{S_W} x_T^2)\dot{q}_p + \frac{1}{2}\rho U^2 S_W (a_0 x_W - a_1 \frac{S_T}{S_W} x_T (1 + \frac{v_\alpha}{U}))q_p$$

$$= -\frac{1}{2}\rho U S_W (a_0 x_W^2 + a_1 \frac{S_T}{S_W} x_T^2)\dot{q}_p + \frac{1}{2}\rho U^2 S_W (a_0 x_W - a_1 \frac{S_T}{S_W} x_T (1 - \frac{d\varepsilon}{d\alpha}))q_p$$

$$= \overset{o}{M}_q \dot{q}_p + C_2 q_p$$

$$(5.19)$$

These terms are then introduced into the dynamic stability matrix of Chapter 4. At this stage downwash is incorporated within the terms Z_W and M_W but the lag effects have yet to be introduced via the unsteady aerodynamic wing circulation provided by Eq.(5.6) and the unsteady wake distribution given by Eq.(5.3).

5.4 Selection of N_ζ

Once the full unsteady model of the wake is constructed, with the addition of the elastic modes, a parametric analysis was carried out to select the optimum number of integration points N_ζ to adequately represent a vortex cell.

The generalised tailplane aerodynamic matrix including downwash effects is plotted against N_ζ for a range of reduced frequencies and airspeeds to ascertain the value of N_ζ for adequate convergence for the induced tailplane aerodynamics. For comparison purposes, results are obtained for a fictitious aircraft with a rectangular wing of aspect ratio 12 and possessing elastic and inertia properties common in most large aspect ratio sailplanes (particulars are shown in Table 5.1).

As the proposed aerodynamic model is frequency dependent, the case for an aircraft undertaking harmonic motion, as in flutter, was considered. In this example two elastic modes namely the first bending and first torsional modes were incorporated in addition to the two rigid body modes of heave and pitch. These elastic modes were selected as a result of their dominance in bending/torsion flutter. Hence the resulting aerodynamic matrix is complex and of order 4X4. If $a_h = -0.5$ there is no moment contribution to the aerodynamic matrix except for the non-circulatory terms which are usually small. As a result of this fact the real and imaginary terms of Q(1,1) will be approximately equal to Q(2,1) and Q(1,2) will be approximately equal to Q(2,2). Therefore the terms Q(1,1) and Q(1,2) are selected for observation and non-dimensionalised with respect to ρU^2. The case for k = 0.1 is shown for example in Figure 5.4 and for the real and imaginary parts of $Q(1,1)/\rho U^2$ and $Q(2,1)/\rho U^2$ and in addition the term $Q(3,3)/\rho U^2$ is included. This last term is included as it was found to be the largest value amongst the pure elastic terms. As one can see however, this term is small compared to the rigid body contribution. These results were obtained using 11 integration points on the wing as this is the number thought best representative of the points that will be used in subsequent analyses on other aircraft.

Shown in Figure 5.5 is the time taken in seconds for generalised aerodynamic matrix to be formed for a given N_ζ up to

N_ζ = 110, on a SUN SPARK workstation. As one can see the time required in computation using even a moderate value of N_ζ is large and variation with N_ζ is quite drastic. This is as a result of the time taken for the NAG routine E01ACF[104] to interpolate each strip within the vortex cells for both the starboard and port side of the aircraft. It is seen from Figures 5.4 and 5.5 that a value of N_ζ = 30 establishes a reasonable compromise between computational time and numerical accuracy. At k = 0.1 the percentage difference between the value at N_ζ = 30 and the converged value for Q(1,1) is 6.5% and 1.5% for the real and imaginary terms. For Q(1,2) this difference is 1.0% and 1.7% respectively. For the pure elastic term Q(3,3) the values are 9.1% and 21.2% but as small numbers are being dealt with this is considered not unreasonable. However to achieve faster processing time N_ζ = 20 can also be considered consuming just under half the time needed for N_ζ = 30.

It is interesting to note that once the generalised airforces have been non-dimensionalised with respect to ρU^2 the values and trend as shown in Figure 5.4 are identical for all speeds.

5.4.1 Variation of Induced Generalised Forces with l_{wt} and Z_T

The variation of the induced generalised aerodynamic forces on the tailplane with l_{wt} (distance between wing trailing edge and tailplane leading edge) is shown in Figure 5.6 for k = 0.1 and Z_T = 0.0 , 5.0 and 10.0m, (vertical distance from tailplane to plane of wake, measured positive up). In this example the forces plotted are those induced on Q(1,1) and Q(1,2). Although the expressions provided by Eq.(5.18) are derived on the basis of quasi-steady aerodynamics, it can be seen that considering the induced contributions to Q(i,j), that Q(1,1) and Q(1,2) are due solely to heave motion and pitching motion respectively.

Referring to both the real and imaginary curves in Figure 5.6, it can be seen that as the tailplane moves downstream the real part of v_h increases and the imaginary part or phase difference decreases. When the imaginary part is zero the tailplane is in phase with the vortices being shed form the main aerofoil, due to heave motion, resulting in the maximum value of the real part. As the phase difference increases the subsequent

real part decreases until further downstream the process is repeated and the sign of the real part is reversed.

The heave motion and the pitching rotation are out of phase by 90°. Therefore once the real part of v_h has attained its maximum value the corresponding real part of v_α will be a minimum and this is in fact shown for v_α in Figure 5.6.

It is seen from the curves that as the vertical height between the tailplane and wake increases the influence of the wake diminishes.

5.5 Case Study on High Aspect Ratio Rectangular Wing Aircraft

For this case study the downwash obtained had to be readily compared with those obtained either theoretically or semi-empirically from reliable sources. The only notable reference of this type was found from ESDU sheets.[105] Unfortunately the highest aspect ratios considered in ESDU is 12, which means that the example aircraft, used to represent the stability derivatives in Chapter 4, is not appropriate.

Hence the wing for this example aircraft is reduced from an aspect ratio of 20 to 12 to be compatible with Ref.(105).Before the unsteady aerodynamic model is dealt with the steady downwash was evaluated at the tailplane and compared with those obtained from Ref.(105). The theory is implemented by replacing the loading on the wing by a single bound horseshoe vortex with its trailing vortex stretched out to infinity at the wing tips. The circulation is taken for the steady case i.e. $\Gamma_n = 2\pi Ub\alpha$ and the loading is assumed to be uniform along the span (which is a reasonable assumption for high aspect ratio wings). As mentioned earlier the static displacement of the vortex sheet is neglected.

The mean downwash is obtained from the distribution on the tailplane and reduced in terms of $d\varepsilon/d\alpha$. The comparisons with Ref. (105) can be seen in Table 5.2. As can be seen from this table the discrepancy is quite significant and can be probably attributed to the assumption of the loading on the wing and the location of the trailing vortex from the root. It is usual when replacing an elliptical loading by an equivalent uniform distribution, that the trailing vortex is situated further inboard to take up this

132

discrepancy.[106] As the trailing vortex is situated on the wing tips the errors made are more severe in this case. Although the option of moving the trailing vortex is available at this stage it would not be so easy when incorporating taper and the elastic modes of the wing and tailplane. Secondly it is not compatible with the vortex lattice model considered. One suggestion might be to actually replace the loading with a distribution obtained by more refined 3-dimensional codes as reported in the literature[99] or using the existing modified strip theory.

However in this work, it was judged adequate within the assumptions already made to just simply multiply the induced velocities in the downwash code by the appropriate factor to arrive at the ESDU value. The multiplying factor turned out to be 1.7833 assuming a value of $a_0 = 2\pi$ /rad for the wing distribution.

5.5.1 Rigid Body Dynamics

As in Chapter 4 the roots of the stability determinant for the s.p.p.o mode were obtained and compared with the classical solution employing stability derivatives and $d\varepsilon/d\alpha$, using Ref.(14). However various factors were accounted for before the full effects of the unsteady downwash were incorporated. These are:

i) The introduction of the modified aerodynamic parameters a_0 and a_1 for the aircraft, without taking into account any downwash effects:

Also as assumed before quasi-steady wing and tailplane aerodynamics were considered with $C(k) = 1.0$ (i.e. $k = 0$) and omitting the non-circulatory terms (this is elaborated in Chapter 4). The aerodynamic parameters were calculated as $a_0 = 5.04$ /rad and $a_1 = 4.56$ /rad using Ref.(73), The roots of the s.p.p.o were obtained and compared with those from Babister[14] this is shown in Table 5.3. The results are virtually identical and this is borne out from the theoretical derivation carried out in Chapter 4. Also shown are the roots obtained by including the full effects of wing and tail unsteady aerodynamics.

ii) The inclusion of the corrected steady downwash:

These results are also displayed in Table 5.3. In this model no unsteady downwash effects were considered hence this is

equivalent to no lag effects in the Babister approach i.e. neglecting the terms $Z_{\dot{w}}$ and $M_{\dot{w}}$. The agreement between the two theories at this stage inferred in the theoretical treatment in section 5.3 is well demonstrated in Table 5.3 for the two speeds considered.

iii) The full inclusion of an unsteady wake at the tailplane (as proposed in appendix G):

Although the wing circulation is evaluated in the convergent plane for arbitrary motion of the form $e^{\lambda t}$, the resulting wake circulation was assumed to be of harmonic distribution. It was thought unwise to consider downwash of arbitrary nature as this did not provide the necessary convergence for the induced velocities and is in addition conceptually dubious. In this model downwash lag effects are accounted for by the phase shift of the wake at the tailplane, hence there is no need to introduce the additional derivatives[14] $Z_{\dot{w}}$ and $M_{\dot{w}}$ as they are already represented as phase shifts in the terms Z_w and M_w.

Using quasi-steady wing and tailplane aerodynamics the effect of an unsteady downwash was introduced to compare with the s.p.p.o quantity obtained using $Z_{\dot{w}}$ and $M_{\dot{w}}$ provided by the classical approach. This is shown in Table 5.3. It is seen that the damping generated using the unsteady wake model is marginally larger than that predicted by following the approach of Ref.(14). However the resulting s.p.p.o frequency is reduced by 20% compared to a 40% reduction predicted by a downwash lag assumption[14] This is reflected in the larger damping ratio predicted using the classical approach.

The next step was the full introduction of unsteady aerodynamics for the wing and tailplane. The general effect, as observed in Chapter 4, is now for the unsteady wing and tailplane aerodynamics to reduce the damping and increase the stiffness in the s.p.p.o mode. Essentially the damping predicted is comparable with that when using Ref.(14), but using the current theory the effect of unsteady aerodynamics is to reduce the damping ratio even further, the corresponding reduction in the frequency is now only 7%.

Subsequent investigation at higher speeds yielded identical

stability roots, within the accuracy of the eigen value search procedure. This is also inferred by the aerodynamic forces, non-dimensionalised with respect to ρU^2 shown in Figure 5.6.

The effect of varying tailplane height was also investigated for the rigid case and these results are shown in Table 5.4. As expected the influence of the wake diminishes as the tailplane height increases to such an extent that at 10m vertically above the the centre of the wake the influence is negligible.

5.5.2 Inclusion of Elastic modes

The full effect of flexibility and unsteady aerodynamics was next investigated. As the time required to generate the induced velocities was quite significant, even for $N_\zeta = 30$, the analysis was restricted to two elastic modes in addition to the two rigid body modes (modes 1 and 2). These elastic modes were the first bending and first torsional modes (modes 3 and 4), which are normally prevalent in classical bending/torsion flutter.

The analysis was first carried out employing unsteady aerodynamics but without the influence of an unsteady wake, for three selected speeds U = 30, 60 and 90 m/s. The corresponding roots are shown in Table 5.5. The short period pitching frequency and damping are given in Table 5.6. The effect of an unsteady wake was next introduced and these results are presented for comparison with the aforementioned tables.

It is noted from these results that without the influence of downwash, the damping appears to be non-variant for the range of speeds considered. When the unsteady wake is taken into account the s.p.p.o damping appears to decrease with speed this is accompanied by a decrease in damping ratio. The effect this has on the flutter speed of this particular configuration is uncertain as no flutter was found within the practical flight speed range of this aircraft employing conventional flutter analysis.

5.6 Effect of Downwash on Flutter of Kestrel

The effect of an unsteady downwash on the flutter of Kestrel was initially carried out using the two rigid body modes and the first bending and first torsional elastic modes taking the tailplane height as 1.5 m. As harmonic motion is being considered

135

the circulation is now dependent on the reduced frequency k as well as the downwash wake. The corresponding flutter speed and flutter frequency is found to be 74.6 m/s and 49.6 rad/s respectively. This figure represents a negligible decrease in flutter speed, in comparison to the corresponding analysis neglecting downwash effects.

When the number of modes is increased to six the flutter speed and flutter frequency are found to be 72.2 m/s and 49.6 rad/s respectively. The corresponding values are 72.3 m/s and 49.7 rad/s when downwash is neglected. Thus the influence of the wake is seen to be negligible for this aircraft and the inclusion of additional modes does not alter the strength of the vortices. It can be seen from these results that as the Kestrel posses a high aspect ratio wing and is a T - tail configuration the effect of the wake vortices on the tailplane are rather small. However as seen above the combination of flexibility, unsteady aerodynamics and the unsteady downwash may be still critical for different configurations, in particular for low aspect ratio aircraft.

5.7 The Effect of Downwash on Stability of the Kestrel and the Cranfield A1

5.7.1 The Kestrel

5.7.1.1 Rigid Body Modes

The first analysis involved the rigid body modes (modes 1 and 2) as before and the roots of the s.p.p.o mode were evaluated for U = 30 m/s and 60 m/s. These roots are shown in Table 5.7 and the corresponding frequencies and damping ratios are given in Table 5.8. Considering just rigid body motion the independence of the roots with speed is exhibited again as seen form the analysis so far. Comparing this result with the previous analysis carried out in Chapter 4, neglecting the wake, the effect of the wake is seen to increase the damping by 46.5% and decrease the frequency of the s.p.p.o mode by 13%. An analysis was then carried out using Ref.(14) and taking $\frac{d\varepsilon}{d\alpha}$ = 0.097, ($\frac{d\varepsilon}{d\alpha}$ was calculated from Ref.(107) and is based on empirical data). This set of results is also shown in Tables 5.7 and 5.8. It can be seen from Table 5.8 that although the predicted damping is higher using the current

method, the damping ratio obtained using the classical approach is larger and the subsequent short period frequency is smaller.

5.7.1.2 Inclusion of Elastic Modes

The first bending and first torsional elastic modes (modes 3 and 6) were next introduced. The corresponding roots are shown in Table 5.7. As it can be seen there is no longer a close non-dimensional consistency about the roots. In fact at U = 60 m/s, the Kestrel is close to its flutter speed and this is reflected in the decrease in damping. However it may be noted that for this mode the damping encountered is higher with the inclusion of downwash effects. The subsequent rate of pitch (dα/dt) is also plotted against time, as in Chapter 4, but this time with effects of unsteady downwash included. This is compared with the rigid case using classical downwash lag assumptions. The results are shown in Figure 5.7 for the two speeds considered.

5.7.2 The Cranfield A1

5.7.2.1 Rigid Body Modes

As in the case of Kestrel an initial analysis was carried out using just the rigid body modes. The two speeds selected were as used previously in Chapter 4 and are U = 41.1 m/s and 61.7 m/s. The aerodynamic density was taken as $\rho = 1.055$ kg/m^3 in accordance with the altitude during flight trials. The results of the current analysis are shown in Table 5.9 and compared with the flight test results[76] shown in Table 5.10. The results using the classical assumption taking $\frac{d\varepsilon}{d\alpha} = 0.4$, ($\frac{d\varepsilon}{d\alpha} = 0.4$ was reported in the original design specification of the A1.[108]), are also shown for comparison purposes.

First the results for the rigid case based on modes 1 and 2 in Table 5.9 are compared with the corresponding results of Table 4.14 where the wake effects were neglected. It is clearly evident that the introduction of the unsteady wake alters the results very drastically both in the present theory and also in the classical theory. The effect is very significant giving rise to a 28.5% reduction in the short period frequency and an average 203% increase in the short period damping. The A1 has an aspect ratio much lower than that of the current sailplanes considered, therefore the induced velocities at the tailplane and the

137

subsequent damping can be expected to be higher.

5.7.2.2 Inclusion of Elastic Modes

Referring to Table 5.9 it is seen from the results obtained from the present theory that the introduction of elastic modes in the wake model has almost no influence. This is due to the relatively high stiffnesses and moderate aspect ratio of A1. Results shown for the two speeds indicate that the short period frequency and the corresponding damping ratio are virtually unaltered when the analysis is carried out for the rigid aircraft (using mode 1 and mode 2) and the elastic aircraft (using modes 1,2,3 and 7) respectively. However when the results from the present theory are compared with the ones obtained using the classical theory, the large discrepancy in short period damping given by the two methods is noticeable which is in contrast to very close agreement (well within 3%) found in the short period frequency.

The results obtained from the flight test data are compared with the theoretical results in Table 5.10. The present theory predicts the short period frequency and damping more accurately than the classical theory particularly at lower speeds. However both the present theory and the classical theory underestimate the damping (with greater discrepancy being found with the classical theory). The underestimation in damping obtained from the classical approach could be attributable to the simplification of the downwash lag effects at the tailplane introduced by using $d\varepsilon/d\alpha$. For the two speeds considered Fig. 5.8 shows the plot of the rate of pitch ($d\alpha/dt$) against time obtained applying the present theory to both the rigid and the flexible aircraft. Results from the flight test are only available for the latter speed and these are plotted for comparison. The agreement between the present theory and the flight test results is reasonable as shown.

138

Geometric Details			
Wing		**Tailplane**	
Span	12 m	Span	4 m
Area	12 m^2	Area	2 m^2
Aspect ratio	12	Aspect ratio	8
Root chord	1 m	Root chord	0.5 m
Tip chord	1 m	Tip chord	0.5 m
Sweep angle	0^0	Sweep angle	0^0
a_0	5.04 /rad	a_1	4.56 /rad

Stiffness Details			
Wing stiffnesses		**Wing frequencies** **(free root values)**	
EI	200 kNm^2	ω_h	10.81 rad/s
GJ	20 kNm^2	ω_α	82.89 rad/s
M/l	22.5 kg/m		
I_p/l	0.2 kgm		

Inertia Details	
Total Mass	600 kg
Pitching Inertia	800 kgm^2

Table 5.1 Particulars of representative aircraft of aspect
ratio 12

	Downwash program $(\Gamma)_{k=0}$	ESDU ref.105	percentage diff (%)
$d\varepsilon/d\alpha$	0.2141	0.3818	78.3

Table 5.2 Comparison of downwash ratios

Approach	(i) $\dfrac{d\varepsilon}{d\alpha} = 0$ (ζ_{sp})	(ii) $\dfrac{d\varepsilon}{d\alpha} = 0.3818$ (neglecting lag terms) (ζ_{sp})	(iii) $\dfrac{d\varepsilon}{d\alpha} = 0.3818$ (including lag terms) (ζ_{sp})
Stability derivatives approach (Ref.14)	$-10.40 + i14.3$ (0.59)	$-10.26 + i10.79$ (0.69)	$-12.87 + i7.32$ (0.87)
Present theory with C(k) = 1	$-10.27 + i14.1$ (0.59)	$-9.98 + i10.74$ (0.68)	$-13.24 + i11.31$ (0.76)
C(k) ≠ 1	$-8.65 + i14.8$ (0.50)		$-12.80 + i13.73$ (0.68)

Table 5.3 Stability roots for representative aircraft using only rigid body modes

Height, Z_T (m)	$\bar{\lambda}$
0	-12.80 + i13.73
1.0	-12.24 + i14.09
10.0	-8.97 + i14.93

Table 5.4 Variation of stability roots with tailplane height

Speed (m/s)	Present theory without downwash using modes (1,2,3,4) $\bar{\lambda}$	Present theory with downwash using modes (1,2,3,4) $\bar{\lambda}$
30	-9.16 + i15.13	-12.63 + i13.08
60	-10.00 + i14.57	-10.05 + i14.10
90	-9.54 + i14.35	-7.5 + i10.89

Table 5.5 Stability roots for representative aircraft with the introduction of elastic modes (numbers within parenthesis in the first row represent the modes used in the analysis)

Speed (m/s)	Present theory without downwash using modes (1,2,3,4)			Present theory with downwash using modes (1,2,3,4)		
	ω_{sp} rad/s	μ_{sp} 1/sec	ζ_{sp}	ω_{sp} rad/s	μ_{sp} 1/sec	ζ_{sp}
30	5.53	-3.37	0.52	4.83	-4.64	0.69
60	10.74	-7.35	0.57	10.37	-7.39	0.58
90	15.83	-10.52	0.55	12.00	-8.27	0.57

Table 5.6   Short period pitching oscillation frequency and damping term and ratio for representative aircraft

	U = 30 m/s		U = 60 m/s	
	$\bar{\lambda}$	ζ_{sp}	$\bar{\lambda}$	ζ_{sp}
Stability derivative approach[14] $d\varepsilon/d\alpha = 0.097$	$-6.09 + i1.45$	0.97	$-6.09 + i1.45$	0.97
Present theory with modes :				
1,2	$-9.16 + i3.53$	0.93	$-9.42 + i3.62$	0.93
1,2,3,6	$-11.25 + i5.13$	0.91	$-5.51 + i8.02$	0.57

Table 5.7   Stability roots for the Kestrel with downwash

	U = 30 m/s			U = 60 m/s		
	μ_{sp} 1/sec	ω_{sp} rad/s	$T_{1/2}$ sec	μ_{sp} 1/sec	ω_{sp} rad/s	$T_{1/2}$ sec
Stability derivative approach[14] $d\varepsilon/d\alpha = 0.097$	-3.35	0.80	0.21	-6.70	1.60	0.10
Present theory with modes :						
1,2	-5.04	1.94	0.14	-10.36	3.98	0.07
1,2,3,6	-6.19	2.82	0.11	-6.06	8.82	0.11

Table 5.8   Short period pitching oscillation frequency and
damping term and ratio for Kestrel

	U = 41.1 m/s		U = 61.7 m/s	
	$\overline{\lambda}$	ζ_{sp}	$\overline{\lambda}$	ζ_{sp}
Stability derivative approach[14] $d\varepsilon/d\alpha = 0.4$	-5.09 + i6.94	0.60	-5.09 + i6.94	0.60
Present theory with modes :				
1,2	-11.42 + i7.13	0.85	-11.27 + i7.04	0.85
1,2,3,6	-11.42 + i7.13	0.85	-11.68 + i7.03	0.86

Table 5.9   Stability roots for the A1 with downwash

	U = 41.1 m/s			U = 61.7 m/s		
	μ_{sp} 1/sec	ω_{sp} rad/s	$T_{1/2}$ sec	μ_{sp} 1/sec	ω_{sp} rad/s	$T_{1/2}$ sec
Stability derivative approach[14] $d\varepsilon/d\alpha = 0.4$	-1.89	2.58	0.37	-2.83	3.90	0.24
Present theory with modes : 1,2 1,2,3,7	 -4.24 -4.24	 2.64 2.64	 0.16 0.16	 -6.28 -6.51	 3.92 3.90	 0.11 0.11
Flight test[76] results	(---)	2.70	(---)	-9.88	4.21	0.07

Table 5.10 Comparison of Theoretical results with flight test data for short period pitching oscillation characteristics of the A1

U

SMC

Wing

Γ

Aerodynamic
centre

• 1

• 2

• 3

•

$d\zeta$

•

•

Vortex
cell

•

Collocation
point

•

• Nζ

Tailplane

Tailplane

z_T

U

Wing
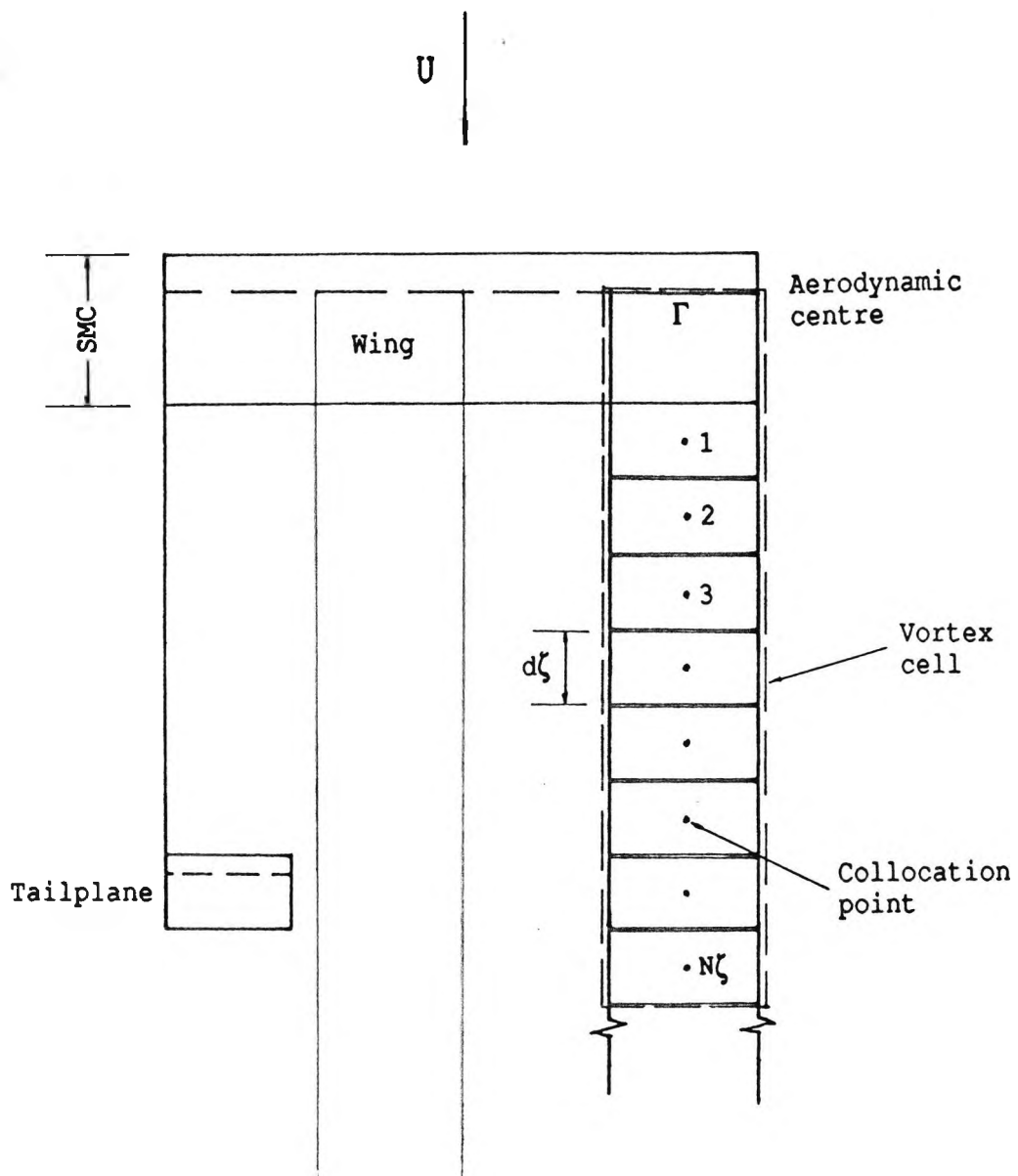
Fig. 5.1 Vortex field generation

L.E. = Leading edge

T.E. = Trailing egde
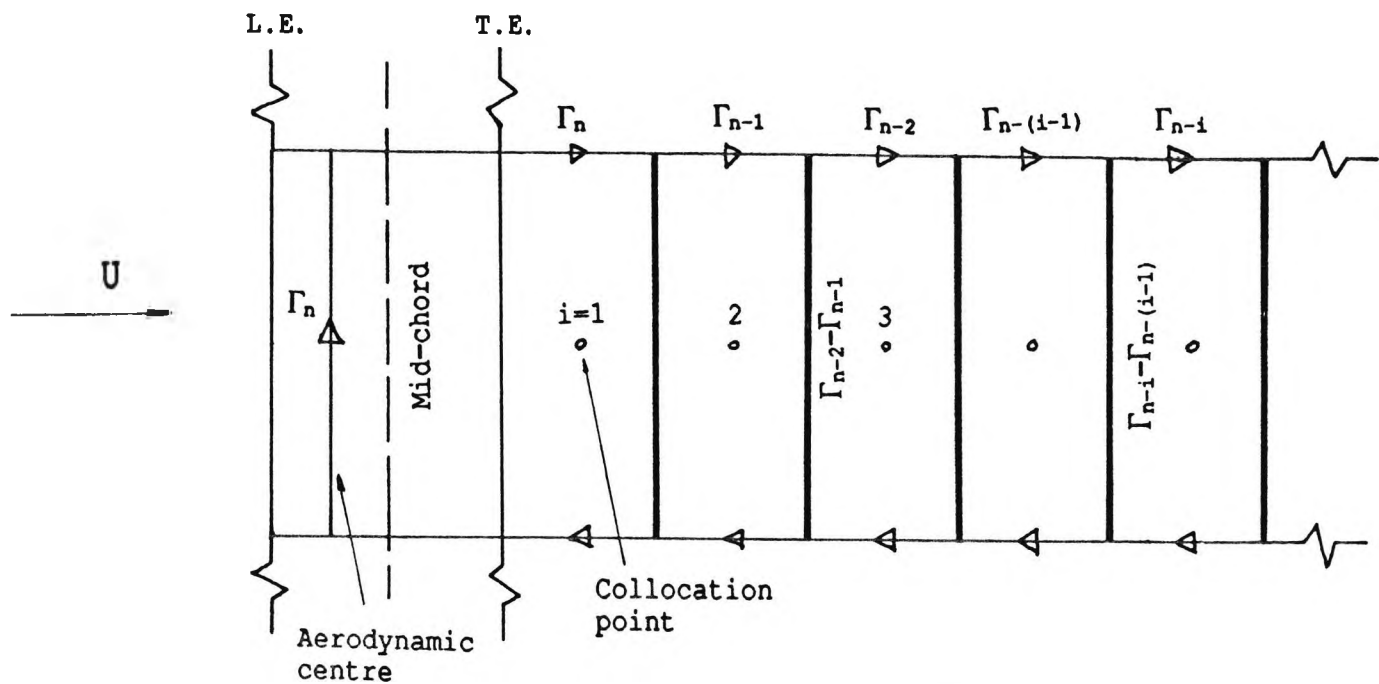
$i=1,2,3,\ldots\ldots MN\zeta$

$n=MN\zeta$

$\Gamma_{n-i}-\Gamma_{n-(i-1)}=$ Net change in wake
circulation
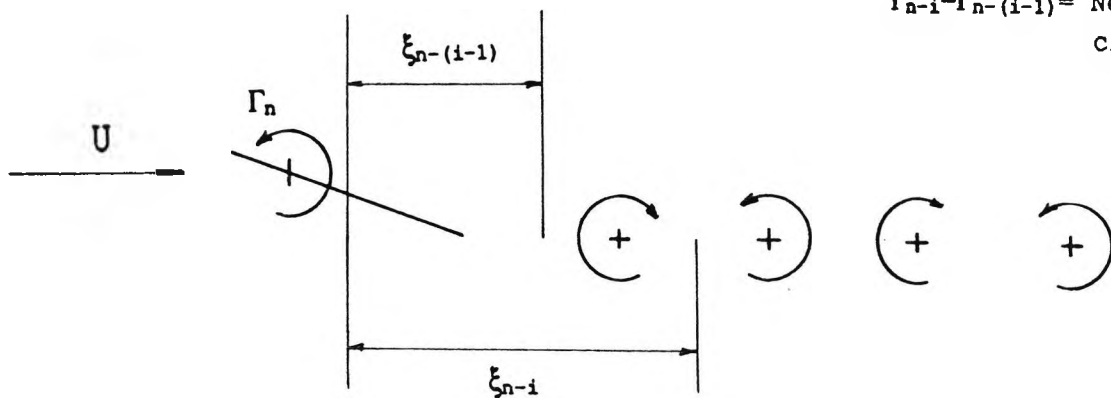
Fig. 5.2 Representation of wake circulation

```
                ┌─────────────────────┐
                │   Mass and Stiffness │
                │      Matrices        │
                └──────────┬──────────┘
                           │
                ┌──────────┴──────────┐
        ┌───────┤ Natural Frequencies ├────────┐
        │       │        and          │        │
        │       │     Mode Shapes     │        │
        │       └─────────────────────┘        │
        │                                       │
┌───────┴──────────┐        ┌───────────────┐   │
│ Generalised Mass │  NO ───┤   Downwash    ├── YES ───┐
│ and Stiffness    │        └───────────────┘          │
│ Matrices from    │                          ┌────────┴────────┐
│ selected modes   │                          │  Velocities     │
└───────┬──────────┘                          │  induced by     │
        │                                      │  unsteady       │
        │                                      │  Wake Vₕ,Vα     │
        │                                      └────────┬────────┘
        │              ┌───────────────┐       ┌────────┴────────┐
┌───────┴──────────┐   │ Generalised   │       │ Generalised     │
│ Generalised Wing │   │ Tailplane     │       │ Tailplane       │
│ Aerodynamic      │   │ Aerodynamic   │       │ Aerodynamic     │
│ Matrix           │   │ Matrix        │       │ Matrix +        │
└───────┬──────────┘   └───────┬───────┘       │ Lift induced    │
        │                      │                │ from Vₕ,Vα      │
        │                      │                └────────┬────────┘
        │       ┌──────────────┴──────────────┐         │
        └───────┤    Formulation of           ├─────────┘
                │   Stability Determinant      │
                └──────────────┬──────────────┘
                ┌──────────────┴──────────────┐
                │   Solution of Complex        │
                │   Stability Determinant      │
                └──────────────┬──────────────┘
                ┌──────────────┴──────────────┐
                │  Short period frequency      │
                │     and damping             │
                └─────────────────────────────┘
```

Fig. 5.3   Stability analysis incorporating downwash
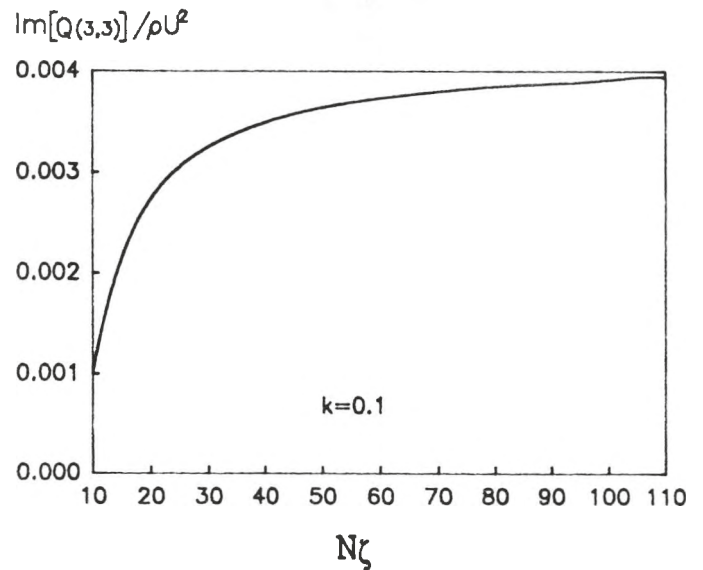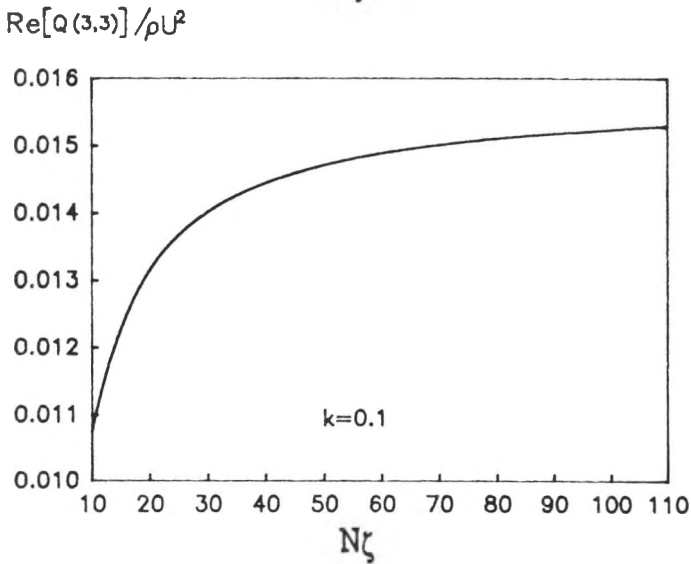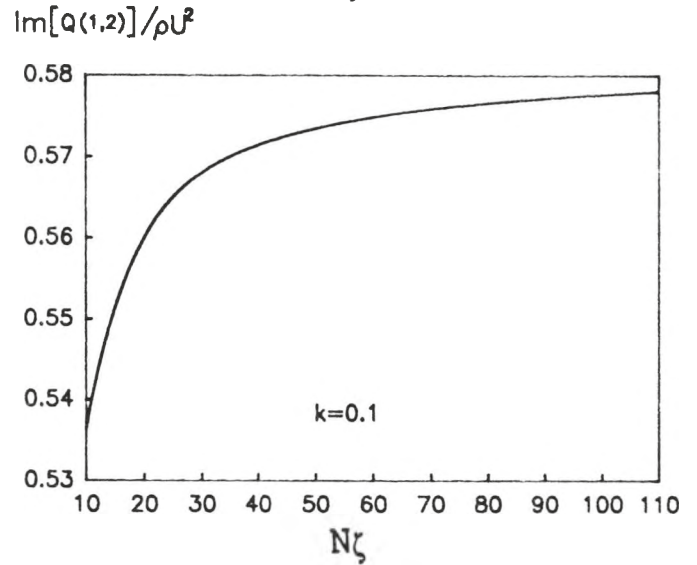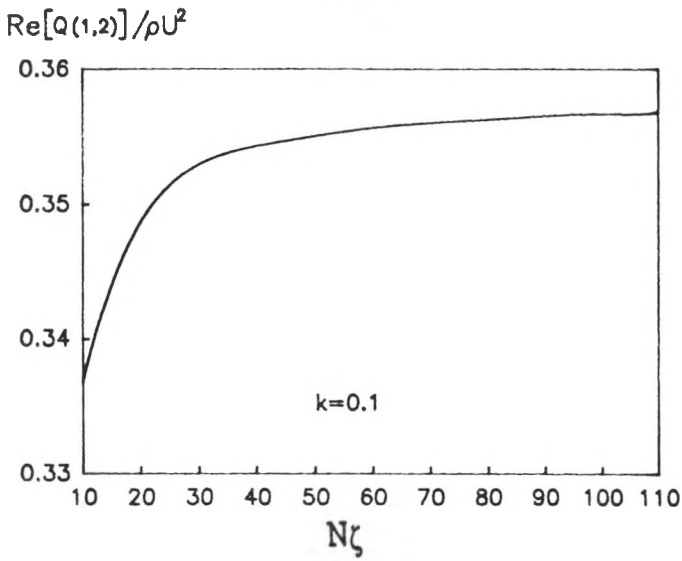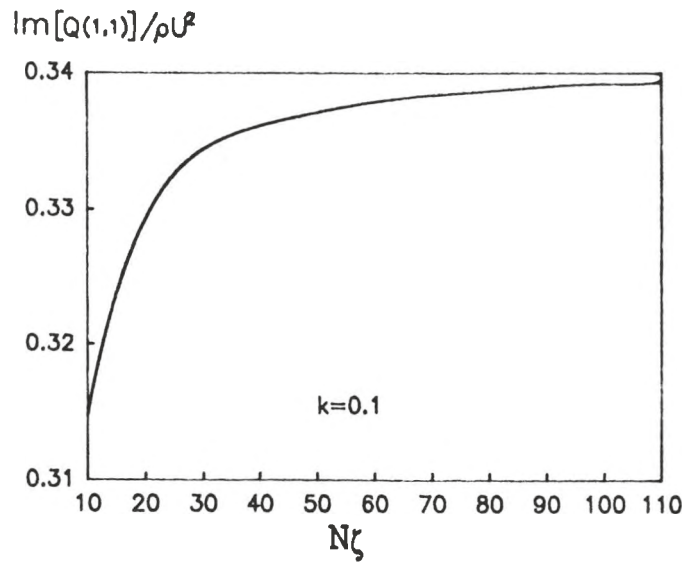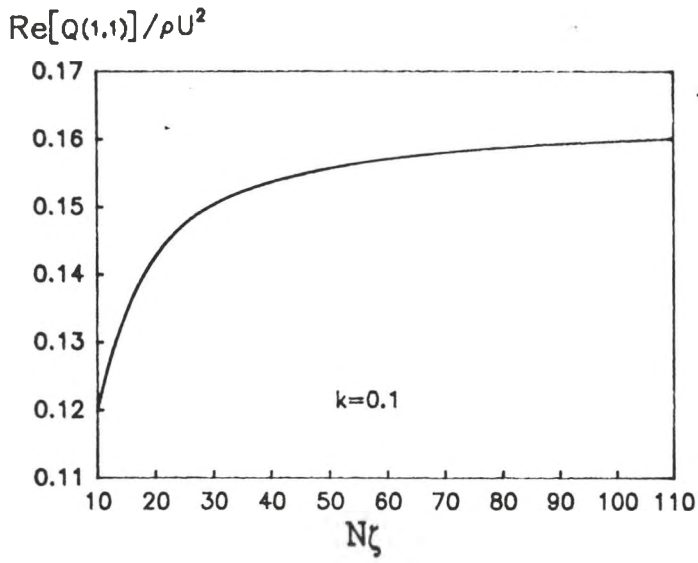
Fig. 5.4   Convergence of tailplane generalised aerodynamic forces
for rigid and elastic modes
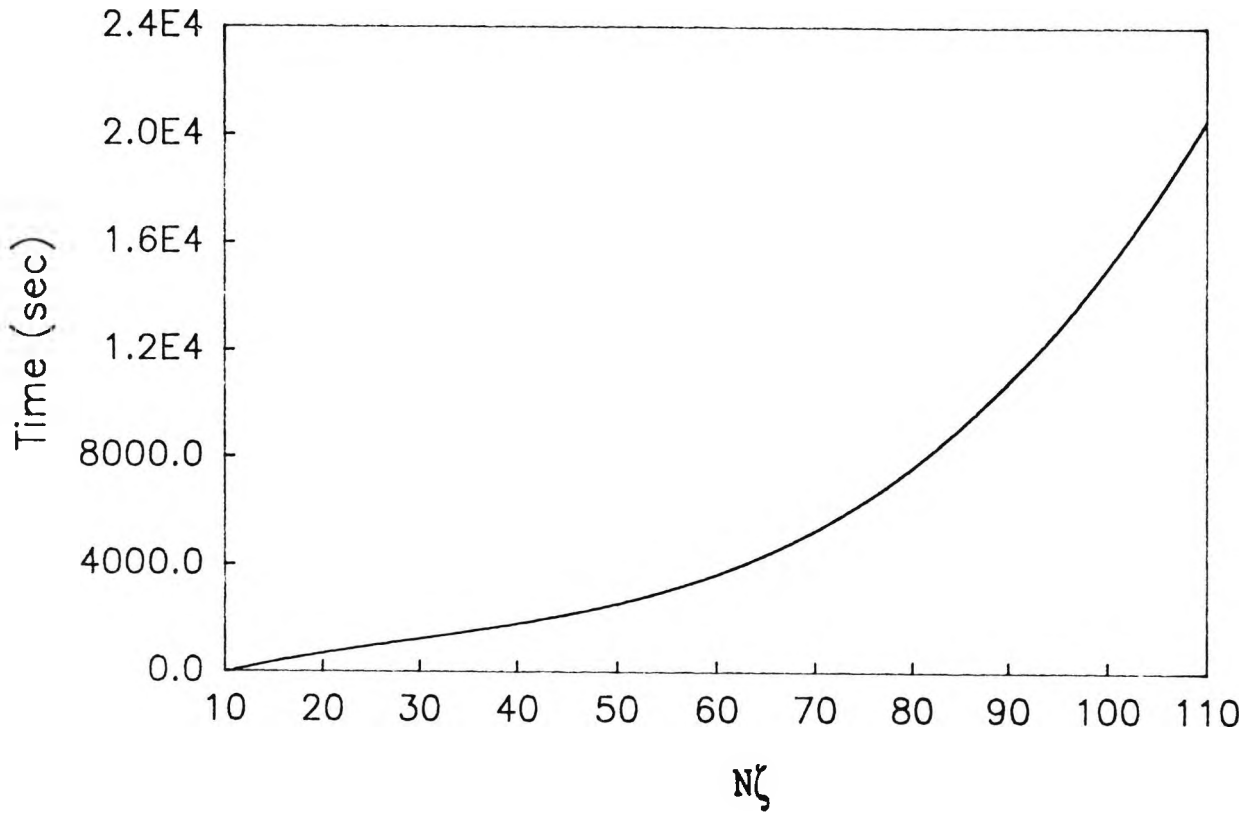
Fig. 5.5 Time taken to generate tailplane generalised aerodynamic matrix with $N\zeta$
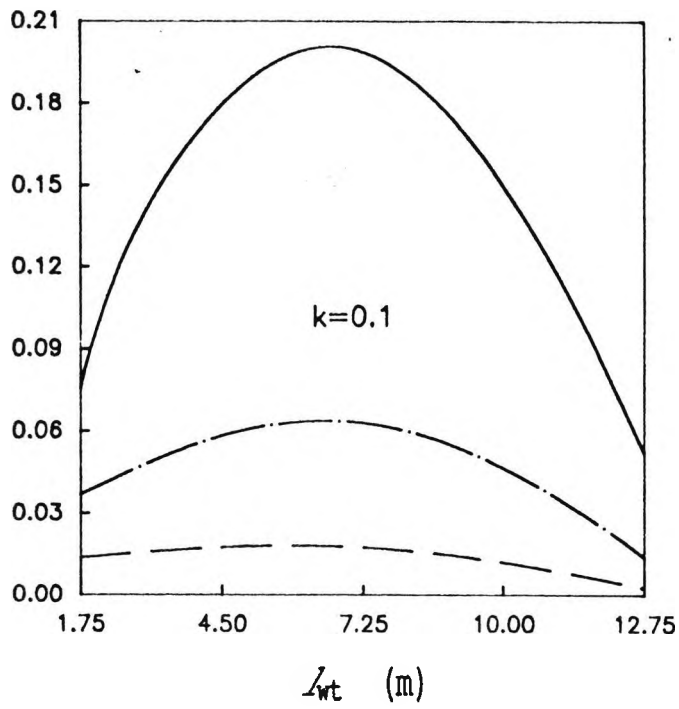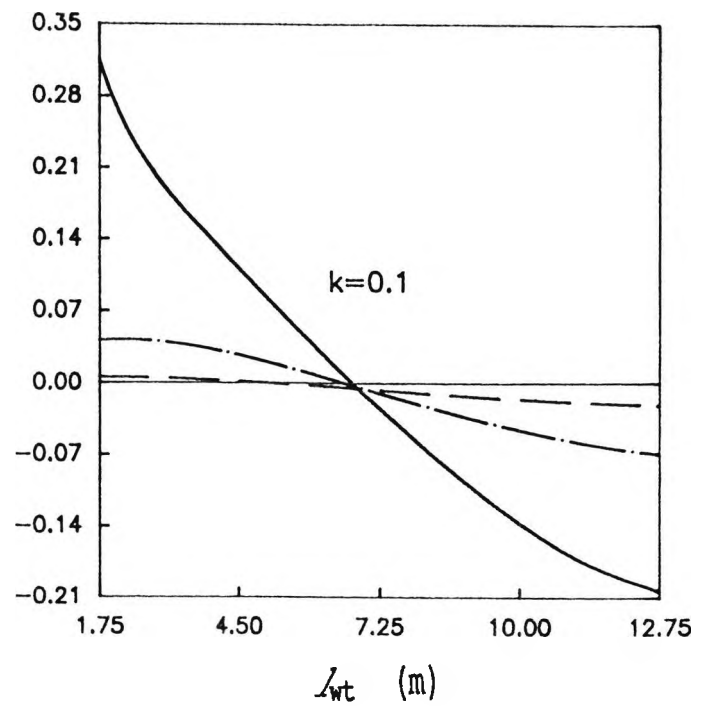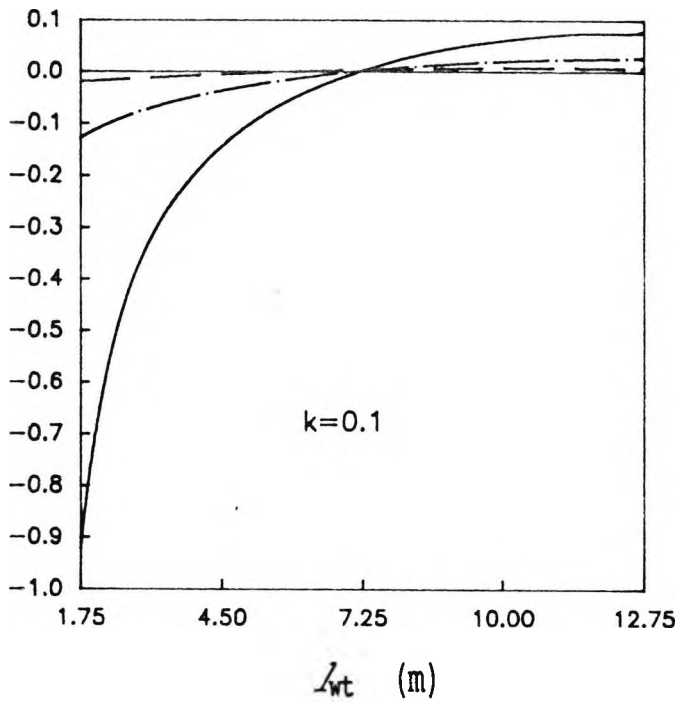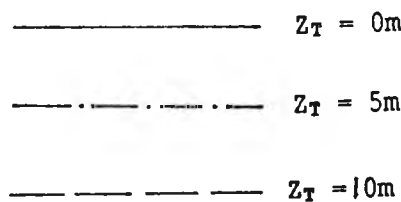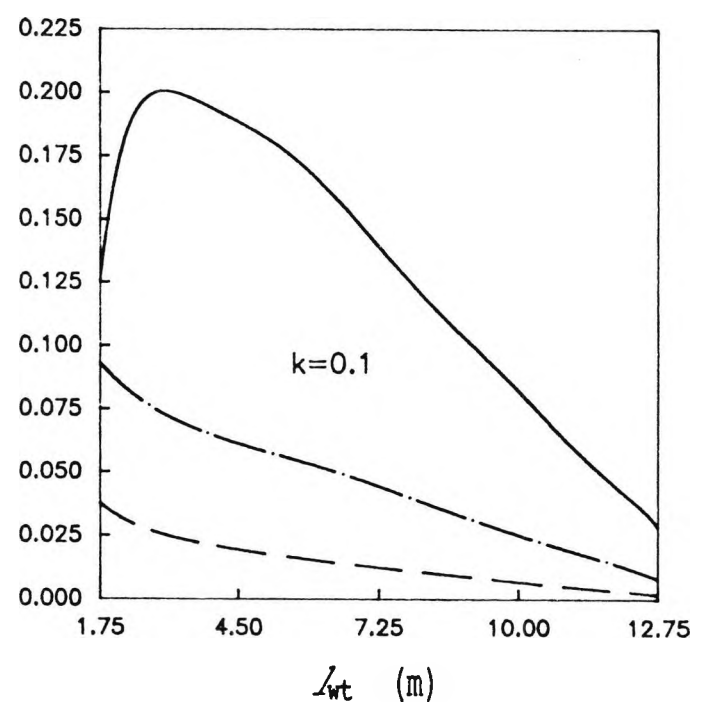
Fig. 5.6 Variation of induced tailplane generalised aerodynamic
forces with l_{wt} and Z_T
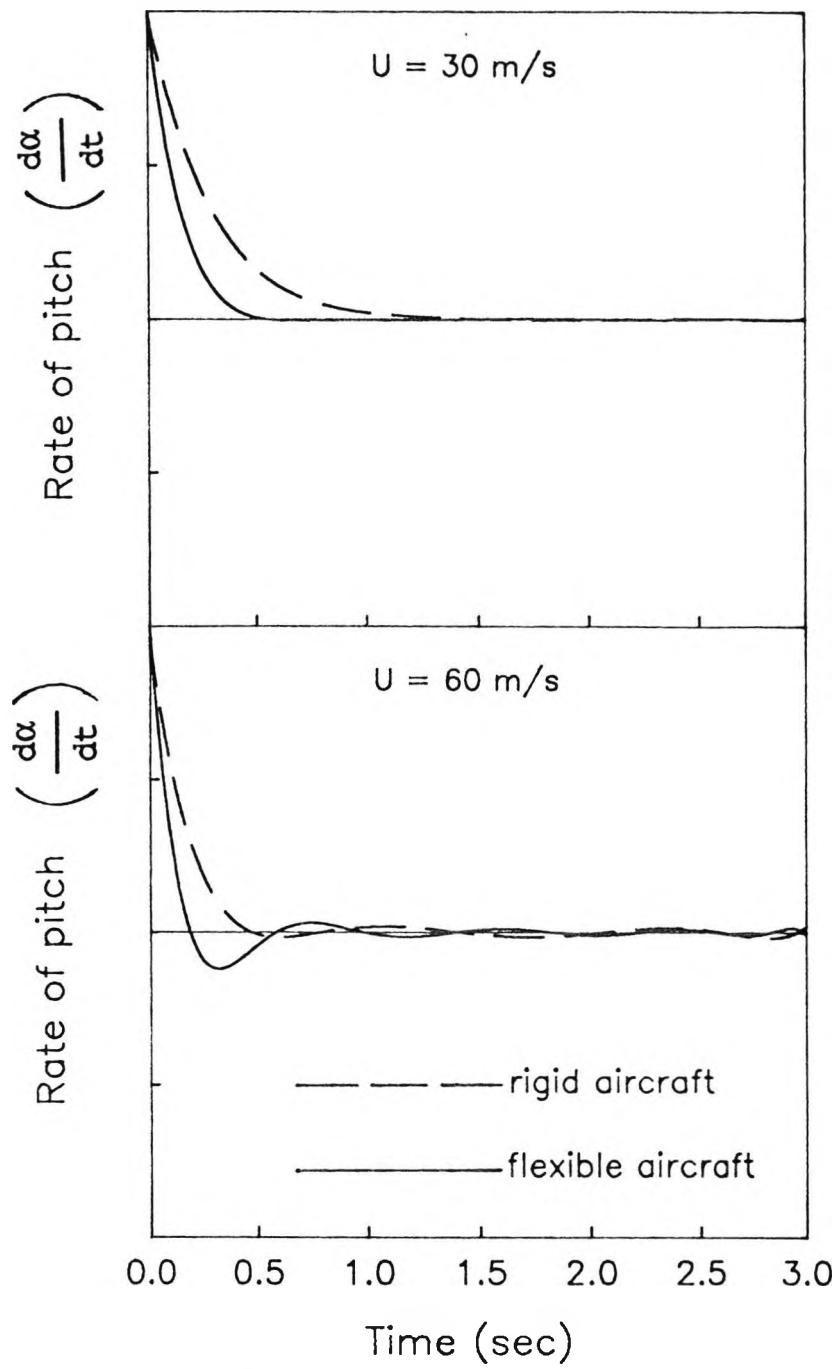
Fig. 5.7 Short period mode for Kestrel with inclusion of
unsteady wake at the tailplane
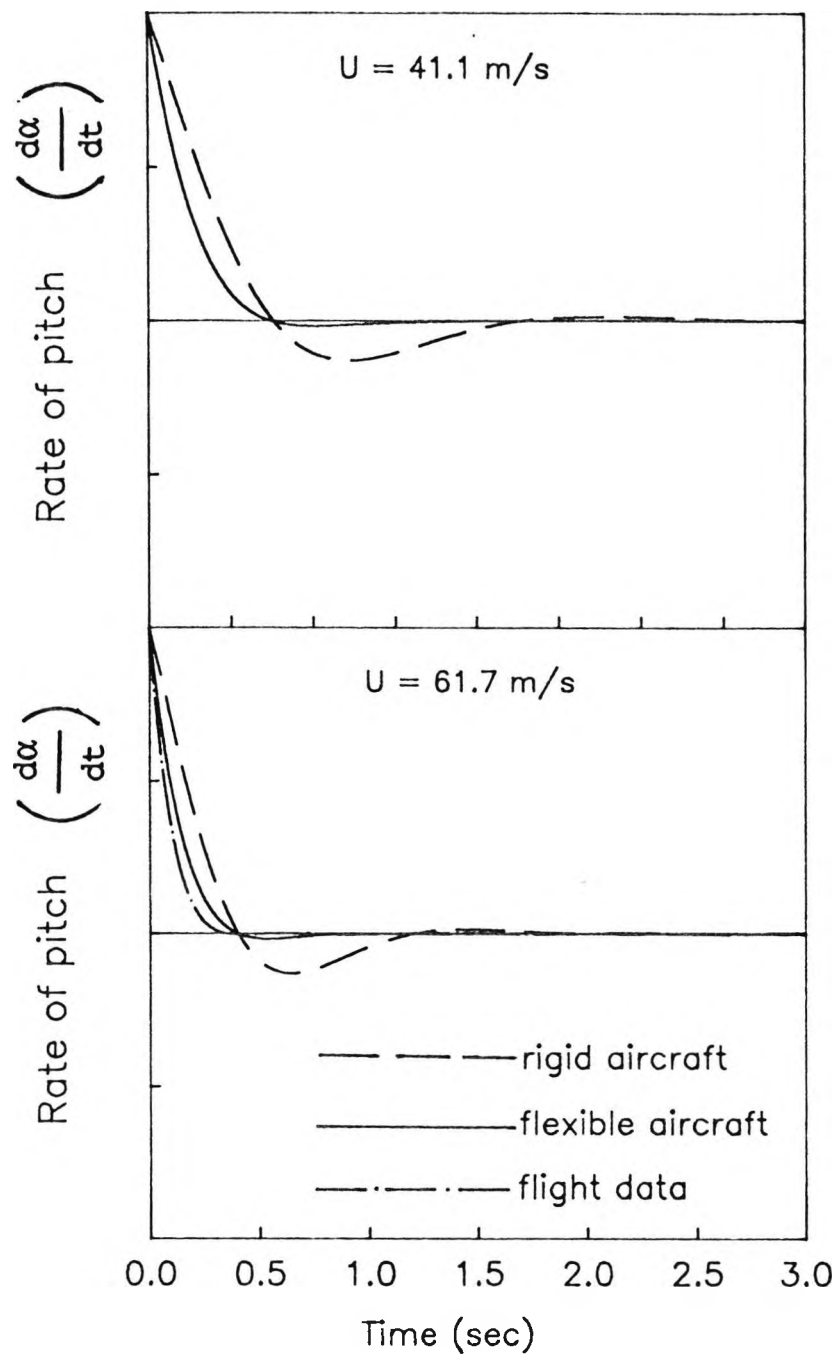
Fig. 5.8 Short period mode for A1 with inclusion of unsteady
        wake at the tailplane

6.0 AIRCRAFT RESPONSE TO DISCRETE GUSTS AND CONTINUOUS TURBULENCE

6.1 Introduction

Classical methods to obtain aircraft response to gusts and turbulence, have relied on rigid body assumptions in idealising the aircraft. The method also relied on modelling atmospheric turbulence in terms of discrete and/or isolated gusts. The earlier investigations[14,33] also restricted the degrees of freedom of the aircraft. Atmospheric turbulence is in reality a continuous phenomenon in which the airplane is subjected to repeated gustiness. In an attempt to account for this, statistical approaches have been established such as the power spectral density (PSD) method whose application can be traced back to the aircraft turbulence response problem as early as 40 years ago.[25] Since that time the PSD method has become widely accepted, such that the Civil aviation authority as part of its airworthiness regulations, namely JAR[109] (see section 25.305(d)) require that effects of dynamic response to turbulence be assessed by the PSD method. The particular advantage this method has over its discrete counterpart is its application to mission analysis or design envelope analysis, to predict the frequency exceedence of load and stress quantities with respect to reducing fatigue and improving ride quality.[110] However as automatic flight control systems become more and more complex and the capability of operating at frequencies close to the natural modes of the aircraft increases, the effects of flexibility and unsteady aerodynamics need to be accounted for.

A complementary approach to the computation of gust loads is that based on the statistical discrete gust (SDG) method.[26,32] The SDG method is attractive, because of its ability to compute (i) maximized and time-correlated gust loads and (ii) the gust profiles that produce these loads. Time correlation provides knowledge of the values (magnitudes and signs) of all loads when one particular load has attained its maximum (positive or negative) value. If the particular maximum load is critical for design, then an aircraft manufacturer may employ the SDG method to obtain a set of design loads to physically apply to a test specimen. This is not possible with the PSD method.

Although the two methods above are different it has been claimed by Jones,[27] developer of the SDG method, that under certain circumstances SDG and PSD methods produce essentially the same numerical results. This claimed SDG-PSD "overlap" has been extensively investigated and supported, by Perry et al,[111] for a combination of rigid and flexible aircraft response analyses. It is in this context of this claim that the current investigation will evaluate the response characteristics of deformable aircraft within the scope of strip theory, incorporating the effects of flexibility and unsteady aerodynamics.

6.2 Gust Analysis Methods
6.2.1 Power Spectral Density Method

The fundamental quantity of the PSD method is the PSD function, or power spectrum. A power spectrum contains all the statistical information describing a random process, including the root-mean-square (r.m.s) value. The random processes in question in the present application are respectively atmospheric turbulence as the input random process of r.m.s magnitude w_g and the resulting aircraft response as the output random process. Both the input and the output are assumed to be Gaussian. It is also assumed that the turbulence is one-dimensional (that is, uniform across the span), homogeneous, isotropic, and "frozen" in space during the time it takes the aircraft to traverse its own length.

The input and output PSD functions are related to each other through the square of the modulus of the airplane frequency response function, as given by the following equation[111]

$$\Phi_y(\omega) = |H_y(i\omega)|^2 \, \Phi_{w_g}(\omega) \qquad (6.1)$$

where $\Phi_y(\omega)$ is the airplane response power spectrum and $\Phi_{w_g}(\omega)$ is the atmospheric turbulence power spectrum. The aircraft frequency response function or mechanical admittance function $H_y(i\omega)$ represents the response (magnitude and phase), over a range of frequencies, of quantity y to a unit sinusoidal gust velocity. $H_y(i\omega)$ contains all the dynamics of the airplane (rigid-body modes

146

and elastic modes).

The frequency response function $H_y(i\omega)$ for the aircraft can be represented in terms of N number of modes multiplied by an N number of frequency response functions associated with each generalized co-ordinate. Thus

$$H_y(i\omega,x,y,z) = \sum_{i=1}^{N} \phi_i(x,y,z) \; H_i(i\omega) \qquad (6.2)$$

The first two modes are rigid-body modes and the remaining (N-2) modes are the independent natural vibration modes of the elastic structure (i.e. the aircraft).

$H_i(i\omega)$ is solved from Eq.(6.3) for i = 1,2,....N

$$H_i(i\omega) = \frac{\left[Q_{G_i} \right]}{\left[\left[\diagdown K \diagdown \right] - \omega^2 \left[\diagdown M \diagdown \right] - \left[Q_M \right] \right]} \qquad (6.3)$$

where $\left[Q_M \right]$ is the generalized aerodynamic matrix due to disturbed motion and is generated as in the flutter case, from Theodorsen's expressions for lift and moment and the Theodorsen's function $C(k)$ for harmonic motion. The generalized aerodynamic gust matrix $\left[Q_G \right]$ is assembled from expressions for the lift and moment induced by a sinusoidal gust given as[33]

$$L_G = -2\pi\rho U b w_g \left\{ C(k)(J_0(k) - iJ_1(k)) + iJ_1(k) \right\} e^{i\omega t} \qquad (6.4a)$$

$$M_G = b(\tfrac{1}{2} + a_h) L_G \qquad (6.4b)$$

The values obtained numerically for the frequency response function using the above method was checked with those explicit

147

expressions for response in heave and pitch for a rigid wing resting on two springs, as was the case in Chapter 2, but utilising quasi-steady aerodynamics.[35] (Details of the derivation of expressions for the transfer function are given in Appendix H).

The Indicial admittance required for the SDG analysis is obtained from Bromwich's integral using the mechanical admittance of the aircraft (see Appendix I). This procedure is illustrated in Fig. 6.1.

For the present investigation , the Dryden and Von Karman form[33,111] of $\Phi_{W_g}(\omega)$ is chosen which are respectively given by the following equations.

$$\Phi_{W_g}(\omega) = \frac{\sigma_{W_g}^2 L}{\pi U} \frac{1 + 3\left(\frac{\omega L}{U}\right)^2}{\left[1 + \left(\frac{\omega L}{U}\right)^2\right]^2} \tag{6.5}$$

$$\Phi_{W_g}(\omega) = \frac{\sigma_{W_g}^2 L}{\pi U} \frac{1 + (8/3)\left(1.339 \frac{\omega L}{U}\right)^2}{\left[1 + \left(1.339 \frac{\omega L}{U}\right)^2\right]^{11/6}} \tag{6.6}$$

Figure 6.2 shows a log-log plot of $\Phi_{W_g}(\omega)$ as a function of ω for the Von Karman spectrum. For simple illustration purposes the quantity $\sigma_{W_g}^2$ and the ratio L/U are chosen to be unity. At low values of frequency, the function asymptotically approaches a constant value $(\sigma_{W_g}^2 L/\pi U)$; at high values of frequency, the function asymptotically approaches zero as $\omega^{-5/3}$ At intermediate values of frequency, the function makes a transition between the low and high frequency asymptotes and reaches a maximum, referred to as the "knee", (see Ref.(111)). The corresponding frequency is referred to as the "knee frequency", ω_{knee} where

148

$$\omega_{knee} = 0.457(U/L) \qquad (6.7)$$

The r.m.s values of random processes w_g and y may be obtained by performing the following operations.

$$\sigma_{w_g} = \left[\int_0^\infty \Phi_{w_g}(\omega) \, d\omega \right]^{1/2} \qquad (6.8)$$

and

$$\sigma_y = \left[\int_0^\infty \Phi_y(\omega) \, d\omega \right]^{1/2} \qquad (6.9)$$

$\bar{A}$ is the normalized response quantity, defined as the ratio of the r.m.s of the output to the r.m.s of the input.

$$\bar{A} = \frac{\sigma_y}{\sigma_{w_g}} \qquad (6.10)$$

6.2.2 Statistical Discrete Gust Method

The objective of the SDG method[26] is to determine analytically the maximum, or worst-case, responses of an airplane to discrete gusts representative of atmospheric turbulence. The method is carried out in the time domain through calculation of response time histories.

The SDG method is based on the assumption that atmospheric turbulence is comprised of a family of discrete equiprobable, smoothly varying, ramp-hold gusts, whose maximum magnitudes w_g vary as indicated by the dashed envelope in Fig. 6.3 and as defined by the following equation.

$$\bar{w}_g(H) = U_0 H^k \qquad \text{for } 0 \le H \le L \qquad (6.11)$$

where U_0 is a gust-intensity parameter, H the gradient distance, K the fractional exponent and L the scale of turbulence.

Each discrete gust is defined by a transient portion (the

149

first half of a one-minus-cosine wave) followed by a steady-state portion (whose value is equal to the value of the transient portion at the end of the transient). The length of the transient is the gradient distance. The expression for one member of the family of gusts is

$$
w_g(s,H) = \begin{cases} \dfrac{\overline{w}_g(H)}{2} \left[1 - \cos\left(\dfrac{\pi s}{H}\right) \right] & \text{for } 0 \le s \ge H \\[20pt] \overline{w}_g(H) & \text{for } H < s \le L \end{cases}
\tag{6.12}
$$

where s is the distance and is related to time through the velocity U.

In the implementation of the method, an airplane is subjected to the following inputs, applied one at a time: 1) all possible single gusts, 2) all possible combinations of two gusts with all possible "spacings" (defined later) between the gusts, 3) all possible combinations of three gusts with all possible combinations of spacing between the gusts, and ...n) all possible combinations of n gusts with all possible combinations of spacing between the gusts.

In general, time histories of each airplane response quantity due to each of the (extremely large number of) inputs is examined to find the worst-case response (that is, the largest positive or negative peak value) of each response quantity. The combination of gusts that produces the worst-case response is referred to as the critical gust pattern.

Figure 6.4 contains a sketch of a combination of three gusts, labeled 1,2 and 3, in the time domain. Quantities t_1 and t_2 in the figure represent spacings in time between the completion of the transient of one gust and the start of the transient of the next. As indicated in the figure by the direction of the arrows, t_1 and t_2 are positive; however, t_1 and t_2 may also be negative. When either t_1 or t_2 is negative, the associated gusts are said to overlap one another.

For an aircraft modeled as a linear system, this extremely

large number of inputs may be reduced to a manageable number by taking advantage of superposition, as described in Ref.(112). With superposition, worst-case response to combinations of two or more gusts are determined by the responses to single gusts only.

As the number of gusts in a combination increases from 1 to n, the probability of encountering that combination in the assumed atmospheric turbulence decreases, and this decrease in probability is accounted for analytically through the use of amplitude reduction factors.[26,32] The amplitude reduction factors reduce the magnitudes of the inputs (and for a linear system, reduce the magnitudes of the responses by the same ratio), thereby bringing the response to all single gusts and the responses to all combinations of gusts to the same level of probability of occurrence.

The following equation illustrates how the overall worst case response is determined.

$$\bar{\gamma} = \max \begin{cases} p_1 \; \gamma_1 \\ p_2 \; \gamma_2 \\ p_3 \; \gamma_3 \\ p_4 \; \gamma_4 \\ \vdots \\ p_n \; \gamma_n \end{cases} \qquad (6.13)$$

The γ_i in Eq.(6.13) are the individual worst-case response to a combination of i gusts and the p_i are the corresponding amplitude reduction factors. The overall worst-case response $\bar{\gamma}$ is the worst of the worst or the maximum of the products of the sums of the γ_i and their corresponding p_i. The critical gust pattern is constructed by summing single ramp inputs associated with $\bar{\gamma}$.

In this particular investigation the SDG analysis program developed by Purcell[31] is incorporated within the current computer code FLUSTAR. This analysis is equivalent to method 1 in Ref.(111), but restricted to a maximum of two gusts. In method 1, there is restrictions concerning the characteristics of the critical gust patterns. Critical gust patterns are comprised of

151

single gusts whose magnitudes must have alternating negative and positive signs (representing alternating up and down gusts) and whose spacing in time must be positive (representing subsequent gusts that do not overlap each other).

Following the procedure given in Ref.(111) (method 1), the amplitude reduction factors are computed based on the following formula.

$$p_1 = 1$$

$$p_i = \frac{1}{0.88\sqrt{i}} \qquad \text{for } i \geq 2$$

(6.14)

Therefore in this investigation the two individual worst-case responses γ_1 and γ_2, obtained using Purcell's program,[31] are multiplied by $p_1 = 1$ and $p_2 = 0.8035$ respectively and the subsequent $\bar{\gamma}$ ascertained using equation (6.13).

6.3 Influence of Quasi-Steady and Unsteady Aerodynamics on the Response to Turbulence

6.3.1 Introduction

The PSD analysis was carried out on the representative aircraft in chapter 5, employing both quasi-steady and unsteady aerodynamics. The layout was as before and motion in this case was restricted to just rigid body motion, in line with classical dynamic stability analysis.[14,15] This investigation stems from work carried out by Huntley[113] on the spectral gust alleviation factor K, which represents the non-dimensional root mean square normal c.g. acceleration. In Ref.(113) transfer functions for a second order system were derived via Laplace transforms in displacement, velocity and acceleration for an aircraft in longitudinal motion, for which the effects of the phugoid and unsteady aerodynamics were neglected. Using an input power spectrum based on the autocorrelation form of the Dryden function, closed form solutions for quantities such as the spectral gust alleviation factor K and the root mean square angular velocity were presented.

152

6.3.2 Quasi-Steady Aerodynamics

In this current investigation it is assumed that the gust encounters the wing and tailplane at the same time, and the effects of transport lag are neglected.[114] Therefore the results provided by the analytical solution for a tailless aircraft in Ref.(113) is directly compared to results obtained for the current tailed aircraft using the present theory and assuming quasi-steady aerodynamics. A PSD analysis was carried out using three scale lengths L = 75m, 150m and 300m. Table 6.1 shows the alleviation factor K and the root mean square angular velocity obtained from expressions provided by Ref.(113) along with these quantities obtained from the present theory employing quasi-steady aerodynamics. As it can be seen the agreement between the present analysis and the analytical technique is good, well within engineering accuracy. It must be noted that the present PSD analysis is carried out within the frequency domain and can not be practically taken to infinity and is subject to errors introduced from truncation of the numerical integration of Eq.(6.5). Referring again to table 6.1 it is seen that the gust alleviation factor at the aircraft centre of gravity, K is sensitive to the scale length taken, decreasing as this parameter increases as noted in prior investigations.[31],[115] This analysis was carried out at other speeds and the agreement was found to be consistent.

6.3.3 Unsteady Aerodynamics

Next unsteady aerodynamics was introduced as the present theory in the program FLUSTAR and the respective normalized quantities are shown in Table 6.1 as well. Comparing the respective values for K from both aerodynamic models, it is seen that for both speeds the effect of unsteady aerodynamics is to reduce the alleviation factor, by 18% in this case, this is concurrent with observations carried out by Ref.(113), considering just the heaving of the aircraft, using independent unsteady aerodynamic models provided by the Wagner and Küssner functions. It is also observed from Table 6.1 that the angular velocity is increased marginally.

153

6.4 Investigation of the SDG-PSD Overlap
6.4.1 Definition of the SDG-PSD Overlap

Jones claims that under certain circumstances the SDG and PSD methods produce essentially the same numerical results,[27] and he refers to this situation as the SDG-PSD overlap. The quantitative definition of the overlap is given by the following equation.

$$\bar{\gamma} = 10.4 \; \bar{A} \qquad\qquad (6.15)$$

Where $\bar{\gamma}$ is defined by Eq.(6.13) and $\bar{A}$ is defined by Eq.(6.10). The relationship in Eq.(6.15) implies that design loads are proportional to $\bar{A}$, which is consistent with the design envelope gust loads criterion.[116]

The circumstances under which Eq.(6.15) is valid are summarized in Table 6.2. Quantities from the SDG method are found in Eq.(6.11) and Eq.(6.12) and quantities from the PSD method, in Eqs.(6.6) and (6.8). The value 1/3 for exponent k in Eq.(6.11) corresponds to the -5/3 high-frequency asymptote of the Von Karman power spectrum in Eq.(6.6). For both the SDG and PSD methods, unit gust velocities and the standard value of scale of turbulence are used. In addition, there is a requirement that the aircraft under investigation be described by linear equations and that the frequency of the short-period mode be much greater than the Knee frequency of the Von Karman power spectrum. With these conditions met, Jones claims that the 10.4 factor of Eq.(6.15) will be obtained if SDG and PSD analyses are performed for the same vehicle.

6.4.2 Response to Continuous Turbulence of the Kestrel, Ricochet and A1 Using the PSD Method

A PSD and SDG analyses was carried out on these aircraft at the same speeds considered in the prior dynamic stability analysis. The SDG method as implemented by Purcell's program requires input data in Imperial units, therefore to maintain this consistency and requirement for the SDG-PSD "overlap" investigation, the input data for the whole analysis were converted into Imperial units. Hence all response quantities including those

results from the PSD method are in Imperial units. The effects of downwash and transport lag are neglected in this investigation. The frequency response functions for the considered response quantities are obtained to a sinusoidal input gust of amplitude 1 ft/sec.

6.4.2.1 The Kestrel

A PSD analysis was first carried out on the Kestrel with four elastic modes in addition to the two rigid body modes and the aerodynamic parameters were kept the same as in prior investigations. For the Kestrel as with the other aircraft, 700 points were found sufficient in the integration of Eq.(6.8) to adequately cover the influence of the elastic modes.

Representative results for the aircraft frequency response function and response power spectrum are shown for the lowest speed, in this case 30 m/s, representing a typical cruise speed. Figures 6.5 and 6.6 shows the squared modulus of the frequency response function for vertical acceleration and angular acceleration respectively, at the three spanwise stations, namely the wing tip, mid-span and wing root. Referring to Fig. 6.5 it is seen that the peak responses in vertical acceleration closely coincide with the natural frequencies of the Kestrel, including the largest contribution at the wing tip from wing torsion. The torsional mode is excited as the shear centre is offset from the wing aerodynamic centre. The size of these peaks are functions of the acceleration responses of the individual modes and their respective position within the frequency spectrum. Although the contribution to vertical acceleration from the torsional mode may be small, the resulting moduli, which are multiplied by ω^2, will be large. Therefore the higher up in the frequency spectrum the mode is, the higher the possible frequency response. It must also be noted that the finite element model used here for the Kestrel includes the effects of wing structural sweep, thus introducing small amounts of coupled bending from the torsional mode.

Further inboard the magnitude of the response function decreases towards the root, which in this case is coincident with the aircraft c.g. The influence of the torsional mode at the c.g. has significantly decreased and is dominated by the bending modes.

155

The absence of any peaks associated with rigid body modes, seems to confirm the initial conclusions of the flutter analysis carried out on the Kestrel, that this instability is dominated by the elastic modes.

Referring to Fig. 6.6 the dominant contribution to the angular acceleration appears to come from the wing torsional mode, with a small contribution from the third elastic mode which is tailplane bending with coupled wing torsion/bending. Again further inboard the magnitudes decrease, until at the c.g. the acceleration is solely driven from the wing torsional mode.

The frequency response functions are then multiplied with the input power spectrum, of the Von Karman form, taking the mean square of the gust velocity $\sigma_{w_g}^2$ as 1 (ft/sec)^2, in accordance with the criterion set for the SDG-PSD "overlap" case in Table 6.2. Figures 6.7 and 6.8 show the response output spectrum for both vertical and angular acceleration respectively. It can be seen from Figure 6.7 that although there is a large torsional contribution to the response function its resulting influence in the output power spectrum for vertical acceleration is negligible. It is the elastic modes in bending which are seen to contribute the most, in particular the first bending at the wing tip. Further inboard the lower frequency modes, including perhaps the rigid body modes begin to appear, although much smaller compared to the wing tip values. The high contribution of the lower frequency modes can be explained from the the nature of the input spectrum. It can be seen from Fig. 6.2 that the spectrum attains its highest values at low frequencies and then goes asymptotically to zero for higher frequencies, thus magnifying the influence of the lower order modes.

As suggested from Fig. 6.6 the dominance of the torsional modes is observed, in the output power spectrum for angular acceleration in Figure 6.8. Although at the c.g. there again appears a small rigid body contribution.

From these output power spectra the r.m.s vertical and angular accelerations are obtained, and are normalized with respect to the r.m.s input gust velocity σ_{w_g} to give $\bar{A}$, as defined

156

by Eq.(6.10). The spanwise distribution of $\bar{A}$ for both vertical and angular acceleration are shown in Fig. 6.9 and 6.10 respectively at 30 m/s and 60 m/s along with quantities assuming a rigid aircraft. The trends suggested from these figures, appear not to differ that much with speed except in magnitude. It is seen that the introduction of flexibility predictably increases the outboard response in both vertical and angular acceleration, especially close to the wing tip. Referring to Fig. 6.9 the inclusion of flexibility is demonstrated on the vertical acceleration, at the tip, the ratio of flexible acceleration to rigid acceleration is 3.4 at 30 m/s and 5 at 60 m/s. Referring to the angular acceleration encountered in Fig. 6.10 the respective ratios at the two speeds considered are 237 and 326. The response is greater at the latter speed as the Kestrel is close to its flutter speed. It can be seen that effect of vertical acceleration will be to increase the local bending moment and shear stresses along the wing, whereas the angular acceleration will increase the torsional moments encountered.

6.4.2.2 The Ricochet

In the absence of a tail the Ricochet is expected to be much more sensitive to atmospheric turbulence, in particular the role of its rigid body modes will be significant. The Ricochet was allowed the two rigid body freedoms in addition to the four elastic modes. Aerodynamic parameters were maintained from the earlier dynamic stability studies carried out in Chapter 4. As before the cases for a speed of 25 m/s and 40 m/s were selected. Representative results are shown for 25 m/s. Figure 6.11 and 6.12 show the frequency response function for both vertical and angular acceleration, at the tip, mid span and root locations.

Referring to Figure 6.11 the peak responses due to the elastic modes are clearly defined. The largest contribution at the wing tip coming from the bending modes. However the effect of wing torsion is negligible at this position. It is seen that as one moves further inboard the contribution from the bending modes decays, also the rigid body or s.p.p.o mode becomes more pronounced, such that at the root it begins to coalesce with the wing first bending mode, (this as already mentioned is

characterised as the mode of flutter for the Ricochet). As observed with the Kestrel the modulus of the frequency response at the wing tip is similarly about 10 times the magnitude at the root, but the effect of the torsional mode (elastic) is less pronounced and the response is dominated by the bending modes and a noticeable input from rigid body motion.

Figure 6.12 high lights the dominance of the wing torsional mode in the angular acceleration response of the Ricochet. Once at the root, a small contribution from the bending modes is observed. This is perhaps due the to swept nature of the Ricochet, where wing bending is providing additional pitching moments at the root.

The subsequent output power spectrum for the vertical and angular acceleration quantities are shown in Fig. 6.13 and 6.14 respectively for 25 m/s. From Fig. 6.13 it is seen that at the wing tip the response is dominated by the first and second wing bending modes. As one progresses further inboard their influence diminishes and the response is taken up by the s.p.p.o mode, which provides a constant contribution along the span of the wing. From Fig. 6.14 the torsional modes is seen to dominate the outboard angular acceleration response. This component diminishes towards the root. Until at the root the contribution from the first bending mode, seen in Fig. 6.13, dominates the response at this position.

Figures 6.15 and 6.16 show the normalized vertical and angular response quantities $\bar{A}$ respectively for the flexible and rigid case at 25 m/s and 40 m/s. Referring to Fig. 6.15 and the normalized vertical acceleration, in addition to the effects of flexibility their is also a noticeable rigid body contribution to the increase in response. At 25 m/s the ratio of flexible aircraft acceleration to rigid aircraft acceleration at the tip is 3.3 and 1.2 at the root. As the Ricochet approaches the flutter speed the role of the rigid body freedoms becomes apparent, such that at 40 m/s, the ratios at the tip and root are now 2.1 and 3.3 respectively. Considering angular acceleration in Fig. 6.16, the respective ratios at the same locations are 108 and 11 at 30 m/s, 131 and 12 at 40 m/s.

6.4.2.3 The Cranfield A1

In Chapters 3 and 4 it was established that the A1 was essentially a stiff aircraft. As in the previous studies the speeds selected for the current response analysis were 41.1 m/s and 61.7 m/s with atmospheric density taken as before, but all the quantities converted to imperial units as required. However representative data is presented for 41.1 m/s, considered as a typical cruise speed for the A1. Analysis was carried out with two rigid body and four elastic modes. Aerodynamic parameters were the same as used in the dynamic stability analysis in Chapter 4.

Figure 6.17 shows the frequency response function in vertical acceleration for the A1. The frequency is extended in this case as the A1 is a stiffer aircraft and the frequencies of the elastic modes that much higher. At the wing tip, in the frequency range presented the first three elastic modes are observed, but there is apparently no contribution from the wing torsional mode, as observed for the Kestrel and the Ricochet suggesting the high torsional stiffness of the A1 wing. The dominate peak appears to be that associated with third elastic mode, which is primarily a wing bending mode with significant wing torsional displacements present. The peak is particularly dominant towards the flexible part of the aircraft (i.e. towards the tip). As expected further inboard the wing the overall modulus of the frequency response function decreases. At the wing root (which is close to the aircraft c.g.), the highest peak is due to the second elastic mode which involved significant tailplane bending with some amount of coupling between the wing-bending and wing-torsional displacements (see Fig. 3.19). This mode has earlier been characterised by large movement of the root. Unlike the rest of the other modes. This explains why it is prevalent in the frequency response function at the root. It is also observed in Fig. 6.17 that at the lower end of the frequency band, the peak in the frequency response arising out from the short-period mode is particularly high.

Figure 6.18 shows the frequency response function in angular acceleration. Here the overall magnitude for this quantity is smaller compared to those encountered for the Kestrel and Ricochet, which are far more structurally flexible. At the tip the

dominant peak is again associated with the third elastic mode which is primarily a wing bending mode with significant coupling present between the wing-bending and wing-torsional displacements (see Fig. 3.19). As the Al wing is swept (the angle of sweep is around 10^{0}) the wing bending in this mode is contributing to the frequency response function corresponding to the angular acceleration of the wing. However as the this wing has a high torsional stiffness the contribution from high frequency torsional mode is seen to be negligible in comparison. Towards the root the response is seen to decrease , until the contribution from the third elastic mode becomes apparent as was the case with the normal acceleration.

Considering the resulting power output spectrum for the vertical acceleration in Fig. 6.19 the spectra are similar to those shown in Fig. 6.17 for the frequency response function. However inaddition there is seen a low frequency contribution from the s.p.p.o mode, which is found to prevail and dominate the root location.

Figure 6.20 represents the output power spectrum for angular acceleration. This again shows the same trend and the relative dominance of the elastic modes reflected by the frequency response function in Fig. 6.20. Also there appears to be a contribution from the s.p.p.o mode.

The spanwise distribution of normalized vertical and angular accelerations are respectively shown in Fig. 6.21 and Fig. 6.22 for both the rigid and flexible aircraft. It is seen from these figures that the introduction of flexibility increases the outboard response, especially close to the wing tip as expected. At the wing tip the ratio of the normal accelerations obtained for the flexible and the rigid aircraft is found to be 4.2 and 4.6 for aircraft speeds at 41.1 m/s and 61.7 m/s respectively. The corresponding ratio for angular acceleration at the wing tip was found to be 3.9 and 5.1 respectively at the above two speeds.

However comparing the angular accelerations, with those encountered on the Kestrel and Ricochet, it is seen that the Al response is much smaller. In particular at the wing tip and close to the flutter speed, the angular accelerations encountered on the

Kestrel and Ricochet are some 45 and 25 times higher, respectively. This is because of the high torsional stiffness of the A1, which is on average about 19 times that of the Kestrel and 9 times that of the Ricochet.

6.4.3 SDG-PSD Overlap

6.4.3.1 Introduction

The only thorough investigation of the SDG-PSD overlap that the author can ascertain was that carried out by Perry et al[111] at NASA, Langley Research Centre. In this reference, symmetric rigid body analyses and symmetric fully flexible analyses were performed using linear equations of motion. Two forms of the SDG method were implemented, referred to as method 1, mentioned above and method 2. In Method 2, there are no restrictions concerning the characteristics of the critical gust patterns. Critical gust patterns are comprised of single gusts whose magnitude may be negative or positive (representing either up or down gusts) in any order and whose spacing in time may be negative or positive (representing subsequent gusts that either do or do not overlap each other). Method 2 is a more accurate form of the SDG method and is reserved for the more complicated fully flexible analyses in Ref.(111)

This investigation[111] concluded that "an SDG-PSD overlap does appear to exist. However, this overlap appears to be characterized, not by a 10.4 factor, but rather by a "10.4 plus or minus approximately five percent factor", when rigid body equations are involved, and by a "10.4 plus or minus approximately ten percent factor" when fully flexible equations are involved".

Using Purcell's program the current response analysis was extended to carry out also a SDG analysis. This SDG method in this case, is equivalent to method 1 for a maximum of two gusts, to ascertain the SDG-PSD overlap for the Kestrel, Ricochet and A1. The indicial admittances, obtained for each aircraft from Bromwich's integral[117] were used as input into Purcell's program from which the maximum responses were evaluated and compared with those from the prior PSD analysis. An alternative technique for obtaining the indicial admittance is that provided by Mitchell[118]

6.4.3.2 Rigid Body analyses

The rigid-body analyses was carried out by suppressing the elastic degrees of freedom and relying on the two rigid body modes of heave and pitch, provided in the finite element model, by the light springs at the aircraft c.g. For this investigation strip theory was used first employing quasi-steady aerodynamics and then later the effects of full unsteady aerodynamics were introduced. The employment of quasi-steady aerodynamics, as shown in Chapter 4, is equivalent to the classical approach of evaluating the dynamic stability. Response quantities for these analyses are angular velocity (or pitch rate) and vertical acceleration at the wing root, and vehicle centre of gravity wherever possible. Referring to Table 6.3 it is seen that the ratio $\omega_{sp}/\omega_{knee}$ for each aircraft considered, is sufficiently large for the present investigation. Although the s.p.p.o frequencies quoted are based on quasi-steady aerodynamics, the introduction of unsteady aerodynamics for harmonic motion, (as in this case) will be small, especially considering the low frequency nature of the short period mode.

6.4.3.3 Flexible Analyses

For these analyses the configurations and elastic modes allowed, for each aircraft considered, were those used for the PSD analyses. The full effects of unsteady aerodynamics were implemented via strip theory and the Theodorsen's expressions for lift and moment. Response quantities for these analyses are pitch rate, angular acceleration and vertical acceleration at three spanwise locations, namely the tip, mid-span and root. For this investigation it was thought best to concentrate on aircraft for which practical and realistic structural and aerodynamic details are available, so the fictitious aircraft of aspect ratio 12 was omitted in these analyses.

6.4.3.4 Rigid Body Results

For the PSD method over 700 points were used in the numerical integration of Eq. (6.8). For the SDG method, the aircraft were subjected to critical gust patterns comprised of either one (n=1) or two (n=2) single gusts, as presented by Purcell[31] The SDG method employed here is equivalent to method 1 in Ref.(111).

Table 6.4 displays the results of the analyses using

quasi-steady aerodynamics for the Kestrel, Ricochet and A1 for a random selection of speeds. All ratios are above the 10.4 factor the largest discrepancy being 12.19 (17.2% above 10.4) and the lowest is 8.95 (13.9% below 10.4). The mean value of the ratios is 10.31 with a standard deviation of 1.072.

Next the effect of unsteady aerodynamics is shown in Table 6.5. Here the ratios fall between 12.03 (15.7% above 10.4) and 9.70 (6.7% below 10.4). The subsequent mean is found to be 10.65 with a standard deviation of 0.791. It is noted for the aircraft considered that the effect of unsteady aerodynamics, is to reduce the vertical acceleration, and in particular the spectral gust alleviation factor K for the Kestrel, as observed by Huntley.[113] Also the pitch rate increases in the case of the Kestrel and A1. This is not observed on the Ricochet, as the pitch rate for this aircraft is dependent primarily on the aerodynamic damping of its wings, which are subject to the general reduction in vertical acceleration.

6.4.3.5 Flexible Results

Before concentrating on the spanwise distribution of the response quantities for the flexible case, the quantities so far shown in Tables 6.4 and 6.5 are calculated for the rigid aircraft. Table 6.6 shows the same response quantities for the flexible aircraft, employing unsteady aerodynamics. As noted earlier the introduction of flexibility has increased the vertical acceleration for both the Ricochet and A1, but the c.g. acceleration remains virtually unchanged for the Kestrel. Also the introduction of flexibility and unsteady aerodynamics increases further the angular pitch rate encountered by the Kestrel and A1.

The spanwise distributions of vertical and angular accelerations obtained, using the PSD and SDG methods were next evaluated and are displayed in Tables 6.7, 6.8 and 6.9 for the Kestrel, Ricochet and A1 respectively.

Considering overlap ratios from these tables, in addition to the angular velocity quantities from Table 6.6, we see a larger band of ratios about the 10.4 factor. The maximum value is 12.54 (in the case of the Ricochet which is 20.5% above 10.4) and a minimum of 7.20 (for the A1 which is 30.7% below 10.4). However

the mean is found to be 10.45 with a standard deviation of 1.455. Although the mean is very close to the expected factor the large value of the standard deviation must be noted, this large variation in results could due to the inadequacies of the current SDG method (method 1) in coping with the added complexity of flexibility.

A summary of the above comparison is shown in Table 6.10. There is a certain amount of consistency about the results for the mean factor in the rigid body case using both quasi-steady and unsteady aerodynamics. It is noted that the response in pitch is smaller in the case of the Kestrel and the Ricochet, thus in the SDG analysis it was more difficult to obtain a worst case response, this is reflected to a certain extent in the standard deviation results. As the response in pitch for the A1 and the representative aircraft in the rigid analyses are much higher, the results appear more encouraging. Thus for the rigid body case, considered here, the suggested overlap factor is between 10.31 and 10.65.

	Spectral Gust alleviation Factor K and Mean square response of angular velocity $\dfrac{\sigma_{\dot\alpha}}{\sigma_{w_g}}$ (rad/s/m/s)		
Scale Length L (m)	Quasi-steady Aerodynamics		Unsteady Aerodynamics
	Ref.113	FLUSTAR	FLUSTAR
75	0.3566	0.3400	0.2768
	0.04332	0.04406	0.04605
150	0.2548	0.2428	0.1978
	0.03137	0.03196	0.03316
300	0.1811	0.1723	0.1402
	0.02244	0.02281	0.02356

Table 6.1   Response quantities using quasi-steady aerodynamics and unsteady aerodynamics

165

SDG quantities (Refer to Eqs.(6.9) and (6.10))	PSD quantities (Refer to Eqs.(6.1) and (6.6))
$K = 1/3$	Von Karman form of $\Phi_{w_g}(\omega)$
$U_0 = 1$ ft/sec	$\sigma_{w_g} = 1$ ft/sec
$L = 2500$ ft	$L = 2500$ ft
————	$\omega_{sp} \gg \omega_{knee}$

Table 6.2 Conditions for the statistical discrete gust and power spectral density overlap

Aircraft	Speed m/s (ft/sec)	Short period frequency, ω_{sp} (rad/sec)	$\dfrac{\omega_{sp}}{\omega_{knee}}$
Kestrel	30 (98.43)	1.66	92.3
Ricochet	40 (131.23)	2.64	50.3
Cranfield A1	61.7 (202.36)	5.28	66.5
AR 12	30 (98.43)	5.38	293.5

Table 6.3 Example aircraft for rigid body analysis

Aircraft	Response quantity (units)	PSD result $\overline{A}$ (units)/fps	SDG result $\overline{\gamma}$ (units)	$\dfrac{\overline{\gamma}}{\overline{A}}$
Kestrel 30 m/s	Pitch rate, $\dot{\alpha}$ (rad/s)	0.001157	0.01410	12.19
	c.g vert. accel., Δn (g's)	0.02365	0.2368	10.01
Ricochet 40 m/s	Pitch rate, $\dot{\alpha}$ (rad/s)	0.002473	0.02835	11.45
	vert. accel., $\ddot{h}$ (g's)	0.03401	0.3178	9.34
A1 61.68 m/s	Pitch rate, $\dot{\alpha}$ (rad/s)	0.005661	0.06131	10.18
	vert. accel., $\ddot{h}$ (g's)	0.02229	0.2187	9.81
AR12 30 m/s	Pitch rate, $\dot{\alpha}$ (rad/s)	0.007116	0.07521	10.57
	c.g vert. accel., Δn (g's)	0.01229	0.1100	8.95

Table 6.4   Summary of statistical discrete gust and power spectral density results for rigid body analysis using quasi-steady aerodynamics

Aircraft	Response quantity (units)	PSD result $\overline{A}$ (units)/fps	SDG result $\overline{\gamma}$ (units)	$\dfrac{\overline{\gamma}}{\overline{A}}$
Kestrel 30 m/s	Pitch rate, $\dot{\alpha}$ (rad/s)	0.001254	0.01509	12.03
	c.g vert. accel., Δn (g's)	0.02012	0.1952	9.70
Ricochet 40 m/s	Pitch rate, $\dot{\alpha}$ (rad/s)	0.002329	0.02677	11.48
	vert. accel., $\ddot{h}$ (g's)	0.02858	0.3039	10.63
A1 61.68 m/s	Pitch rate, $\dot{\alpha}$ (rad/s)	0.005883	0.06111	10.39
	vert. accel., $\ddot{h}$ (g's)	0.01865	0.1998	10.71
AR12 30 m/s	Pitch rate, $\dot{\alpha}$ (rad/s)	0.007375	0.07743	10.50
	c.g vert. accel., Δn (g's)	0.009483	0.09255	9.76

Table 6.5 Summary of statistical discrete gust and power spectral density results for rigid body analysis using unsteady aerodynamics

168

Aircraft	Response quantity (units)	PSD result $\overline{A}$ (units)/fps	SDG result $\overline{\gamma}$ (units)	$\dfrac{\overline{\gamma}}{\overline{A}}$
Kestrel 30 m/s	Pitch rate, $\dot{\alpha}$ (rad/s)	0.01592	0.0193	12.15
	c.g vert. accel., Δn (g's)	0.02086	0.2400	11.51
Ricochet 40 m/s	Pitch rate, $\dot{\alpha}$ (rad/s)	0.02007	0.2122	10.58
	vert. accel., $\ddot{h}$ (g's)	0.0648	0.7176	11.07
A1 61.68 m/s	Pitch rate, $\dot{\alpha}$ (rad/s)	0.005901	0.06296	10.67
	vert. accel., $\ddot{h}$ (g's)	0.01950	0.2160	11.07

Table 6.6   Summary of statistical discrete gust and power spectral density results for flexible and unsteady aerodynamic analysis

169

Spanwise location	Response quantity (units)	PSD result $\overline{A}$ (units)/fps	SDG result $\overline{\gamma}$ (units)	$\dfrac{\overline{\gamma}}{\overline{A}}$
Tip	Ang. accel., $\ddot{\alpha}$ (rad/s^2)	1.5755	17.33	10.99
	vert. accel., $\ddot{h}$ (g's)	0.06784	0.7372	10.87
Mid-span	Ang. accel., $\ddot{\alpha}$ (rad/s^2)	0.8698	9.817	11.29
	vert. accel., $\ddot{h}$ (g's)	0.02324	0.2361	10.16
Root	Ang. accel., $\ddot{\alpha}$ (rad/s^2)	0.04666	0.5733	12.29
	c.g vert. accel., Δn (g's)	0.02086	0.2400	11.51

Table 6.7   Summary of statistical discrete gust and power spectral density results for flexible Kestrel at U = 30 m/s

Spanwise location	Response quantity (units)	PSD result $\overline{A}$ (units)/fps	SDG result $\overline{\gamma}$ (units)	$\dfrac{\overline{\gamma}}{\overline{A}}$
Tip	Ang. accel., $\ddot{\alpha}$ (rad/s^2)	2.3509	26.05	11.08
	vert. accel., $\ddot{h}$ (g's)	0.1019	1.279	12.54
Mid-span	Ang. accel., $\ddot{\alpha}$ (rad/s^2)	1.379	14.86	10.77
	vert. accel., $\ddot{h}$ (g's)	0.06489	0.7124	10.98
Root	Ang. accel., $\ddot{\alpha}$ (rad/s^2)	0.2092	2.2405	10.71
	vert. accel., $\ddot{h}$ (g's)	0.06482	0.7176	11.07

Table 6.8   Summary of statistical discrete gust and power spectral density for flexible Ricochet at U = 40 m/s

Spanwise location	Response quantity (units)	PSD result $\overline{A}$ (units)/fps	SDG result $\overline{\gamma}$ (units)	$\dfrac{\overline{\gamma}}{\overline{A}}$
Tip	Ang. accel., $\ddot{\alpha}$ (rad/s^2)	0.1797	1.478	8.22
	vert. accel., $\ddot{h}$ (g's)	0.09179	0.7912	8.62
Mid-span	Ang. accel., $\ddot{\alpha}$ (rad/s^2)	0.09388	0.7676	8.18
	vert. accel., $\ddot{h}$ (g's)	0.02930	0.2109	7.20
Root	Ang. accel., $\ddot{\alpha}$ (rad/s^2)	0.05801	0.4959	8.55
	vert. accel., $\ddot{h}$ (g's)	0.01949	0.2159	11.08

Table 6.9   Summary of statistical discrete gust and power spectral density for flexible A1 at U = 61.7 m/s

Type of analysis	$\dfrac{\overline{\dot{\gamma}}}{\overline{A}}$ Statistics	
	Mean	Standard deviation
Rigid-body (quasi-steady aerodynamics)	10.31	1.072
Rigid-body (Unsteady aerodynamics)	10.65	0.791
Flexibility	10.45	1.455

Table 6.10 Summary of statistical discrete gust-power spectral density comparisons
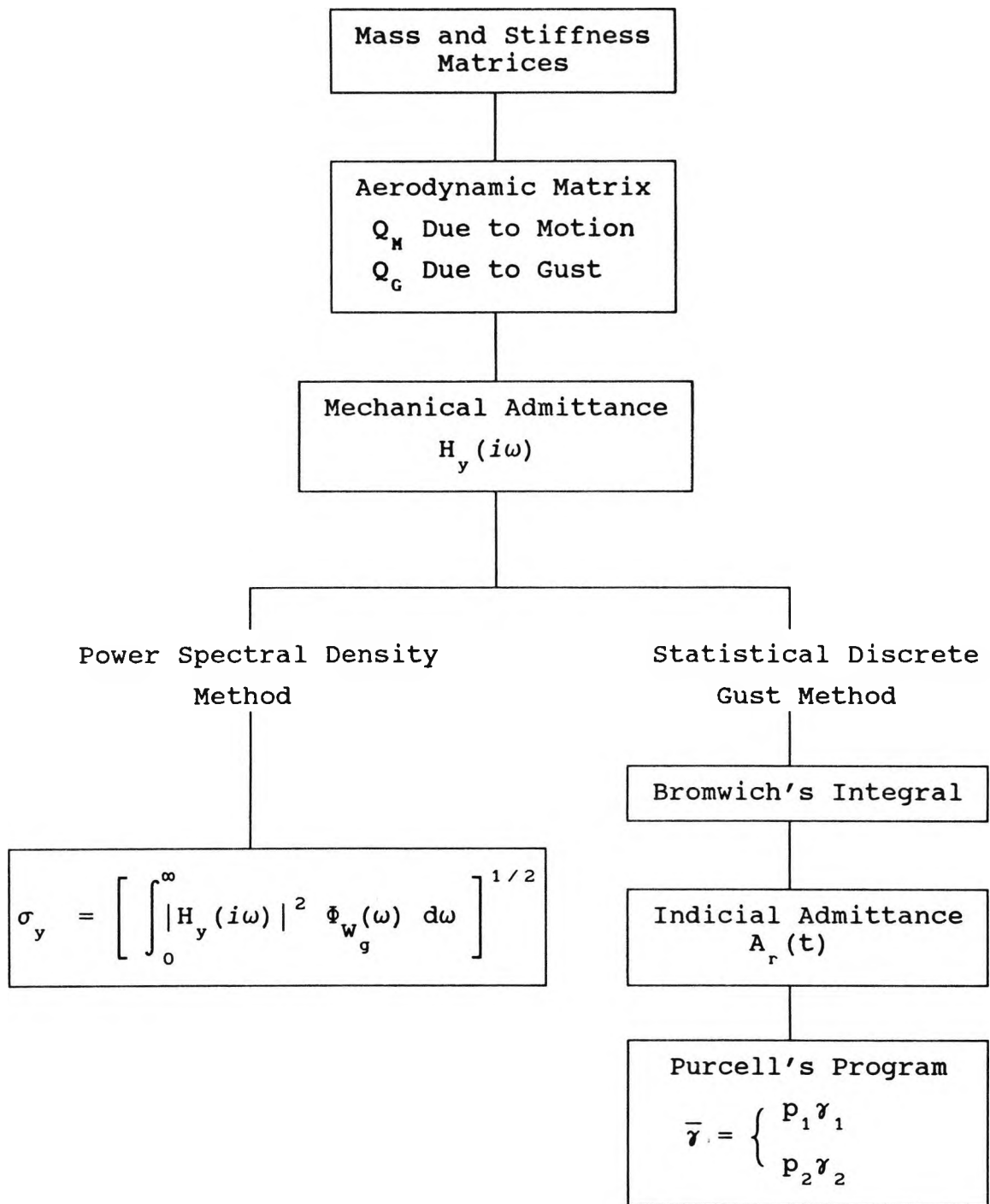
Fig. 6.1   Formulation of response analysis
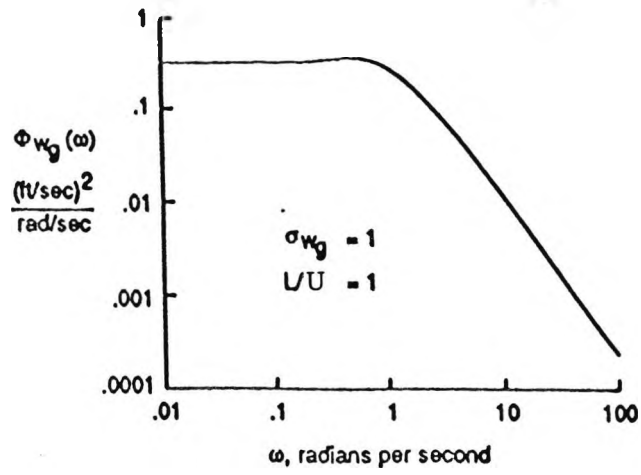
Fig. 6.2 Von karman power spectral density (PSD) for atmospheric turbulence
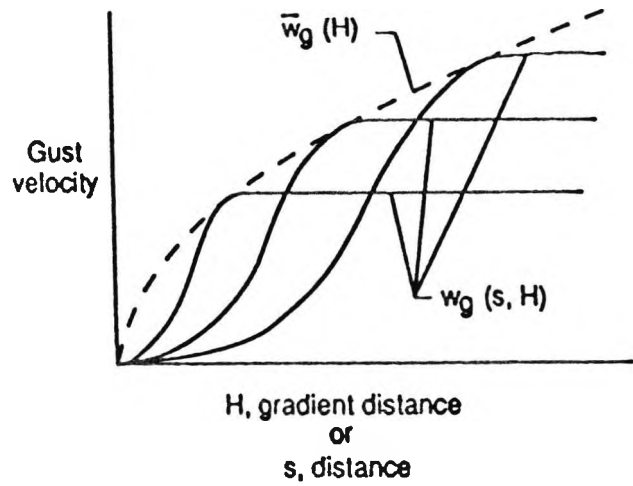
Fig. 6.3 Family of equi-probable smoothly varying ramp-hold gusts for SDG method
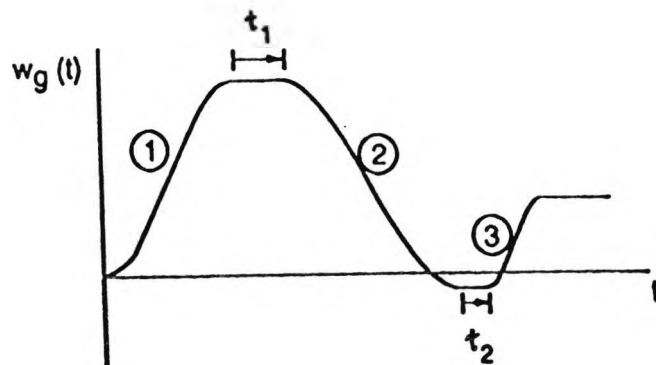
Fig. 6.4 Combination of three single gusts
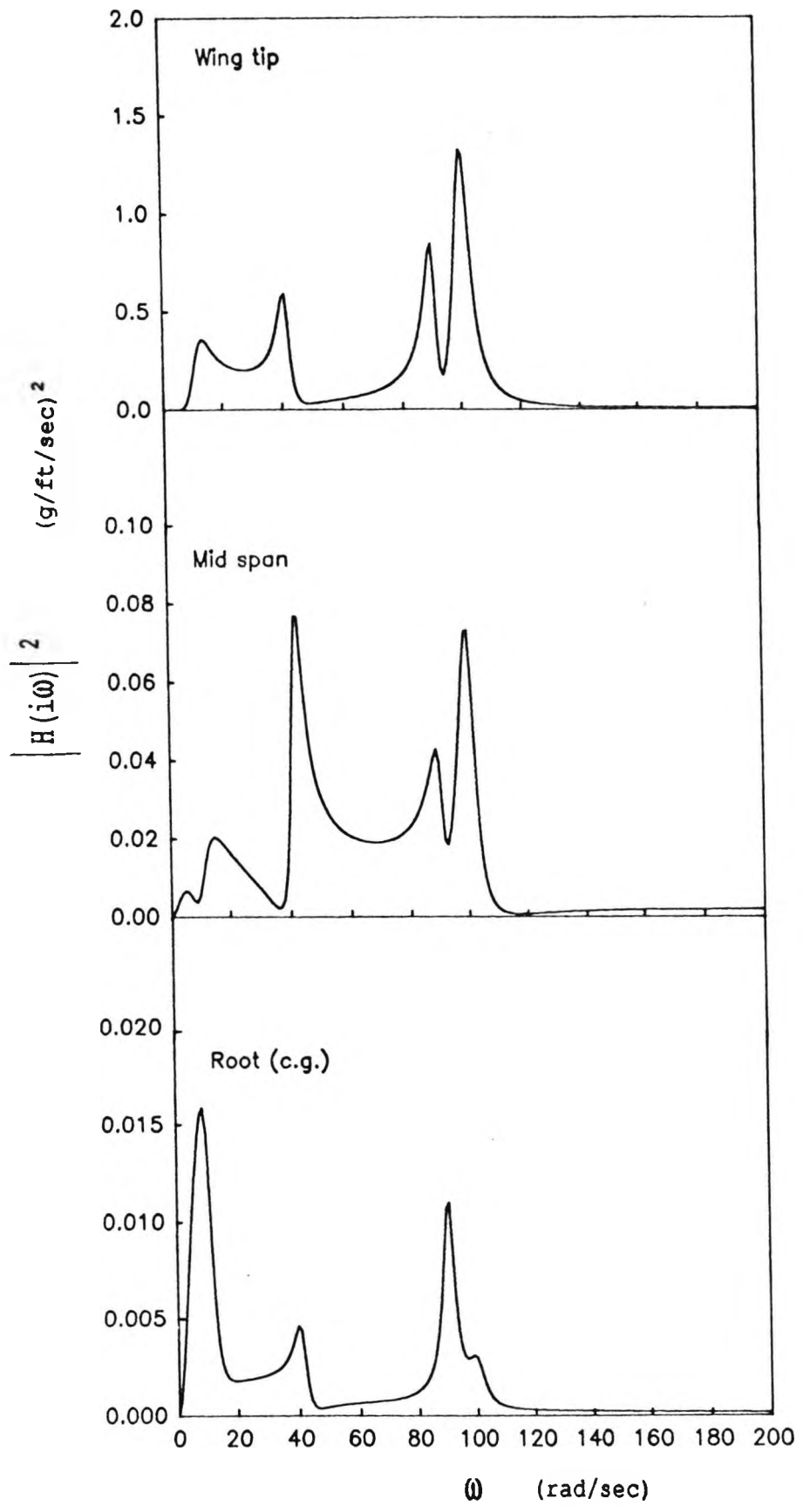
Fig. 6.5   Frequency response function in vertical
acceleration for Kestrel
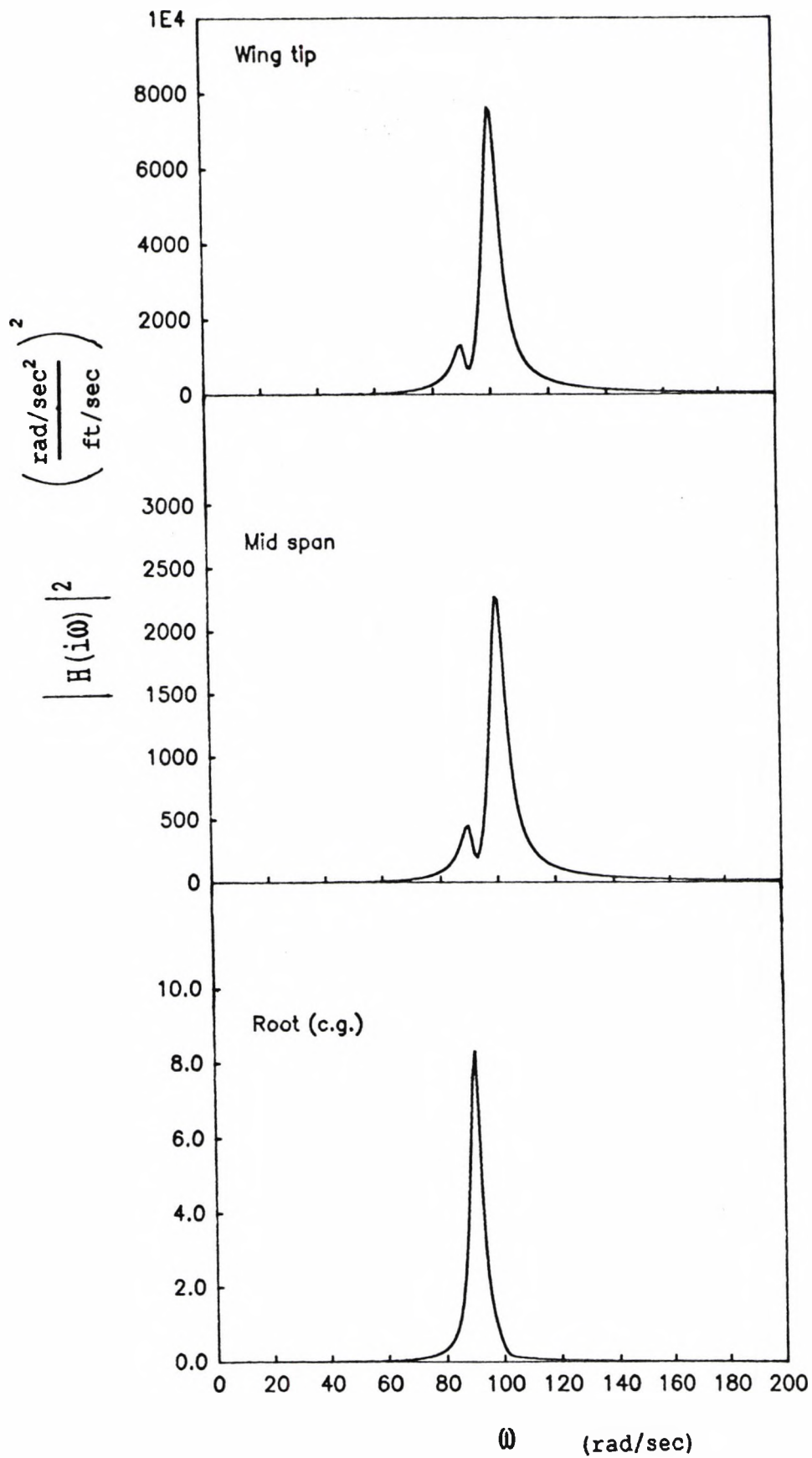
Fig. 6.6 Frequency response function in angular
acceleration for Kestrel
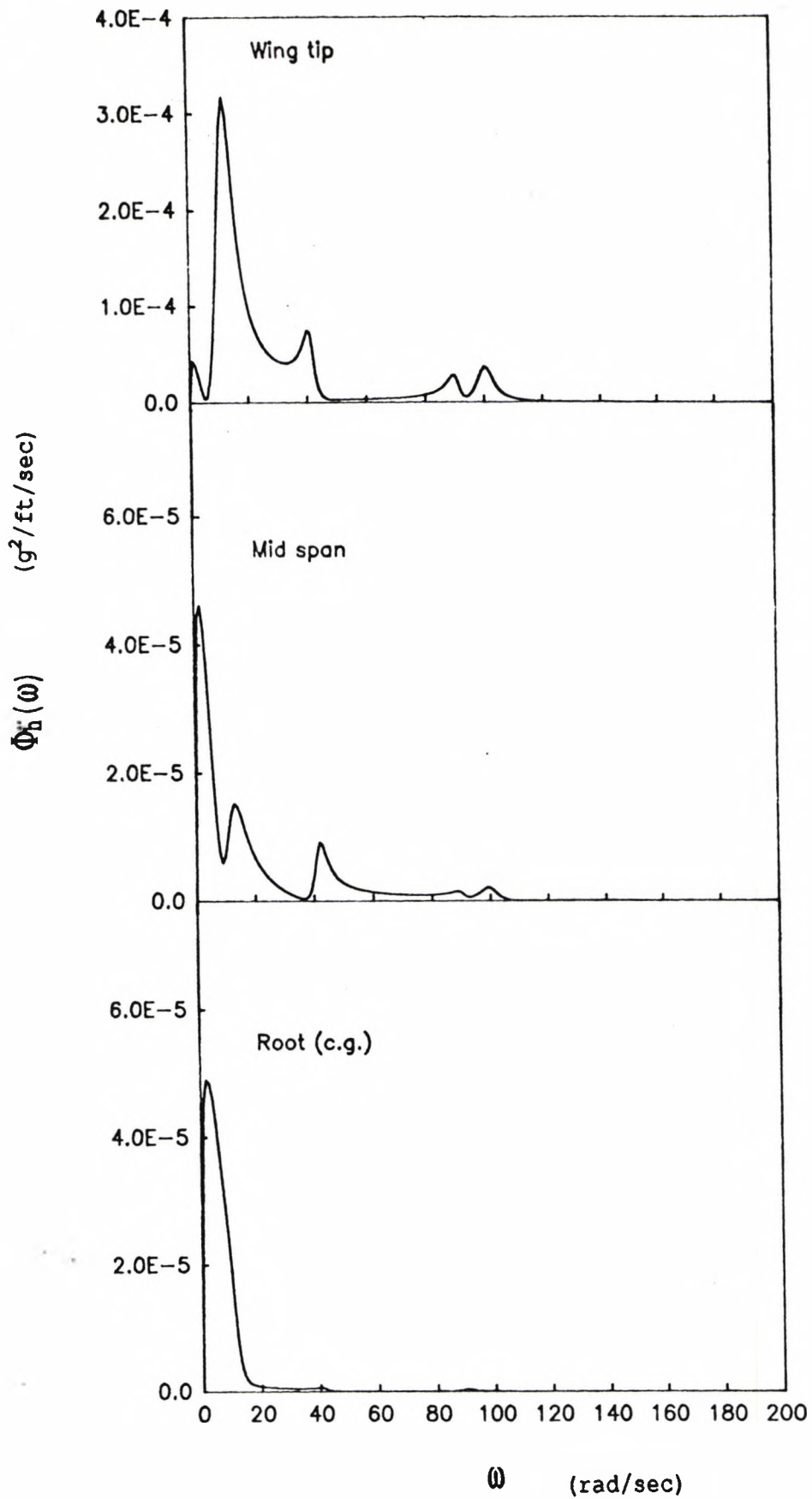
Fig. 6.7   PSD of vertical acceleration for Kestrel
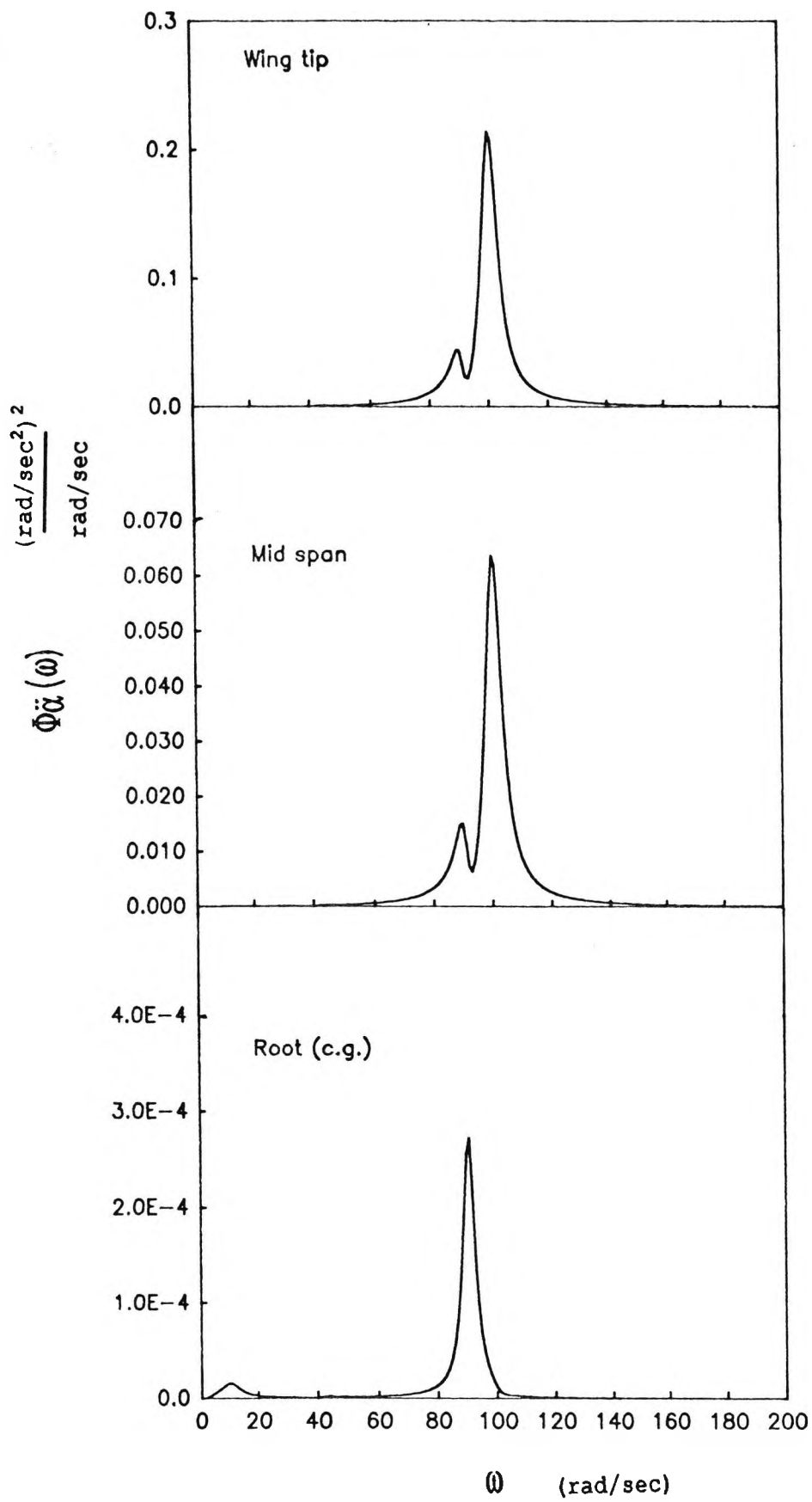
Fig. 6.8 PSD of angular acceleration for Kestrel
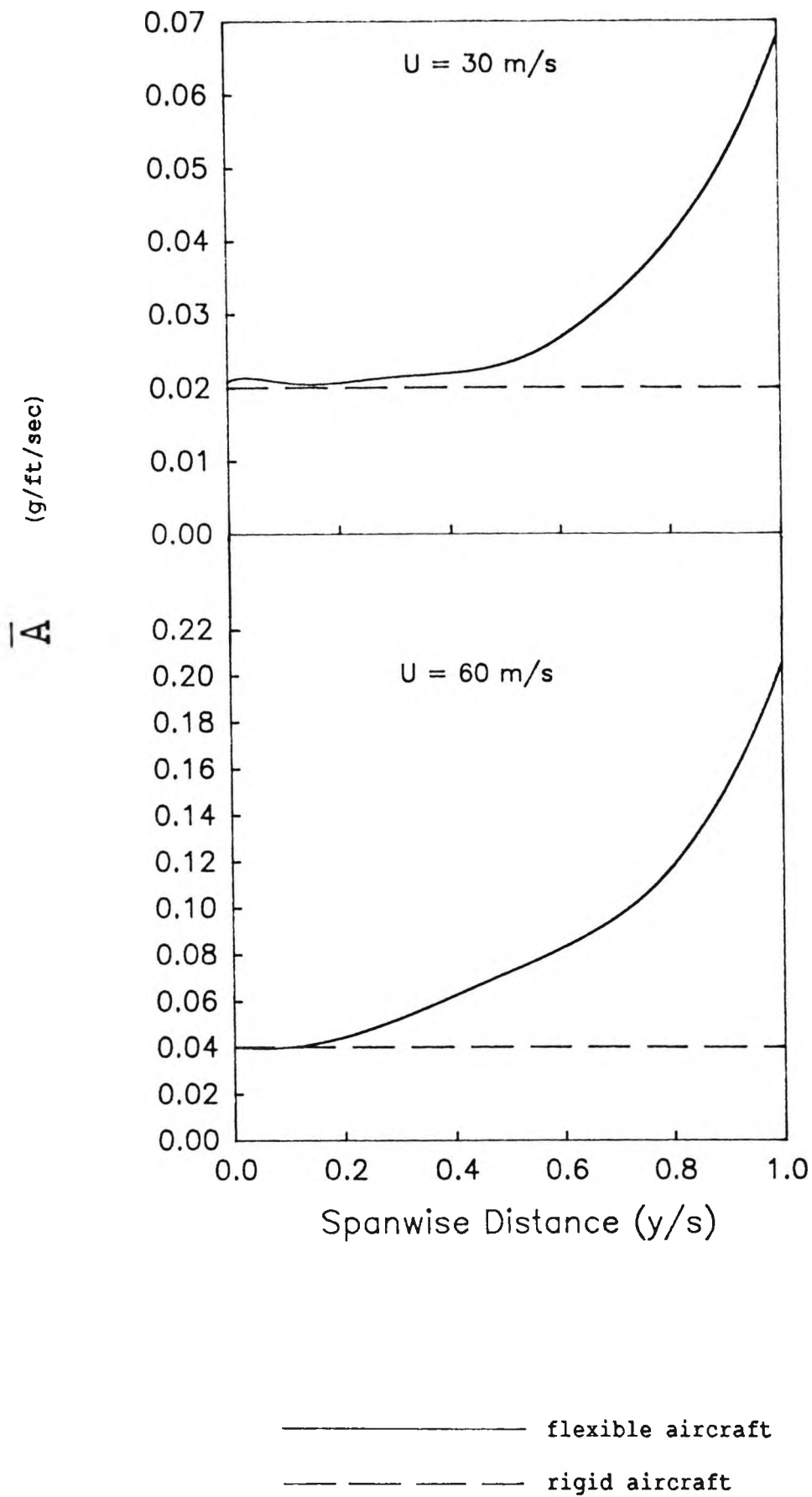
Fig. 6.9   Spanwise distribution of normalised vertical
acceleration for Kestrel
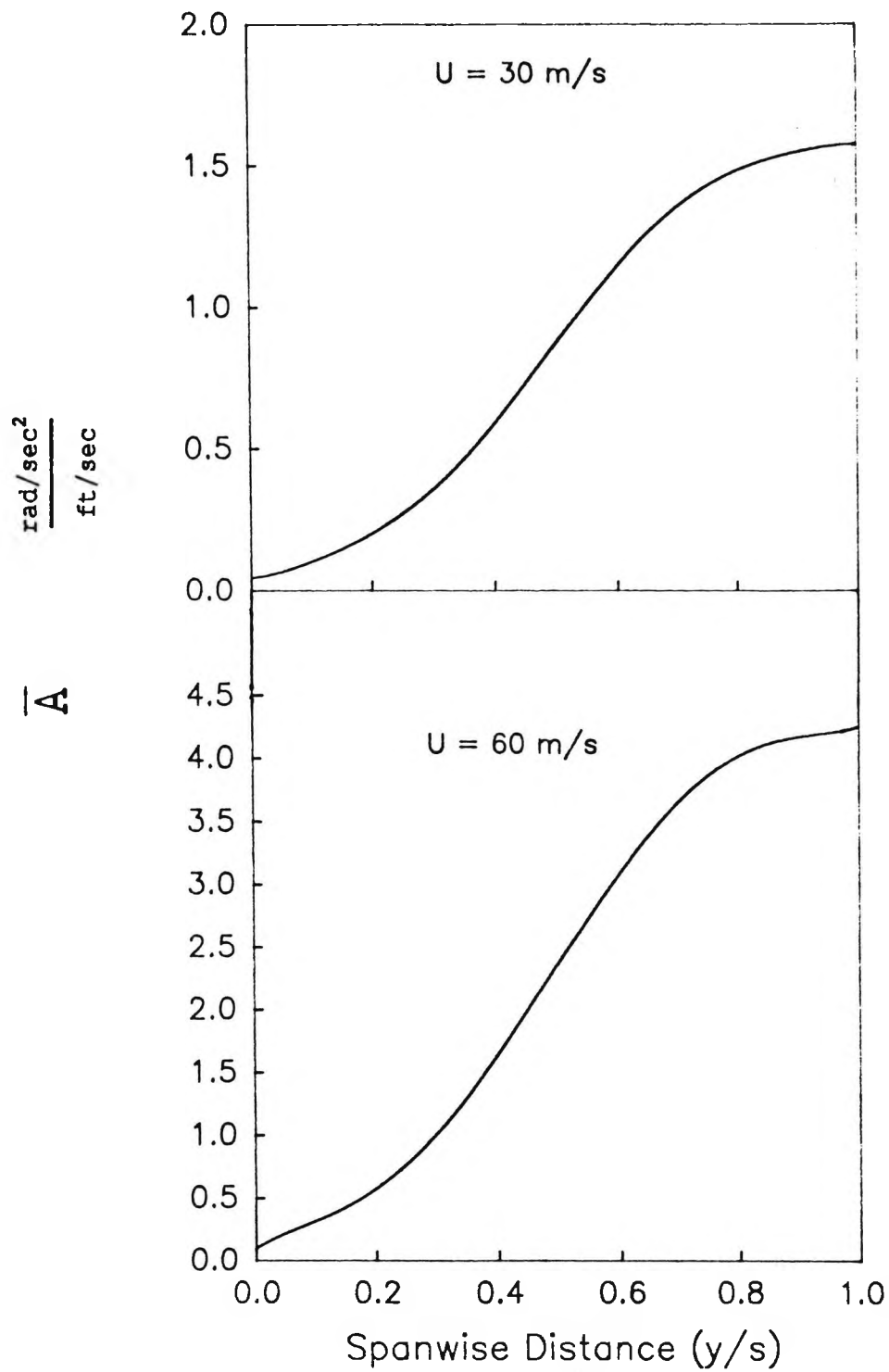
Fig. 6.10   Spanwise distribution of normalised angular
acceleration for Kestrel
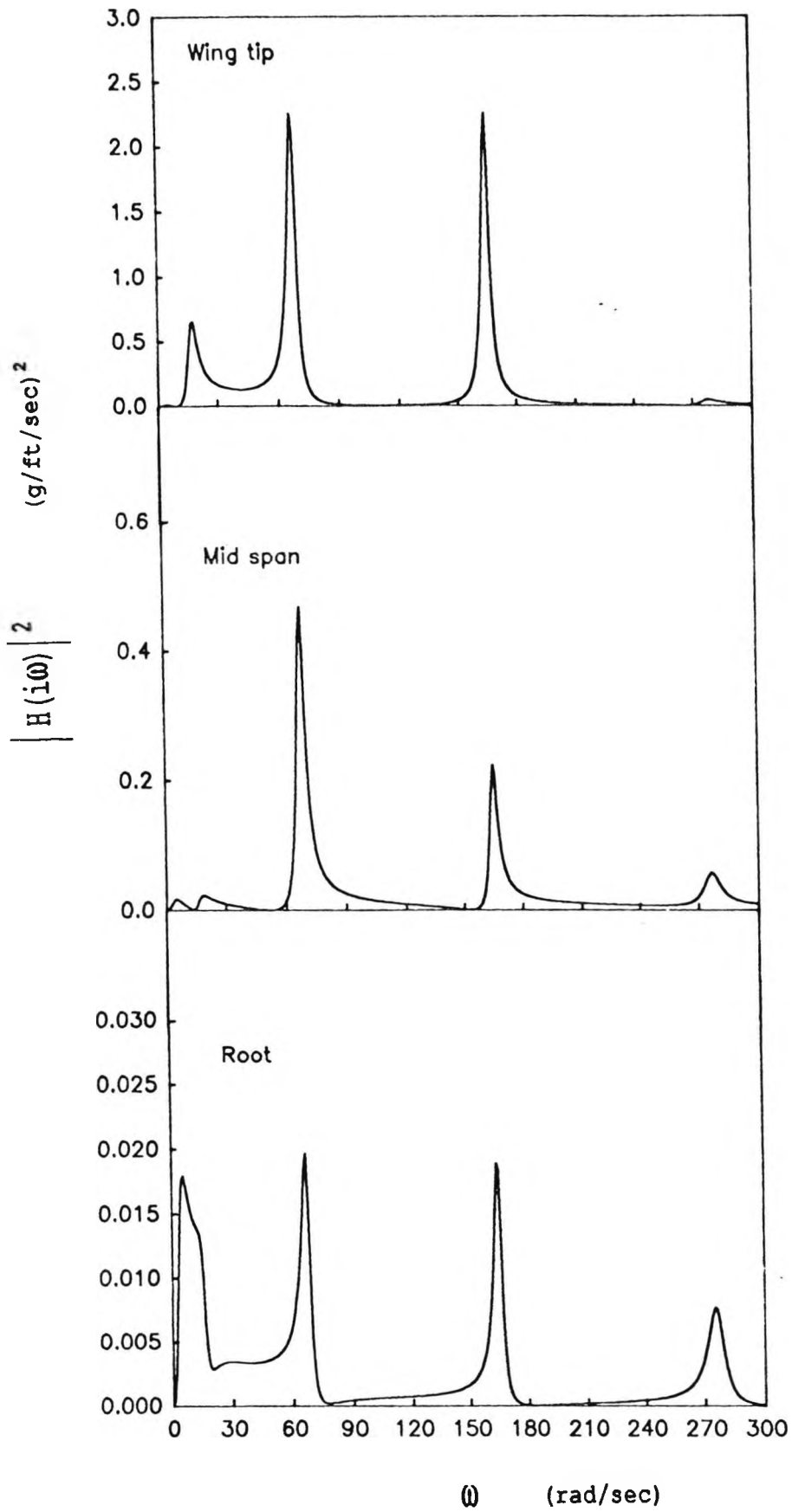
Fig. 6.11   Frequency response function in vertical
acceleration for Ricochet
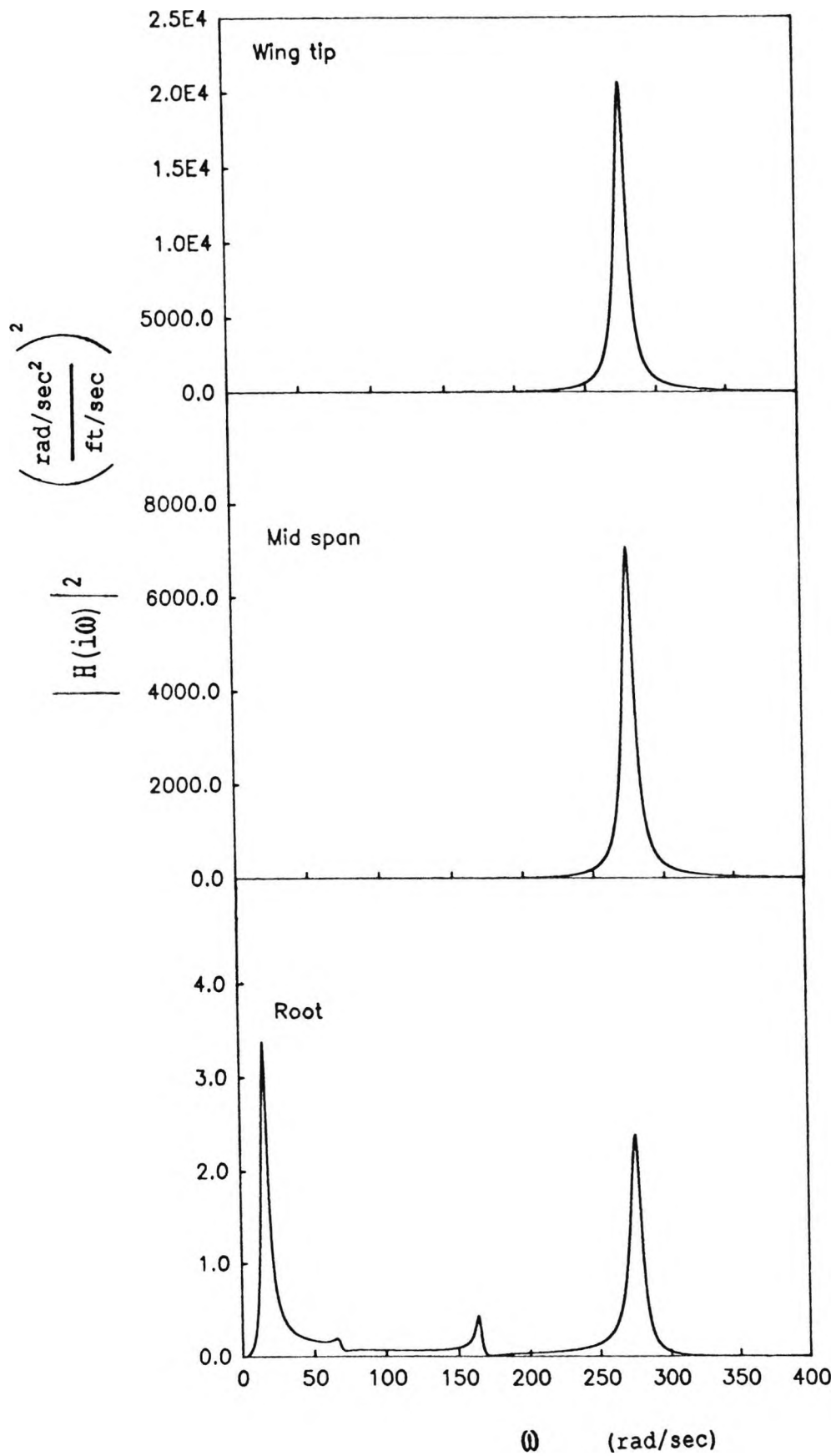
Fig. 6.12   Frequency response function in angular
            acceleration for Ricochet
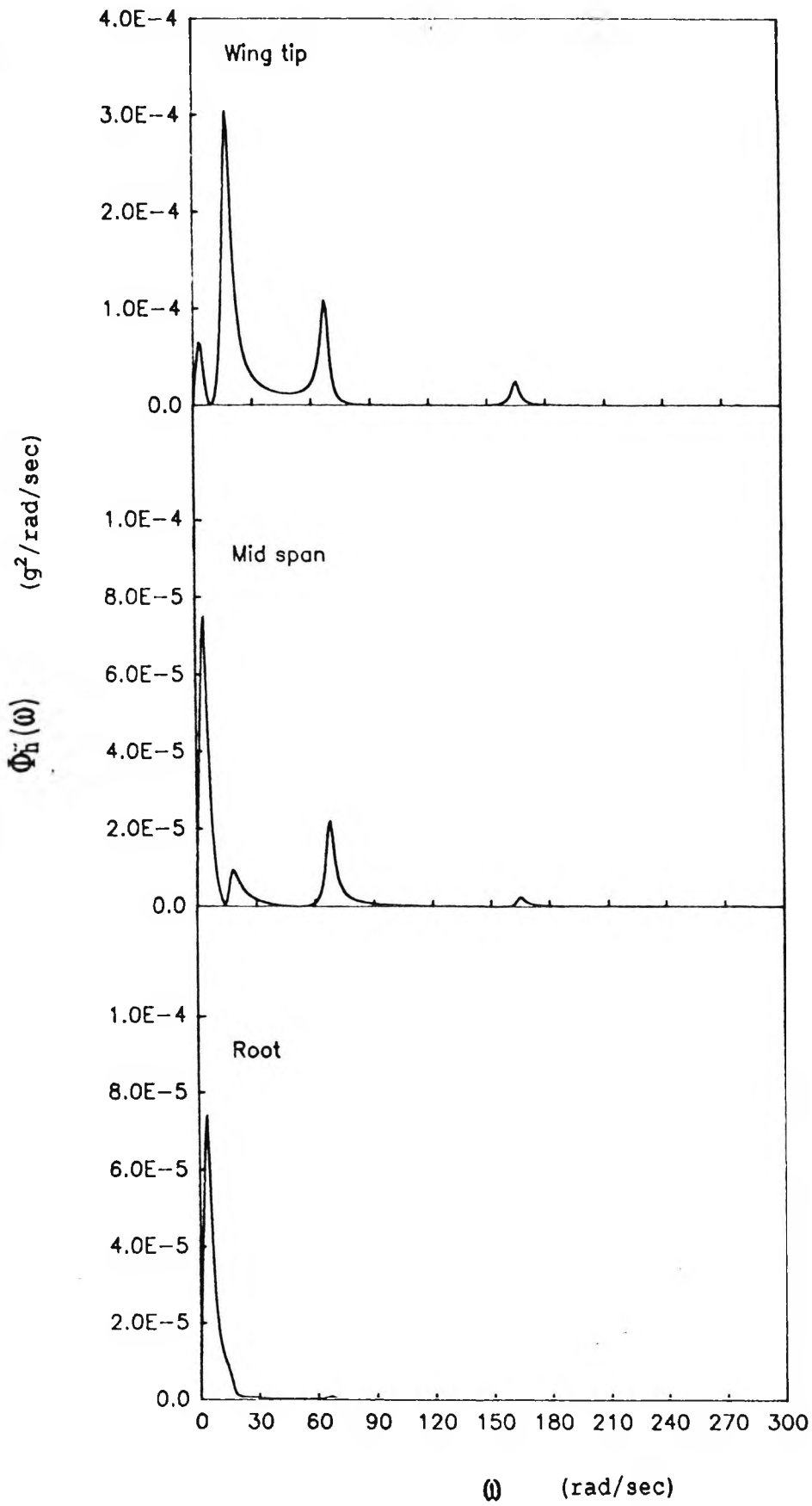
Fig. 6.13 PSD of vertical acceleration for Ricohet
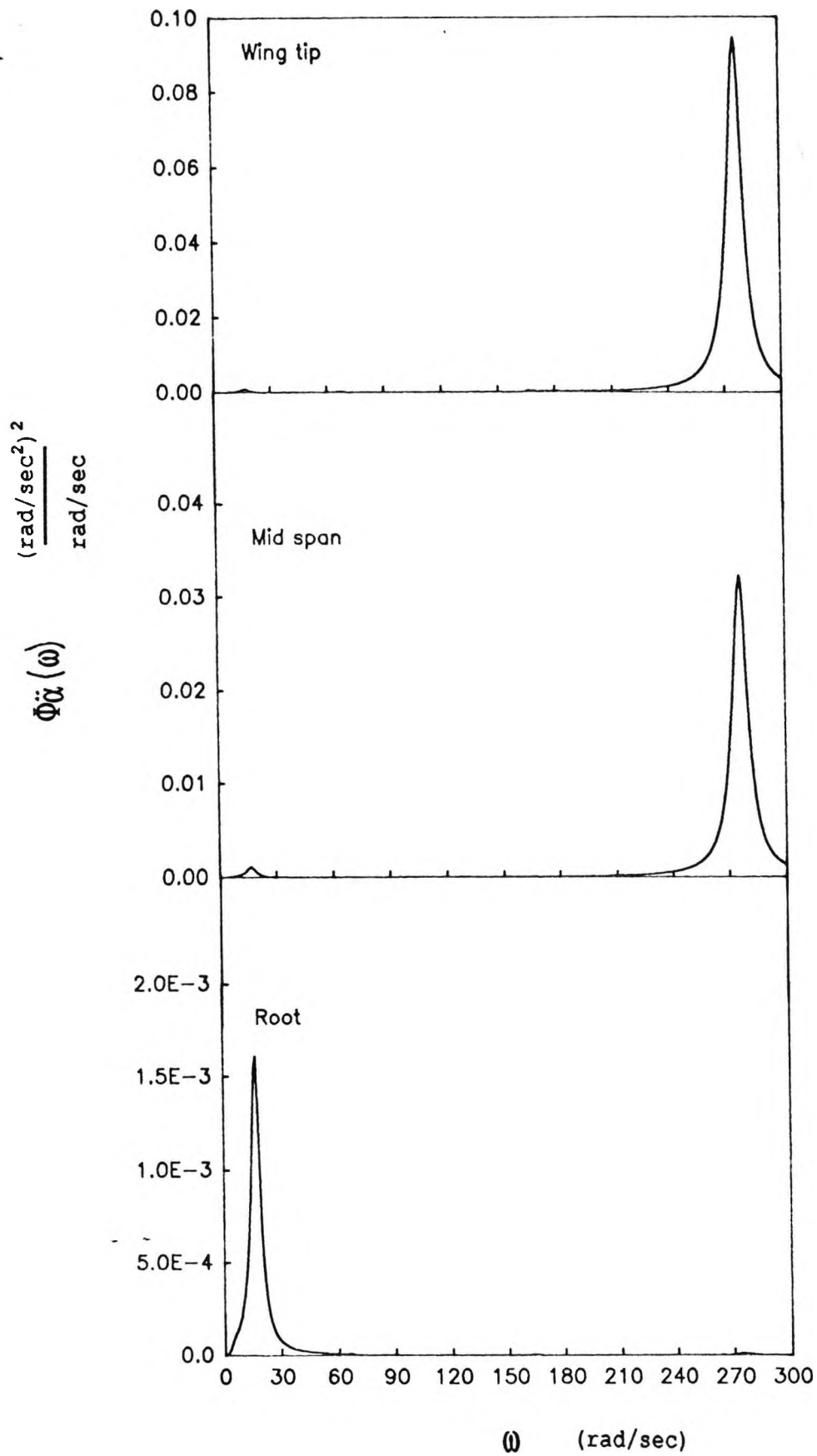
Fig. 6.14 PSD of angular acceleration for Ricochet
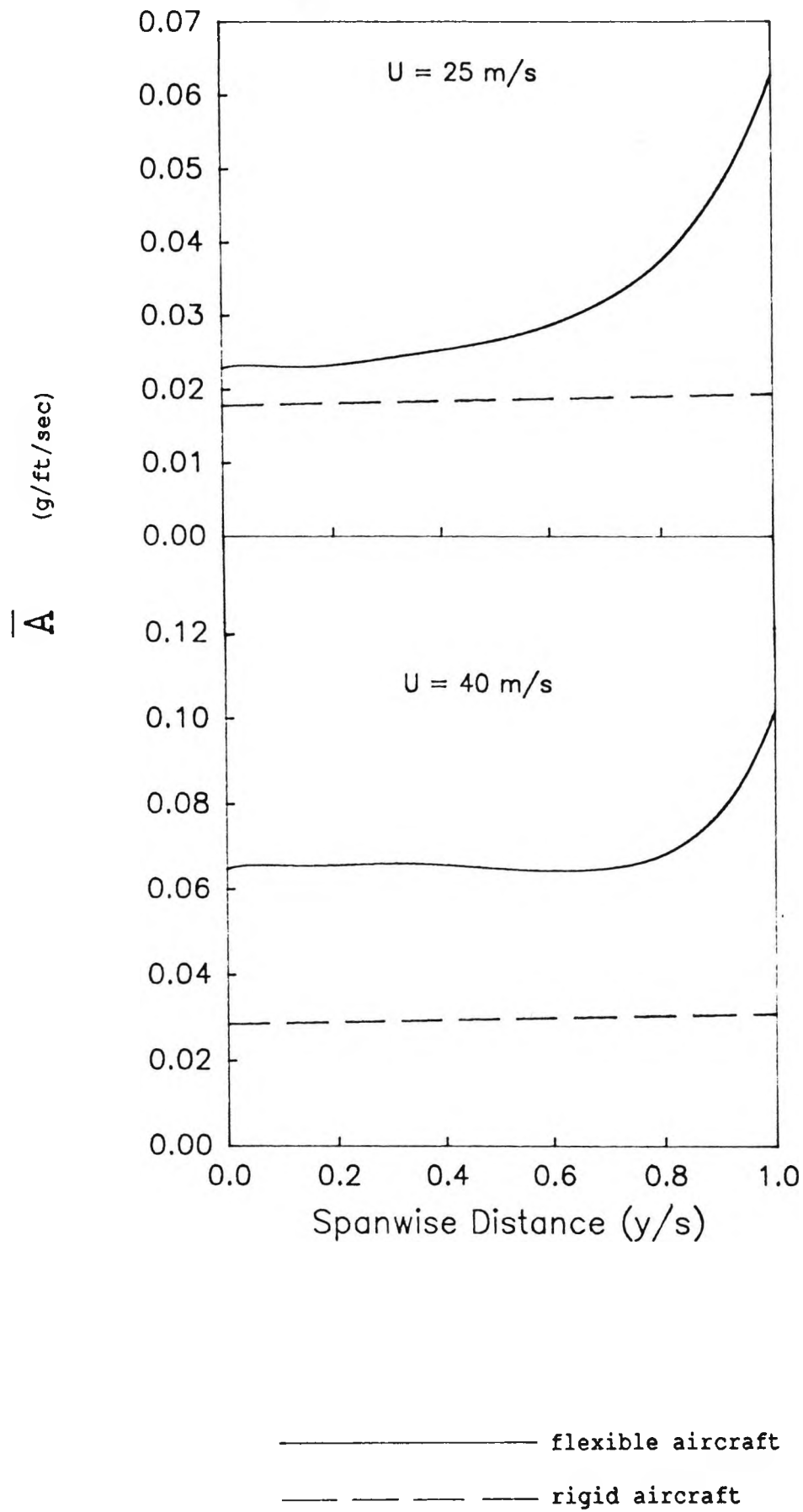
Fig. 6.15 Spanwise distribution of normalised vertical
acceleration for Ricochet
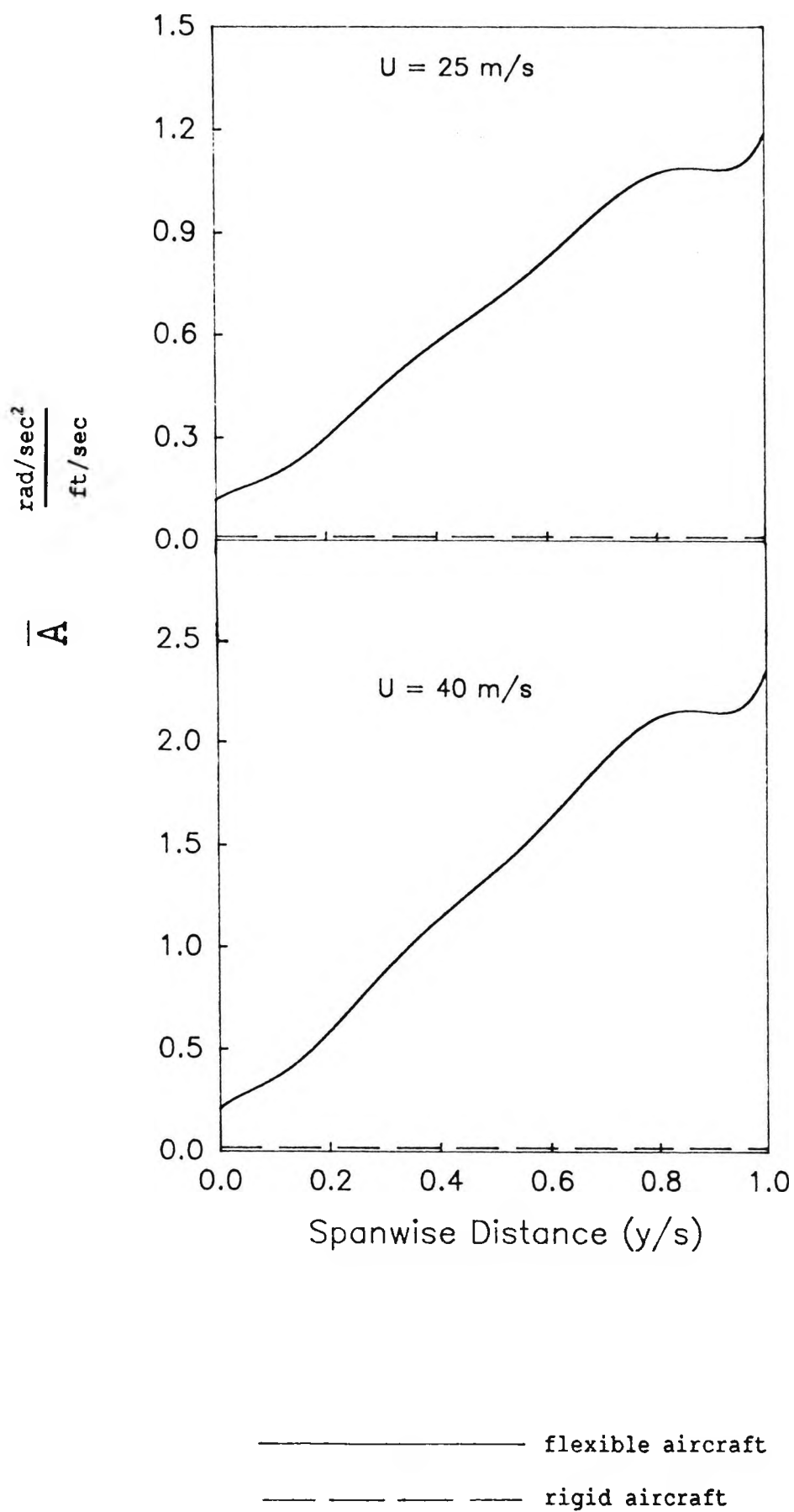
Fig. 6.16   Spanwise distribution of normalised angular
acceleration for Ricohet
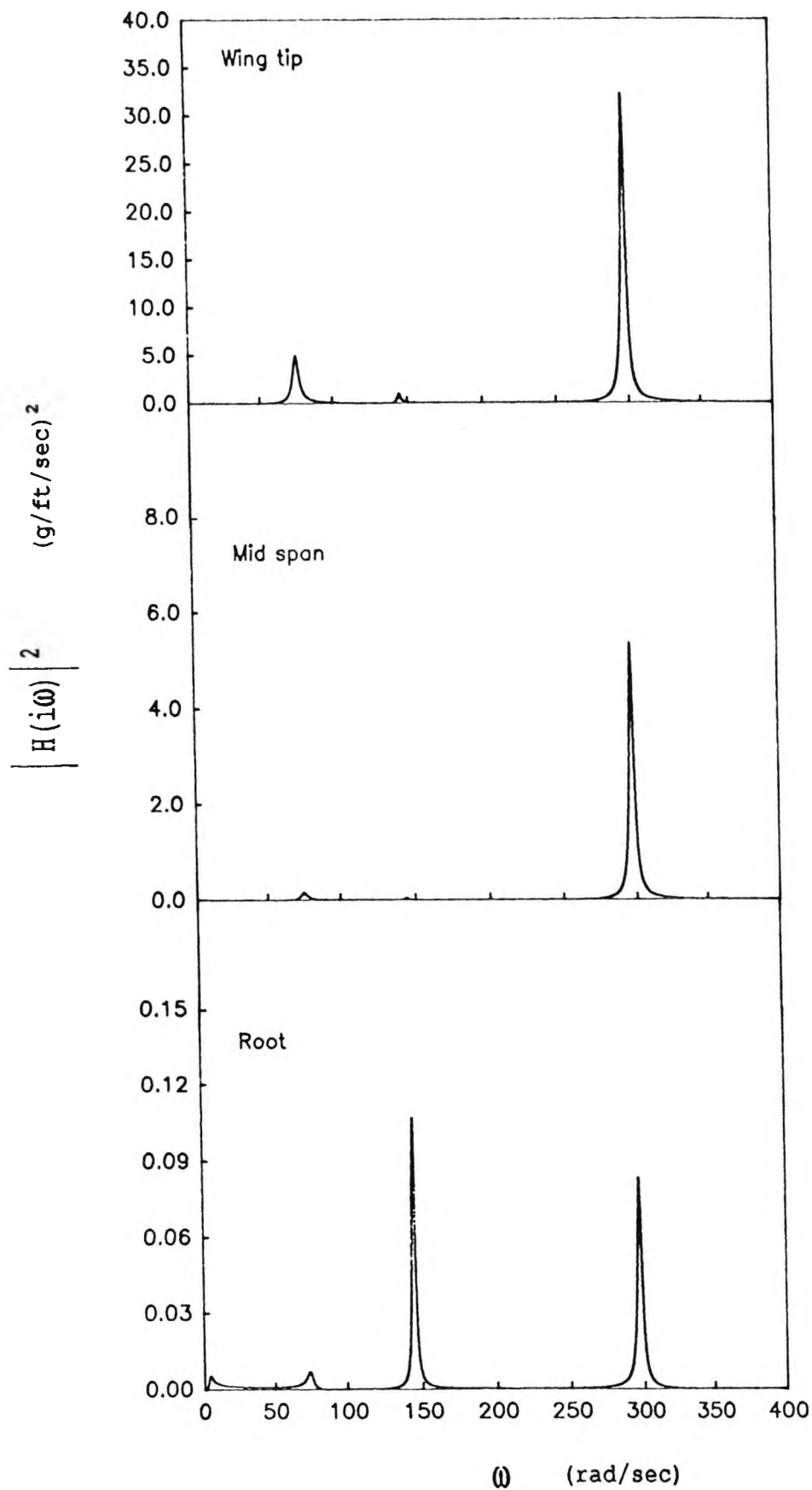
Fig. 6.17 Frequency response function in vertical
acceleration for A1
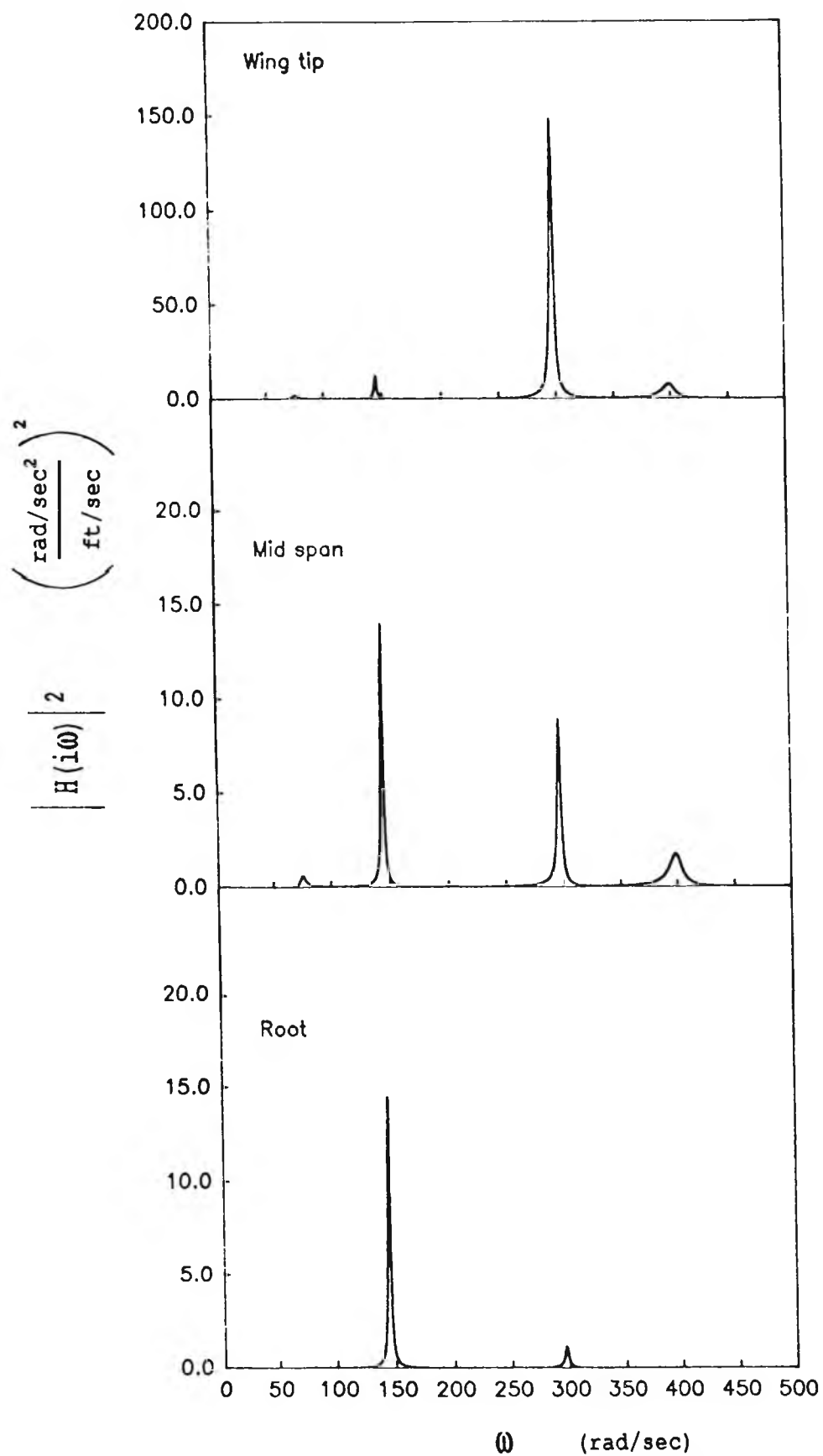
Fig. 6.18   Frequency response function in angular
            acceleration for A1
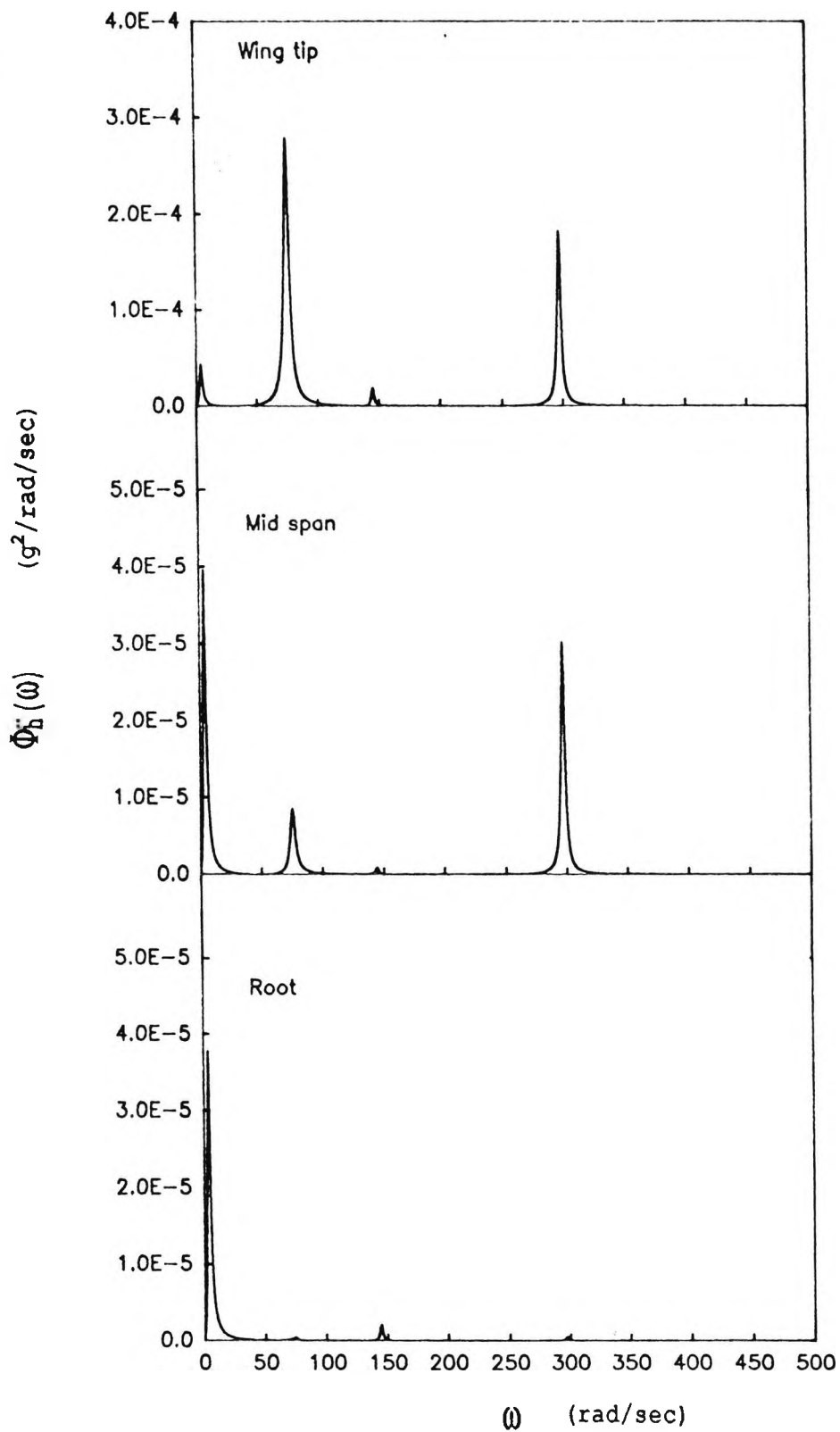
Fig. 6.19 PSD of vertical acceleration for A1
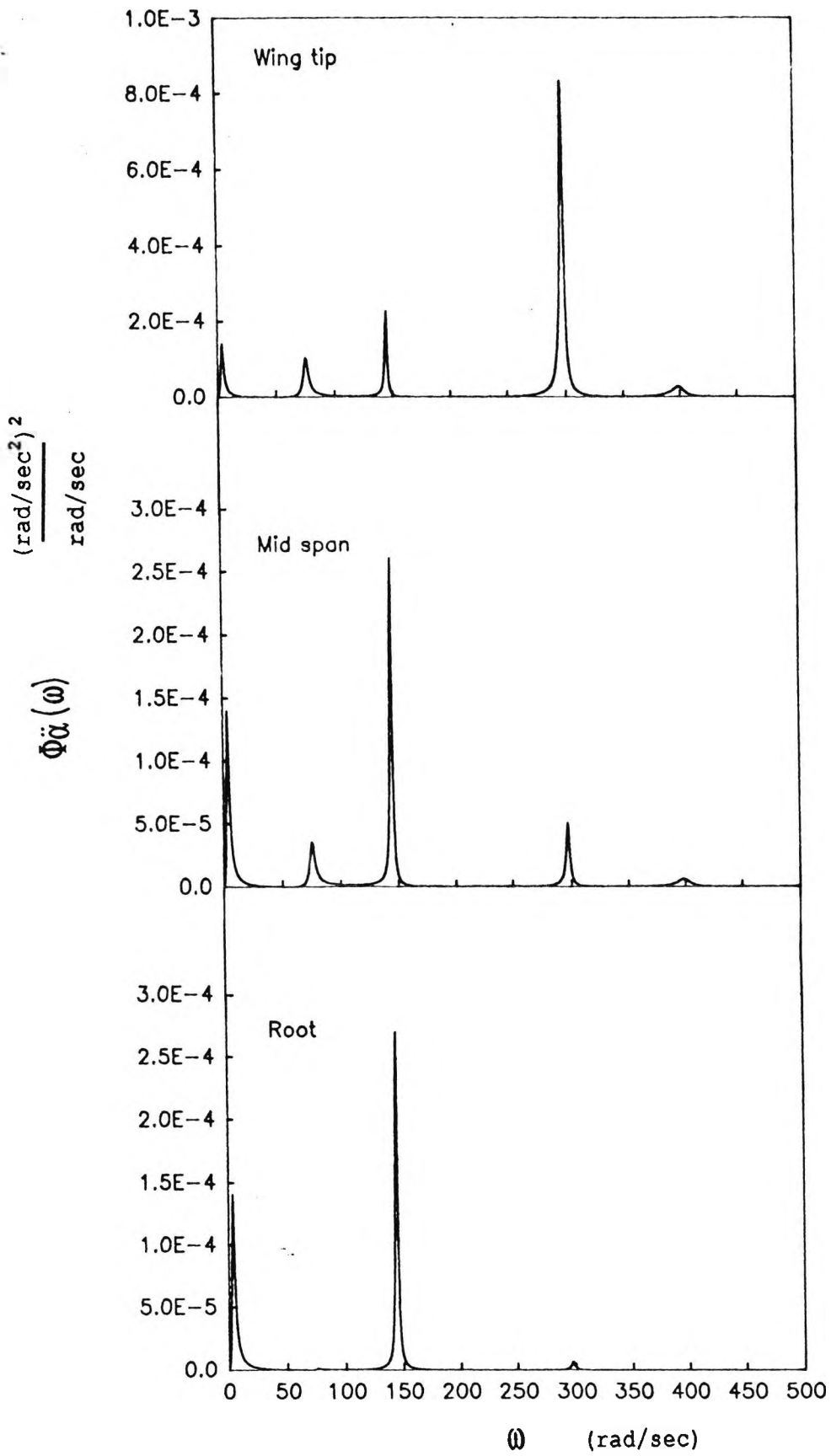
Fig. 6.20 PSD of angular acceleration for A1
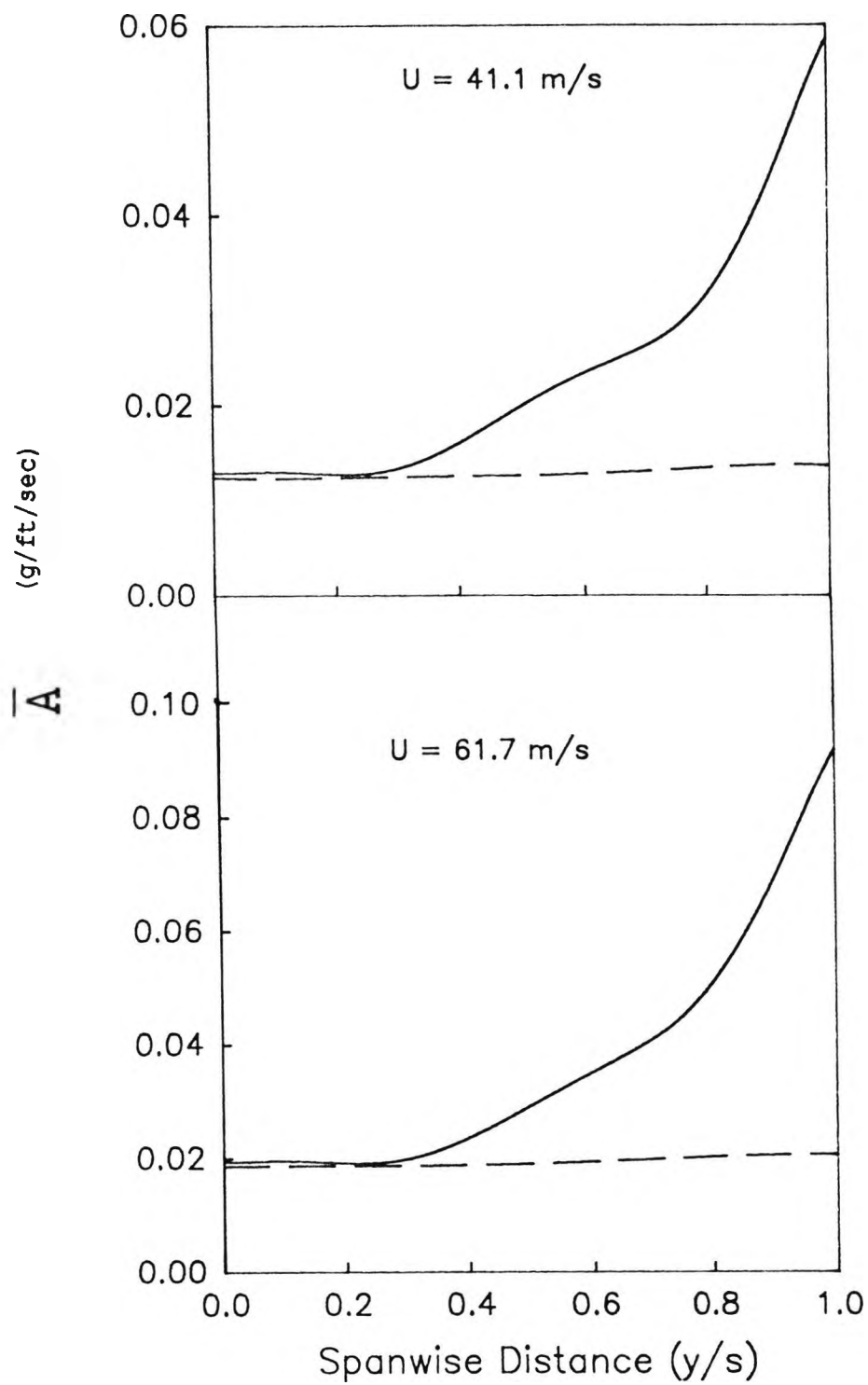
Fig. 6.21   Spanwise distribution of normalised vertical acceleration for A1
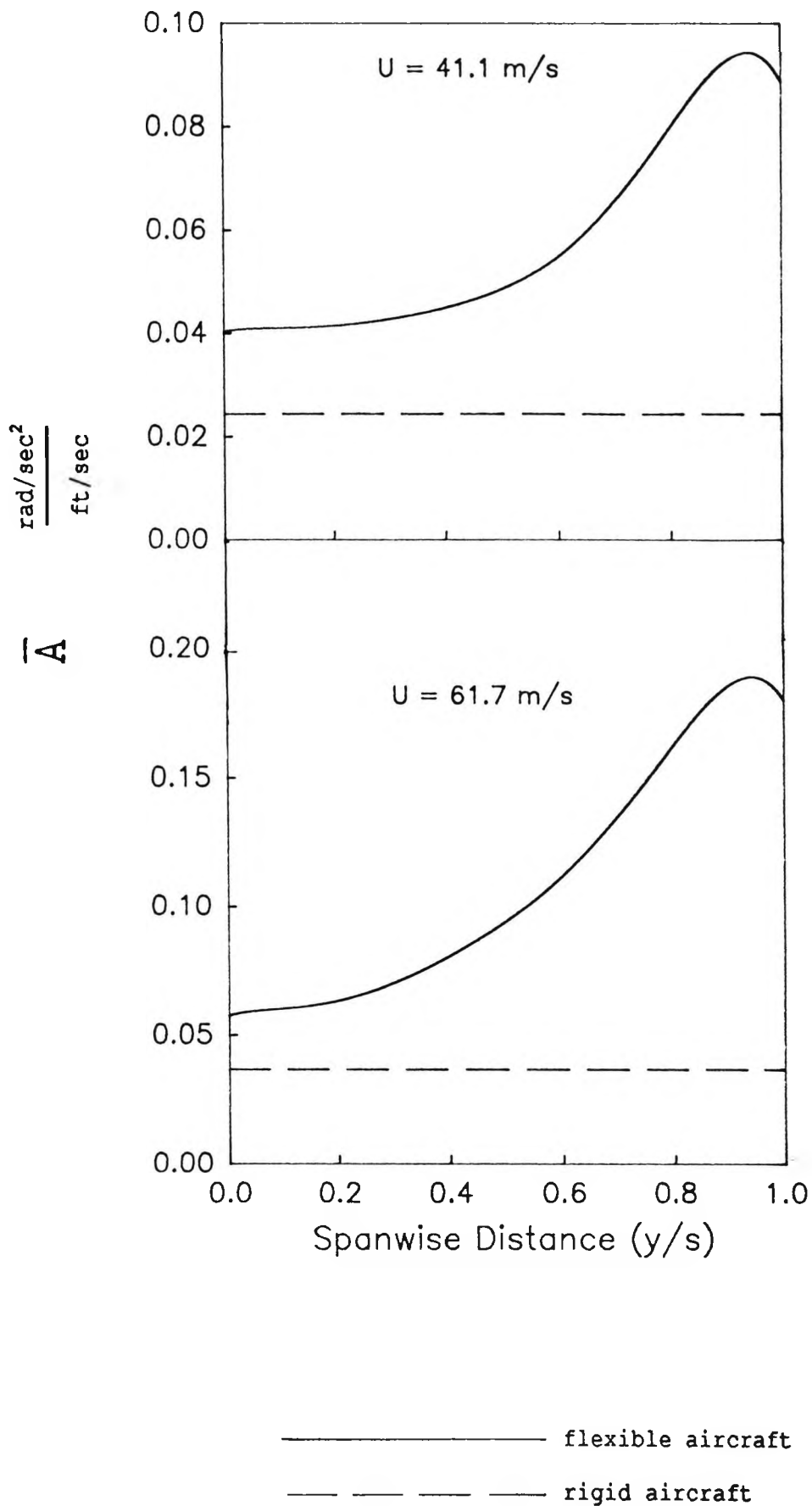
Fig. 6.22 Spanwise distribution of normalised angular acceleration for A1

7.0 SUMMARY OF RESULTS

7.1 Introduction

A unified method of flutter, dynamic stability and response analysis of deformable aircraft has been presented. The theory developed has been applied to three case aircraft. The work described in this thesis can be summarised as follows:

7.1.1 Validation of Strip Theory

Strip theory is revalidated as an aerodynamic tool for flutter analysis of high aspect ratio aircraft wings at low speeds. The investigation has shown that the lower limit of the aspect ratio for good flutter prediction is about 6. However, on occasions with suitable combination of other parameters, this limit can be decreased to as low as 4 and an acceptable engineering accuracy on the flutter speed can still be achieved. Within the most practical range of interest for the reduced frequency parameter, the oscillatory aerodynamic forces obtained from the strip theory show good agreement with those obtained from the lifting line theory. Care must be exercised when considering taper and sweep effects particularly for wings at the lower end of the aspect ratio (i.e. below 6). Considering the introduction of sweep at low subsonic speeds the cosine theory (as described in Chapter 2) is shown to yield comparable, if not closer agreement with experimental results, when compared with the classical velocity component theory. A study of the variation in flutter speed with variation of EI, GJ, M/l and I_p/l for the Kestrel wing and two wings of Refs.(37) and (50), show that the sensitivities are well behaved, so that potential future applications to optimisation are possible.

7.1.2 Flutter Behaviour of the Kestrel

The Kestrel is found, with the inclusion of the rigid body modes, to exhibit an example of classical wing bending/torsion flutter. The analysis of the Kestrel wing as a cantilever gave sufficiently accurate results when compared with the results obtained for the whole aircraft configuration. The tailplane aerodynamics has a marginal effect on the flutter of the Kestrel. The effect is found to be beneficial as the flutter speed increased in the presence of the tailplane aerodynamics as

174

expected. This stabilising effect is attributed to the fact that the tailplane provides additional aerodynamic damping to the aircraft. The fuselage bending stiffness played a relatively minor role on the symmetric flutter of Kestrel. Anti-symmetric flutter of Kestrel was found to be close to its symmetric value and exhibited another possible mode of instability.

7.1.3 Flutter Behaviour of the Ricochet

The Ricochet suffers from a phenomenon known as body freedom flutter, as a result of the fundamental wing bending mode coupling with the short period pitching oscillation. The two rigid body modes along with the fundamental wing bending mode are found to be sufficient in predicting the flutter of the Ricochet. The accuracy of quasi-steady aerodynamic theory was checked by applying the theory on the Kestrel and the Ricochet. The theory was found to predict flutter accurately at low reduced frequencies (for example, when body freedom flutter is encountered ($k < 0.1$)). However the theory was more conservative at higher frequencies, typical in bending/torsion flutter and in this case some account of aerodynamic lag and unsteadiness of the wake needs to be made.

7.1.4 Flutter Behaviour of the Cranfield A1

Fuselage flexibility is seen not to have a significant effect on the symmetric natural frequencies and modes of the Cranfield A1. The undercarriage mass, a third of the mass of the wing, needs to be accounted for, as this quantity is seen to affect the wing bending frequencies and in particularly the torsional frequencies and modes. A subsequent symmetric and anti-symmetric flutter analysis demonstrated that this aircraft is free from mainplane flutter. This is primarily as a result of the low aspect ratio and overall high stiffness of its construction.

7.1.5 Flutter Results of a Wind Tunnel Model

The current analysis successfully predicts body freedom flutter of a wind tunnel model of forward sweep configuration. However, care must be taken in applying an isotropic model to composites with high cross stiffness coupling terms. Modified wing aerodynamic parameters are seen in this particular type of flutter to lower the aerodynamic stiffness and damping and subsequently raise the flutter speed.

175

7.1.6 Short Period Oscillation Characteristics of the Kestrel, Ricochet and A1

Flexibility is seen to be quite fundamental to the determination of the stability and control of sailplanes. For both the Kestrel and the Ricochet the introduction of flexibility, in particular the first bending and first torsional modes, has a destabilising influence on the short period mode. Close to the flutter speed, classical rigid body assumptions are no longer valid. At 60 m/s, close to the Kestrel flutter speed, the classical rigid assumption overestimates the short period damping by 35.2% and underestimates the frequency by 60.6%, for the flexible case based on four elastic modes. Similarly at 45 m/s the corresponding discrepancies for the Ricochet are 110.4% and 57.3% respectively. Predictably the A1 being very stiff, these values are only 19.4% and 0.9% respectively. The damping predicted was generally higher for the unsteady model. For the Ricochet the agreement between quasi-steady and unsteady aerodynamics is closer as this aircraft's aeroelastic stability is dominated by the low frequency rigid body modes. The inclusion of the fundamental bending and torsional modes, in addition to the rigid body modes, is found to be sufficient in predicting the dynamics characteristics of these deformable aircraft (the Kestrel and the Ricochet).

7.1.7 Effect of Unsteady Wake on Dynamic Stability and Flutter

The effects of an unsteady wake at the tailplane are investigated using a simple vortex lattice method employing strip aerodynamics and wing flexibility. The influence of the wake is found to be predominantly aspect ratio dependent. Considering only rigid body modes in symmetric motion for the Kestrel, (aspect ratio 31), the s.p.p.o damping is seen to increase by 46.5% and the frequency decrease by 13% in comparison to the case when the effect is neglected. For the A1, (aspect ratio 6.7), the discrepancy for these respective quantities are found to be 203% and 28.5%. Wing flexibility for the A1 has a marginal effect on the wake as expected. There is found to be a negligible decrease in the flutter speed and flutter frequency of Kestrel with the introduction of a wake, as the combination of T-Tail and high

176

aspect ratio reduces the influence of this wake.

7.1.8 Response to Discrete Gusts and Continuous Turbulence

Unsteady aerodynamics is found to decrease the spectral gust alleviation factor K by as much as 18% for the rigid aircraft. The addition of flexibility is seen to substantially increase the overall aircraft response, especially at subcritical speeds. In particular for the Ricochet in the absence of a tailplane, the influence of the flexible modes on the rigid body modes is seen to induce significant accelerations at the wing root as well as at the wing tip. As the A1 is torsionally much stiffer than both the Kestrel and Ricochet, the response to angular acceleration is seen to be much smaller. The PSD and SDG methods were applied to all the case aircraft, for both the rigid and the flexible case. From these results, an SDG-PSD overlap does appear to exist. However this overlap appears to be characterised in this investigation not by a 10.4 factor, but rather by a 10.4 plus or minus approximately 17% of this value when only the aircraft is considered to be rigid. For the flexible case this range was found to be plus or minus 31% of the factor. However this large variation could be due to the inadequacies of the current SDG method (method 1) in dealing with the aircraft of considerable flexibility.

7.2 Development of Computer Program

Based on the method presented in this thesis, a FORTRAN program called FLUSTAR has been developed. Using the geometry of the aircraft together with its inertia and stiffness properties, the program will accomplish with a minimum of data the following tasks:

1) Evaluation of flutter speed and aeroelastic modes at flutter speed of an aircraft using normal modes.

2) Investigation of the short period oscillation characteristics of an aircraft with or without the inclusion of flexibility.

3) Calculation of both linear and angular acceleration responses to continuous random atmospheric turbulence using the frequency response function and the power spectral density (PSD) method.

4) Determination of the acceleration response of a flexible aircraft to unit step gust velocity. Evaluation of the statistical discrete gust (SDG) method and identification of the worst case response to a pair of step gusts.

8.0 CONCLUSIONS AND SUGGESTIONS FOR FURTHER WORK

8.1 Principal Conclusions

This investigation has shown that the lower limit for good flutter prediction, using strip theory, is about 6. However, in some cases, this limit can be lowered to as low as 4 and an acceptable engineering accuracy on the flutter speed can still be achieved. The cosine theory has been shown to be adequate in accurately predicting the flutter speed of swept wings.

In symmetric motion the Kestrel is found to exhibit classical wing/torsion flutter and tailplane aerodynamics is found to have a marginal if not stabilising influence on the flutter speed. Fuselage bending flexibility plays a relatively minor role on the flutter of Kestrel. Anti-symmetric flutter close to the Kestrel's symmetric value, was discovered as another possible mode of instability. The Ricochet in the absence of a tailplane is found to suffer from body-freedom flutter involving coupling of the short period mode with the first wing bending mode and these modes are found to be sufficient in predicting the flutter of the Ricochet. Fuselage flexibility is seen not to be of great significance on the symmetric natural frequencies and modes of the Cranfield A1. However the undercarriage needs to be accounted for, because its presence influences the torsional wing frequencies and modes significantly. As the A1 is relatively stiff and of comparatively low aspect ratio, it is found to be free from mainplane flutter.

For both the Kestrel and the Ricochet the introduction of flexibility has a destabilising influence on the short period mode. Close to the flutter speed of the Kestrel and the Ricochet the classical stability derivative approach, employing rigid body assumptions is found to be inadequate in predicting the short period characteristics but predictably not for the relatively stiffer A1. The inclusion of the fundamental bending and torsional modes, in addition to the rigid body modes, is found to be sufficient in predicting the dynamic characteristics of the Kestrel and the Ricochet. An unsteady wake introduced at the tailplane is seen to increase the short period damping of the Kestrel and in particular that of the low aspect ratio A1

significantly. However the wake is found to have a negligible effect on the Kestrel flutter.

Flexibility is seen to substantially increase the overall aircraft response, especially at subcritical speeds. In particular for the Ricochet in the absence of a tailplane, the influence of the flexible modes on the rigid body modes is seen to induce significant accelerations at the wing root as well as at the wing tip. As the A1 is torsionally much stiffer than both the Kestrel and the Ricochet, its response to angular acceleration is seen to be much smaller. From the response analysis carried out on all the three aircraft, an SDG-PSD overlap does appear to be characterised in this investigation not exactly by a 10.4 factor as reported by Jones, but rather by a 10.4 plus or minus approximately 17% of this value, when rigid body modes are considered. For the flexible case this range is found to be plus or minus 31% of this factor.

8.2 Suggestions for Further Work

In order to verify the accuracy of the proposed theory, a dynamic aeroelastic model, as proposed in Appendix J, should be tested. This will enable evaluation of subcritical or otherwise flutter quantities. Additionally this model could be modified to simulate flexible aircraft response to atmospheric turbulence.

The effect of inertial coupling may need to be introduced for some critical planforms. Accurate determination of mode shapes is important for flutter analysis, therefore a method of matching mode shapes obtained from ground resonance tests in the analysis directly, should be investigated. The current dynamic stiffness matrix employed can be further developed to take into account materials with cross coupling stiffnesses, as present in composites. This is essential before extending the current theory for practical aeroelastic tailoring or optimisation problems.

Wing loading distribution and finite span effects on flutter and stability should be thoroughly investigated with the use of the current modified aerodynamic terms. The present unsteady downwash model can be easily extended to cover the anti-symmetric case, in particular to investigate probable downwash induced component flutter. However to improve the current aerodynamic

model to deal with low aspect ratio planforms (AR < 6) in general, it is suggested that a more refined 3-dimensional theory should be implemented, such as one of the vortex lattice theories.

The effect of control surfaces on both the anti-symmetric and symmetric flutter needs to be investigated, as an extension of the current dynamic stability theory for the stick free situation.

A method of obtaining response quantities has been developed, a program is now required to convert this data, to obtain the spanwise shear stress, bending and torsional moment distributions. This needs to be carried out before the case of aircraft response can be resolved and included in the unified theory.

REFERENCES

1. Collar, A.R., "The Expanding Domain of Aeroelasticity", *Journal of the Royal Aeronautical Society,* Aug. 1946, pp.613-636.

2. Fraser, R.A. and Duncan, W.J., "The Flutter of Aeroplane Wings", ARC, R. & M. Rept. No. 1155, Aug. 1928.

3. Glauert, H., "The Force and Moment on an Oscillating Aerofoil", ARC, R. & M. Rept. No. 1242, 1929.

4. Wagner, H., "Uber die Entshehung des Dynamischen Auftriebs von Tragflugeln", Z. Angew. Math, U, Mech., Bd. 5, Heft 1, Feb. 1925, pp.17-35.

5. Theodorsen, T., "General Theory of Aerodynamic Instability and Mechanisms of Flutter", NACA Tech. Rept. No. 496, 1934.

6. Rodden, W.P., "The Role of Structural and Aerodynamic Damping on the Aeroelastic Behaviour of Wings", Technical Comments, *Journal of Aircraft*, Vol.25, No.3, March 1988, pp.286-288.

7. Davies, D.E., "Theoretical Determination of Subsonic Oscillatory Airforce Coefficients", RAE Tech. Rept. No. 76059, May 1976.

8. Albano, E. and Rodden, W.P., "A doublet-Lattice method for Calculating the Lift distribution on Oscillating Surfaces in Subsonic Flow", *AIAA Journal*, Vol.7, Feb. 1969, pp.279-285; and Vol. 7, Nov. 1969, p.2192.

9. Collar, A.R., "The First Fifty Years of Aeroelasticity", *Aerospace*, Vol.5, (Paper No.545), Feb. 1978, pp.12-20.

10. Garrick, I.E. and Wilmer, R.H., "Historical Development of Aircraft Flutter", *Journal of Aircraft,* Vol.18, No.11, Nov. 1981, pp.897-912.

11. Davies, D.E., "Calculations of Generalised Airforces on Two Parallel Lifting Surfaces Oscillating Harmonically in Subsonic

Flow", RAE, R. & M. Rept. No. 3749, 1974.

12. Mykytow, W.J., Noll, T.E., Huttsell, L.J., and Shirk, M.H., "Investigations concerning the Coupled Wing-Fuselage-Tail Flutter Phenomenon", *Journal of Aircraft,* Vol 9, No 1, Jan. 1972, pp.48-54.

13. Triplett, W.E., Burkhart, T.H., and Birchfield, E.B., "A Comparison of Methods for the Analysis of Wing-Tail interaction Flutter", *Journal of Aircraft,* Vol 8, No.5, May 1971, pp.361-367.

14. Babister, A.W., "Aircraft Dynamic Stability and Response", Pergamon Press, 1980.

15. Etkin, B., "Dynamics of Flight", Chapman & Hall 1959.

16. Gaukroger, D.R., "Wind-Tunnel Tests on the Symmetric and Antisymmetric Flutter of Swept-Back Wings", RAE Report Structures 123, R. & M. Rept. No. 2911, March 1953.

17. Banerjee, J.R., "Flutter Characteristics of High Aspect Ratio Tailless Aircraft", *Journal of Aircraft*, Vol.21, No.9, Sept. 1984, pp.733-736.

18. Weisshaar, T.A., Zeiler, T.A., Hertz, T.J., and Shirk, M.H., "Flutter of forward Swept Wings, Analysis and Tests", *AIAA* Paper 82-0646, May 1982.

19. Shirk, M.H., Hertz, T.J. and Weisshaar, T.A, "Aeroelastic Tailoring Theory, Practice and Promise", *Journal of Aircraft*, Vol.23, Jan. 1986.

20. Van Schoor, M.C., and Von Flotow, A.H., "Aeroelastic Characteristics of a Highly Flexible Aircraft", *Journal of Aircraft*, Vol.27, No.10, Oct. 1990, pp.901-908.

21. Taylor, A.S. and Woodcock, D.L., "Mathematical Approach to Dynamics of Aircraft", ARC, R. & M. Rept. No. 3776, Monograph 1976.

22. Taylor, A.S., "The Present Status of Aircraft Stability Problems in the Aeroelastic Domain", *Journal of the Royal Aeronautical Society,* Vol.63, April 1959, pp.227-238.

23. Swaim, R.L. and Fullman, D.G., "Prediction of Elastic Airplane Longitudinal Dynamics from Rigid-Body Aerodynamics", *Journal of Aircraft*, Vol.14, Sept. 1977, pp.868-873.

24. MSC/NASTRAN, "Handbook for Aeroelastic Analysis", The MacNeal-Schwendler Corporation, Los Angeles, California, Vol.1, Nov. 1987.

25. Clementson, G.C., "An Investigation of the Power Spectral Density of Atmospheric Turbulence," Ph.D. Thesis, Massachusetts Institute of Technology, Cambridge, MA, 1950.

26. Jones, J.G., "Statistical Discrete Gust Theory for Aircraft Loads", RAE Tech. Rept. No. 73167, 1983.

27. Jones, J.G., "A Unified Procedure for Meeting Power-Spectral-Density and Statistical-Discrete-Gust Requirements for Flight in Turbulence", *AIAA* Paper 86-1011, May 1986.

28. Banerjee, R., "CALFUN, A Program for Calculation of Flutter Speed Using Normal Modes", The City University, London, 1988.

29. Luke, Y.L., and Dengler, M.A., "Tables of the Theodorsen Circulation Function for Generalised Motion", *Journal of the Aeronautical Sciences*, Vol.18, July 1951, pp.478-483.

30. Yates, E.C., Jr., "Modified-Strip-Analysis Method for Predicting Wing Flutter at Subsonic to Hypersonic Speeds", *Journal of Aircraft,* Vol.3, No. 1, Jan-Feb. 1968.

31. Purcell, A.G., "The Response of Aircraft to Discrete Ramp Gusts", RAE Tech. Rept. No. 77165, Nov. 1977.

32. Jones, J.G., "The Statistical Discrete Gust (SDG) Method in its Developed Form", *Proceedings of the AIAA/ASME/ASCE/AHS 30th Structures, Structural Dynamics and Materials Conference, Mobile,*

AL, USA., *AIAA* Paper 89-1375, May 1989.

33. Bisplinghoff, R.L., Ashley, H., and Halfman, R.L., "Aeroelasticity", Addison-Wesley, Reading, Mass, 1955.

34. Fung, Y.C., "An Introduction to the Theory of Aeroelasticity", Wiley, New York, 1955.

35. Dowell, E.H., Curtiss Jr, H.C., Scanlan, R.H., and Sisto, F., "A Modern Course in Aeroelasticity", Kluwer Academic Publishers, 2nd Edition, 1989.

36. Niblett, L.T., "A Guide to Classical Flutter". *The Aeronautical journal,* Vol.92, No. 919, Nov. 1988, pp.339-354.

37. Loring, S.J., "Use of Generalised Co-ordinates in Flutter Analysis", *SAE Journal* (Transaction) Vol.52, April 1944.

38. Banerjee, J.R., "Flutter Modes of High Aspect Ratio Tailless Aircraft", *Journal of Aircraft,* Vol.25, No.5, May 1988, pp.473-476.

39. Banerjee, J.R. and Cal, A.A., "A Unified Approach to Stability Characteristics of Tailless Aircraft", paper presented at the *29th AIAA/ASME/AHS/ASC Structures, Structural Dynamics and Materials Conference, Williamsburg, Va., USA,* Paper No. 88-2212, 18-22 April 1988.

40. Jones, R.T., "The Unsteady Lift of a Wing of Finite Aspect Ratio", NACA Rept. No. 681, 1940.

41. Lomax, H., Heaslet, M.A., Fuller, F.B., and Sluder, L., "Two-and Three Dimensional Unsteady Lift Problems in High-Speed Flight", NACA Rept. No. 1077, 1952.

42. Försching, H.W., "Prediction of the Unsteady Airloads on Oscillating Lifting Systems and Bodies for Aeroealastic Analysis", *Progresses in Aerospace Sciences,* Vol.18, Pergamon Press, 1978, pp.211-269.

43. AGARD "Manual on Aeroelasticity", Part II, London, 1961.

44. Davies, D.E., "On the Use of Fortran Programs for Evaluating the Generalised Airforces and Aerodynamic Loading on a Flat Plate Wing Oscillating Harmonically in Subsonic Flow", RAE Tech. Memo., Structures 881, Jan. 1976.

45. Multhopp, H., "Methods for Calculating the Lift Distribution of Wings (Subsonic Lifting Surface Theory)", ARC, R. & M. Rept. No. 2884, 1950.

46. Rollerson, J., Boor, R.G., and Green M.J., "Quasi 3-Dimensional Unsteady Aerodynamics Strip Theory", British Aerospace p.l.c, Weybridge Division, Report No. BAE-MAE-R-GEN-600, 14 March 1985.

47. Bramwell, A.R.S., *Helicopter Dynamics*, John Wiley and Sons, New York, 1976.

48. Lottati, I., Reply to Ref.(6), *Journal of Aircraft*, Vol.25, No.3, March 1988, pp.288.

49. Goland, M., "The Flutter of a Uniform Wing", *Journal of Applied Mechanics,* Trans. ASME, Vol. 12, No. 4, 1945, pp.A-197 to pp.A-208.

50. Goland,M., "The Flutter of a Uniform Wing with Tip Weights", *Journal of Applied Mechanics,* Trans. ASME, Vol. 15, No. 1, March 1948, pp.13-20.

51. Benton, J, (Department of Aerodynamics, BAe Woodford) Private Communication, June 1988.

52. Babister, A.W., "Flutter and Divergence of Swept-Back and Swept-Forward Wings", ARC, R. & M. Rept. No. 2761, 1950.

53. Fettis, H.E., "Calculations of the Flutter Characteristics of Swept Wings at Subsonic Speeds", Air Force Air Material Command Memo. Rept. TSEAC5-4595-2-9, May 1946.

54. Molyneux, W.G., "The Flutter of Swept and Unswept Wings with Fixed-Root Conditions", ARC, R. & M. No 27, Jan. 1950.

55. Molyneux, W.G., and Hall, H., "The Aerodynamic Effects of Aspect Ratio and Sweepback on Wing Flutter", ARC, R. & M. Rept. No. 3011, Feb. 1955.

56. Broadbent, E.G., "Some Considerations of the Flutter problems of High Speed Aircraft", Second International Aeronautical Conference, Published by Institute of the Aeronautical Sciences, Inc, New York, 1949.

57. Barmby, J.G., Cunningham, H.J., and Garrick, I.E., "Study of Effects of sweep on the Flutter of Cantilever Wings", NACA Rept. NO. 1014, 1951.

58. Scanlan, R.H. and Rosenbaum, R., "Introduction to the Study of Aircraft Vibration and Flutter", The Macmillan Company, New York, N.Y., 1951.

59. Shelton, W.L., "Flutter Prediction in Forward-Swept Wings by Assumed Modes and Strip Theory", M.Sc. Thesis, Air Force Institute of Technology, AFIT/GAE/AA/82D-27, Dec. 1982.

60. Diederich, F.W., and Budiansky, B., "Divergence of Swept Wings", NACA TN 1680, 1948.

61. Yates, E.C., Jr., Eleanor C.W., Moses G.F., and Desmarais R.N., "Prediction of Transonic Flutter for a Supercritical Wing by Modified Strip Analysis", *Journal of Aircraft*, Vol. 19, No. 11, Nov. 1982, pp.999-1004.

62. Hallauer Jr, W.L., and Liu, R.Y., "Beam Bending-Torsion Dynamics Stiffness Method for Calculation of Exact Vibration Modes", *Journal of Sound and Vibration*, Vol.85, No.1, 1982, pp.105-113.

63. Cunningham, H.J., "Analysis of Pure-Bending Flutter of a Cantilever Swept Wing and its Relation to Bending-Torsion

Flutter", NACA TN 2461, 1951.

64. Atiq, R., "Aeroelastic Analysis of Wings", B.Eng Aeronautical Engineering project, The City University, London, 1990.

65. Frazer, R.A. and Duncan, W.J.,"Wing Flutter as Influenced by the Mobility of the Fuselage", ARC, R. & M. Rept. No. 1207, 1929.

66. Miller, G.D., Wykes, J.H., and Brosnan, M.J.,"Rigid Body Structural Mode Coupling on a Forward Swept Wing Aircraft", *AIAA* Paper 82-0683, May 1982.

67. Weisshaar, T.A., and Zeiler, T.A.,"Dynamic Stability of Forward Swept Wing Aircraft", *Journal of Aircraft,* Vol.20, Dec. 1983.

68. Gaukroger, D.R., "Body Freedom Flutter of Ground Launched Rocket Models at Supersonic and High Subsonic Speeds", RAE Report Structures 227, R. & M. Rept. No. 3198, Sept. 1957.

69. Niblett, L.T. "The Fundamentals of Body-Freedom Flutter". *The Aeronautical journal,* Vol.90, No. 899, Nov. 1986, pp.373-377.

70. Buchanan, E.J., "Design Study of a Tailless Glider", M.Sc., Thesis, Cranfield Institute of Technology, Cranfield, U.K., 1975.

71. Banerjee, J.R., and Williams F.W., "User's Guide to the Computer program BUNVIS (Buckling or Natural Vibration of Space Frames)", Department of Civil Engineering and Building Technology, UWIST, Department Report N0.5, 1982.

72. BAC, Dynamics Department, "Ground Resonance Test on Slingsby 22m Kestrel Sailplane", Report No BAe/D/SLY/2, 5 April 1978.

73. Engineering Science Data Unit, U.K., Data Sheet 01.01.01.

74. Schweiger, J. and Sensburg, O., "Aeroelastic Problems and Structural Design of a Tailless CFC-Sailplane", Presented at the *Second International Symposium on Aeroelasticity and Structural Dynamics, Aachen, FRG,* April 1985.

75. Tunstall, I., "Flying Wing Gliders", Wingspan Magazine, No.71, Dec/Jan. 1991.

76. Martin, C.A., and Ward, R.E., "Cranfield A1 The first Fifty Flights", Cranfield Institute of Technology, C. of A. Memo 7703, April 1977.

77. Trotman, C.K., "A1 Aerobatic Aircraft - Fuselage Proof Test", Cranfield College of Aeronautics, Test Report: TR/A1/14, 13 Aug. 1976.

78. Anderson, M.S., Williams, F.W.,Banerjee, J.R., Durling, B.J., Herstrom, C.L., Kennedy D., and Warnaar, D.B., "User's Guide to the Computer Program BUNVIS-RG (An Exact Buckling and Vibration Program for Lattice Structures, with Repetitive Geometry and Substructuring Options", NASA Tech. Memo. 87669, Nov. 1986.

79. Howe D, (College of Aeronautics, Cranfield Institute of Technology), Private Communication, Oct. 1987.

80. Howe D, (College of Aeronautics, Cranfield Institute of Technology), Private Communication, Oct. 1990.

81. Lottati, I., "The Role of Structural and Aerodynamic Damping on the Aeroelastic Behaviour of Wings", *Journal of Aircraft,* Vol.23, No 7, July 1986, pp.605-608.

82. Hollowell, S.J. and Dugundji, J., "Aeroelastic Flutter and Divergence of Stiffness Coupled Graphite/Epoxy Cantilevered Plates", *Journal of Aircraft*, Vol. 21, Jan. 1984, pp.69-76.

83. Landsberger, B. and Dugundji, J., "Experimental Aeroelastic Behaviour of Unswept and Forward Swept Graphite/Epoxy Wings", *Journal of Aircraft*, Vol. 22, Aug. 1985, pp.679-686.

84. Chen, G. and Dudundji, J., "Experimental Aeroelastic Behaviour of Forward-Swept Graphite/Epoxy Wings with Rigid-Body Freedom", *Journal of Aircraft*, Vol. 24, July 1987.

85. McLaughlin, M.D., "A Theoretical Investigation of the Short-Period Dynamic Longitudinal Stability of Airplane Configurations having Elastic Wings of $0°$ to $60°$ Sweepback", NACA TN 3251, Dec. 1954.

86. Milne, R.D., "Dynamics of the Deformable Aeroplane", ARC, R. & M. Rept. No. 3345, Sept. 1962.

87. Kemp, W.B., "Definition and Application of Longitudinal Stability Derivatives of Elastic Airplanes", NASA TN D-6629, March 1972.

88. Warzak, M.R., and Schmidt, D.K., "On the Flight Dynamics of Aeroelastic Vehicles", *Journal of Aircraft*, Vol.25, June 1988, pp.563-571.

89. Dusto, A.R., "An Analytical Method for Predicting the Stability and Control Characteristics of Large Elastic Airplanes at Subsonic and Supersonic Speeds", Part 1, AGARD CP No.46, March 1970.

90. Rodden, W.P. and Love, J.R., "Equations of Motion of an Elastic Flight Vehicle Utilising Static Aeroelastic Characteristics of the Restrained Vehicle", *25th Structures, Structural Dynamics and Materials Conference, Palm Springs, USA*, 17-18 May 1984, *AIAA* Paper 84-0986, pp.236-250.

91. Dusto, A.R., Brune, G.W., Dornfeld, G.M., Mercer, J.E., Pilet, S.C., Rubbert, P.E., Schwanz, R.C., Smutny, P., Tinoco, E.N., and Weber, J.A., "A Method for Predicting the Stability Derivatives of an Elastic Airplane", Vol.1-FLEXSTAB Theoretical Description, NASA CR-114712, Oct. 1974; or AFFDL TR-74-91, Vol.1, Nov. 1974, pp.4-4 to 4-26, 5-11 to 5-14.

92. Goland, M., "The Quasi-steady Air Forces for Use in Low-Frequency Stability Calculations", *Journal of the Aeronautical Sciences*, Vol.17, No.10, Oct. 1950, pp.601-608.

93. White, R.J., and Dean, G.K., "Force and Moment Coefficents for

a Thin Airfoil with Flap and Tab in a Form Useful for Stability and Control Calculations", NACA TN 960, Jan. 1945.

94. Goland, M., "Stick-Fixed, Short-Period Stability Based on the Wagner Air Forces", Reissner Anniversary Volume, Contributions to Applied Mechanics, J.W. Edwards, Ann Arbour, Mich., 1949.

95. Edwards, J.W., "Unsteady Aerodynamic Modelling and Active Aeroelastic Control", Ph.D. Thesis, Dept. of Aeronautics and Astronautics, Stanford University, 1976.

96. Karpel, M., "Design for Active Flutter Suppression and Gust Alleviation Using State-Space Aeroelastic Modeling", *Journal of Aircraft*, Vol.19, No.3, March 1982, pp.221-227.

97. Topp, L.J., Rowe, W.S., and Shattuck, A.W., "Aeroelastic Considerations in the Design of Variable Sweep Airplanes", *The 5th Congress of the International Council of the Aeronautical Sciences, London,* Paper 66-12, 1966.

98. Sensberg, O, and Laschkin, B., "Flutter Induced by Aerodynamic Interference between Wing and Tail", *Journal of Aircraft,* Vol 7, No.4, July-Aug. 1970, pp.319-324.

99. Shelton, J.D., Tucker, P.B., and Davis, J.C., "Wing -Tail Interaction Flutter of Moderately Spaced Tandem Airfoils", *AIAA* Paper 69-57, New York, 1969.

100. Balcerak J.C., "Flutter Tests of Variable Sweep Configurations", Air Force Flight Dynamics Lab., Wright-Patterson Air Force Base, Ohio. AFFDL-TR-68-101, Sept. 1968.

101. *Proceedings of the Symposium on Unsteady Aerodynamics for Aeroelastic Analysis of Interfering Surfaces, Tonsberg, Norway,* AGARD-CP-80-71, Nov. 1970,

102. Hancock, G.J., and Lam, J.S., "On the Application of Axiomatic Aerodynamic Modeling to Aircraft Dynamics, Part 1 - Introduction to the Concept of Axiomatic Aerodynamic Modeling", *The Aeronautical Journal,* Jan. 1987.

103. Bertin, J.J., and Smith M.L., "Aerodynamics for Engineers", Prentice Hall, 1979.

104. NAG FORTRAN MANUAL, Mark 12, Vol.4, Numerical Algorithms Group, Oxford, UK, March 1987.

105. Engineering Science Data Unit, U.K., Data Sheet 80020

106. Houghton, E.L., and Carruthers, N.B., "Aerodynamics for Engineering Students", 3rd Edition, Edward Arnold, 1986.

107. Stinton, D., "The Design of the Aeroplane", Blackwell Scientific Publications, 1987.

108. Cranfield Institute of Technology, "Cranfield A1 Specification". Flight Invert Ltd, June 1976.

109. JAR-25, Joint Aviation Requirements, Joint Aviation Authorities Committee, 1991.

110. Mitchell, C.G., "Assessment of the Accuracy of Gust Response Calculations by Comparison with Experiments", *Journal of Aircraft*, Vol.7, No.2, March-April 1970, pp.117-125.

111. Perry III, B., Pototzky, A.S, and Woods, J.A., "NASA Investigation of a Claimed "Overlap" Between Two Gust Response Analysis Methods", *Journal of Aircraft*, Vol.27, NO.7, July 1990, pp.605-611.

112. Jones, J.G., "On the Formulation of Gust-Load Requirements in Terms of the Statistical Discrete Gust Method", RAE Tech. Memo. FS 208, 1978.

113. Huntley, E., "Spectral Gust Alleviation Factor", *The 6th Congress of the International Council of the Aeronautical Sciences, Munich, FRG,* Paper No. 68-47, 9-13 Sept. 1968.

114. Zbrozek, J.K., "Longitudinal response of Aircraft to Oscillatory vertical gusts", RAE Rep. Aero. 2559, 1955.

115. Huntley, E. and Littlewood, P.G., "Spectral Gust Alleviation Factors for Pitching Aircraft", *The Aeronautical Journal*, July 1972, pp.433-442.

116. Hoblit, F.M., *Gust Loads on Aircraft: Concepts and Applications, AIAA* Publications, New York, 1988.

117. Karman, T. Von. and Biot, M.A., "Mathematical Methods in Engineering", McGraw-Hill Book Company Inc., New York, 1940.

118. Mitchell, C.G.B., "Calculation of the Response of a Flexible Aircraft to Harmonic and Discrete Gusts by a Transform Method", ARC, R. & M. Rept. No. 3498, Nov. 1965.

119. Craig, R.R., "Structural Dynamics an Introduction to Computer Methods", John Wiley & Sons, 1981.

120. Kron, N.J. Jr., "Divergence Elimination with advanced composites," *AIAA* Paper 75-1009, 1975.

121. Weisshaar, T.A.,"The influence of Aeroelasticity on swept composite wings," AFWAL-TR-80-3137, Nov. 1980.

122. Weisshaar, T.A.,"Aeroelastic Tailoring of Forward Swept Composite Wings," *Journal of Aircraft*, Vol.18, Aug. 1981, pp.669-676.

123. Sherrer, V.C., Hertz, T.J., and Shirk, M.H.," Wind Tunnel Demonstration of Aeroelastic Tailoring Applied to Forward Swept Wings," *Journal of Aircraft*, Vol.18, Nov. 1981, pp.976-983.

124. Wilkinson, K. and Rauch,F.,"Predicted and Measured Divergence Speeds of an Advanced Composite Forward Swept Wing Model," AFWAL TR-80-3059, July 1980.

125. Ellis, J.W., Dobbs, S.K., and Miller, G.D.,"Structural Design and Wind Tunnel Testing of a Forward Swept Fighter Wing," AFWAL TR-80-3073, July 1980.

126. Hertz, T.J., Shirk, M.H., Ricketts, R.H., and Weisshaar, T.A., "On the Track of Practical Forward Swept Wings," *AIAA Journal*, Vol.20, Jan. 1982, pp.40-53.

127. Weisshaar, T.A., Zeiler, T.A., Hertz, T.J., and Shirk, M.H.,"Flutter of Forward Swept Wings, Analyses and Tests," *Proceedings of the 23rd AIAA/ASME/ASCE/AHS Structures, Structural Dynamics, and Materials Conference, New Orleans, La., USA,* May 1982, pp.111-121.

128. Jensen, D.W.,"Natural Vibration of Cantilevered Graphite/Epoxy Plates with Bending-Torsion Coupling", M.S. Thesis, M.I.T. Department of Aeronautics and Astronautics, Cambridge, Mass., Aug. 1981.

129. Jensen, D.W., Crawley, E.F., and Dugundji, J.,"Vibration of Cantilevered Graphite/Epoxy Plates with Bending-Torsion Coupling," Journal of Reinforced Plastics and Composites, Vol.1, July 1982, pp.254-269.

130. Ashton, J.E. and Whitney, J.M., Theory of laminated Plates, Technomic Publishing Co., Stamford, Conn., 1970.

131. Crawley, E.F. and Dugundji, J.,"Frequency Determination and Non-dimensionalization for Composite Cantilever Plates," Journal of Sound and Vibration, Vol.72(1), 1980, pp.1-10.

132. FEAL, 1984: LUSAS: Finite Element Stress Analysis System, User's manual, Finite Element Analysis Ltd., 25 Holborn Viaduct, London EC1A 2BP.

133. Toll, T., and Queijo, M.J., "Approximate Relations and Charts for Low Speed Stability Derivatives of Swept Wings", NACA TN 1581, 1948.

134. "Tables of the Bessel Functions $J_0(z)$ and $J_1(z)$ for Complex Arguments", 2nd Edition, Mathematical Tables Project, National Bureau of Standards, Columbia University Press, 1947.

135. "Tables of the Bessel Functions $Y_0(z)$ and $Y_1(z)$ for Complex

Arguments", Mathematical Tables Project, National Bureau of Standards, Columbia University Press, 1950.

136. Kinnaman, E.B., "Flutter Analysis of Complex Airplanes by Experimental Methods", *Journal of the Aeronautical Sciences*, Vol.19, Sept. 1952, pp.577-584.

137. Cook, M.V., and Malik, I.A., "A Wind Tunnel Facility for Dynamically Testing Aircraft Models with Active Controls", *Aerogram*, 1987. pp.12-14.

138. Cook, M.V., and Heydari, F., "Research into the Stability and Control Characteristics of Combat Aircraft with Forward Swept Wings", *Aerogram*, 1985, pp.11-14.

APPENDIX A

A.0 Equations of Motion
A.1 Method of Analysis
A.1.1 Assumed Modes

This present means of solution involves solving this dynamic system in terms of Lagranges equation. This is some what a specialised form of the principle of virtual work. In order to generate an N degree of freedom model of a continuous system its space configuration has to be described by a set of discrete generalised co-ordinates as shown below.

$$w(x,y,z,t) = \sum_{i=1}^{N} \psi_i(x,y,z) \, u_i(t) \qquad (A.1)$$

where w can represent any type of displacement by the system. If the system were a wing then these would be heave and rotation about the elastic axis. Ψ is a functional relationship between displacement and generalised co-ordinate. It is by choosing the function $\psi_i(x,y,z)$ that we define the N degree of freedom model. The functions $\psi_i(x,y,z)$ must form a linearly independent set. In addition each $\psi_i(x,y,z)$ must possess derivatives up to the order appearing in V (The potential work done) and must satisfy all prescribed boundary conditions, that is, displacement-type boundary conditions.

$u_i(t)$ are the time dependent set of generalised co-ordinates set about the system. These can represent translation and rotation about the system. After a short derivation, relating the Virtual work done (δW) due to external forces to the Potential (V) and the Kinetic energy (T) Lagranges equation is obtained.

$$\frac{d}{dt} \left(\frac{\partial T}{\partial \dot{u}_i} \right) - \frac{\partial T}{\partial u_i} + \frac{\partial V}{\partial u_i} = Q_i, \qquad i = 1,2,\ldots N \qquad (A.2)$$

where Q_i is the generalised forces and is multiplied by the generalised co-ordinates to give the Virtual work.

$$\delta W = \sum_{i=1}^{N} Q_i \, \delta u_i \qquad\qquad (A.3)$$

where

$$Q_i = \int_S F(x,y,t) \; \frac{\partial w}{\partial u_i} \; dS$$

The kinetic energy T may be written as

$$T = \frac{1}{2} \int_S \left(\sum_{i=1}^{N} \frac{\partial w}{\partial u_i} \, \dot{u}_i \right)^2 m(x,y,z) \; dS$$

$$T = \frac{1}{2} \sum_{i=1}^{N} \sum_{j=1}^{N} \int_V \psi_i(x,y,z) \, \psi_j(x,y,z) \, m(x,y,z) \; dV \, \dot{u}_i \, \dot{u}_j$$

$$(A.4)$$

This may be written as

$$T = \frac{1}{2} \sum_{i=1}^{N} \sum_{j=1}^{N} m_{ij} \, \dot{u}_i \, \dot{u}_j$$

where

$$m_{ij} = \int_V m(x,y,z) \, \psi_i \, \psi_j \; dV \qquad\qquad (A.5)$$

This is known as the <u>consistent mass matrix</u>

The potential energy U may be expanded in a Taylor series about the equilibrium position ignoring second order terms we have.[119]

$$U = \frac{1}{2} \sum_{i=1}^{N} \sum_{j=1}^{N} \left(\frac{\partial U}{\partial u_i \, \partial u_j} \right) u_i \, u_j$$

This may be written as

$$U = \frac{1}{2} \sum_{i=1}^{N} \sum_{j=1}^{N} K_{ij} \, u_i \, u_j \qquad (A.6)$$

where
$$K = \left(\frac{\partial U}{\partial u_i \, \partial u_j} \right)^2 \qquad (A.7)$$

Applying expressions (A.5) and (A.7) the elemental mass matrix and stiffness matrix are created for a 3-dimensional frame element as shown in Fig. 3.4 consisting of beam elements undergoing longitudinal, lateral and torsional displacements. The finite element method[119] is used to obtain the mass M andstiffness K matrix for the system. Hence with these mass and stiffness matrices the equation for free motion.

$$\sum_{i=1}^{N} M_{ij} \, u_j + \sum_{j=1}^{N} K_{ij} \, u_j = 0 \qquad \text{for } i = 1,2 \text{ --- } N \qquad (A.8)$$

A.1.2 Mode-Superposition Method

In order to solve this equation efficiently it has to be rendered more manageable. To do this the normal modes of the continuous system are incorporated and the principal of orthogonality applied.

To obtain these natural modes the right hand is set to zero and motion of the form $u = \phi e^{i\omega t}$ assumed. The resulting dynamic stiffness matrix is solved for

$$\left| \; K \; - \; \omega^2 M \; \right| \; \phi \; = \; 0 \qquad\qquad (A.9)$$

where ω is the natural frequency and ϕ is the corresponding mode shape.

A.1.3 Orthogonality

For modes with distinct frequencies, that is $\omega_i \neq \omega_j$ it is necessary that

$$\phi_i^T \; m \; \phi_j \; = \; 0 \qquad (\; \omega_i \neq \omega_j \;)$$

The i and j modes are said to be orthogonal with respect to the mass matrix. The same principle can be applied to the stiffness matrix in which case the i mode and j mode are also orthogonal with respect to the stiffness matrix that is

$$\phi_i^T \; k \; \phi_j \; = \; 0 \qquad (\; \omega_i \neq \omega_j \;)$$

Once the frequencies ω and mode shapes Φ where $\Phi = (\; \phi_1, \; \phi_2,$ -- $\phi_n)$ have been established the following co-ordinate transformation $u(t) = \Phi q(t)$ is introduced. Where $q(t)$ are referred to as normal co-ordinates. Since they are generalised co-ordinates of a particular type they may be substituted into the Lagranges equation and the following equation of forced motion becomes.

$$\left[\begin{smallmatrix} \diagdown \\ M \\ \diagdown \end{smallmatrix} \right] \left[\; \ddot{q} \; \right] \; + \; \left[\begin{smallmatrix} \diagdown \\ K \\ \diagdown \end{smallmatrix} \right] \left[\; q \; \right] \; = \; \left[\; P \; \right] \qquad (A.10)$$

where

$$\left[\begin{smallmatrix} \diagdown \\ M \\ \diagdown \end{smallmatrix} \right] = \Phi^T \; M \; \Phi \quad \text{Diagonalised generlised mass Matrix}$$

$$\left[\begin{smallmatrix} \diagdown \\ k \\ \diagdown \end{smallmatrix} \right] = \Phi^T \; K \; \Phi \quad \text{Diagonalised generalised stiffness matrix}$$

$$\left[\; P \; \right] = \Phi^T \; P(t) \quad \text{Generalised force}$$

This transformation has the effect of uncoupling the equations of motion, This leads to N separate single degree of freedom equations. This significantly reduces the computational time for solving the equations. This technique is known as the mode-superposition method.[119]

B.0 Unsteady Aerodynamic Model

B.1 Aerodynamic Strip Theory

B.1.1 Straight Wing

The generalised forces are the unsteady aerodynamic forces generated across the wing on a representative section shown in Fig. 2.2. Where the two displacements considered are heave and rotation of the wing about the elastic axis.

To create the necessary displacement dependent forces, Theodorsen's[5] explicit expressions for lift L and pitching moment M_α per unit spanwise distance are implemented, taking streamwise sections denoted in Fig. 2.2.

$$L = -\pi\rho b^2 \left\{ \ddot{h} + U\dot{\alpha} - ba_h\ddot{\alpha} \right\} - 2\pi\rho UbC(k)\left\{ \dot{h} + U\alpha + b(\tfrac{1}{2} - a_h)\dot{\alpha} \right\}$$

(B.1)

$$M_\alpha = \pi\rho b^2 \left\{ ba_h\ddot{h} - Ub(\tfrac{1}{2} - a_h)\dot{\alpha} - b^2(\tfrac{1}{8} + a_h^2)\ddot{\alpha} \right\}$$
$$+ 2\pi\rho Ub^2(a_h + \tfrac{1}{2})C(k)\left\{ \dot{h} + U\alpha + b(\tfrac{1}{2} - a_h)\dot{\alpha} \right\}$$

(B.2)

In the flutter problem sinousoidal motion is assumed to exist, so the Theodorsen expressions used for lift and moment in the flutter analysis are valid for aerofoil oscillation of the form $e^{i\omega t}$ or $e^{ik\hat{t}}$. Making the appropiate substitutions and assuming $h = he^{ik\hat{t}}$ and $\alpha = \alpha e^{ik\hat{t}}$, where $\hat{t} = ut/b$ Eqs.(B.1) and (B.2) can be rearranged to give.

$$\frac{L}{\rho\pi bU^2} = \left[-k^2\left\{ a_h\alpha - \frac{h}{b} \right\} - ik\alpha - 2C(k)\left\{ \frac{ikh}{b} + \alpha + (\tfrac{1}{2} - a_h)ik\alpha \right\} \right]$$

(B.3)

$$\frac{M_\alpha}{\pi\rho b^2 U^2} = \left[(a_h + \tfrac{1}{2}) 2C(k) \left\{ \frac{ikh}{b} + \alpha + (\tfrac{1}{2} - a_h) ik\alpha \right\} + \frac{k^2}{8}\alpha \right.$$

$$\left. -k^2 a_h \left\{ \frac{h}{b} - a_h\alpha \right\} - \left\{ \tfrac{1}{2} - a_h \right\} i\alpha k \right]$$

(B.4)

Where $C(k) = F(k) + iG(k)$ is known as the Theodorsen function. $C(k)$ has the effect of modifying the phase between the forcing and damping components of the oscillatory aerodynamic forces.

In matrix form Eqs.(B.3) and (B.4) can be isolated in terms of the displacements considered.

$$\begin{bmatrix} L \\ M_\alpha \end{bmatrix} = \begin{bmatrix} A_{11} & A_{12} \\ A_{21} & A_{22} \end{bmatrix} \begin{bmatrix} h \\ \alpha \end{bmatrix}$$

(B.5)

where

$$A_{11} = -\pi\rho U^2 \left\{ -k^2 + 2C(k)ik \right\}$$

$$A_{12} = -\pi\rho U^2 b \left[\left\{ a_h k^2 + ik \right\} + 2C(k) \left\{ 1 + (\tfrac{1}{2} - a_h) ik \right\} \right]$$

$$A_{21} = \pi\rho b U^2 \left[2C(k)(a_h + \tfrac{1}{2}) ik - k^2 a_h \right]$$

$$A_{22} = \pi\rho b^2 U^2 \left[2(a_h + \tfrac{1}{2})C(k) \left\{ 1 + (\tfrac{1}{2} - a_h) ik \right\} + \frac{k^2}{8} \right.$$

$$\left. + k^2 a_h^2 + (a_h - \tfrac{1}{2}) ik \right]$$

(B.6)

B.2 Formulation of the Generalised Aerodynamic Matrix

In order to apply the transformation into normal co-ordinates uncoupled or coupled normal modes are chosen to represent heave h and pitch α about the elastic axis.

$$h(y,t) = \sum_{i=1}^{N} h_i(y)\, q_i(t) \qquad\qquad (B.7)$$

$$\alpha(y,t) = \sum_{i=1}^{N} \alpha_i(y)\, q_i(t) \qquad\qquad (B.8)$$

Utilising the virtual work done by the aerodynamic forces

$$\delta W_i = \sum_{i=1}^{N} \delta q_i \int_0^S (L(y)h_i(y) + M_\alpha(y)\alpha_i(y))\; dy \qquad (B.9)$$

Equations (B.7) − (B.9) can be written as :

$$
\begin{bmatrix} \dfrac{\delta W_1}{\delta q_1} \\[2mm] \dfrac{\delta W_2}{\delta q_2} \\[2mm] \vdots \\[1mm] \vdots \\[1mm] \dfrac{\delta W_n}{\delta q_n} \end{bmatrix}
= \int_0^S
\begin{bmatrix} h_1 & \alpha_1 \\ h_2 & \alpha_2 \\ \vdots & \vdots \\ h_n & \alpha_n \end{bmatrix}
\begin{bmatrix} L \\ M_\alpha \end{bmatrix}
dy \qquad (B.10)
$$

Substituting for $\begin{bmatrix} L \\ M_\alpha \end{bmatrix}$ from Eq.(B.5) into Eq.(B.10),

$$
\begin{bmatrix} \dfrac{\delta W_1}{\delta q_1} \\[6pt] \dfrac{\delta W_2}{\delta q_2} \\ \vdots \\ \dfrac{\delta W_n}{\delta q_n} \end{bmatrix}
=
\int_0^s
\begin{bmatrix} h_1 & \alpha_1 \\ h_2 & \alpha_2 \\ \vdots & \vdots \\ h_n & \alpha_n \end{bmatrix}
\begin{bmatrix} A_{11} & A_{12} \\ A_{21} & A_{22} \end{bmatrix}
\begin{bmatrix} h_1 & h_2 & \cdots & h_n \\ \alpha_1 & \alpha_2 & \cdots & \alpha_n \end{bmatrix}
\begin{bmatrix} q_1 \\ q_2 \\ \vdots \\ q_n \end{bmatrix} dy
$$

$$
=
\begin{bmatrix} Q_{11} & Q_{12} & \cdots & Q_{1n} \\ Q_{21} & Q_{22} & \cdots & Q_{2n} \\ \vdots & \vdots & & \vdots \\ Q_{n1} & Q_{n2} & \cdots & Q_{nn} \end{bmatrix}
\begin{bmatrix} q_1 \\ q_2 \\ \vdots \\ q_n \end{bmatrix}
\tag{B.11}
$$

where

$$
Q(i,j) = \int_0^s A_{11} h_i h_j + A_{12} h_i \alpha_j + A_{21} h_j \alpha_i + A_{22} \alpha_i \alpha_j \ dy
\tag{B.12}
$$

B.3 Unsteady Aerodynamic Model for a swept Wing

B.3.1 Cosine Theory

Equations (B.1) and (B.2) can be modified to take into account the effect of sweep for streamwise sections by factoring the lift and moment by $\cos \Lambda$, Hence $A_{(\Lambda)\,i,j} = A_{(\Lambda=0)\,i,j} \cos \Lambda$

B.3.2 Velocity Component Theory

For sections normal to the elastic axis as denoted in Fig. 2.2, the explicit expressions for lift and moment per unit distance along the swept span are given by Barmby, Cunningham and Garrick,[57] retaining second order terms,

$$
\bar{L} = -2\pi\rho U_n \bar{b} \, C(k_n) \left\{ \dot{h} + U_n \bar{\alpha} + U_n \sigma \tan \Lambda + \bar{b} \left(\tfrac{1}{2} - a_h \right) (\dot{\bar{\alpha}} + \right.
$$

204

$$U_n \tau \tan \Lambda) \Big\} - \pi\rho\bar{b}^2 \Big\{ \ddot{h} + U_n\dot{\alpha} + 2U_n\dot{\sigma} \tan \Lambda + U_n^2\tau \tan \Lambda +$$

$$U_n^2 \frac{\partial\sigma}{\partial\bar{y}} \tan^2\Lambda \Big\} + \pi\rho\bar{b}^3 a_h \Big\{ \ddot{\alpha} + 2U_n\dot{\tau} \tan \Lambda + U_n^2 \frac{\partial\tau}{\partial\bar{y}} \tan^2\Lambda \Big\}$$

(B.13)

and

$$\bar{M}_\alpha = 2\pi\rho U_n \bar{b}^2 \Big\{ (\tfrac{1}{2} + a_h) C(k_n) (\dot{h} + U_n\bar{\alpha} + U_n\sigma \tan \Lambda +$$

$$\bar{b}(\tfrac{1}{2} - a_h)(\dot{\bar{\alpha}} + U_n\tau \tan \Lambda) \Big\} - \pi\rho U_n \bar{b}^3 \Big\{ (\tfrac{1}{2} - a_h)\dot{\alpha} - \tfrac{1}{2} U_n\tau \tan \Lambda) \Big\}$$

$$+ \pi\rho\bar{b}^3 a_h \Big\{ \ddot{h} + 2U_n\dot{\sigma} \tan \Lambda + U_n^2\tau \tan \Lambda + U_n^2 \frac{\partial\sigma}{\partial\bar{y}} \tan^2\Lambda \Big\}$$

$$- \pi\rho\bar{b}^4 \Big\{ (\tfrac{1}{8} + a_h^2)(\ddot{\alpha} + 2U_n\dot{\tau} \tan \Lambda + U_n^2 \frac{\partial\tau}{\partial\bar{y}} \tan^2\Lambda) \Big\}$$

(B.14)

where $k_n = \dfrac{\omega b_n}{U_n}$, $\sigma = \dfrac{\partial h}{\partial\bar{y}}$ and $\tau = \dfrac{\partial\bar{\alpha}}{\partial\bar{y}}$

Assuming sinusoidal motion

$$\frac{\bar{L}}{\pi\rho\bar{b}U_n^2} = \Big[-2 C(k_n) \Big\{ ik_n \frac{h}{\bar{b}} + \bar{\alpha} + \sigma \tan \Lambda + (\tfrac{1}{2} - a_h)(ik_n\bar{\alpha} +$$

$$\bar{b}\tau \tan \Lambda) \Big\} - \Big\{ -k_n^2 \frac{h}{\bar{b}} + ik_n\bar{\alpha} + 2ik_n\sigma \tan \Lambda + \bar{b}\tau \tan \Lambda$$

$$+ \bar{b} \frac{\partial\sigma}{\partial\bar{y}} \tan^2\Lambda) \Big\} + a_h \Big\{ -k_n^2\bar{\alpha} + 2ik_n\bar{b}\tau \tan \Lambda + \bar{b}^2 \frac{\partial\tau}{\partial\bar{y}} \tan^2\Lambda \Big\} \Big]$$

(B.15)

and

$$\frac{\overline{M}_\alpha}{\pi\rho\overline{b}^2 U_n^2} = \left[2(\tfrac{1}{2} + a_h) C(k_n) \left\{ ik_n \frac{h}{\overline{b}} + \overline{\alpha} + \sigma \tan \Lambda + \right. \right.$$

$$\left. (\tfrac{1}{2} - a_h)(ik_n\overline{\alpha} + \overline{b}\tau \tan \Lambda) \right\} - \left\{ (\tfrac{1}{2} - a_h) ik_n\alpha - \tfrac{1}{2}\overline{b}\tau \tan \Lambda) \right\}$$

$$+ a_h \left\{ -k_n^2 \frac{h}{\overline{b}} + 2ik_n\sigma \tan \Lambda + \overline{b}\tau \tan \Lambda + \overline{b} \frac{\partial\sigma}{\partial\overline{y}} \tan^2\Lambda \right\}$$

$$\left. - \left\{ (\tfrac{1}{8} + a_h^2)(-k_n^2\overline{\alpha} + 2ik_n\overline{b}\tau \tan \Lambda + \overline{b}_n^2 \frac{\partial\tau}{\partial\overline{y}} \tan^2\Lambda) \right\} \right]$$

$$(B.16)$$

In matrix form equations (B.15) and (B.16) can be expressed, in terms of the displacements considered.

$$\begin{bmatrix} \overline{L} \\ \overline{M}_\alpha \end{bmatrix} = \begin{bmatrix} A_{11} & A_{12} \\ A_{21} & A_{22} \end{bmatrix} \begin{bmatrix} h \\ \overline{\alpha} \end{bmatrix} + \begin{bmatrix} DA_{11} & DA_{12} \\ DA_{21} & DA_{22} \end{bmatrix} \begin{bmatrix} \sigma \\ \tau \end{bmatrix}$$

$$+ \begin{bmatrix} DDA_{11} & DDA_{12} \\ DDA_{21} & DDA_{22} \end{bmatrix} \begin{bmatrix} \sigma' \\ \tau' \end{bmatrix} \qquad (B.17)$$

$$\sigma' = \frac{\partial\sigma}{\partial\overline{y}} \qquad \text{and} \qquad \tau' = \frac{\partial\tau}{\partial\overline{y}}$$

where

$$A_{11} = -\pi\rho U_n^2 \left\{ -k_n^2 + 2C(k) ik \right\}$$

206

$$A_{12} = -\pi\rho U_n^2 \bar{b} \left[\left\{ a_h k_n^2 + i k_n \right\} + 2C(k) \left\{ 1 + \left(\frac{1}{2} - a_h \right) i k_n \right\} \right]$$

$$A_{21} = \pi\rho \bar{b} U_n^2 \left\{ 2C(k) \left(a_h + \frac{1}{2} \right) i k_n - k_n^2 a_h \right\}$$

$$A_{22} = \pi\rho \bar{b}^2 U_n^2 \left[2 \left(a_h + \frac{1}{2} \right) C(k) \left\{ 1 + \left(\frac{1}{2} - a_h \right) i k_n \right\} + \left\{ \frac{1}{8} k_n^2 \right. \right.$$

$$\left. \left. + k_n^2 a_h^2 + \left(a_h + \frac{1}{2} \right) i k_n \right\} \right]$$

(B.18)

first order terms

$$DA_{11} = -2\pi\rho U_n^2 \bar{b} \tan \Lambda \left\{ i k_n + C(k_n) \right\}$$

$$DA_{12} = 2\pi\rho U_n^2 \bar{b}^2 \tan \Lambda \left\{ a_h i k_n - C(k_n) \left(\frac{1}{2} - a_h \right) \right\}$$

$$DA_{21} = 2\pi\rho U_n^2 \bar{b}^2 \tan \Lambda \left\{ a_h i k_n + C(k_n) \left(\frac{1}{2} + a_h \right) \right\}$$

$$DA_{22} = -2\pi\rho U_n^2 \bar{b}^3 \tan \Lambda \left\{ \left(\frac{1}{8} + a_h^2 \right) i k_n + \frac{1}{4} - C(k_n) \left(\frac{1}{2} - 2a_h^2 \right) \right.$$

$$\left. - \frac{1}{2} a_h \right\}$$

(B.19)

The second order terms

$$DDA_{11} = -\pi\rho U_n^2 \bar{b}^2 \tan^2 \Lambda$$

$$DDA_{12} = \pi\rho U_n^2 \bar{b}^3 a_h \tan^2 \Lambda$$

$$DDA_{21} = \pi\rho U_n^2 \bar{b}^3 \tan^2 \Lambda$$

207

$$DDA_{22} = -\pi\rho U_n^2 \bar{b}^4 \left(\frac{1}{8} + a_h^2 \right) \tan^2\Lambda$$

<div align="right">(B.20)</div>

Substituting these new expressions for the lift and moment into Eq.(B.10) and taking modes along the swept span.

$$
\begin{bmatrix} \dfrac{\delta W_1}{\delta q_1} \\ \dfrac{\delta W_2}{\delta q_2} \\ \vdots \\ \dfrac{\delta W_n}{\delta q_n} \end{bmatrix}
= \int_0^l \left[\begin{bmatrix} h_1 & \bar{\alpha}_1 \\ h_2 & \bar{\alpha}_2 \\ \vdots & \vdots \\ h_n & \bar{\alpha}_n \end{bmatrix} \begin{bmatrix} A_{11} & A_{12} \\ A_{21} & A_{22} \end{bmatrix} \begin{bmatrix} h_1 & h_2 & \cdots & h_n \\ \bar{\alpha}_1 & \bar{\alpha}_2 & \cdots & \bar{\alpha}_n \end{bmatrix} + \right.
$$

$$
\begin{bmatrix} h_1 & \bar{\alpha}_1 \\ h_2 & \bar{\alpha}_2 \\ \vdots & \vdots \\ h_n & \bar{\alpha}_n \end{bmatrix} \begin{bmatrix} DA_{11} & DA_{12} \\ DA_{21} & DA_{22} \end{bmatrix} \begin{bmatrix} \sigma_1 & \sigma_2 & \cdots & \sigma_n \\ \tau_1 & \tau_2 & \cdots & \tau_n \end{bmatrix} +
$$

$$
\left. \begin{bmatrix} h_1 & \bar{\alpha}_1 \\ h_2 & \bar{\alpha}_2 \\ \vdots & \vdots \\ h_n & \bar{\alpha}_n \end{bmatrix} \begin{bmatrix} DDA_{11} & DDA_{12} \\ DDA_{21} & DDA_{22} \end{bmatrix} \begin{bmatrix} \sigma_1' & \sigma_2' & \cdots & \sigma_n' \\ \tau_1' & \tau_2' & \cdots & \tau_n' \end{bmatrix} \right] \begin{bmatrix} q_1 \\ q_2 \\ \vdots \\ q_n \end{bmatrix} d\bar{y} \quad \text{(B.21)}
$$

Therefore the expression for the generalised forces is written as

$$
Q(i,j) = \int_0^l \left[\left\{ A_{11} h_i h_j + A_{12} h_i \bar{\alpha}_j + A_{21} \bar{\alpha}_i h_j + A_{22} \bar{\alpha}_i \bar{\alpha}_j \right\} + \right.
$$

$$\left\{ DA_{11}h_1\sigma_j + DA_{12}h_1\tau_j + DA_{21}\bar{\alpha}_1\sigma_j + DA_{22}\bar{\alpha}_1\tau_j \right\} +$$

$$\left\{ DDA_{11}h_1\sigma'_j + DDA_{12}h_1\tau'_j + DDA_{21}\bar{\alpha}_1\sigma'_j + DDA_{22}\bar{\alpha}_1\tau'_j \right\} \Bigg] d\bar{y}$$

(B.22)

B.4 Implementation of Davies Lifting Line Program
B.4.1 Theory and Data Preparation

There was originally a suite of four programs, each written in FORTRAN provided by Ref.(44), namely

    i)   STORAGE,

    ii)   MODAL DATA,

    iii)   ISOLATED WINGS,

    iv)   LOADING,

The STORAGE program evaluates two integers which are used to allocate space for the arrays ocurring in the execution of the ISOLATED WINGS programs.

The MODAL DATA program will determine numbers which form the data for input into the ISOLATED WINGS program for the particular case of a wing under-going oscillation in the three modes of heave, pitch and symmetric control surface rotation.

The ISOLATED WINGS program will determine, for given subsonic Mach number and given frequency parameter, the generalised airforce coefficient associated with oscillation of a wing in a number of given modes of oscillation. Also, at the option of the user, it will determine the values of the loading function, corresponding to each mode of oscillation, at the set of points on the wing known as the loading points.

The LOADING program will determine the values of the loading function at a series of points along a chord at any given spanwise position. Output from the ISOLATED WINGS program is used as data for input into the LOADING program. The loading may, for instance, be required for comparison with experimentally determined values.

The co-ordinate system is as shown in Fig.B1, where a flat plate wing with an axis of symmetry is situated in the space with

209

all its points fixed relative to the co-ordinate system OXYZ. The wing axis of symmetry passes through the origin 0, the axis OX is along the wing axis of symmetry, the axis OY lies in the plane of the wing and the axis OZ is then perpendicular to thr plane of the wing.

The flat plate wing is immersed in a uniform airstream having speed U in the direction of the positive X-axis. It is made to oscillate with circular frquency ω about its mean position in the Z = 0 plane in one of a number of modes of oscillation. In the mode K of Oscillation the displacement Z (x,y,t) in the direction of the positive X-axis at time t of a point on the wing from the point (x,y,0) is given by

$$Z_K(x,y,t) = l\zeta_K(x,y)e^{i\omega t} \qquad (B.23)$$

The modal function $\zeta_K(x,y)$ is non-dimensional

At the point on the oscillating wing displaced along the Z direction from the point (x,y,0) there is a pressure $p_K^+(x,y,t)$ acting on the upper surface of the wing and a pressure $p_K^-(x,y,t)$ acting on the lower surface of the wing in thhe mode k of oscillation the corresponding aerodynamic loading $L_K(x,y,t)$ acting on the wing in the mode k of oscillation is given by

$$L_K(x,y,t) = p_K^-(x,y,t) - p_K^+(x,y,t) \qquad (B.24)$$

and is the aerodynamic force per unit area acting on the wing in the direction of the positive Z-axis at time t.

we may write

$$L_K(x,y,t) = \rho U^2 l_K(x,y;\upsilon,M)e^{i\omega t} \qquad (B.25)$$

$$\upsilon = \frac{\omega\ l}{U} \qquad (B.26)$$

is the frequency parameter based on the typical length l and M is the Mach number. The loading function $l_K(x,y;\upsilon,M)$ is a non-dimensional complex function which depends directly on the

upwash function $\alpha_K(x,y;\upsilon)$, where $\alpha_K(x,y;\upsilon)$ is the non-dimensional function defined by

$$\alpha_K(x,y;\upsilon) = 1\,\frac{\partial\zeta_K(x,y)}{\partial x} + i\upsilon\zeta_K(x,y) \tag{B.27}$$

The dependence is expressed in the integral relationship.

$$\alpha_K(x,y;\upsilon) = \frac{1}{1^2}\iint_S 1_K(x_0,y_0;\upsilon,M)\ Ker\!\left(\frac{x-x_0}{1},\frac{y-y_0}{1};\upsilon,M\right)\ dx_0 dy_0 \tag{B.28}$$

where S is the planform of the complete wing and $Ker(x,y;\upsilon,M)$ is a kernel function whose form is known.

The generalised airforce coefficient $Q_{jk}(\upsilon,M)$ for the wing. Corresponding to the loading in the mode k and displacement in the mode j, is the non-dimensional quantity given by the formula.

$$Q_{jk}(\upsilon,M) = \frac{1}{1^2}\iint_S \zeta_j(x,y)\ 1_K(x,y;\upsilon,M)\ dxdy \tag{B.29}$$

It is convenient to write

$$Q_{jk}(\upsilon,M) = Q'_{jk}(\upsilon,M) + Q''_{jk}(\upsilon,M) \tag{B.30}$$

where $Q'_{jk}(\upsilon,M)$ and $Q''_{jk}(\upsilon,M)$ are real quantities.

The modal function $\zeta_K(x,y)$ for all the modes k of oscillation are taken as known and then the upwash functions $\alpha_K(x,y;\upsilon)$ are then determined from the integral equation (B.28) and finally the generalised airforce coefficients $Q_{jk}(\upsilon,M)$ are determined from formula (B.29) on substituting for the known functions $\zeta_j(x,y)$ and the already determined functions $1_K(x,y;\upsilon,M)$.

The loading function $1_K(x,y;\upsilon,M)$ is determined by solving the integral equation (B.28) numerically. To do this an approximation

$\hat{1}_K(x,y)$ to the loading function $1_K(x,y;\upsilon,M)$ must first be specified, involving a finite number of parameters whose values are initially unknown. These parameters can be taken to be approximate values of $1_K(x,y;\upsilon,M)$ at a finite number of separate points on the wing, which we shall call the loading points. The approximation $\hat{1}_K(x,y)$ to the loading function $1_K(x,y;\upsilon,M)$ is then expressed as an interpolation function on the approximations to $1_K(x,y;\upsilon,M)$ at the loading points, which properly takes into account the edge behaviour of the loading in the peripheral regions of the wings as a result of the condition that the loading at the trailing edge of S vanishes. The approximation to $1_K(x,y;\upsilon,M)$ at the loading points occur in the expression for the approximation $\hat{1}_K(x,y)$, as a linear combination. Hence using this approximation to the generalised force may be obtained $\hat{Q}_{ij}$ using expression (B.29).

The exact details of the input data for the lifting line code are given in Ref.(44). However as a brief summary the procedure is outlined below and its extension to cover the elastic modes.

The modal function ζ_j for the mode K is defined at m spanwise and n chordwise stations.

$$\zeta_{j,r,p} = \zeta'_{j,r,p} + i\upsilon\zeta''_{j,r,p} = \zeta_j\,(x^{(n,m)}_{r,p},y^{(m)}_p) \qquad (B.31)$$

where, referring to Fig. B2

$$x^{(n,m)}_{r,p} = e(y^{(m)}_p) + \tfrac{1}{2}\,c(y^{(m)}_p)\left[\,1 - \cos\left(\frac{(2r-1)\pi}{(2n+1)}\right)\right]$$

$$\eta^{(m)}_p = \cos\left(\frac{p\pi}{m+1}\right) \qquad\qquad j = 1,2 \,---\, K$$
$$r = 1,2 \,---\, n$$
$$p = 1,2 \,---\, m_H$$

$$y^{(m)}_p = s\eta_p$$

$$m_H = \tfrac{1}{4}\left(\,2m + L - (-1)^m L\right)$$

The upwash function $\alpha_K(x,y;\upsilon)$ is then obtained from the modal function hence.

$$\alpha_K = 1 \frac{\partial \zeta_K(x,y)}{\partial x} + i\upsilon \zeta_K(x,y) = \alpha_K(x_{1,u}^{(n,m)}, y_u^{(m)}; \upsilon) \tag{B.32}$$

where $\quad \alpha_{k,1,u} = \alpha'_{k,1,u} + i\upsilon \, \alpha''_{k,1,u}$

$$x_{1,u}^{(n,m)} = e(y_u^{(m)}) + \frac{1}{2} c(y_u^{(m)}) \left[1 - \cos\left(\frac{2i\pi}{(2n+1)} \right) \right]$$

$$\eta_u^{(m)} = \cos\left(\frac{n\pi}{m+1} \right) \qquad \begin{aligned} k &= 1,2 \ \text{---} \ K \\ i &= 1,2 \ \text{---} \ n \\ u &= 1,2 \ \text{---} \ m_H \end{aligned}$$

$$y_u^{(m)} = s\eta_u$$

$$m_H = \frac{1}{4} \left[2m + L - (-1)^m L \right]$$

$$L = \begin{cases} + 1 \text{ for symmetric modes} \\ - 1 \text{ for antisymmetric modes} \end{cases}$$

For the purpose of studying rigid-body binary flutter only the MODAL DATA program is required to obtain the modal function ζ_K and upwash function α_K neglecting control surfaces. These modes of oscillation are then used as input for the ISOLATED WING program to obtain the generalised forces.

The generalised forces are then corrected to account for difference between the current set of axis and Davies notation. As these generalised forces are generated by uncoupled rigid-body modes they may be substituted directly into the existing program FLUST. Using the existing mass and stiffness matrices provided by FLUST the resulting flutter determinant can be solved as before. This new FORTRAN program is called LIFST.

213

A significant amount of time was required to produce output from ISOLATED WING depending on the number of collocation points used. Therefore a range of reduced frequency and Mach number was selected, that was thought best to cover the likely range of flutter. The resulting series of generalised forces were placed into an input data file called RES2 from which LIFST could read from. The subroutine within FLUST, that generates the aerodynamic matrix is altered in LIFST, to accommodate the lifting line values. This new subroutine interpolates for a given Mach number and reduced frequency from RES2 for the corresponding generalised forces provided by lifting line theory. This interpolation is carried out by the NAG routine E01ACF.[104] This routine deals only with two modes, however as discussed later this was later extended to cover N number of modes. The process of analysis is shown in Fig.B3.

B.4.2 Introduction of Elastic Modes

When dealing with elastic modes the MODAL DATA program is no longer suitable, as this deals solely with the rigid-body modes.

A FORTRAN program INTP was subsequently written to generate the required modal functions and upwash functions for a given coupled mode. Referring to Fig.B4 of a representative chord and neglecting chordwise deformation. The modal function can be written as:

$$\zeta(x,y) = \frac{z}{1} = \left(z_0 - \frac{x\,\theta_y}{1} \right) \tag{B.33}$$

setting $1 = 1.0$

$$\zeta_j(x_{r,p}^{(n,m)}, y_p^{(m)}) = \left(z_0(y_p^{(m)}) - x_{r,p}^{(n,m)}\theta_y(y_p^{(m)}) \right) \tag{B.34}$$

Hence the upwash function (B.32) can be expressed in terms of Eq.(B.34).

$$\alpha_K(\overline{x}_{1,u}^{(n,m)}, y_u^{(m)}) = 1\frac{\partial}{\partial x}\left\{z_0(y_u^{(m)}) - \frac{x_{1,u}^{(n,m)}\theta_y(y_u^{(m)})}{1}\right\} +$$

$$iv\left\{z_0(y_u^{(m)}) - \frac{x_{1,u}^{(n,m)}\theta_y(y_u^{(m)})}{1}\right\} \qquad (B.35)$$

Again, setting $1 = 1.0$, we have

$$\alpha_K(\overline{x}_{1,u}^{(n,m)}, y_u^{(m)}) = \theta_y(y_u^{(m)}) + iv\left\{z_0(y_u^{(m)}) - x_{1,u}^{(n,m)}\theta_y(y_u^{(m)})\right\}$$

$$(B.36)$$

The number, N, of coupled modes is supplied by the program CALFUN[28] This is used as input for INTP which interpolates at the required chordwise and spanwise loading points to obtain ζ_K and α_K using the NAG routine E01AAF[104] Modal data are used as input to ISOLATED WING to provide the required generalised forces. These results are stored again in RES2.

As coupled modes are dealt with the existing dynamic stiffness matrix, provided by the code CALFUN, is used to generate the flutter determinant. This program is called COUPLFT for reference. As before a substitute aerodynamic subroutine is used to interpolate for the required Mach number and reduced frequency. As the flutter speed may be sensitive to the number of modes, the routines mentioned have the facility to deal with N modes. The process is shown in Fig.B5.

B.5 Modified Lift Curve Slope in Strip Theory

In strip theory, another set of expressions for sections normal to the elastic axis but arranged in a manner to allow the incorporation of a modified lift curve slope, is presented by Yates[30]

215

$$\overline{L} = -\pi\rho\overline{b}^2\left\{\ddot{h} + U_n\dot{\overline{\alpha}} + U_n\dot{\sigma}\tan\Lambda - ba_h(\ddot{\overline{\alpha}} + U_n\dot{\tau}\tan\Lambda)\right\}$$

$$-\left\{a_0\rho U_n\overline{b}\ C(k_n)\right\}\overline{W}$$

$$\text{(B.37)}$$

and

$$\overline{M}_\alpha = -\pi\rho\overline{b}^4\left\{(\tfrac{1}{8} + a_h^2)(\ddot{\overline{\alpha}} + U_n\dot{\tau}\tan\Lambda)\right\} + \pi\rho\overline{b}^2U_n\left\{\dot{h} + U_n\sigma\tan\Lambda\right\}$$

$$+ \pi\rho\overline{b}^3a_h\left\{\ddot{h} + U_n\dot{\sigma}\tan\Lambda\right\} + \pi\rho\overline{b}^2U_n^2\left\{\overline{\alpha} - a_hb\tau\tan\Lambda\right\}$$

$$- 2\pi\rho U_n\overline{b}^2\left\{\tfrac{1}{2} - (a_h - a_c)\ C(k_n)a_0/2\pi\right\}\overline{W}$$

$$\text{(B.38)}$$

where the downwash expression $\overline{W}$ is given by

$$\overline{W} = \left\{\dot{h} + U_n\overline{\alpha} + U_n\sigma\tan\Lambda + \overline{b}(a_0/2\pi + a_c - a_h)(\dot{\overline{\alpha}} + U_n\tau\tan\Lambda)\right\}$$

$$\text{(B.39)}$$

If aerodynamic parameters for two-dimensional incompressible flow are employed, the modified strip analysis reduces to the method of Barmby, Cunningham and Garrick[57] with second order terms neglected. In addition if the elastic axis is unswept both methods become identical with that of Theodorsen[5] as above.

Assuming sinusoidal motion as above.

$$\overline{L} = -\pi\rho U_n^2\left\{-k_nh + ik_n\overline{b}\overline{\alpha} + ik_n\overline{b}\sigma\tan\Lambda - \overline{b}a_h(-k_n^2\overline{\alpha} + ik_nb\tau\tan\Lambda)\right\}$$

$$-\left\{a_0\rho U_n^2\ C(k_n)\right\}\overline{W} \qquad\qquad \text{(B.40)}$$

$$\overline{M}_\alpha = -\pi\rho U_n^2 \overline{b}^2 \left\{ \left(\frac{1}{8} + a_h^2 \right)(-k_n\overline{\alpha} + ik_n\overline{b}\tau \tan \Lambda) \right\}$$

$$+ \pi\rho U_n^2 \overline{b} \left\{ ik_n\overline{\alpha} + \overline{b}\sigma \tan \Lambda \right\} + \pi\rho U_n^2 \overline{b}a_h \left\{ -k_n h + ik_n\overline{b}\sigma \tan \Lambda \right\}$$

$$+ \pi\rho U_n^2 \overline{b}^2 \left\{ \overline{\alpha} - a_h\overline{b}\tau \tan \Lambda \right\} - 2\pi\rho U_n^2 \overline{b} \left\{ \frac{1}{2} - (a_h - a_c) \ C(k_n)a_0/2\pi \right\} \overline{W}$$

(B.41)

where
$$\overline{W} = \left\{ ik_n h + \overline{\alpha} + \overline{b}\sigma \tan \Lambda + \overline{b}(a_0/2\pi + a_c - a_h)(ik_n\overline{\alpha} + \overline{b}\tau \tan \Lambda) \right\}$$

(B.42)

From Eqs.(B.40) through (B.42), negecting sweep terms and taking parameters parallel to the flight direction, the modified lift and moment per unit spanwise distance can be expressed as in Eq.(B.5), in terms of the displacements considered.

$$A_{11} = \rho U^2 \left\{ \pi k^2 - a_0 C(k)ik \right\}$$

$$A_{12} = -\rho U^2 b \left[\pi(ik + a_h k^2) - a_0 C(k) \left\{ 1 + (a_0/2\pi + a_c - a_h)ik \right\} \right]$$

$$A_{21} = -\pi\rho U^2 b \left[a_h k^2 - ik + 2ik \left\{ \frac{1}{2} - (a_h - a_c) \ C(k)a_0/2\pi \right\} \right]$$

$$A_{22} = \pi\rho U^2 b^2 \left[\left\{ \left(\frac{1}{8} + a_h^2 \right)k + 1 \right\} - 2 \left\{ \frac{1}{2} - (a_h - a_c) \right. \right.$$

$$\left. \left. a_0/2\pi C(k) \right\} \left\{ 1 + (a_0/2\pi + a_c - a_h)ik \right\} \right]$$

(B.43)

These new expressions for lift and moment which take into account modified aerodynamic parameters are used in the analysis

for the complete aircraft and are multiplied by Cos Λ to take into account any sweep effects.

B.6 Generalised Aerodynamic Matrix for Complete Aircraft

When considering the complete aircraft, the aerodynamic forces are assumed to be generated entirely by the wings and the tailplane. The total virtual work done by these surfaces on the system is:-

$$\delta W = \delta W_{Wing} + \delta W_{Tail} \qquad (B.44)$$

As before the displacements considered are solely heave $h(y,t)$ and pitch $\alpha(y,t)$ in the symmetric case. Therefore the virtual work done by these respective surfaces is

$$\delta W_{Wing} = \sum_{i=1}^{N} \delta q_i \int_{0}^{S_W} (L(y)h_i(y) + M_\alpha(y)\alpha_i(y)) \; dy \qquad (B.45)$$

$$\delta W_{Tail} = \sum_{i=1}^{N} \delta q_i \int_{0}^{S_T} (L_T(y)h_{iT}(y) + M_{\alpha_T}(y)\alpha_{iT}(y)) \; dy \qquad (B.46)$$

Equations (B.44) - (B.46) can be written in matrix form as:

$$
\begin{bmatrix} \dfrac{\delta W_1}{\delta q_1} \\[2mm] \dfrac{\delta W_2}{\delta q_2} \\ \vdots \\ \vdots \\ \dfrac{\delta W_n}{\delta q_n} \end{bmatrix} = \int_0^{S_W} \begin{bmatrix} h_{1W} & \alpha_{1W} \\ h_{2W} & \alpha_{2W} \\ \vdots & \vdots \\ \vdots & \vdots \\ h_{nW} & \alpha_{nW} \end{bmatrix} \begin{bmatrix} L \\ M_\alpha \end{bmatrix} dy \; + \; \int_0^{S_T} \begin{bmatrix} h_{1T} & \alpha_{1T} \\ h_{2T} & \alpha_{2T} \\ \vdots & \vdots \\ \vdots & \vdots \\ h_{nT} & \alpha_{nT} \end{bmatrix} \begin{bmatrix} L_T \\ M_{\alpha_T} \end{bmatrix} dy
$$

$$\qquad (B.47)$$

Substituting for $\begin{bmatrix} L \\ M_\alpha \end{bmatrix}$ from Eq.(B.5) into Eq.(B.47)

$$
\begin{bmatrix} \dfrac{\delta W}{\delta q_1} \\ \dfrac{\delta W}{\delta q_2} \\ \vdots \\ \dfrac{\delta W}{\delta q_n} \end{bmatrix} = \int_0^{S_W} \begin{bmatrix} h_{1W} & \alpha_{1W} \\ h_{2W} & \alpha_{2W} \\ \vdots & \vdots \\ h_{nW} & \alpha_{nW} \end{bmatrix} \begin{bmatrix} A_{11} & A_{12} \\ A_{21} & A_{22} \end{bmatrix} \begin{bmatrix} h_{1W} & h_{2W} & \cdots & h_{nW} \\ \alpha_{1W} & \alpha_{2W} & \cdots & \alpha_{nW} \end{bmatrix} \begin{bmatrix} q_1 \\ q_2 \\ \vdots \\ q_n \end{bmatrix} dy
$$

$$
+ \int_0^{S_T} \begin{bmatrix} h_{1T} & \alpha_{1T} \\ h_{2T} & \alpha_{2T} \\ \vdots & \vdots \\ h_{nT} & \alpha_{nT} \end{bmatrix} \begin{bmatrix} A_{11} & A_{12} \\ A_{21} & A_{22} \end{bmatrix} \begin{bmatrix} h_{1T} & h_{2T} & \cdots & h_{3T} \\ \alpha_{1T} & \alpha_{2T} & \cdots & \alpha_{3T} \end{bmatrix} \begin{bmatrix} q_1 \\ q_2 \\ \vdots \\ q_n \end{bmatrix} dy
$$

$$(B.48)$$

$$
= \begin{bmatrix} QF_{11} & QF_{12} & \cdots & QF_{1n} \\ QF_{21} & QF_{22} & \cdots & QF_{2n} \\ \vdots & \vdots & & \vdots \\ QF_{n1} & QF_{n2} & \cdots & QF_{nn} \end{bmatrix} \begin{bmatrix} q_1 \\ q_2 \\ \vdots \\ q_n \end{bmatrix} \qquad (B.49)
$$

where

$$QF(i,j) = \int_0^{S_W} A_{11}h_ih_j + A_{12}h_i\alpha_j + A_{21}\alpha_ih_j + A_{22}\alpha_i\alpha_j \ dy$$

$$+ \int_0^{S_T} A_{11}h_{iT}h_{jT} + A_{12}h_{iT}\alpha_{jT} + A_{21}\alpha_{iT}h_{jT} + A_{22}\alpha_{iT}\alpha_{jT} \ dy$$

$$(B.50)$$
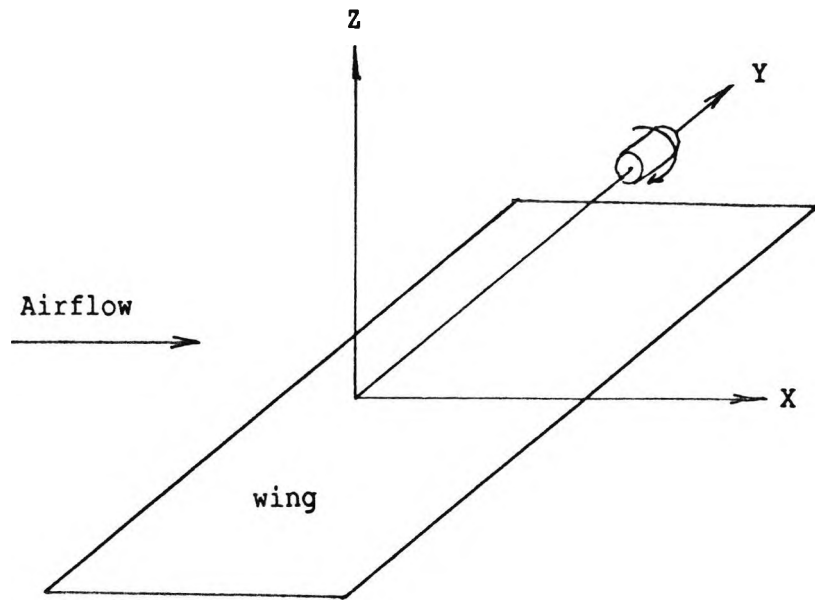
Fig. B1 Co-ordinate system for Davies' lifting line program
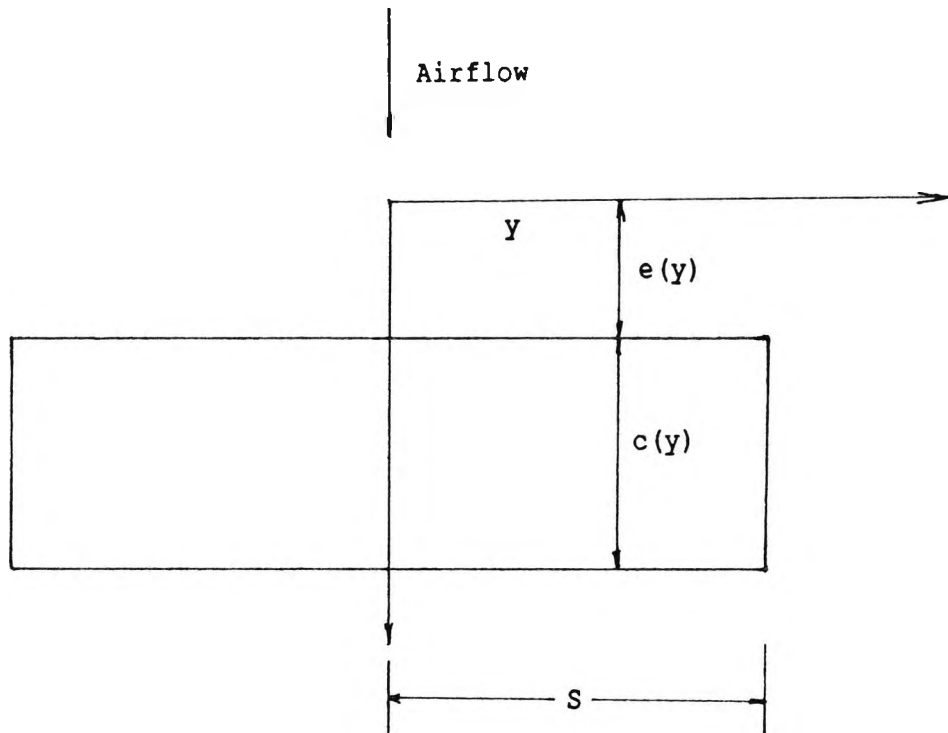
Fig. B2 Planform of a symmetric flat plate wing

```
┌─────────────────┐          ┌──────────────────────────┐
│      Mass       │          │       MODAL DATA         │
│     Matrix      │          │ Rigid Body Modal functions│
│                 │          │       ζ_K  and  α_K       │
└─────────────────┘          └──────────────────────────┘
```

Mass
Matrix

MODAL DATA
Rigid Body Modal functions
ζ_K and α_K

Rigid
Mode Shapes

ISOLATED WING
Generalised Aerodynamic
Force $Q_{i,j}(\upsilon,M)$

Generalised Mass
Matrix

RES2
Generalised Aerodynamic
Forces $Q_{i,j}(\upsilon,M)$
$\upsilon = (\upsilon_1,\upsilon_2,\upsilon_3,\ldots\ \upsilon_i)$
$M = (M_1,M_2,M_3,\ldots\ M_i)$

Aerodynamic Matrix
NAG E01ACF

Formation of
Flutter Determinant
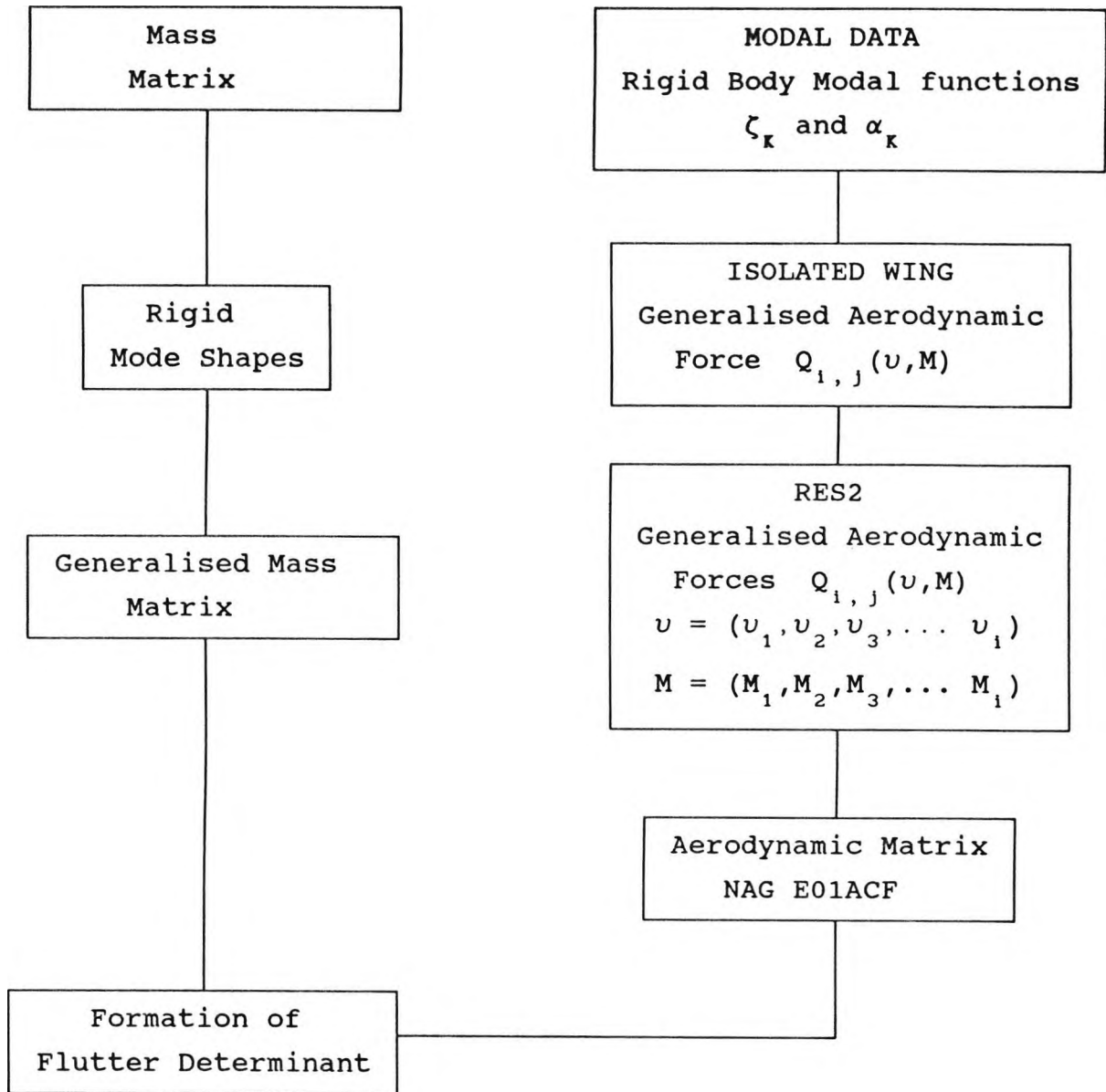
Fig.B3   Implementation of Davies′ program within   current
flutter analysis

Fig. B4   Representative section

```
                 ┌─────────────────────────┐
                 │   Idealised Wing Model  │
                 │    (i)  Beam elements   │
                 │    (ii) Wing Geometry   │
                 └─────────────────────────┘
                              │
        ┌─────────────┐               ┌─────────────┐
        │   CALFUN    │               │   TPAPCMG   │
        └─────────────┘               └─────────────┘
                 │                          │
                 ┌──────────────────────────┐
                 │   Natural Frequencies    │
                 │          and             │
                 │      Mode Shapes         │
                 └──────────────────────────┘
                      │               │
     ┌────────────────────────┐   ┌────────────────────────────┐
     │  Mass and Stiffness    │   │          INTP              │
     │      Matrices          │   │  Elastic Modal Functions   │
     │                        │   │     ζ_K and α_K            │
     └────────────────────────┘   └────────────────────────────┘
```
$$\zeta_K \text{ and } \alpha_K$$

Mass and Stiffness Matrices	INTP — Elastic Modal Functions ζ_K and α_K
Natural Frequencies and Mode Shapes	ISOLATED WING — Generalised Aerodynamic Force $Q_{i,j}(\upsilon, M)$
Generalised Mass and Stiffness Matrices	RES2 — Generalised Aerodynamic Forces $Q_{i,j}(\upsilon, M)$ $\upsilon = (\upsilon_1, \upsilon_2, \upsilon_3, \ldots \upsilon_i)$ $M = (M_1, M_2, M_3, \ldots M_i)$
	Aerodynamic Matrix NAG E01ACF

Formation of Flutter Determinant

Fig. B5   Incorporation of elastic modes within current
flutter analysis using Davies' program

APPENDIX C

C.0 Aeroelastic Behaviour of Metallic and Composite Wings

C.1 Introduction

Aeroelastic tailoring, which exploits the anisotropic character of advanced composites, has received considerable attention since Krone Jr.[120] concluded that forward-swept wings without divergence or weight penalties may be possible through certain lay-up sequences and material combinations. Analytical designs were suggested by Weisshaar[121,122] based on Krone's conclusions. He suggested that the bending-torsion stiffness coupling could be useful to overcome divergence in forward-swept wings. Sherrer et al.[123] performed wind tunnel tests on simple plate like models of a forward-swept wing as a verification of Weisshaar's conclusions. In addition to this, he also showed that the prevailing analytical techniques for prediction of divergence dynamic pressures were adequate for the majority of the test conditions. Wilkinson and Rauch[124] of Grumman Aircraft and Ellis et al.[125] of Rockwell North American Aircraft provided additional information on specific forward-swept wing model designs, (more exhaustive discussion on these efforts can be found in ref.(126)), whereas Weisshaar et al.[127] explored the inclusion of rigid body freedoms.

Hollowell and Dugundji[82] provided useful experimental data on aeroelastic tailoring of graphite/epoxy cantilevered plates. The effect of bending-torsion stiffness coupling on divergence and flutter velocities of unswept lifting surfaces in incompressible flow was described. Furthermore, Landsberger and Dugundji[83] analytically and experimentally investigated the aeroelastic deflections, divergence and flutter behavior of both unswept and 30° forward-swept rectangular, graphite/epoxy, cantilevered plate-type wings, with various amounts of bending-torsion stiffness coupling.

In the light of the current literature survey, two steps were taken. Firstly, various parameters were evaluated theoretically for the plates used in Ref.(82) and they were idealised as beams. Then natural frequencies, mode shapes, flutter speed and flutter

frequency were predicted using CALFUN[28] The second step was to conduct similar experiments at the City University, in order to have a feel of the flutter phenomenon. Detailed discussion of each stage follows.

C.2 Comparison with CALFUN[28]

Orthotropic engineering constants for Hercules AS1/3501-6 uni-directional graphite/epoxy are tabulated in Table C1 as per Ref.(82), along with sectional parameters. The in-plane, on-axis lamina modulus components Q_{ij} were obtained from the orthotropic engineering constants. Flexural moduli for six different laminates were found by a LAMINATE program (developed at The City University). These results were identical to Ref.(82) and are shown in Table C2.

In order to establish norms for comparison, it is necessary to first briefly discuss the theory behind the M.I.T. predictions[82]

C.2.1 Theory (according to Hollowell and Dugundji[82])

The Rayleigh-Ritz energy method due to its simplicity and relative ease of application was employed to analyse free vibrations, flutter and divergence by approximating plate deflections. The wing was considered as a rectangular cantilevered flat plate with uniform thickness. By assuming the deflection shapes for the first three vibration modes, a five term deflection equation was chosen. These terms comprised first and second bending, first and second torsion and first chordwise vibration modes. Jensen et al.[128,129] showed that the last two terms were important to obtain accurate approximations for the first three vibration modes. Therefore, in terms of generalized coordinates, the deflection equation is, referring to Fig.C1

$$w = \sum_{i=1}^{5} \gamma_i(x,y) \; q_i(t) \qquad (C.1)$$

where w = lateral deflection

$\gamma_i(x,y)$ = the nondimensional deflection or mode shape of the ith mode and can be written as

$$= \phi_1(x)\ \psi_1(y) \qquad\qquad \mathsf{i}=1,2,3,4,5$$

ϕ = single-dimension mode shape in x direction

ψ = single-dimension mode shape in y direction

The mode shapes assumed were as follows

$\phi_1(x)$ = first cantilever beam mode

$\phi_2(x)$ = second cantilever beam mode

$\phi_3(x) = \sin(\pi x/2\ell)$

$\phi_4(x) = \sin(3\pi x/2\ell)$

$\phi_5(x) = \dfrac{x}{\ell}(1-x/\ell)$

$\psi_1(y) = 1$

$\psi_2(y) = 1$

$\psi_3(y) = y/c$

$\psi_4(y) = y/c$

$\psi_5(y) = [4(y/c)^2 - \ell/3]$

and

$q_1(t)$ = generalised displacement of the ith mode, such that all of the modes satisfy the geometric boundary conditions for a cantilevered plate

$q_1(t)$ has units of length and it is a function of time

In the case of a symmetric anisotropic laminated plate, the strain energy is[130]

$$U = \frac{1}{2} \int_0^\ell \int_{-c/2}^{c/2} \left[D_{11}\left(\frac{\partial^2 w}{\partial x^2}\right)^2 + 2\,D_{12}\left(\frac{\partial^2 w}{\partial x^2}\right)\left(\frac{\partial^2 w}{\partial y^2}\right) + D_{22}\left(\frac{\partial^2 w}{\partial y^2}\right)^2 \right.$$

$$\left. + 4\,D_{16}\left(\frac{\partial^2 w}{\partial x^2}\right)\left(\frac{\partial^2 w}{\partial x\partial y}\right) + 4\,D_{26}\left(\frac{\partial^2 w}{\partial y^2}\right)\left(\frac{\partial^2 w}{\partial x\partial y}\right) + 4\,D_{66}\left(\frac{\partial^2 w}{\partial x\partial y}\right)^2 \right]dy\ dx$$

$$(C.2)$$

Taking the partial derivative of the deflection equation (C.1), we can write equation (C.2) in summation notation as follows

$$U = \frac{1}{2} \sum_{i=1}^{5} \sum_{j=1}^{5} K_{ij}\ q_i\ q_j$$

where K_{ij} = element of a symmetric 5 x 5 matrix

223

$$= \int_0^\ell \int_{-c/2}^{c/2} \left[\; D_{11}\left(\frac{\partial^2 \gamma_1}{\partial x^2}\right)\left(\frac{\partial^2 \gamma_J}{\partial x^2}\right) \; + \; D_{22}\left(\frac{\partial^2 \gamma_1}{\partial y^2}\right)\left(\frac{\partial^2 \gamma_J}{\partial y^2}\right) \right.$$

$$+ \; 4 \; D_{66}\left(\frac{\partial^2 \gamma_1}{\partial x \partial y}\right)\left(\frac{\partial^2 \gamma_J}{\partial x \partial y}\right) \; + \; D_{12}\left\{\left(\frac{\partial^2 \gamma_1}{\partial x^2}\right)\left(\frac{\partial^2 \gamma_J}{\partial y^2}\right) + \left(\frac{\partial^2 \gamma_1}{\partial y^2}\right)\left(\frac{\partial^2 \gamma_J}{\partial x^2}\right)\right\}$$

$$+ \; 2 \; D_{16} \left\{\left(\frac{\partial^2 \gamma_1}{\partial x^2}\right)\left(\frac{\partial^2 \gamma_J}{\partial xy}\right) + \left(\frac{\partial^2 \gamma_1}{\partial xy}\right)\left(\frac{\partial^2 \gamma_J}{\partial x^2}\right)\right\} \; + \; 2 \; D_{26}$$

$$\left. \left\{\left(\frac{\partial^2 \gamma_1}{\partial y^2}\right)\left(\frac{\partial^2 \gamma_J}{\partial xy}\right) + \left(\frac{\partial^2 \gamma_1}{\partial xy}\right)\left(\frac{\partial^2 \gamma_J}{\partial y^2}\right)\right\} \; \right] dy \; dx$$

The kinetic energy for the plate is

$$T = \frac{1}{2} \int_0^\ell \int_{-c/2}^{c/2} m \left(\frac{\partial w}{\partial t}\right)^2 dy \; dx$$

where $\quad m = \rho_G t_G$

$\qquad$ = mass per unit area

$\quad \rho_G$ = density of the graphite/epoxy

$\quad t_G$ = total plate thickness

Rewriting in summation notation

$$T = \frac{1}{2} \sum_{i=1}^{5} \sum_{j=1}^{5} M_{ij} \; \dot{q}_i \; \dot{q}_j$$

where $\quad M_{ij}$ = is an element of 5 x 5 matrix

$$= \int_0^\ell \int_{-c/2}^{c/2} \gamma_i \; m \; \gamma_j \; dy \; dx$$

Similarly the variation in external work can be written as

$$\delta W_e = \int_0^\ell \int_{-c/2}^{c/2} \Delta p_z \; \delta w \; dy \; dx$$

where

$\qquad \Delta p_z$ = distributed lateral load per unit area

The above expression in summation notation can be written as follows:

$$\delta W_e = \sum_{i=1}^{5} Q_i \; \delta q_i$$

where

Q_1 = Generalized force

$$= \int_0^\ell \int_{-c/2}^{c/2} \Delta p_z \, \gamma_1 \, dy \, dx$$

Lagrange's equation provides the equations of state, and is a statement of Hamilton's energy principle. This is in fact the basis of the Rayleigh-Ritz method.

$$\frac{d}{dt} \left(\frac{\partial T}{\partial \dot{q}_i} \right) - \frac{\partial T}{\partial q_i} + \frac{\partial U}{\partial q_i} = Q_i$$

Substituting the respective quantities in Lagrange's equation, five equations of motion will be obtained. In matrix form these can be expressed as

$$[M]\ddot{q} + [K]q = Q \qquad (i,j = 1,2,\ldots,5)$$

Where $[M]$ = diagonal mass matrix

            $[K]$ = symmetric stiffness matrix

Their details can be seen in Ref.(82).

In order to observe the function of coupling D-matrix terms we go back to Hamiltons's principle and assume a solution

$$w(t) = w \, \sin \omega t$$

and suitable substitutions yield

$$\delta \int \int_A \frac{1}{2} \left[D_{11}\left(\frac{\partial^2 w}{\partial x^2}\right)^2 + 2 \, D_{12} \left(\frac{\partial^2 w}{\partial x^2}\right)\left(\frac{\partial^2 w}{\partial y^2}\right) + D_{22}\left(\frac{\partial^2 w}{\partial y^2}\right)^2 \right.$$
$$+ 4 \, D_{16} \left(\frac{\partial^2 w}{\partial x^2}\right)\left(\frac{\partial^2 w}{\partial x \partial y}\right) + 4 \, D_{26} \left(\frac{\partial^2 w}{\partial y^2}\right)\left(\frac{\partial^2 w}{\partial x \partial y}\right) + 4 \, D_{66} \left(\frac{\partial^2 w}{\partial x \partial y}\right)^2$$
$$\left. - \omega^2 m \, w^2 \right] dA = 0$$

In the case of a uniform rectangular plate clamped at x=0 , the governing equations are, where $(\;)'' = \dfrac{\partial^2 (\;)}{\partial x^2}$ and θ = angle of twist

$$w'''' - \omega^2 \, m \, (\ell^4 / D_{11}) \, w + (2 \, D_{16} \, \ell / D_{11})\theta''' = 0$$

$$-(D_{16}/ 2 \, D_{66})w''' + (D_{11} \, c^2 / 48 \, D_{66} \, \ell^2)\theta'''' - \theta'' - \omega^2(m \, c^2\ell^2/48 D_{66})\theta = 0$$

These two ordinary differential equations are coupled by the bending-twisting stiffness factor D_{16}. The stiffness ratios D_{16}/D_{11} and D_{16}/D_{66} as shown in Table C3 are negligibly small and can be ignored.

This results in uncoupled bending and torsion equations and eventually yields relatively simple solutions,

$$w'''' - \omega^2 m \left(\ell^4 / D_{11} \right) w = 0$$

which is identical to the equation of transverse vibration of a bar

$$w'''' - \omega^2 \rho_G A \ell^4 / E I \, w = 0$$

Comparing both equations shows that the usual ratio

$$\rho_G A / E I = m / D_{11}$$

therefore,

$$E I = \rho_G A \, D_{11} / m = \rho_G A \, D_{11} / \rho_G t_G = D_{11} c$$
$$\text{since} \qquad A = c \, t_G$$

resulting in the following expression for natural bending frequencies,

$$\omega_{nB} = \left(k_{nB} / \ell^2 \right) \sqrt{D_{11} / m} \qquad n = 1, 2, 3, \ldots\ldots$$

where k_{nB} = nth eigenvalue of the equation, subject to the boundary conditions on w

The second equation

$$\left(D_{11} c^2 / 48 \, D_{66} \ell^2 \right) \theta'''' - \theta'' - \omega^2 \left(\rho \, c^2 \ell^2 / 48 D_{66} \right) \theta = 0$$

still contains terms that represent warping stiffness, St. Venant torsion stiffness ($4 D_{66} c = GJ$ for an isotropic plate) and the torsional polar inertia about y=0 respectively.

226

Substitute $R = \ell/c$

$\beta = D_{11}/48D_{66}R^2$

= representing the influence of warping stiffness

= depending both on aspect ratio (i.e. geometry) and ratio of bending to torsion stiffness (i.e. laminate properties)

$K_T^2 = \omega^2 \rho \ell^4 / 48 D_{66} R^2$

so the equation becomes

$$\beta\, \theta^{''''} - \theta^{''} - K_T^2\, \theta = 0$$

Finally the frequencies are given by the expression

$$\omega_{nT} = (\, K_{nT}/\ell^2) \sqrt{48 D_{66} R^2}/\rho$$

where K_{nT} = eigenvalue being function of β

can be obtained from figures (2 & 3) or from Table 2 of Ref.(131)

value approaches that for a long thin bar as the warping stiffness β goes to zero.

This can be compared with the expression for torsional frequencies of a prismatic bar made of isotropic material,

$$\omega_n = K_n \sqrt{GJ/\ell^2}\, I_p$$

Based on these expressions frequencies were predicted and are repeated for convenience in Tables C4a and C4b.

C.2.2 Theory (using CALFUN)

CALFUN[28] is an aeroelastic program that evaluates the flutter speed and frequency for isotropic, straight wings. Normal modes are implemented to express the mass, stiffness and aerodynamic matrices of the wing in terms of generalised coordinates.

Beam elements are used in the finite element idealisation of the wing to obtain the mass and stiffness matrices. The elements employed are based on a Vlasov beam idealisation, however warping

227

stiffness and rotary inertia are not accounted for. Natural frequencies and mode shapes are obtained following an eigen-solution procedure. The mode-superposition method is used to generate the generalized mass and stiffness matrices using the normal modes obtained from the finite element analysis.

The generalized aerodynamic matrix is formed by applying the principle of virtual work. The strip theory based on Theodorsen's expressions[5] for unsteady lift and moment and the normal modes are used in the process, with no account for chordwise deformation. The flutter matrix is formed is formed by summing the generalized mass, stiffness and aerodynamic matrices. The solution of the flutter determinant is a complex eigenvalue problem because the determinant above is primarily a complex function of two unknown variables, the airspeed and the frequency. The method used selects an airspeed and evaluates the real and imaginary parts of the flutter determinant for a range of frequencies. The process is repeated for a range of airspeeds until both the real and imaginary parts of the flutter determinant (and hence the whole flutter determinant) vanish completely.
The input to CALFUN includes,
1. flexural and torsional rigidities,(EI,GJ)
2. mass per unit length,(M/l)
3. polar mass moment of inertia about the elastic axis,(I_α)
4. distance between the elastic axis and the centroid and (x_α)
5. beam length, (dl)

CALFUN will then compute natural frequencies and mode shapes for the structure, taken normal to the flight direction. The next stage requires input of the geometric details of the wing for evaluation of the aerodynamic forces. This involves taking streamwise sections.
1. semi-chord length (b)
2. the ratio of the distance between elastic axis and the mid-chord to semi-chord length. (a_h)

In the original Ref.(82) there was no straight forward account of flexural and torsional rigidities. Therefore, they were determined by using relations discussed in the theory stated above.

228

i.e.

$$EI = D_{11} c$$

$$GJ = 4 D_{66} c$$

Rigidities calculated using these expressions will be referred to as scheme No.1. Alternatively, by making use of composite mechanics, one can arrive at the following relations.

$$EI = c/ D_{11}^*$$

$$GJ = 4 c/ D_{66}^*$$

where D_{11}^* and D_{66}^* are members of the inverted D-matrix.
This will be termed as scheme No.2. Calculated rigidities are given in Table C5.

This table shows that only in the case of $[0_2/90]_s$ do the values obtained for rigidities agree using both calculation schemes. In all others there are large discrepancies. At the moment we do not have any good reasons to doubt what Crawley and Dugundji[82] suggested and Scheme 2 is obviously limited in its applications. If we proceed with rigidities that we obtained from scheme No.1, we obtain the natural frequencies by CALFUN and compare with another finite package, LUSAS.[132]

Laminate overall moduli E_x, E_y, G_{xy} and ν_{xy} values were computed by making use of following relationships.

$$E_x = 1/ t_G A_{11}^*$$
$$E_y = 1/ t_G A_{22}^*$$
$$G_{xy} = 1/ t_G A_{66}^*$$

where A_{11}^*, A_{22}^*, and A_{66}^* are members of the inverted A-matrix.

LUSAS was used to establish the frequencies of these orthotropic plates. These results are shown Tables C6a and C6b along with those from Ref.(82) for comparison.

A comparative study between CALFUN and M.I.T. results revealed useful facts about the use of CALFUN. As long as we are dealing with simple lay-ups the program is capable of accurately predicting the frequencies and flutter characteristics, but as the layer sequence becomes more complex, a significant drift appears. This suggests that the capability for analysing composite materials requires inclusion of anisotropic characteristics in the program.

229

Apart from establishing the natural frequencies for these plates by CALFUN, the flutter speeds and frequencies were also determined. These results are summarised as follows:

The percentage difference shown in Table C7 is based on comparison between CALFUN predicted value and M.I.T. experimental figure. An experimental value was not available for $[\overset{+}{-}45_2/0]_s$ due to speed limitations of the wind tunnel. While in case of $[-45_2/0]_s$ and $[-30_2/0]_s$, plates suffered from divergence before it could exhibit flutter.

It is appropriate to make comments on each of these lay-ups individually first and then as an attempt to summarise, some overall conclusions may be drawn.

C.2.2.1 $[0_2/90]_s$

Since the D_{16} term is zero, then the above mentioned assumptions are valid. This enabled an accurate prediction of first and second bending frequencies to be made. However the eigen value for torsional vibration depends on the material type and lay-up, as well as the end conditions. Therefore, the usual means employed for analysing isotropic materials will yield poor predictions for the frequencies. This will eventually affect the theoretical estimate of both flutter speed and frequency. Table C7 demonstrates the large percentage differences in flutter speed and frequency, caused by the anisotropic materials and lay-ups.

C.2.2.2 $[\overset{+}{-}45/0]_s$

Although a value of D_{16} does exist but the ratios of D_{16}/D_{11} and D_{16}/D_{66} are still negligible. Therefore, the predictions of CALFUN are very near to the M.I.T. results for both frequencies and flutter velocity.

C.2.2.3 $[+45_2/0]_s$ $[-45_2/0]_s$ $[+30_2/0]_s$ $[-30_2/0]_s$

In these cases ratios of D_{16}/D_{11} and D_{16}/D_{66} are becoming appreciably large enough to make the assumptions invalid. This resulted in grave disagreement between theoretical and experimental figures in all aspects.

C.3 Experimental Investigation of Aluminium and Composite Plates

Experimental investigation were carried out by the author

and J.Z. Khan at City University on similiar lines to those at M.I.T. Two objectives were set forth. First to acquire a feel for the phenomenon and secondly to experimentally investigate the rigidities, fundamental frequencies and the flutter speed and frequency by the authors themselves.

One Aluminium and three Composite plates were prepared for flutter investigation. The Aluminium plate was used to check the accuracy of CALFUN for an Isotropic material. The material properties for the Aluminium specimen are shown in Table C8.

Experiments were carried out to determine the and check stiffness and inertia properties for the plate and these are summarised in Table C9.

Using the experimental and theoretical quantities above, the fundamental frequencies flutter speed and flutter frequency are evaluated using CALFUN and compared with the experimental values. This is shown in Table C10.

The aeroelastic predictions showed that in the unswept configuration the wing would suffer from divergence prior to flutter. Therefore, this wing was studied for 10° and 20° sweep angles. Since sweeping backward cured the problem of divergence. As sweep is now introduced it is decided to compare the current aerodynamic model as employed by CALFUN with that provided by the veloci y component theory, developed by Barmby et al[57].

C.3.1 /elocity Component Theory

Here aerodynamic and structural parameters are taken normal to the elastic axis. Normal modes are taken along the spar. There it is sufficient to implement the frequencies and modes for the unswept wing. However the aerodynamics are modified to incorporate the changed aerodynamics. In the Velocity component theory, the effects of sweep are introduced via the aerodynamic coupling terms $\partial h/\partial \bar{y}$ and $\partial \bar{\alpha}/\partial \bar{y}$, and second order terms are retained in the present analysis[57]. The input data is identical to CALFUN but parameters, normal to the elastic axis are taken.

C.3.2 Cosine Theory

The cosine theory multiplies the lift and moment at $\Lambda = 0$, by $\cos \Lambda$ and uses normal modes taken normal to the flight direction. To take into account structural sweep, additions to the original

231

data items are the x and y coordinates in local axis, instead of the elemental length.

The subsequent experimental flutter speeds and frequencies are shown in Tables C11a and C11b respectively. In addition theoretical results from both aerodynamic theories are applied where appropriate.

Hence, in the case of a conventional isotropic material the results are of reasonable engineering accuracy. A parametric study showed that, at moderate sweep angles (up to 25° sweep back) the flutter speed initially drops and then sharply increases with sweep angle. The magnitude of this drop in flutter speed greatly depends on the ratio of rigidities. This will be more obvious, when we try to compare the possible drop in case of various lay-ups of composite plates in the following paragraphs.

C.3.3.1 Graphite/Epoxy

Graphite/Epoxy C920 unidirectional prepreg composite material was selected for the manufacture of plates due to their properties having been established previously in the University. These orthotropic characteristics are shown in Table C12.

The lay-up sequence in the case of the composite plates were $[0_3]_s$, $[\pm 30]_s$, $[\pm 45,0]_s$. The edges were properly trimmed and they were weighed. The span, chord and thickness were measured. Static tests for flexural and torsional rigidities were carried out. The D-matrix was evaluated by the LAMINATE program for every lay-up, tabulated in Table C13.

Then as before two schemes of calculations were applied to predict the flexural and torsional rigidities. They were compared with the experimentally established figures. They are shown in Tables C14a and C14b respectively.

These results show that rigidities computed by the Dugundji method are more accurate as compared to the second scheme for certain lay-ups. These plates were then dynamically tested on ISAP (a signal analysis package available on GENRAD; a PDP computer) for their natural frequencies. These results are shown in Table C15.

Flutter tests to establish flutter speed and frequency were carried out in the T3 wind tunnel at The City University. The

results are tabulated as follows in Tables C16a and C16b. Where appropriate, results from the velocity component analysis are shown for comparison.

In general for both the aluminum and composite plates considered the present cosine theory is seen to be marginally more accurate in predicting flutter speeds, than the classical velocity component theory. A summary of the percentage differences for the fundamental frequencies is shown in Fig. C2 and for the flutter speed and frequency in Fig. C3 , using the cosine theory.

C.4 Conclusion

In the evaluation of fundamental frequencies, the validity of applying a beam-element idealisation to various composite lay ups is confirmed for low flexural coupling ratios D_{16}/D_{11} and D_{16}/D_{66}. Further the validity of "Strip Theory" in flutter calculations is also confirmed for these low ratios for the swept conditions considered as well as the unswept case. For the particular plates considered the present cosine theory is seen to be marginally more accurate than the classical velocity component theory However when dealing with higher coupling terms it is advised to apply the more rigorous methods as outlined in Ref.(82).

```
+-----------------------------------------------+
|            MATERIAL PROPERTIES                |
|            Out-of-Plane loading               |
|                                               |
|         E₁ = 98.0 x 10⁹  N/m²                 |
|         Eₜ =  7.9 x 10⁹  N/m²                 |
|         νₗₜ =  0.28                           |
|         Gₗₜ =  5.6 x 10⁹  N/m²                |
|    Ply thickness = 0.134 x 10⁻³ m             |
|    Density       = 1520.0 Kg/m³               |
|            SECTIONAL PROPERTIES               |
|                                               |
|      Total length     = 0.33  m               |
|      Effective length = 0.305 m               |
|      Chord length     = 0.076 m               |
|      Aspect Ratio     = 4                     |
+-----------------------------------------------+
```

$$E_1 = 98.0 \times 10^9 \ N/m^2$$
$$E_t = 7.9 \times 10^9 \ N/m^2$$
$$\nu_{lt} = 0.28$$
$$G_{lt} = 5.6 \times 10^9 \ N/m^2$$

Ply thickness $= 0.134 \times 10^{-3} \ m$
Density $= 1520.0 \ Kg/m^3$

Table C1   Material properties and geometry of
Graphite/Epoxy wing

No.	Lay-up	Flexural Moduli. ...D-matrix (Nm)					
		D_{11}	D_{12}	D_{16}	D_{22}	D_{26}	D_{66}
1	$[0_2/90]s$	4.125	0.096	0.0	0.49	0.0	0.243
2	$[\pm45/0]s$	1.55	0.928	0.437	1.404	0.437	1.075
3	$[45_2/0]s$	1.55	0.928	0.946	1.404	0.946	1.075
4	$[-45_2/0]s$	1.55	0.928	-.946	1.404	-.946	1.075
5	$[30_2/0]s$	2.704	0.72	1.18	0.666	0.459	0.866
6	$[-30_2/0]s$	2.704	0.72	-1.18	0.666	-.459	0.866

Table C2   Flexural Moduli of six different layups from using
the program LAMINATE

234

No.	Lay-up	Stiffness Ratios	
		D_{16}/D_{11}	D_{16}/D_{66}
1	$[0_2/90]_s$	0.0	0.0
2	$[\pm45/0]_s$	0.28	0.407
3	$[45_2/0]_s$	0.61	0.88
4	$[-45_2/0]_s$	-0.61	-0.88
5	$[30_2/0]_s$	0.436	1.36
6	$[-30_2/0]_s$	-0.436	-1.36

Table C3 Stiffness ratios for six different layups

No.	Lay-up	D_{11}	Bending frequency (Hz)			
			First Bending		Second Bending	
			Theo.	Exp.	Theo.	Exp.
1	$[0_2/90]_s$	4.125	10.7	11.1	67.0	69.0
2	$[\pm45/0]_s$	1.55	5.7	6.1	37.0	38.0
3	$[45_2/0]_s$	1.55	4.6	4.8	32.0	30.0
4	$[-45_2/0]_s$	1.55	4.6	4.8	32.0	30.0
5	$[30_2/0]_s$	2.704	6.0	6.0	41.0	36.0
6	$[-30_2/0]_s$	2.704	6.0	6.0	41.0	36.0

Table C4a First and second bending natural frequencies from
         Ref.(82)

235

No.	Lay-up	D₆₆	β	Torsional frequency (Hz)					
				First Torsion			Second Torsion		
				K_{1T}	Theo.	Exp.	K_{2T}	Theo.	Exp.
1	$[0_2/90]_s$	0.243	0.0221	1.87	39.0	42.0	6.30	132.0	−
2	$[\overset{+}{-}45/0]_s$	1.075	0.0019	1.63	69.0	77.0	5.00	216.0	−
3	$[45_2/0]_s$	1.075	0.0019	1.63	55.0	51.0	5.00	205.0	−
4	$[-45_2/0]$	1.075	0.0019	1.63	55.0	51.0	5.00	205.0	−
5	$[30_2/0]_s$	0.866	0.0041	1.68	60.0	58.0	5.20	196.0	−
6	$[-30_2/0]$	0.866	0.0041	1.68	60.0	58.0	5.20	196.0	−

Table C4b First and second torsional natural frequencies from Ref.(82)

No.	Lay-up	inverted D		Bending Rigid		Torsion Rigid	
		$D_{11}*$	$D_{66}*$	$D_{11}\,c$	$c/D_{11}*$	$4D_{66}c$	$4c/D_{66}*$
1	$[0_2/90]_s$	243.49	2051.2	0.3135	0.3121	0.074	0.0737
2	$[\overset{+}{-}45/0]_s$	1095.2	1225.1	0.1178	0.0694	0.327	0.2781
3	$[45_2/0]_s$	1426.3	1789.3	0.1178	0.0533	0.327	0.0995
4	$[-45_2/0]_s$	1426.3	1789.3	0.1178	0.0533	0.327	0.0995
5	$[30_2/0]_s$	928.70	2410.0	0.2055	0.0818	0.263	0.0935
6	$[-30_2/0]_s$	928.70	2410.0	0.2055	0.0818	0.263	0.0935

Table C5 Calculated rigidities using scheme No. 2

236

No.	Lay-up	Bending frequency (Hz)							
		First Bending				Second Bending			
		CALFUN	LUSAS	M.I.T.[82]		CALFUN	LUSAS	M.I.T.[82]	
				Theo.	Exp.			Theo.	Exp.
1	$[0_2/90]_s$	11.025	9.405	10.7	11.1	69.095	58.74	67.0	69.0
2	$[\overset{+}{-}45/0]_s$	6.775	7.69	5.7	6.1	42.46	48.15	37.0	38.0
3	$[45_2/0]_s$	6.775	7.38	4.6	4.8	42.46	45.83	32.0	30.0
4	$[-45_2/0]_s$	6.775	7.38	4.6	4.8	42.46	45.83	32.0	30.0
5	$[30_2/0]_s$	8.95	7.999	6.0	6.0	56.08	46.48	41.0	36.0
6	$[-30_2/0]_s$	8.95	7.999	6.0	6.0	56.08	46.48	41.0	36.0

Table C6a   Comparison of first two bending natural frequencies
with Ref.(82)

237

No.	Lay-up	Torsional Frequency (Hz)			
		First Torsional			
		CALFUN	LUSAS	M.I.T.[82]	
				Theo.	Exp.
1	$[0_2/90]_s$	33.302	38.47	39.0	42.0
2	$[\pm45/0]_s$	70.08	64.69	69.0	77.0
3	$[45_2/0]_s$	70.08	46.14	55.0	51.0
4	$[-45_2/0]_s$	70.08	46.14	55.0	51.0
5	$[30_2/0]_s$	62.87	49.95	60.0	58.0
6	$[-30_2/0]_s$	62.87	49.95	60.0	58.0

Table C6b   Comparison of first torsional natural frequency with Ref.(82)

No.	Lay-up	Flutter Speed (m/s)				Flutter Frequency (Hz)			
		CALFUN	M.I.T.[82]		%diff	CALFUN	M.I.T.[82]		%diff
			Theo.	Exp.			M.I.T	Exp.	
1	$[0_2/90]_s$	17.6	21.0	25.0	-42.0	21.5	25.0	~29.0	-34.9
2	$[\pm45/0]_s$	39.5	39.0	>32.0	---	41.5	39.0	---	---
3	$[45_2/0]_s$	39.5	27.8	28.0	29.1	41.5	28.0	~24.0	42.2
4	$[-45_2/0]_s$	39.5	27.8	Div. 12.5	---	41.5	27.0	Div.	---
5	$[30_2/0]_s$	35.0	27.8	27.0	22.8	36.0	31.0	~28.0	22.2
6	$[-30_2/0]_s$	35.0	30.0	Div. 11.7	---	36.0	29.0	Div.	---

Table C7   Comparison of flutter speed and frequency between CALFUN and Ref.(82)

```
+---------------------------------------------------------+
|              Material : Aluminium                       |
|   Modulus of Elasticity = E = 68.9 x 10^9 N/m^2         |
|   Modulus of Rigidity   = G = 26.5 x 10^9 N/m^2         |
|   Poison's ratio        = ν = 0.3                       |
|   Density               = 2700 Kg/m^3                   |
|   Effective Length      = 300 mm                        |
|   Chord Length          =  75 mm                        |
|   Thickness             = 0.71 mm                       |
|   Cross-sectional area  = 53.25  x 10^-6 m^2            |
+---------------------------------------------------------+
```

Table C8   Material properties of Aluminium plate

Parameter	Unit	Calculated	Measured Experimentally	%dif
Mass per unit length	Kg/m	0.143775	0.1397	2.83
Flexural rigidity EI	Nm^2	0.1541	0.16226	-5.29
Torsional rigidity GJ	Nm^2	0.2357	0.23767	-0.84
Polar mass moment of Inertia I_p	Kg-m	6.74×10^{-5}	----	----

Table C9   Stiffness and inertia properties derived from experiment

239

Frequencies		Theoretical		Exp.	% diff
		using calculated data	using measured data		
First Bending	Hz	6.437	6.7009	5.54	17.32
Second Bending	Hz	40.3405	41.994	36.122	13.98
First Torsion	Hz	49.2798	49.485	48.199	2.60
Third Bending	Hz	112.954	117.584	------	-----
Second Torsion	Hz	147.840	148.456	------	-----
Divergence Speed	m/s	34.546	34.690	39.91	-14.32
Flutter Speed	m/s	33.60	33.40	Diverged before flutter	
Flutter Freq.	Hz	26.66	27.30		

Table C10   Comparison of frequencies and flutter quantities derived from both calculated and measured data with experimental values

Sweep back	Flutter speed (m/s)			% Difference	
	Cosine theory	Vel-comp theory	Exp	Cosine theory	Vel-comp theory
0°	33.40	---	Div	---	---
10°	32.26	32.15	38.87	-20.49	-20.90
20°	30.95	30.65	27.80	10.18	9.30

Table C11a   Comparison of flutter speed from cosine and velocity component theory with experimental values

	Flutter frequency (Hz)			% Difference	
Sweep back	Cosine theory	Vel-comp theory	Exp	Cosine theory	Vel-comp theory
0°	27.30	---	Div	---	---
10°	26.26	26.74	29.00	-10.43	-8.45
20°	24.35	25.15	22.75	6.57	9.54

Table C11b   Comparison of flutter frequency from cosine and velocity component theory with experimental values

Material : graphite/epoxy

$E_l = 98.0 \times 10^9 \ N/m^2$

$E_t = 7.9 \times 10^9 \ N/m^2$

$\nu_{lt} = 0.28$

$G_{lt} = 5.6 \times 10^9 \ N/m^2$

Density = 1520.0 Kg/m^3

Dimensions

Effective Length = 291 mm

Chord Length = 75 mm

Ply Thickness = 0.134 mm

Total number of plies = 6

Cross-sectional Area = 60.3 x 10^{-6} m^2

Mass per unit length = 0.091656 Kg/m

Polar mass moment of Inertia = 6.74 x 10^{-5}

Table C12   Properties and geometry of Graphite/Epoxy plates

Lay-up	Flexural Moduli ... D-matrix (Nm)						Ratios	
	D_{11}	D_{12}	D_{16}	D_{22}	D_{26}	D_{66}	D_{16}/D_1	D_{16}/D_6
$[0_3]_s$	4.271	0.096	0.0	0.344	0.0	0.243	0.0	0.0
$[+-+30]_s$	2.642	0.744	0.589	0.679	0.229	0.890	0.2229	0.662
$[\pm45/0]_s$	1.549	0.928	0.436	1.404	0.436	1.074	0.2815	0.406

Table C13 Flexural moduli of composite plates obtained from
LAMINATE program

Lay-up	Flexural Rigidity --Nm_2				
	$c/D_{11}*$	$c\ D_{11}$	Exp	diff1	diff2
$[0_3]_s$	0.3183	0.32033	0.3043	4.4	5
$[+-+30]_s$	0.1265	0.19815	0.1582	-25	20.16
$[\pm45/0]_s$	0.0685	0.11618	0.0972	-42	16.34

Table C14a   Comparison of flexural rigidities obtained from
schemes 1 and 2 with those obtained experimentally

Lay-up	Torsional Rigidity --- Nm_2				
	$4c/D_{66}$	$4cD_{66}$	Exp	diff1	diff2
$[0_3]_s$	0.0727	0.0729	0.1749	-140	-139
$[+-+30]_s$	0.2249	0.2670	0.24352	-8.3	8.79
$[\pm45/0]_s$	0.2744	0.3222	0.32395	-18	-0.54

Table C14b   Comparison of torsional rigidities obtained from
schemes 1 and 2 with those obtained experimentally

| Lay -up | Fundamental Frequencies (Hz) | | | | | | | |
| | First Bending | | Second Bend | | First Torsion | | Third Bending | |
	Theo.	Exp.	Theo.	Exp.	Theo.	Exp.	Theo.	Exp.
[0₃]s	12.685	12.78	79.589	70.0	37.34	38.06	----	---
[+-+30]s	9.73	8.96	61.04	57.24	69.68	68.59	----	---
[±45/0]s	7.66	5.44	47.996	37.5	75.59	----	----	---

Table C15   Comparison of experimental and theoretical natural
frequencies for composite plates

| Lay-up | Sweep Angle | Flutter speed (m/s) | | | % Difference | |
		Cosine theory	Vel-comp theory	Exp	Cosine theory	Vel-comp theory
[0₃]s	0°	30.6	---	33.8	-10.46	---
	20°	30.6	30.3	32.83	-7.29	-8.35
[+-+30]s	0°	36.8	---	41.59	-13.02	---
	20°	36.1	35.8	38.52	-6.70	-7.60
[±45/0]s	0°	40.0	---	47.22	-18.05	---
	20°	39.6	39.4	40.06	-1.16	-1.68

Table C16a   Comparison of flutter speeds obtained from cosine and
velocity component theory with experimental values.

Lay-up	Sweep Angle	Flutter frequency (Hz)			% Difference	
		Cosine theory	Vel-comp theory	Exp	Cosine theory	Vel-comp theory
[0₃]s	0°	35.09	---	38.74	-10.40	---
	20°	34.98	36.29	38.50	-10.06	-6.09
[+-+30]s	0°	38.99	---	38.67	-0.82	---
	20°	38.20	39.47	41.70	-9.16	-5.65
[±45/0]s	0°	47.27	---	62.00	-31.16	---
	20°	36.61	37.56	35.00	-4.40	6.82

Table C16b Comparison of flutter frequency obtained from cosine and velocity component theory with experimental values.
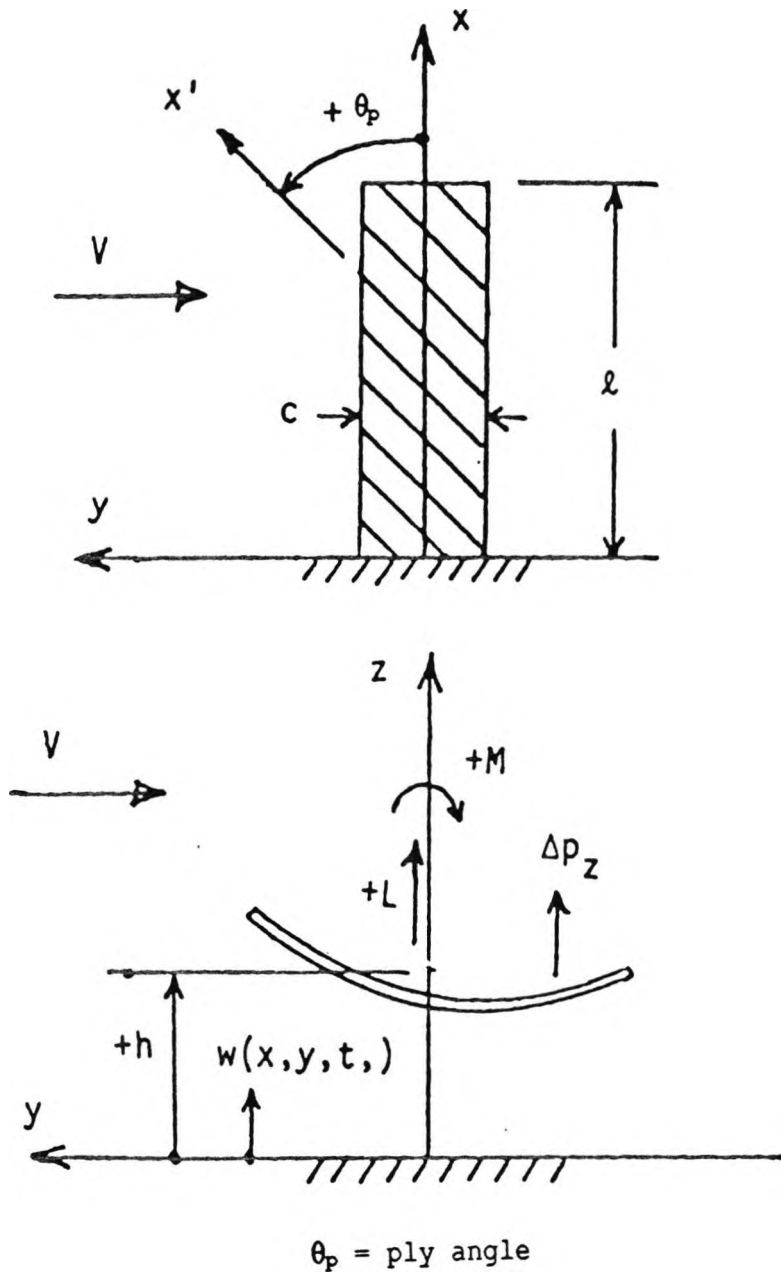
Fig. C1 Plate layout and sign configuration for Ref.(82)

CALFUN & COMPOSITE MATERIALS
Effect of coupling terms of D-matrix
D16/D11 and D16/D66

PLY
LAY-UP

$[-45_2/0]_s$ $[-30_2/0]_s$ $[0_3]_s$ $[0_2/90]_s$ $[+-+30]_s$ $[\pm45/0]_s$ $[\pm45/0]_s$ $[30_2/0]_s$ $[45_2/0]$

Percent difference

D16/D11 and D16/D66 ratios

Percent difference

1st. Bending   1st. Torsion   2nd. Bending

Fig. C2   Summary of percentage differences in fundamental
frequencies for various ply layups

CALFUN & COMPOSITE MATERIALS
Effect of coupling terms of D-matrix
on prediction of Flutter Speed & Freq.

PLY
LAY-UP

$[-45_2/0]_s$ $[-30_2/0]_s$ $[0_3]_s$ $[0_2/90]_s$ $[+-+30]_s$ $[\pm45/0]_s$ $[\pm45/0]_s$ $[30_2/0]_s$ $[45_2/0]_s$

Percent difference

D16/D11 and D16/D66 ratios

Percent difference

Flutter Speed   Flutter Frequency
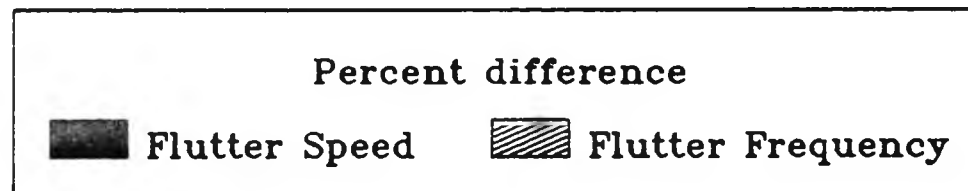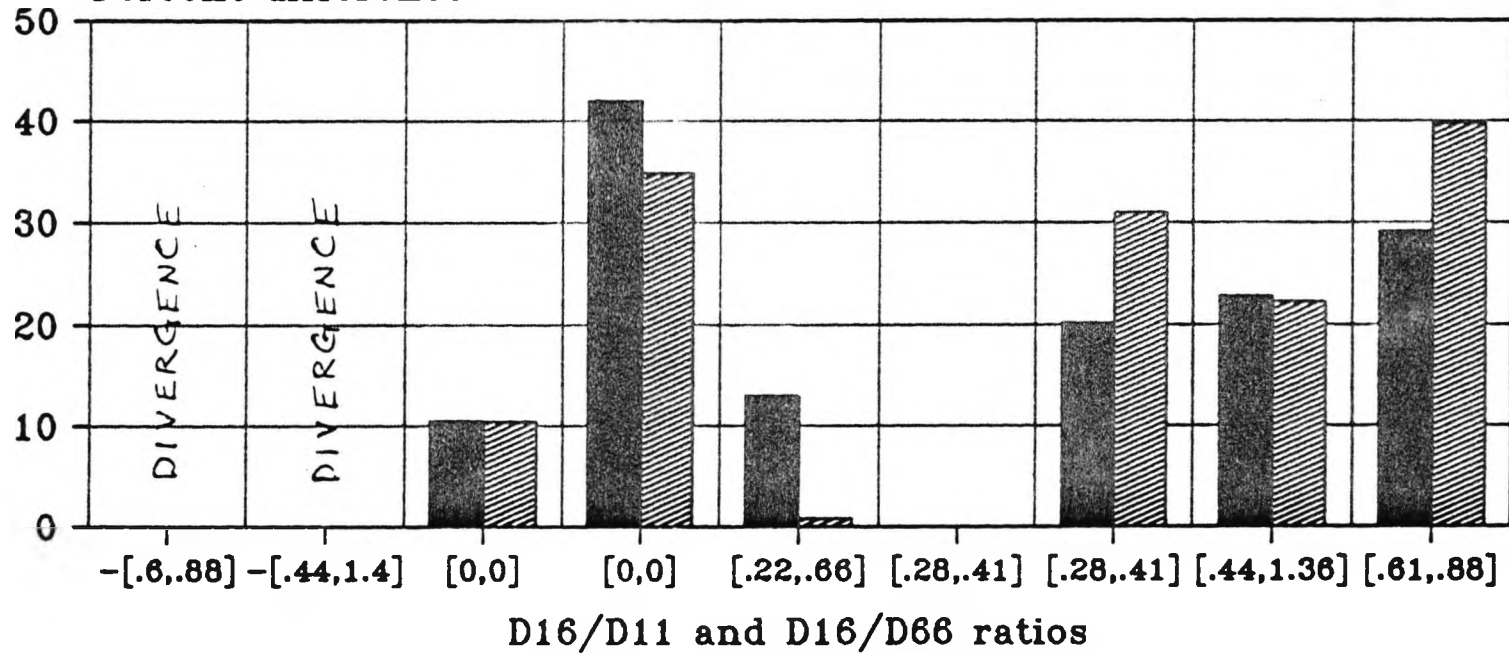
Fig. C3 Summary of percentage differences in flutter
speeds and frequencies for various ply layups

D.0 Aircraft Properties

D.1 The T59H Kestrel

D.1.1 Stiffness and Inertia Properties

The Kestrel is predominantly of glass fibre construction. Stiffness and inertia properties taken in the investigation for the wing, fuselage and tailplane are shown in Figures D1, D2 and D3 respectively.

D.1.2 Wing and Tailplane Geometry

Table D1 shows below the spanwise distribution of the wing and tailplane chord, including the elevators.

η	c (m)
0	0.900
0.1	0.869
0.2	0.838
0.3	0.808
0.4	0.780
0.5	0.750
0.6	0.719
0.7	0.631
0.8	0.539
0.9	0.451
1.0	0.360

i) Wing

η	c (m)
0	0.557
0.2	0.516
0.4	0.474
0.6	0.433
0.8	0.391
1.0	0.350

ii) Tailplane

Table D1 Spanwise variation of wing and tailplane chord lengths for Kestrel

D.1.3 Aerodynamic Properties

Tables D2 and D3 summarise the stability derivatives used to calculate the short period characteristics of the rigid aircraft, using Ref.(14), taking dε/dα as 0.0 and 0.0972 respectively. As

the phugoid mode is neglected in this investigation, terms relating to changes in forward speed are omitted. The wing area used in the evaluation of these derivatives is marginally smaller as the aeroelastic model did not take into account the gross wing area. Inertia and aerodynamic parameters are taken as in Table 3.1.

$S = 15.20$ m	$\mu_1 = 75.32$
$\bar{\bar{c}} = 0.724$ m	$i_y = 3.192$
$l = 4.82$ m	$V = 0.569$
$l_T = 4.58$ m	$\bar{\bar{V}}_T = 0.541$
$h_n = 0.650 \, \bar{\bar{c}}$	
$H_n = 0.0745 \, \bar{\bar{c}}$	
$z_w = 6.685$	$m_w = 11.75$
$z_q = 0.034$	$m_q = 5.04$

Table D2   Stability derivatives for $h = 0.576 \, \bar{\bar{c}}$ and $d\varepsilon/d\alpha = 0.0$ for Kestrel

$h_n = 0.613 \, \bar{\bar{c}}$	
$H_n = 0.0375 \, \bar{\bar{c}}$	
$z_w = 6.646$	$m_w = 5.879$
$z_q = 0.034$	$m_q = 5.04$
$z_{\dot{w}} = 0.003$	$m_{\dot{w}} = 0.490$

Table D3   Stability derivatives for $h = 0.576 \, \bar{\bar{c}}$ and $d\varepsilon/d\alpha = 0.0972$ for Kestrel

D.2 The Ricochet

D.2.1 Stiffness and Inertia Properties

The Ricochet is of aluminium construction and as it is a tailless aircraft stiffness and inertia details for the wing only, are shown in Figure D4.

D.2.2 Wing Geometry

The spanwise variation of wing chord length for the Ricochet is shown in Table D4.

η	c (m)
0.00	0.730
0.08	0.730
0.16	0.730
0.24	0.730
0.32	0.730
0.40	0.730
0.56	0.730
0.64	0.710
0.72	0.662
0.80	0.616
0.88	0.570
1.00	0.500

Table D4   Spanwise variation of wing chord length for Ricochet

D.2.3 Aerodynamic Properties

Here parameters are defined with respect to the standard mean chord, as in Ref.(70). Stability derivatives for the Ricochet are presented in Table D5 additional details of its geometry and aerodynamic parameters are found in Table 3.2. The terms z_q and m_q are calculated from expressions provided by Ref.(133).

$$\bar{c} = 0.685 \text{ m} \qquad \mu_1 = 59.21$$

$$i_y = 0.890$$

$$H_n = 0.0179 \ \bar{c}$$

$$z_w = 5.68 \qquad m_w = 6.768$$

$$z_q = 0.025 \qquad m_q = 3.36$$

Table D5 Stability derivatives for h = 0.21 $\bar{c}$
for Ricochet

D.3 The Cranfield A1

D.3.1 Stiffness and Inertia Properties

The A1 is primarily of aluminium construction and its wing
and tailplane stiffnesses are shown in Figures D5 and D6
respectively.

Component	Contribution to rolling moment of inertia (kgm^2)
Propellor	15.17
Engine,cowl	6.32
Bulkhead	1.26
Fuselage structure (assumed uniform)	9.48
Fuel	1.26
Instruments	2.74
Canopy	3.79
Seat, pilot	8.42
Tailplane/elevator	42.14
Fin/rudder	7.16

Table D6 Distribution of contribution to rolling moment of
inertia along fuselage for A1

Fig. D7 represents the variation of fuselage mass per unit length. Stiffness details pertaining to the fuselage are presented in Fig.3.20. The distribution of rolling moment of inertia for the A1, provided by Ref.(80), is shown in Table D6.

D.3.2 Wing and Tailplane Geometry

Table D7 shows below the spanwise distribution of the wing and tailplane, including the elevators.

η	c (m)
0	2.08
0.1	1.956
0.2	1.854
0.3	1.727
0.4	1.623
0.5	1.499
0.6	1.394
0.7	1.270
0.8	1.143
0.9	1.029
1.0	0.914

i) Wing

η	c (m)
0	1.07
0.2	0.990
0.4	0.910
0.6	0.830
0.8	0.750
1.0	0.670

ii) Tailplane

Table D7   Spanwise variation of wing and tailplane chord lengths for A1

D.3.3 Aerodynamic Properties

As with the Kestrel the short period mode was evaluated for two downwash ratio cases. Tables D8 and D9 present stability derivatives for $d\varepsilon/d\alpha$ = 0.0 and 0.4 respectively. Further geometric and aerodynamic details are shown in Table 3.3.

$$\overline{\overline{c}} = 1.57 \text{ m} \qquad \mu_1 = 70.53$$

$$i_y = 1.22$$

$$l = 4.36 \text{ m} \qquad V = 0.503$$

$$l_T = 4.33 \text{ m} \qquad \overline{V}_T = 0.500$$

$$h_n = 0.614 \, \overline{\overline{c}}$$

$$H_n = 0.348 \, \overline{\overline{c}}$$

$$z_w = 4.86 \qquad m_w = 97.87$$

$$z_q = 0.025 \qquad m_q = 3.979$$

Table D8   Stability derivatives for $h = 0.266 \, \overline{\overline{c}}$ and $d\varepsilon/d\alpha = 0$ for A1

$$h_n = 0.481 \, \overline{\overline{c}}$$

$$H_n = 0.215 \, \overline{\overline{c}}$$

$$z_w = 4.60 \qquad m_w = 57.15$$

$$z_q = 0.025 \qquad m_q = 3.979$$

$$z_{\dot{w}} = 0.009 \qquad m_{\dot{w}} = 1.592$$

Table D9   Stability derivatives for $h = 0.266 \, \overline{\overline{c}}$ and $d\varepsilon/d\alpha = 0.40$ for A1

D.4 Example Aircraft of Aspect Ratio 20 and 12

The stability derivatives for the aspect ratio 20 example aircraft are shown in Table D10. This aircraft is further outlined in Table 4.1.

$$\bar{\bar{c}} = 1.00 \text{ m} \qquad\qquad \mu_1 = 48.98$$

$$l = l_T = 5.125 \text{ m} \qquad\qquad i_y = 1.333$$

$$V = \bar{V}_T = 0.5125 \qquad\qquad \frac{d\varepsilon}{d\alpha} = 0.0$$

$$h_n = 0.716 \, \bar{\bar{c}}$$

$$H_n = 0.466 \, \bar{\bar{c}}$$

$$z_w = 2.2\pi \qquad\qquad m_w = 118.61$$

$$z_q = 0.066 \qquad\qquad m_q = 12.41$$

Table D10   Stability derivatives for $h = 0.25 \, \bar{\bar{c}}$ for representative aircraft of AR = 20

The stability derivatives calculated for the example aircraft of aspect ratio 12, outlined in Table 5.1, with and without the introduction of a downwash are shown in Tables D11 and D12 respectively.

$$\bar{\bar{c}} = 1.00 \text{ m} \qquad\qquad \mu_1 = 81.63$$

$$l = l_T = 5.125 \text{ m} \qquad\qquad i_y = 1.333$$

$$V = \bar{V}_T = 0.854 \qquad\qquad \frac{d\varepsilon}{d\alpha} = 0.0$$

$$h_n = 0.922 \, \bar{\bar{c}}$$

$$H_n = 0.672 \, \bar{\bar{c}}$$

$$z_w = 5.80 \qquad\qquad m_w = 239.09$$

$$z_q = 0.048 \qquad\qquad m_q = 15.00$$

Table D11   Stability derivatives for $h = 0.25 \, \bar{\bar{c}}$ for representative aircraft of AR = 12 without downwash

$$\frac{d\varepsilon}{d\alpha} = 0.3818$$

$h_n = 0.687 \, \bar{\bar{c}}$

$H_n = 0.437 \, \bar{\bar{c}}$

$z_w = 5.51$ $m_w = 147.79$

$z_q = 0.048$ $m_q = 15.00$

$z_w = 0.018$ $m_{\dot{w}} = 5.73$

Table D12   Stability derivatives for $h = 0.25 \, \bar{\bar{c}}$ for representative aircraft of AR = 12 with downwash
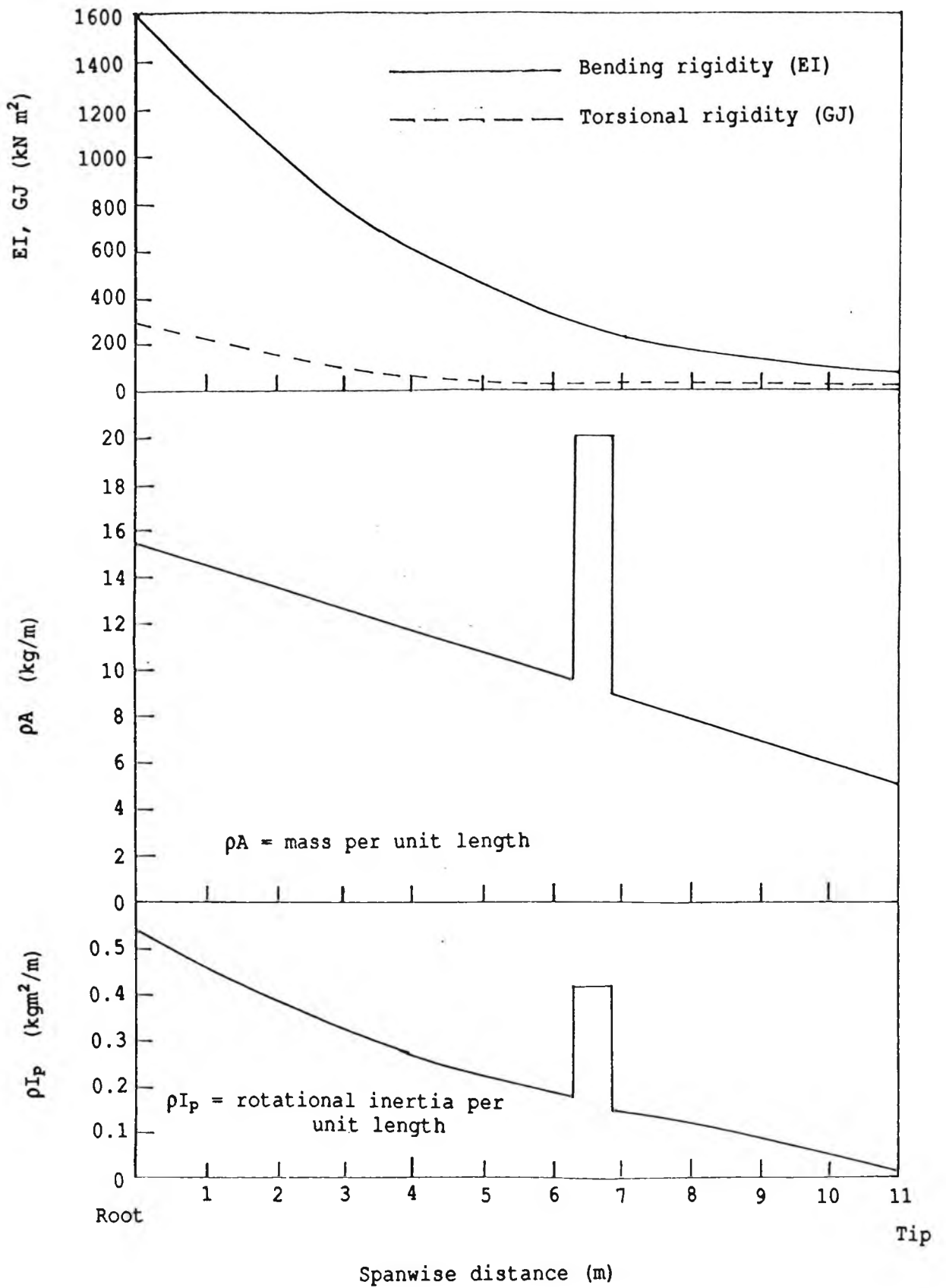
Fig. D1 Stiffness, mass and inertia properties of the Kestrel wing
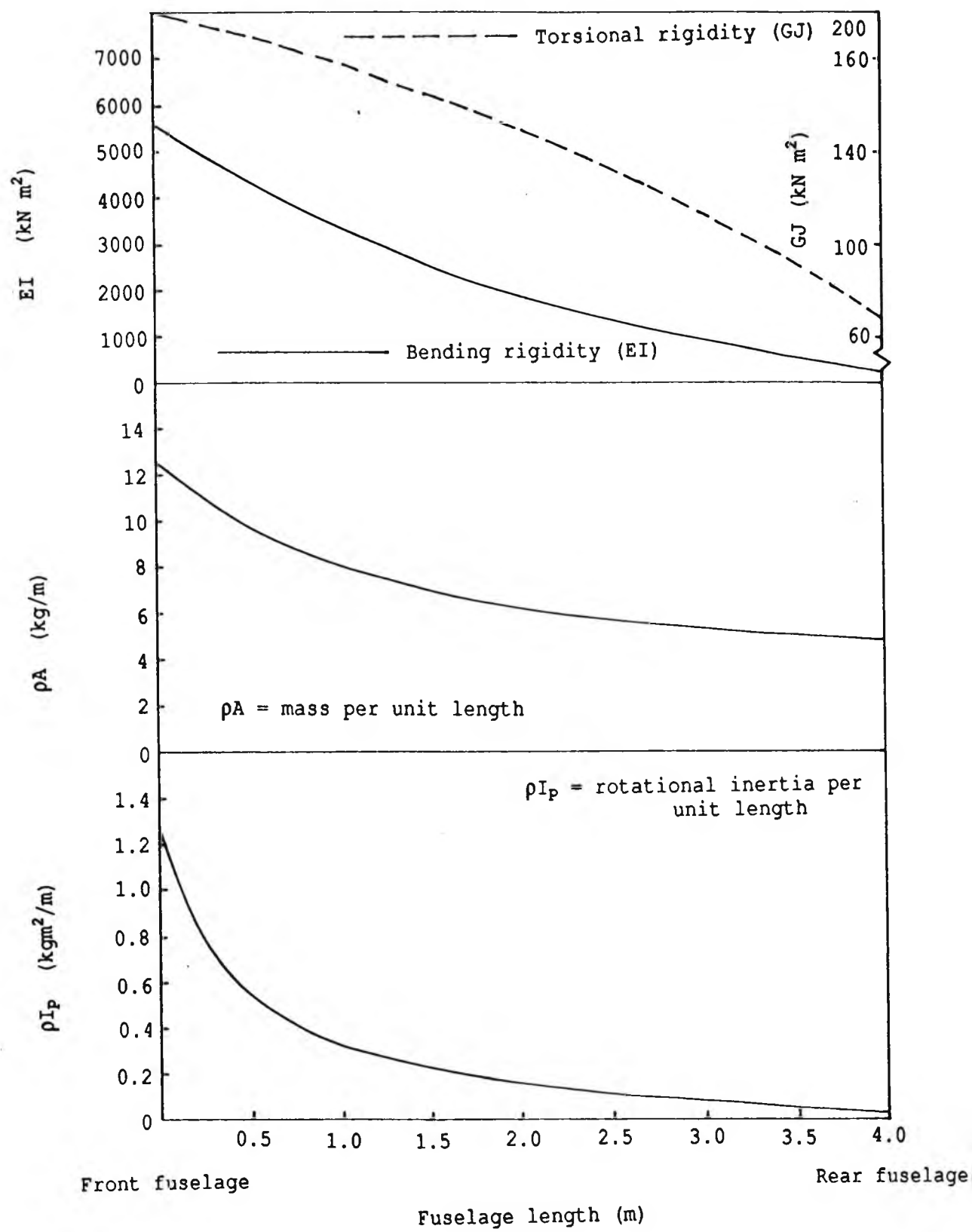
Fig. D2   Stiffness, mass and inertia properties of the Kestrel fuselage
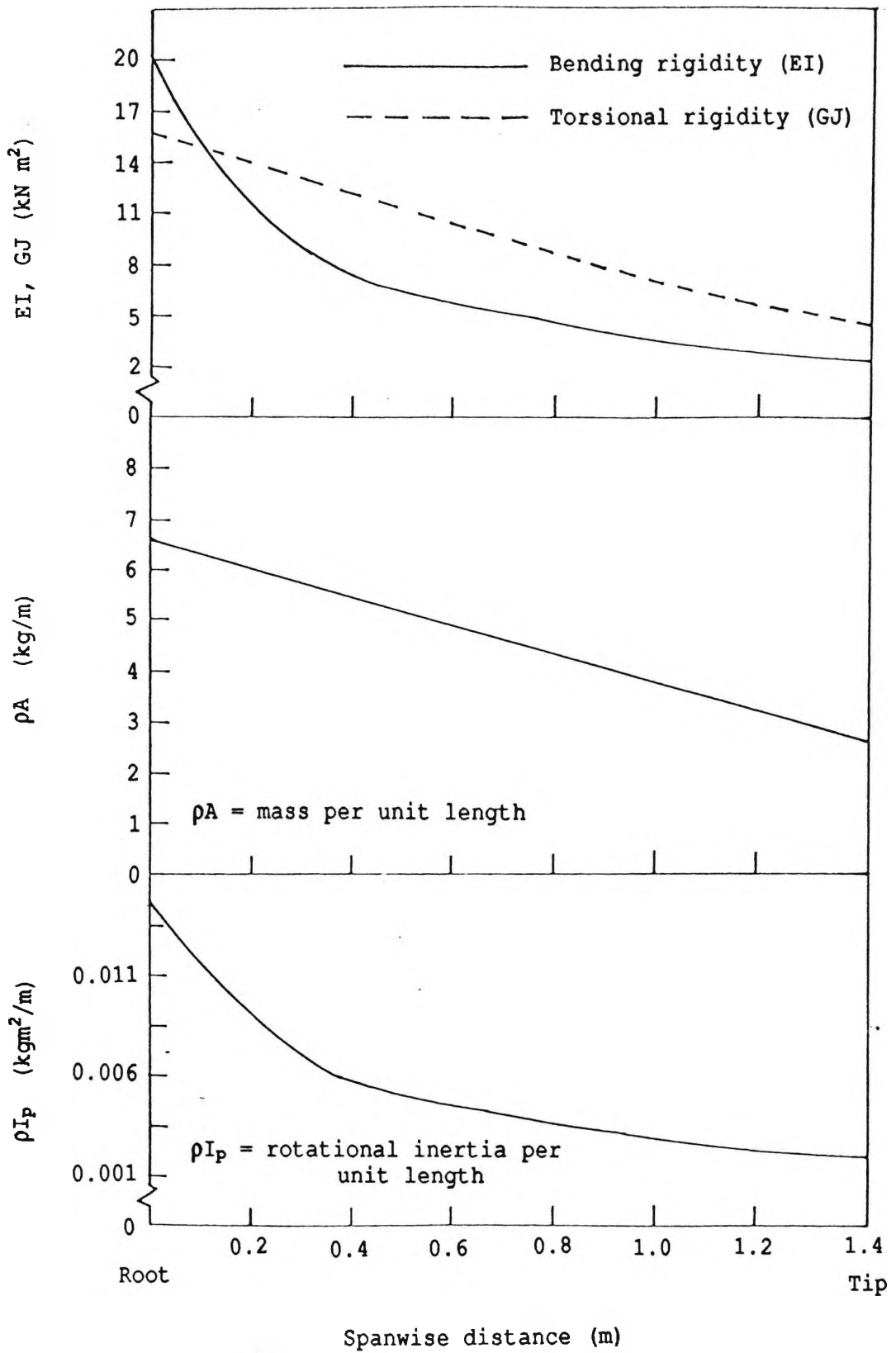
Fig. D3   Stiffness, mass and inertia properties of the Kestrel
          tailplane
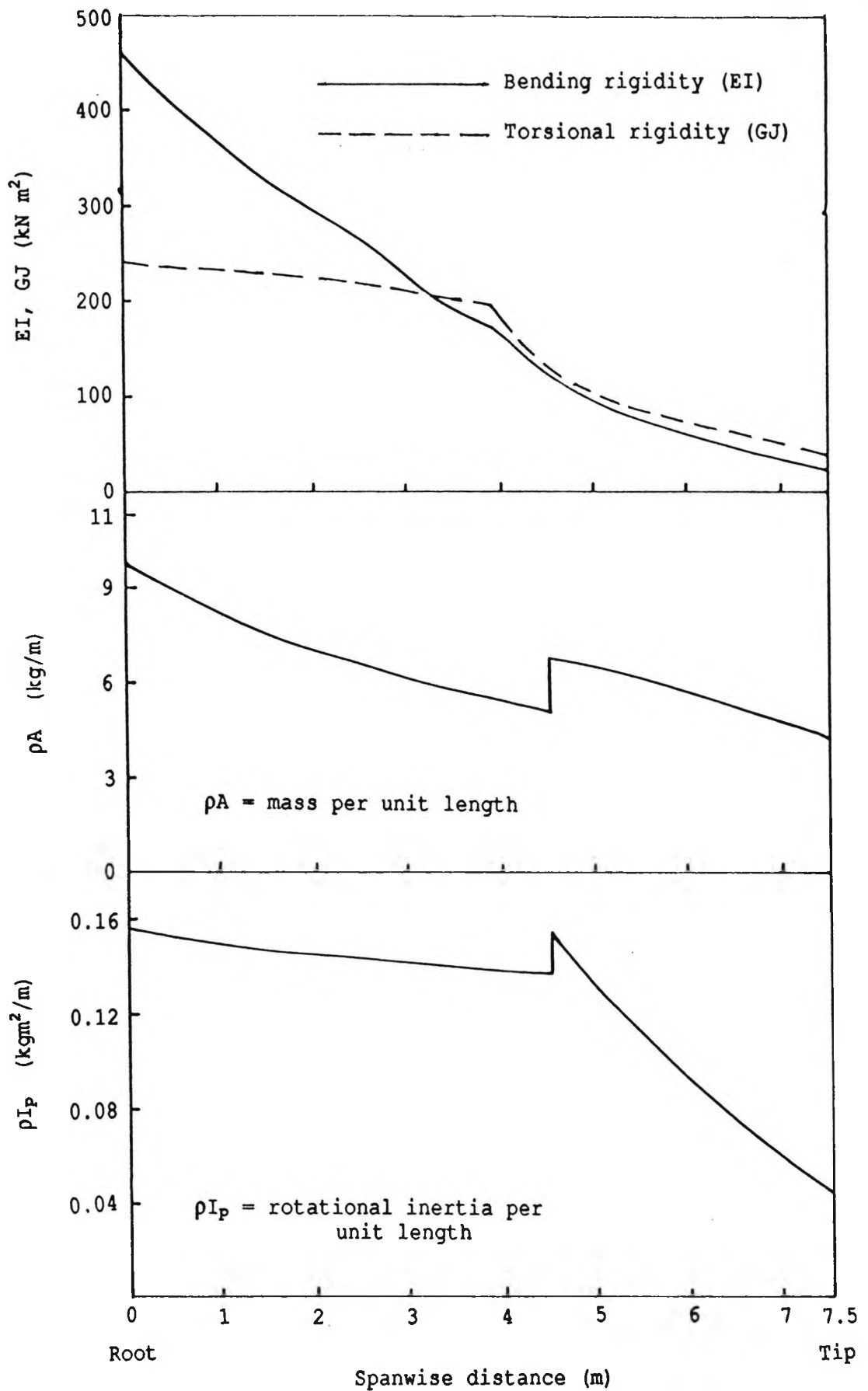
Fig. D4 Stiffness, mass and inertia properties of the Ricochet
wing
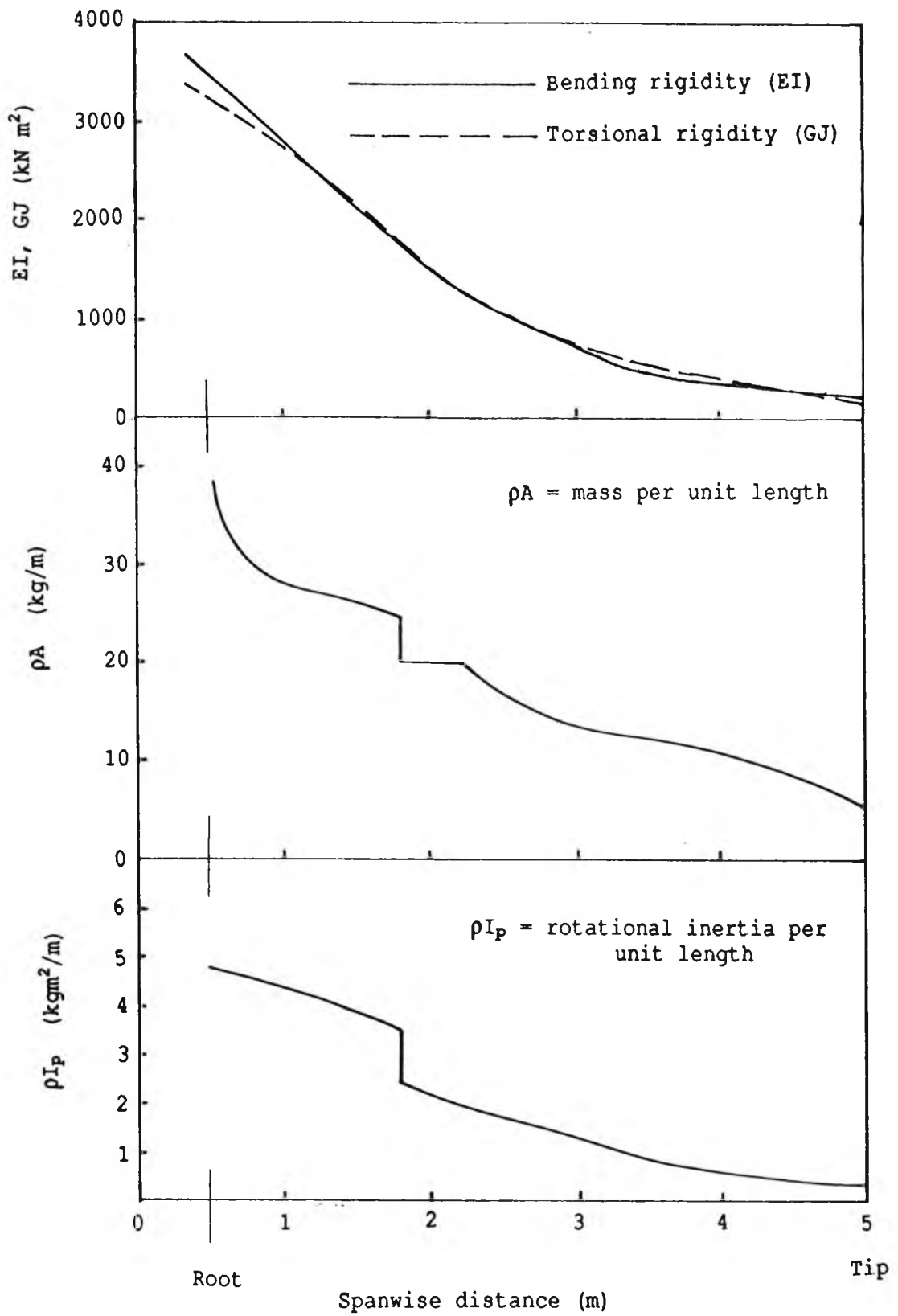
Fig. D5 Stiffness, mass and inertia properties of the A1 wing
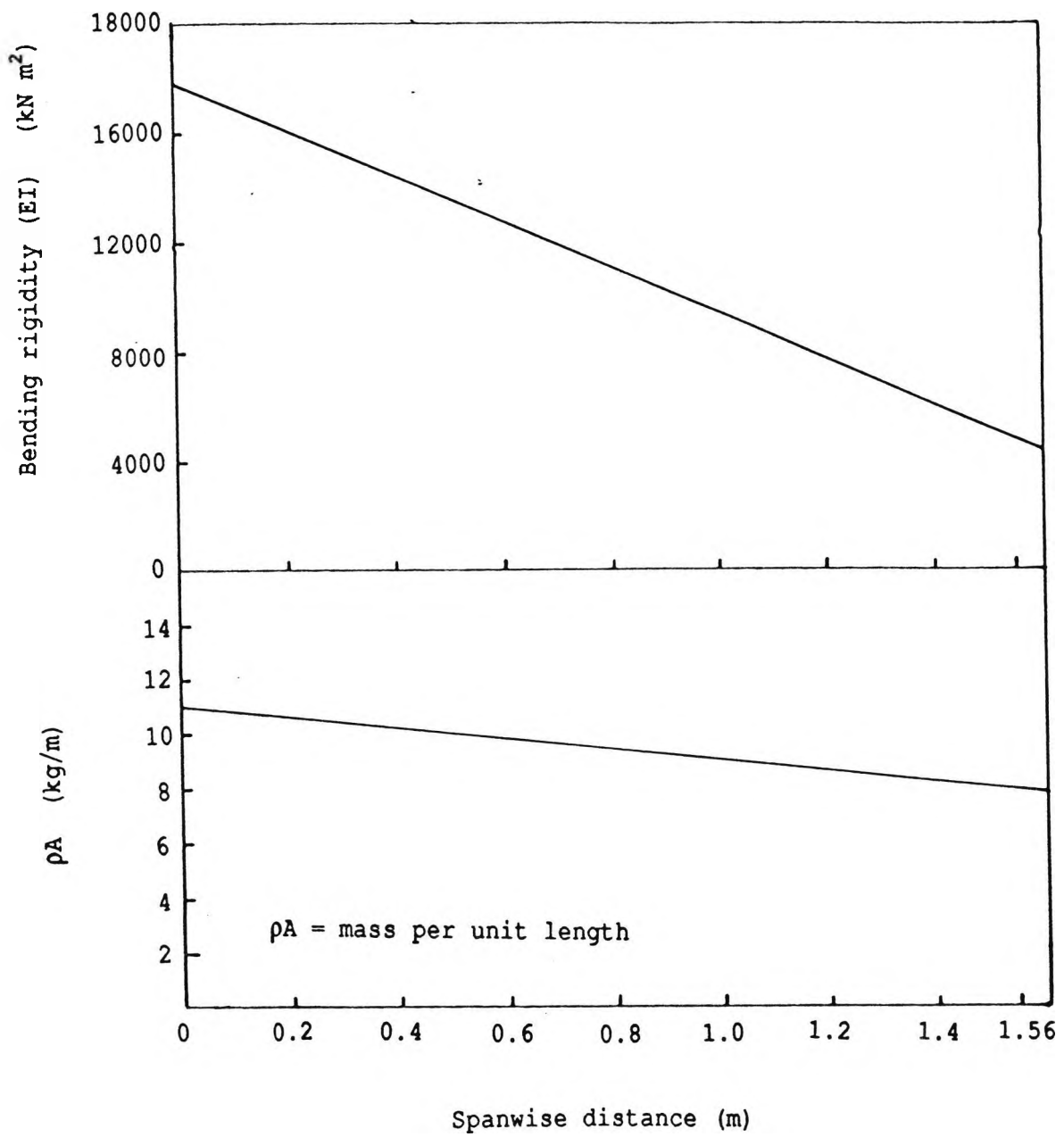
Fig. D6   Stiffness and mass properties of the A1 tailplane
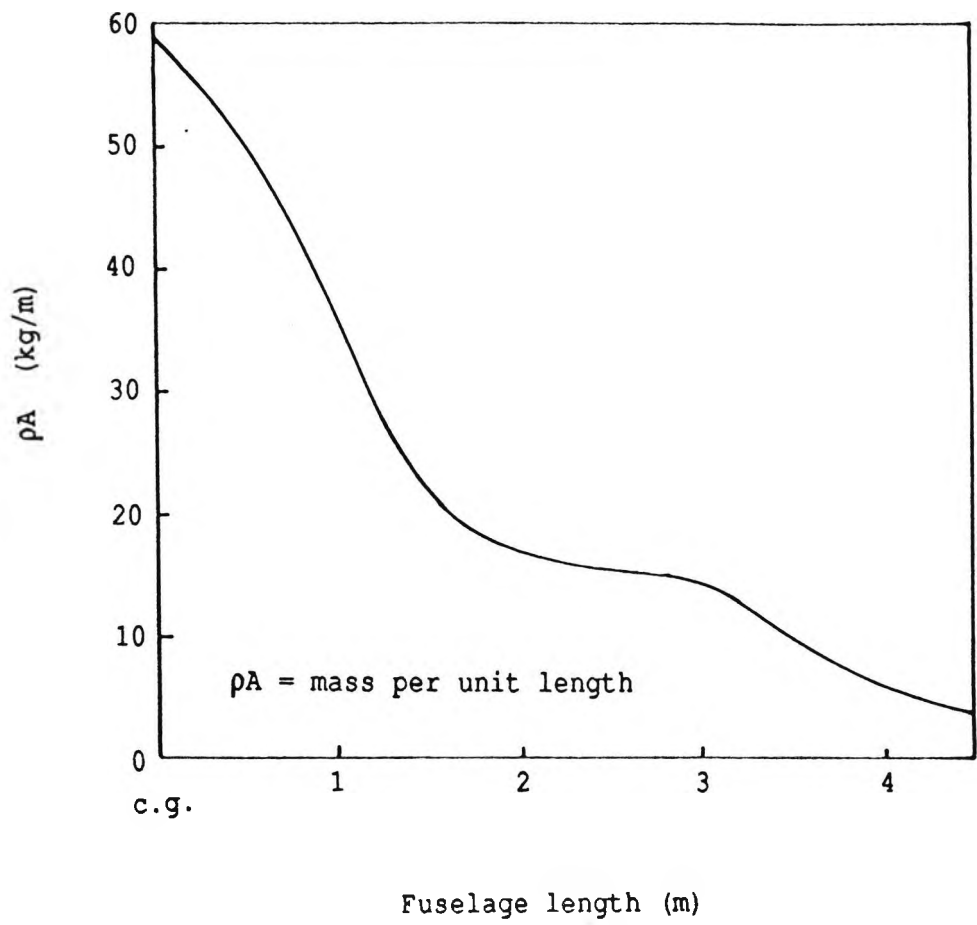
Fig. D7 Mass distribution of the A1 rear fuselage

E.0 Flutter Modes

Once the flutter speed is established, the flutter mode is found by deleting one row of, say, the nth order flutter matrix and solving for (n-1) of the variables in terms of the nth. However, the flutter matrix being complex, this leads to other variables (coordinates) to be complex numbers and so defining the relative contribution of the modes to the flutter motion both in magnitude and phase. The results of this calculation will lead to a complex column matrix q of the generalised coordinates with elements q_1, q_2, q_3,...,q_n. The flutter mode in terms of the vertical displacement h and pitching rotation α can be then be found by multiplying q by the modal matrix formed by the mode shapes. Therefore, at a spanwise distance y on the wing, the flutter mode in bending (vertical displacement) and torsion (pitching rotation) can be expressed as

$$
\begin{bmatrix} H(y) \\ \theta(y) \end{bmatrix} = \begin{bmatrix} h_1(y) & h_2(y) & h_3(y) & \cdots & h_n(y) \\ \alpha_1(y) & \alpha_2(y) & \alpha_3(y) & \cdots & \alpha_n(y) \end{bmatrix} \begin{bmatrix} q_1 \\ q_2 \\ \cdot \\ \cdot \\ q_n \end{bmatrix} \qquad (E.1)
$$

where $h_1(y),h_2(y),...,h_n(y)$ correspond to the bending modes of the n modes (that are included in the flutter analysis) at a spanwise station y and $\alpha_1(y),\alpha_2(y),...,\alpha_n(y)$ are the corresponding torsional modes at that point. H(y) and $\theta(y)$ are complex quantities and their magnitude and phase give relative measure of the vertical displacement (bending) and pitching rotation (torsion) vector at flutter speed at the spanwise station y. It then follows that the column matrix q with elements $q_1,q_2,...,q_n$ relates the contribution of the normal modes of vibration to the flutter motion through the use of Eq.(E.1) to give

$$H(y) = h_1 q_1 + h_2 q_2 + \cdots \cdots + h_n q_n = \sum_{i=1}^{N} h_i q_i \qquad (E.2)$$

$$\theta(y) = \alpha_1 q_1 + \alpha_2 q_2 + \cdots \cdots + \alpha_n q_n = \sum_{i=1}^{N} \alpha_i q_i \qquad (E.3)$$

where $h_i q_i$ in Eq.(E.2) denotes the contribution of the ith mode to the vertical displacement vector of the flutter mode $H(y)$. similarly, $\alpha_i q_i$ in Eq.(E.3) gives the contribution of the ith mode to the pitching rotation vector of the flutter mode $\theta(y)$.

APPENDIX F

F.0 Generalised Theodorsen Function C(k)

F.1 The Theodorsen Circulation Function for Generalised Motion

The Theodorsen circulation function $C(k)$ for generalised motion has been developed by Luke and Dengler. An extract from their work is reproduced here.

In the treatment of aerodynamic forces on an oscilliating aerofoil, it is assumed that the motion follows the law e^{ikt} where t is the time variable and

$$ik = \mu + i\omega \qquad (F.1)$$

Thus ω gives the frequency of motion, while μ defines the rate of decay. If $\mu < 0$ the motion is convergent or stable; if $\mu < 0$ the motion is divergent or unstable. When $\mu = 0$, the motion is said to be neutrally stable.

To accomplish the generation of the Theodorsen function $C(k)$ effectively we will start by the definition of the function as presented by Theodorsen[5].

$$C(k) = \frac{\displaystyle\int_1^\infty \frac{x}{\sqrt{x^2-1}} U\, dx}{\displaystyle\int_1^\infty \frac{x+1}{\sqrt{x^2-1}} U\, dx} \qquad (F.2)$$

where it is supposed that

$$U = U_0 e^{i[k(s/b - x) + \phi]} \qquad (F.3)$$

and that $\omega > 0$. It is well known in the theory of Bessel functions that

$$K_n(z) = \int_0^\infty e^{-z \cosh y} \cosh ny \, dy \qquad (F.4)$$

which is valid if $| \arg z | < \frac{\pi}{2}$. This requires that $Re(z) > 0$. Let

$$z = ik \qquad (F.5)$$

Thus, if $Re(z) > 0$ it follows that $\mu > 0$, so that the motion is assumed to be divergent. Combining Eq.(F.2) through (F.5) with the well-known relation.

$$K_n(z) = (\pi/2) i e^{(1/2)n\pi i} H_n^{(1)}(iz) \qquad (F.6)$$

It is readily deduced that

$$C(k) = \frac{H_1^{(2)}(k)}{H_1^{(2)}(k) + iH_0^{(2)}(k)} \qquad (F.7)$$

which is the generalised Theodorsen $C(k)$ function. It is true that, in the development of Eq.(F.7) it was necessary to require that $\mu > 0$. However Eq.(F.7) has no need for such a restriction and therefore by the method of analytic continuation, one can argue that Eq.(F.7) is valid for all μ's.

The Theodorsen function defined in Eq.(5.7) can be expressed as

$$C(z) = \frac{H_1^{(2)}(z)}{H_1^{(2)}(z) + iH_0^{(2)}(z)} = F(\rho,\theta) + iG(\rho,\theta) \qquad (F.8)$$

where

$$z = \rho e^{i\theta} = \omega - i\mu = k \ , \ \rho \geq 0 \ \ |\theta| \leq \frac{\pi}{2}$$

Thus if the motion is harmonic, $\theta = 0$ therefore, $\rho = k$. In this case, of course, values of $C(k)$ are well known. Since the intention of this section is to study the aerodynamic system for non-harmonic motion it is important and necessary to know the

values of C(k) for generalised z. Luke and Dengler tabulated C(z) for the following range of ρ and θ.

$$\rho : 0(0.1) \ 0.3(0.02) \ 0.5(0.05) \ 1.0(0.5) \ 10.0$$
$$\theta : -5^0(5^0) \ 30^0$$

Although these values have been tabulated they would prove time consuming to type in and insufficent to cover the total range of ρ and θ that might be required. Since equation (F.8) relies on the solution of bessel functions for complex arguments z a subroutine was written in FORTRAN to evaluate these values with a set of series solution provided by Refs.(134) and (135).

F.2 Solution of Bessel Functions for Complex Arguments

From equation (F.8) the definition of C(z) is given by:

$$C(z) = \frac{H_1^{(2)}(z)}{H_1^{(2)}(z) + iH_0^{(2)}(z)} = F(\rho,\theta) + iG(\rho,\theta)$$

where

$$z = \rho e^{i\theta}$$

$$H_0^{(2)} = J_0(z) - i \ Y_0(z)$$

$$H_1^{(2)} = J_1(z) - i \ Y_1(z)$$

F.2.1 Derivation of $J_n(z)$ and $Y_n(z)$

Bessel functions of order υ satisfy Bessel's differential equation

$$z \frac{d^2y}{dz^2} + z \frac{dy}{dz} + (z^2-\upsilon^2)y = 0 \qquad (F.9)$$

One fundamental solution of (F.9) is $J_\upsilon(z)$, which may be defined by the infinite series

$$J_{\upsilon}(z) = \sum_{k=0}^{\infty} \frac{(-1)^k (z/2)^{\upsilon + 2k}}{k! \; \Gamma(\upsilon + k + 1)} \tag{F.10}$$

When υ is non zero or an integer and k also an integer, $J_{-\upsilon}(z)$ is a second independent solution of Bessel's differential equation. However, when υ is an integer n, $J_{-n}(z) = (-1)^n J_n(z)$. In this case a second solution, $Y_{\upsilon}(z)$, may be defined as follows:

$$Y_{\upsilon}(z) = (\cos(\upsilon\pi) \; J_{\upsilon}(z) - J_{-\upsilon}(z))/\sin(\upsilon\pi) \tag{F.11}$$

F.2.2 Computation of $J_0(z)$ and $J_1(z)$
From the definition in Eq.(F.10)

$$J_0(z) = J_0(\rho e^{i\theta}) = \sum_{k=0}^{\infty} (-1)^k \frac{(\rho/2)^{2k}}{(k!)^2} e^{2ki\theta} = U_0(\rho,\theta) + i \; V_0(\rho,\theta)$$

we get

$$U_0(\rho,\theta) = \sum_{k=0}^{\infty} (-1)^k \frac{(\rho/2)^{2k}}{(k!)^2} \cos 2K\theta \tag{F.12}$$

$$V_0(\rho,\theta) = \sum_{k=0}^{\infty} (-1)^k \frac{(\rho/2)^{2k}}{(k!)^2} \sin 2K\theta \tag{F.13}$$

and let

$$J_1(z) = J_1(\rho e^{i\theta}) = U_1(\rho,\theta) + i \; V_1(\rho,\theta)$$

since

$$J_1(z) = -\frac{d}{dz} J_0(z) = -e^{-i\theta} \frac{\partial}{\partial \rho} \left[U_0 + i \; V_0 \right]$$

it follows that

$$U_1(\rho,\theta) = - \frac{\partial}{\partial\rho} \left[U_0 \cos\theta + V_0 \sin\theta \right] \qquad \text{(F.14)}$$

$$V_1(\rho,\theta) = \frac{\partial}{\partial\rho} \left[U_0 \sin\theta - V_0 \cos\theta \right] \qquad \text{(F.15)}$$

From Bessel's differential equation (F.9), the following two relations are readily obtained:

$$U_1 = \rho \left[(U_0 + \frac{\partial^2 U_0}{\partial\rho^2}) \cos\theta + (-V_0 + \frac{\partial^2 V_0}{\partial\rho^2}) \sin\theta \right] \qquad \text{(F.16)}$$

$$V_1 = \rho \left[(U_0 - \frac{\partial^2 U_0}{\partial\rho^2}) \sin\theta + (V_0 + \frac{\partial^2 V_0}{\partial\rho^2}) \cos\theta \right] \qquad \text{(F.17)}$$

Substituting Eqs.(F.12) and (F.13) into Eqs.(F.16) and (F.17)

$$U_1 = \rho \left[\left(\sum_{k=0}^{\infty} (-1)^k \frac{(\rho/2)^{2k}}{(k!)^2} + (2k)(2k-1) \sum_{k=0}^{\infty} (-1)^k \frac{(\rho/2)^{2k-2}}{(k!)^2} \right) \right.$$

$$\cos 2k\theta \cos\theta + \left(-\sum_{k=0}^{\infty} (-1)^k \frac{(\rho/2)^{2k}}{(k!)^2} + (2k)(2k-1) \sum_{k=0}^{\infty} (-1)^k \right.$$

$$\left. \left. \frac{(\rho/2)^{2k-2}}{(k!)^2} \right) \sin 2K\theta \sin\theta \right] \qquad \text{(F.18)}$$

$$V_1 = \rho \left[\left(\sum_{k=0}^{\infty} (-1)^k \frac{(\rho/2)^{2k}}{(k!)^2} - (2k)(2k-1) \sum_{k=0}^{\infty} (-1)^k \frac{(\rho/2)^{2k-2}}{(k!)^2} \right) \right.$$

$$\sin 2k\theta \sin \theta + \left(\sum_{k=0}^{\infty} (-1)^k \frac{(\rho/2)^{2k}}{(k!)^2} + (2k)(2k-1) \sum_{k=0}^{\infty} (-1)^k \right.$$

$$\left. \left. \frac{(\rho/2)^{2k-2}}{(k!)^2} \sin 2K\theta \cos \theta \right] \right] \tag{F.19}$$

F.2.3 Computation of $Y_0(z)$ and $Y_1(z)$

The limiting values of Eq.(F.11), when υ is zero or one, are given below:

$$Y_0(z) = \frac{2}{\pi} \left[J_0(z)(\gamma + \log_e \frac{1}{2} z) + \sum_{k=0}^{\infty} (-1)^{k+1} \frac{(z/2)^{2k}}{(k!)^2} \left(1 + \frac{1}{2} + \cdots \right. \right.$$

$$\left. \left. \cdots + \frac{1}{k} \right) \right] \tag{F.20}$$

$$Y_1(z) = \frac{2}{\pi} \left[J_1(z)(\gamma + \log_e \frac{1}{2} z) - \frac{2}{\pi z} + \frac{1}{\pi} \sum_{k=0}^{\infty} (-1)^{k+1} \frac{(z/2)^{2k+1}}{k!(k+1)!} \left(2 \left(1 \right. \right. \right.$$

$$\left. + \frac{1}{2} + \cdots + \frac{1}{k} \right) + \frac{1}{k+1} \right] \tag{F.21}$$

where $\gamma = 0.577215664901533$ is Eulers constant

For the purposes of computation the real and imaginary part of $Y_0(z)$ and $Y_1(z)$ may be written in the form.

$$U_0(\rho,\theta) = \frac{2}{\pi} \left[u_0(\rho,\theta)(\gamma + \log_e \tfrac{1}{2} \rho) - \theta\, v_0(\rho,\theta) \right] + S_0(\rho,\theta)$$

$$V_0(\rho,\theta) = \frac{2}{\pi} \left[v_0(\rho,\theta)(\gamma + \log_e \tfrac{1}{2} \rho) - \theta\, u_0(\rho,\theta) \right] + T_0(\rho,\theta)$$

$$U_1(\rho,\theta) = \frac{2}{\pi} \left[u_1(\rho,\theta)(\gamma + \log_e \tfrac{1}{2} \rho) - \theta\, v_1(\rho,\theta) \right] - \frac{2}{\pi\rho} \cos\theta$$
$$- S_1(\rho,\theta)$$

$$V_1(\rho,\theta) = \frac{2}{\pi} \left[v_1(\rho,\theta)(\gamma + \log_e \tfrac{1}{2} \rho) + \theta\, u_1(\rho,\theta) \right] + \frac{2}{\pi\rho} \sin\theta$$
$$- T_1((\rho,\theta)$$

$$(F.22)$$

where

$$S_0(\rho,\theta) = \frac{2}{\pi} \sum_{k=0}^{\infty} (-1)^{k+1} \frac{\rho^{2k}}{2^{2k}(k!)^2} \left(1 + \frac{1}{2} + \cdots + \frac{1}{k} \right) \cos 2k\theta$$

$$T_0(\rho,\theta) = \frac{2}{\pi} \sum_{k=0}^{\infty} (-1)^{k+1} \frac{\rho^{2k}}{2^{2k}(k!)^2} \left(1 + \frac{1}{2} + \cdots + \frac{1}{k} \right) \sin 2k\theta$$

$$S_1(\rho,\theta) = \frac{1}{\pi} \sum_{k=0}^{\infty} \frac{(-1)^k \rho^{2k+1}}{2^{2k+1} k!(k+1)!} \left(2\left(1 + \frac{1}{2} + \cdots + \frac{1}{k} \right) \right.$$
$$\left. + \frac{1}{k+1} \right) \cos(2k+1)\theta$$

$$T_1(\rho,\theta) = \frac{1}{\pi} \sum_{k=0}^{\infty} \frac{(-1)^k \rho^{2k+1}}{2^{2k+1} k!(k+1)!} \left(2\left(1 + \frac{1}{2} + \cdots + \frac{1}{k} \right) \right.$$
$$\left. + \frac{1}{k+1} \right) \sin(2k+1)\theta$$

$$(F.23)$$

G.0 Model of Unsteady Wake

G.1 Wake Circulation

The aerofoil and wake is represented by a vortex sheet, where the time dependence of the total circulation around the aerofoil calls for a wake of two-dimensional shed vortices, along the x-axis from the trailing edge to infinity. With γ and γ_w the running circulations of the wing and wake, respectively.[33]

The quantity γ_w can be written in terms of the aerofoil circulation Γ. A physically plausible derivation of their relationship consists of saying that the wake vortex element shed from the trailing edge during any small time interval dt has a circulation equal and opposite to the corresponding change of wing circulation:

$$\gamma_w(b,t) \ dx = - \frac{d \ \Gamma(t)}{dt} \ dt \qquad (G.1)$$

Since the fluid is all moving at approximately U, we assume $dx = Udt$ and

$$U \ \gamma_w(b,t) = - \frac{d \ \Gamma(t)}{dt} \qquad (G.2)$$

The vortex element at a general point ξ of the wake was shed in the past at a moment determined by the time interval $(\xi-b)/U$ required for it to reach ξ Hence,

$$U \ \gamma_w\left(\xi, t + \frac{\xi - b}{U}\right) = - \frac{d \ \Gamma(t)}{dt} \qquad (G.3)$$

Since all variables are proportional to $e^{i\omega t}$, this can be written

$$U \ \gamma_w e^{i\omega\left(t + \frac{\xi - b}{U}\right)} = - i\omega \ \Gamma \ e^{i\omega t} \qquad (G.4)$$

or

$$\gamma_w(\xi) = - \frac{i\omega}{U} \ \Gamma e^{ik} \ e^{-i(\omega\xi/U)}. \qquad (G.5)$$

Therefore to give the net change in the bound circulation between point ξ_A and ξ_B

$$d\Gamma = \int_{\xi_A}^{\xi_B} \gamma_w(\xi) \, d\xi = \int_{\xi_A}^{\xi_B} -\frac{i\omega}{U} \Gamma e^{ik} e^{-i(\omega\xi/U)} \, d\xi$$

$$= -\frac{i\omega}{U} \Gamma e^{ik} \int_{\xi_A}^{\xi_B} e^{-i(\omega\xi/U)} \, d\xi$$

$$= \Gamma e^{ik} \left[e^{-i(\omega\xi/U)} \right]_{\xi_A}^{\xi_B}$$

$$= \Gamma e^{ik} \left[e^{-i(\omega\xi_B/U)} - e^{-i(\omega\xi_A/U)} \right] \qquad (G.6)$$

G.2 Airfoil Circulation

The expression for the aerofoil circulation is given in Ref.(33) as:

$$\Gamma = \frac{4 b e^{-ik} \int_{-1}^{1} \sqrt{\frac{1 + \xi^*}{1 - \xi^*}} \; W_a(\xi^*) \, d\xi^*}{\pi i k \left(H_1^{(2)}(k) + iH_0^{(2)}(k) \right)} \qquad (G.7)$$

where $\xi^* = \xi/b$

$$W_a(\xi^*) = -\dot{h} - U\alpha - \dot{\alpha}b(\xi^* - a_h)$$

Since all variables are proportional to $e^{i\omega t}$

$$W_a(\xi^*) = -i\omega h - U\alpha - i\omega b\alpha(\xi^* - a_h) \qquad (G.8)$$

Substituting Eq.(G.8) into the integral of Eq.(G.7)

$$\int_{-1}^{1} \sqrt{\frac{1 + \xi^*}{1 - \xi^*}} \; W_a(\xi^*) \; d\xi \; =$$

$$(-i\omega h - U\alpha + i\omega\alpha b a_h) \int_{-1}^{1} \sqrt{\frac{1 + \xi^*}{1 - \xi^*}} \; d\xi^* - i\omega\alpha b \int_{-1}^{1} \xi^* \sqrt{\frac{1 + \xi^*}{1 - \xi^*}} \; d\xi^*$$

(G.9)

Evaluation of these integrals leads

$$= \quad \pi(-i\omega h - U\alpha + i\omega\alpha b a_h) - i\omega\alpha b \frac{\pi}{2}$$

$$= \quad \pi(-i\omega h - U\alpha - i\omega\alpha b (\tfrac{1}{2} - a_h)) \qquad (G.10)$$

Inserting Eq.(G.10) back into (G.7)

$$\Gamma = - \; 4 \; b \; e^{-ik} \left[\frac{i\omega h + U\alpha + i\omega\alpha b(\tfrac{1}{2} - a_h)}{ik \; (H_1^{(2)}(k) + iH_0^{(2)}(k))} \right]$$

As $k = \dfrac{\omega b}{U}$

$$\Gamma = - \; 4 \; U \; e^{-ik} \left[\frac{ikh + b\alpha + ikb\alpha(\tfrac{1}{2} - a_h)}{ik \; (H_1^{(2)}(k) + iH_0^{(2)}(k))} \right] \qquad (G.11)$$

As aerofoil motion is assumed convergent of the form $e^{\lambda t}$

Therefore $ik = \lambda = \mu + i\omega$

Equation (G.10) can be re-written as

264

$$\Gamma = 4 \ U \ e^{-\lambda} \left[\frac{\lambda h + \alpha b + \lambda b \alpha \ (\frac{1}{2} - a_h)}{\lambda (H_1^{(2)} (-i\lambda) + i H_0^{(2)} (-i\lambda))} \right]$$

This can be written in matrix form as follows

$$\left[\ \Gamma \ \right] = \left[\ \Gamma_h \quad \Gamma_\alpha \ \right] \left[\begin{array}{c} h \\ \alpha \end{array} \right]$$

where $\qquad \Gamma_h = - \ \dfrac{4 \ U \ e^{-\lambda} \ \lambda}{\lambda \ (H_1^{(2)}(-i\lambda) + i H_0^{(2)}(-i\lambda))}$

(G.12)

$$\Gamma_\alpha = - \ \frac{4 \ U \ e^{-\lambda} \ b \ (\ 1 + (\frac{1}{2} - a_h)\lambda)}{\lambda \ (H_1^{(2)}(-i\lambda) + i H_0^{(2)}(-i\lambda))}$$

G.3 Derivation of Tailplane Generalised Aerodynamic Matrix with Downwash Effects included

Applying the correct transformation the resulting additional lift and moment which take proper account of transport lag effects can be expressed in terms of the induced velocities at the tailplane.

$$\left[\begin{array}{c} L_T \\ M_{\alpha T} \end{array} \right] = \left[\begin{array}{cc} AD_{11} & AD_{12} \\ AD_{21} & AD_{22} \end{array} \right] \left[\begin{array}{c} V_h \\ V_\alpha \end{array} \right]$$

(G.13)

where $\qquad AD_{11} = AD_{12} = - \ a_0 \rho U C(k) b$

(G.14)

$$AD_{21} = AD_{22} = a_1 \rho U C(k) b^2 (\ \frac{1}{2} + a_h)$$

The lift and moment are seen to be both functions of the unsteady velocities induced by the heave and pitch modes at the wing. Applying the transformation into normal co-ordinates

265

$$V_h(y,t) = \sum_{i=1}^{N} V_{ih}(y) \; q_i(t)$$

(G.15)

$$V_\alpha(y,t) = \sum_{i=1}^{N} V_{i\alpha}(y) \; q_i(t)$$

Utilising the virtual work done by the aerodynamic forces at the tailplane

$$\delta W_i = \sum_{i=1}^{N} \delta q_i \int_0^{S_T} (L(y)h_{T_i}(y) + M(y)\alpha_{T_i}(y)) \; dy$$

(G.16)

$$\begin{bmatrix} \dfrac{\delta W_1}{\delta q_1} \\ \dfrac{\delta W_2}{\delta q_2} \\ \vdots \\ \dfrac{\delta W_n}{\delta q_n} \end{bmatrix} = \int_0^{S_T} \begin{bmatrix} h_{1T} & \alpha_{1T} \\ h_{2T} & \alpha_{2T} \\ \vdots & \vdots \\ h_{nT} & \alpha_{nT} \end{bmatrix} \begin{bmatrix} L_T \\ M_{\alpha_T} \end{bmatrix} \; dy$$

(G.17)

Substituting for $\begin{bmatrix} L \\ M_\alpha \end{bmatrix}$ from Eq.(G.13) into Eq.(G.17)

$$\begin{bmatrix} \dfrac{\delta W_1}{\delta q_1} \\ \dfrac{\delta W_2}{\delta q_2} \\ \vdots \\ \dfrac{\delta W_n}{\delta q_n} \end{bmatrix} = \int_0^{S_T} \begin{bmatrix} h_{1T} & \alpha_{1T} \\ h_{2T} & \alpha_{2T} \\ \vdots & \vdots \\ h_{nT} & \alpha_{nT} \end{bmatrix} \begin{bmatrix} AD_{11} & AD_{12} \\ AD_{21} & AD_{22} \end{bmatrix} \begin{bmatrix} V_h \\ V_\alpha \end{bmatrix}$$

266

$$
\begin{bmatrix} \dfrac{\delta W}{\delta q_1}^{1} \\[6pt] \dfrac{\delta W}{\delta q_2}^{2} \\ \vdots \\ \dfrac{\delta W}{\delta q_n}^{n} \end{bmatrix} = \int_0^{S_T} \begin{bmatrix} h_{1T} & \alpha_{1T} \\ h_{2T} & \alpha_{2T} \\ \vdots & \vdots \\ h_{nT} & \alpha_{nT} \end{bmatrix} \begin{bmatrix} AD_{11} & AD_{12} \\ AD_{21} & AD_{22} \end{bmatrix} \begin{bmatrix} V_{1h} & V_{2h} & \cdots & V_{nh} \\ V_{1\alpha} & V_{2\alpha} & \cdots & V_{n\alpha} \end{bmatrix} \begin{bmatrix} q_1 \\ q_2 \\ \vdots \\ q_n \end{bmatrix} dy
$$

$$
= \begin{bmatrix} DQT_{11} & DQT_{12} & \cdots & DQT_{1n} \\ DQT_{21} & DQT_{22} & \cdots & DQT_{2n} \\ \vdots & \vdots & & \vdots \\ DQT_{n1} & DQT_{n2} & \cdots & DQT_{nn} \end{bmatrix} \begin{bmatrix} q_1 \\ q_2 \\ \vdots \\ q_n \end{bmatrix} \qquad (G.18)
$$

where

$$
DQFT(i,j) = \int_0^{S_T} AD_{11}V_{jh}h_{iT} + AD_{12}V_{j\alpha}\,h_{iT} + AD_{21}V_{jh}\,\alpha_{iT} + AD_{22}V_{j\alpha}\,\alpha_{iT}\; dy
$$

$$(G.19)$$

G.4 Evaluation of circulation integrals

Taking x as ξ^* the first term of Eq.(G.9) can be expressed as

$$
\int_{-1}^{1} \sqrt{\frac{1+x}{1-x}}\; dx = \int_{-1}^{1} \frac{1+x}{\sqrt{1-x^2}}\; dx
$$

Applying the substitution $x = \cos\theta$

$$dx = -\sin\theta\; d\theta$$

Also changing the limits of integration

$$
x = \left\{ \begin{array}{c} 1 \\ -1 \end{array} \right. = \theta = \left\{ \begin{array}{c} 0 \\ \pi \end{array} \right.
$$

$$\int_{\pi}^{0} \frac{1 + \cos \theta}{\sqrt{1 - \cos^2 \theta}} \, -\sin \theta \, d\theta$$

since $\sqrt{1 - \cos^2 \theta} = \sin \theta$

$$-\int_{\pi}^{0} (1 + \cos \theta) \, d\theta = - \left[\theta + \sin \theta \right]_{\pi}^{0} = \pi$$

where the second term of Eq.(G.9) can be expressed as

$$\int_{-1}^{1} x \sqrt{\frac{1 + x}{1 - x}} \, dx = - \int_{\pi}^{0} \frac{(1 + \cos \theta)}{\sqrt{1 - \cos^2 \theta}} \cos \theta \sin \theta \, d\theta$$

$$-\int_{\pi}^{0} (\cos \theta + \cos^2 \theta) \, d\theta = - \int_{\pi}^{0} (\cos \theta + \frac{1}{2} + \frac{1}{2} \cos 2\theta) \, d\theta$$

$$\left[\sin \theta + \frac{1}{2} \theta + \frac{1}{4} \sin 2\theta \right]_{\pi}^{0} = \frac{\pi}{2}$$

G.4.1 Case for k → 0

The value of the denominator in expression (G.12) as k → 0 is dealt with below, substituting x for k.

$$\lim_{x \to 0} \frac{1}{ix \, (H_1^{(2)}(x) + iH_0^{(2)}(x))}$$

as

$$ix \, (H_1^{(2)}(x) + iH_0^{(2)}(x)) = xJ_1(z) + xY_0(x) + i(xJ_0(x) - xY_1(x))$$

since

$$J_n(x) = \frac{(x/2)^n}{n!} \left[1 + \frac{(x/2)^2}{1.(n+1)} + \frac{(x/2)^4}{1.2(n+1)(n+2)} - \ldots\ldots \right]$$

$$Y_n(x) = \frac{1}{\pi} \left[2 \, J_n(x)(\gamma + \log_e \tfrac{1}{2} x) + \sum_{s=1}^{n-1} \frac{(n-s-1)!}{s!} (\tfrac{1}{2} x)^{-n+2s} \right.$$

$$\left. - \sum_{s=1}^{n-1} (-1)^s \frac{(x/2)^{n+2s}}{s!(n+s)!} (1 + \frac{1}{2} + \ldots. \frac{1}{s} + 1 + \frac{1}{2} + \frac{1}{n+s}) \right]$$

as $x \to o$

$$xJ_0(x) = xJ_1(x) = xY_0(x) = 0$$

but

$$xY_1(x) = -\frac{2}{\pi}$$

therefore

$$\lim_{x \to 0} \frac{1}{ix \, (H_1^{(2)}(x) + iH_0^{(2)}(x))} = -\frac{\pi}{2}$$

H.0 Aerofoil Response to a Sinusoidal Gust

H.1 Response to Sinusoidal Gust

Using a typical section[35] one can obtain the transfer functions in vertical and angular acceleration due to a sinusoidal gust.

Considering translational and pitching degrees of freedom the equations of motion for the aerofoil can be written as follows, neglecting inertia coupling.

$$M \ddot{h} + K_h h = -L \qquad (H.1)$$

$$I_\alpha \ddot{\alpha} + K_\alpha \alpha = M_\alpha \qquad (H.2)$$

The expression for lift and moment, assuming quasi-steady aerodynamics, about the elastic axis can be written as[35]

$$\left. \begin{array}{l} L = qSa_0 \left[\dfrac{\dot{h}}{U} + \alpha + \dfrac{w_G}{U} \right] \\[2em] M_\alpha = Le \end{array} \right\} \qquad (H.3)$$

where $\quad q = \frac{1}{2}\rho U^2$

e = the distance of the elastic axis from the wing aerodynamic centre.

Assuming aerofoil motion of the form $e^{i\omega t}$ the lift can be re-written as

$$L = qSa_0 \left[\dfrac{i\omega}{U} h + \alpha + \dfrac{w_G}{U} \right]$$

where w_G is the vertical fluid gust velocity, which varies randomly with time but is assumed here to be uniformily disributed

spatially over the aerofoil chord. Then

$$- M\omega^2 h + K_h h = -qSa_0 \left[\frac{i\omega}{U} h + \alpha + \frac{w_G}{U} \right] \qquad (H.4)$$

$$- \omega^2 I_\alpha \alpha + K_\alpha \alpha = qSa_0 \left[\frac{i\omega}{U} h + \alpha + \frac{w_G}{U} \right] e \qquad (H.5)$$

Expanding Eqs.(H.4) and (H.5)

$$h \left(-M\omega^2 + K_h + qSa_0 \frac{i\omega}{U} \right) + qSa_0 \alpha = -qSa_0 \frac{w_G}{U} \qquad (H.6)$$

$$\alpha \left(-\omega^2 I_\alpha + K_\alpha - qSa_0 e \right) - qSa_0 \frac{i\omega}{U} h = qSa_0 \frac{w_G}{U} \qquad (H.7)$$

Eqs.(H.6) and (H.7) are written in matrix form as

$$\begin{bmatrix} R_{11} & R_{12} \\ R_{21} & R_{22} \end{bmatrix} \begin{bmatrix} h \\ \alpha \end{bmatrix} = \begin{bmatrix} -qSa_0 w_G / U \\ qSa_0 e w_G / U \end{bmatrix} \qquad (H.8)$$

where

$$R_{11} = -M\omega^2 + K_h + qSa_0 \frac{i\omega}{U} \qquad\qquad R_{12} = qSa_0$$

$$R_{21} = -qSa_0 \frac{i\omega}{U} e \qquad\qquad R_{22} = -\omega^2 I_\alpha + K_\alpha - qSa_0 e$$

Multiplying both sides of Eq.(H.8) by its determinant the transfer functions for heave and pitch are obtained, with respect to the gust velocity w_G,

APPENDIX I

I.0 Response to a Unit Step

I.1 Bromwich's Integral

Mitchell[118] has introduced a Fourier transform method to find the response of a flexible aircraft to a unit step and thus avoid the direct evaluation of the Küssner functions. If the transfer function (or the frequency response) of the aircraft is known Bromwich's integral formula[33,117] provides an explicit formula for calculating the response to unit step which is also known as the indicial admittance of the aircraft.

The theory presented here is by and large taken from Ref.(33) Let us consider a gust with a velocity history

$$W(t) = 0 \ , \ t < 0$$
$$W(t) = 1 \ , \ t > 0$$

(I.1)

The Fourier transform of this is

$$W(\omega) = \pi\delta(\omega) + \frac{1}{i\omega}$$

(I.2)

where $\delta(\omega)$ is the Dirac delta function which does not pose a problem in the case of the transfer function for acceleration, and velocity which tends to zero as ω tends to zero and the transform response does not become infinite at $\omega = 0$.

Now if $H_r(i\omega)$ is the transfer function (admittance function) of the aircraft then the indicial admittance (response to a unit step) is given by

$$A_r(t) = \frac{1}{2\pi} \int_{\omega = -\infty}^{\omega = +\infty} \frac{H_r(i\omega)}{i\omega} e^{i\omega t} \, d\omega$$

(I.3)

where the path of integration makes an infinitesimal loop below the origin. As it is seen from the above equation that the

integrand has a pole at the origin i.e when $\omega = 0$, the integrand is infinite and unless $H_r(0) = 0$, the integral will not converge. In dealing with the transfer function of acceleration which tends to zero as ω tends to zero, the integral

$$\int_{\omega \, = \, -\infty}^{\omega \, = \, \infty} H(i\omega) \, \delta(\omega) \, d\omega$$

becomes zero and the response to unit step given by Eq. (I.3) can be evaluated without any difficulty in integration. However Eq. (I.3) can be written in the following form

$$A_r(t) = \frac{H_r(0)}{2\pi} \int_{\omega \, = \, -\infty}^{\omega \, = \, +\infty} \frac{e^{i\omega t}}{i\omega} \, d\omega + \frac{1}{2\pi} \int_{\omega \, = \, -\infty}^{\omega \, = \, +\infty} \frac{H_r(i\omega) - H_r(i\omega)}{i\omega} e^{i\omega t} \, d\omega$$

(I.4)

It can be shown that by applying residue theorem (Ref.(33)) that

$$\frac{1}{2\pi} \int_{\omega \, = \, -\infty}^{\omega \, = \, +\infty} \frac{e^{i\omega t}}{i\omega} \, d\omega = 1 \, (t)$$

(I.5)

Equation (I.4) with the help of Eq.(I.5) reduces to

$$A_r(t) = H_r(0) \, 1(t) + \frac{1}{2\pi} \int_{\omega \, = \, -\infty}^{\omega \, = \, +\infty} \frac{H_r(i\omega) - H_r(i\omega)}{i\omega} e^{i\omega t} \, d\omega$$

(I.6)

we make the following substitution in Eq.(I.6)

$$e^{i\omega t} = \cos \omega t + i \sin \omega t \tag{I.7}$$

$$H_r(i\omega) = R_r(\omega) + iI_r(\omega) \tag{I.8}$$

so that Eq.(I.6) becomes

$$A_r(t) = R_r(0)\ 1(t)\ +\ \frac{1}{2\pi} \int_{\omega=-\infty}^{\omega=+\infty} \left[\frac{R_r(\omega) - R_r(i\omega)}{\omega} \sin \omega t \ + \right.$$

$$\left. \frac{I_r(\omega)}{\omega} \cos \omega t \right] d\omega - \frac{i}{2\pi} \int_{\omega=-\infty}^{\omega=+\infty} \left[\frac{R_r(\omega) - R_r(i\omega)}{\omega} \sin \omega t \ - \right.$$

$$\left. \frac{I_r(\omega)}{\omega} \cos \omega t \right] d\omega \tag{I.9}$$

where the assumption $I_r(0) = 0$ requires merely that when the forcing function is statically applied the lag is zero which is a valid assumption in aeroelastic systems.

Because $A_r(t)$ is real, the last term in Eq. (I.9) must vanish. Moreover, we know (Ref.(33))

$$\int_{\omega=-\infty}^{\omega=+\infty} \frac{\sin \omega t}{\omega} d\omega = \pi \text{ for } t > 0 \atop = -\pi \text{ for } t < 0 \Bigg\} \tag{I.10}$$

275

Eq.(I.9) finally becomes

$$A_r(t) = \frac{1}{2} R_r(0) + \frac{1}{2\pi} \int_{\omega = -\infty}^{\omega = +\infty} \left[\frac{R_r(\omega)}{\omega} \sin \omega t + \frac{I_r(\omega)}{\omega} \cos \omega t \right] d\omega$$

(I.11)

Eq. (I.11) provides an explicit formula for computing the indicial admittance $A_r(t)$ if the real and imaginary parts of the mechanical admittance functions are known. Eq. (I.11) can be reduced to a simpler form by putting the conditions that $R_r(\omega)$ is an even function so that $R_r(-\omega) = R_r(\omega)$ and $I_r(\omega)$ is an odd function so that $I_r(-\omega) = -I_r(\omega)$. These conditions are generally satisfied in aeroelastic systems so that we obtain from Eq. (I.11)

$$A_r(t) = \frac{1}{2} R_r(0) + \frac{1}{\pi} \int_{\omega = -\infty}^{\omega = +\infty} \left[\frac{R_r(\omega)}{\omega} \sin \omega t + \frac{I_r(\omega)}{\omega} \cos \omega t \right] d\omega$$

(I.12)

Since $H_r(\omega)$ and $I_r(\omega)$ are most of the time not available in explicit function form but are available as plotted curves, the summation form of Eq. (I.12) is more useful for practical application and computational procedure.

$$A_r(t) = \frac{1}{2} R_r(0) + \frac{2}{\pi} \sum_{n=1}^{\infty} \frac{1}{n} \left[R_r(n\omega_0) \sin n\omega_0 t + I_r(n\omega_0) \cos n\omega_0 t \right]$$

(I.13)

The frequency ω_0 is arbitrarily selected so as to obtain satisfactory convergence. The criterion for convergence is that

$R_r(n\omega_0)$ and $I_r(n\omega_0)$ approach zero for large values of n.

Once the response to a step gust $A_r(t)$ is known, the response $A(t)$ to a general gust $w(t)$ is found by the use of Duhamel's superposition integral.

$$A(t) = A_r(t)w(0) + \int_0^t A_r(t - \tau) \frac{dw}{dt}(\tau) \, d\tau \qquad (I.14)$$

J.0 Design and Construction of an Aeroelastic Tailless Model

J.1 Introduction

Experimental investigations in the field of aeroelasticity have served two major purposes. They have been the guiding influence necessary to the development of useful theory and they have produced solutions to immediate practical problems in the large areas were existing theory is not yet dependable. Particularly in dealing with flutter, the testing of wind-tunnel models with properly scaled mass and stiffness properties has often been more rewarding than equivalent efforts using analytical techniques or even full-scale aircraft.

As we are interested in the effect of structural flexibility on aircraft dynamic stability and control, a program was initiated into constructing a model to view aeroelastic effects within the context of this domain, in particular the effects on the short period mode. In the dynamic stability model we are interested in a subcritical dynamic behaviour, which is dominated by the rigid body modes of motion. Most aeroelastic tests have concentrated on component flutter and neglected the rigid body modes. Nevertheless models have been constructed to the investigate the role of rigid body modes in aircraft subcritical response and flutter.[33,136] However these tests require elaborate support mechanisms to provide the necessary free flight conditions.[33,136-138]

In the work of Chen and Dugundji[84] a free flight model, of forward swept wing (FSW) configuration, with graphite/epoxy wings was constructed to exhibit the effect of different ply orientations on the body freedom flutter. It is in the light of this study that the present model, an aft swept wing (ASW) in this case, is proposed with the aim of extending the tests to a dynamic stability analysis. The model is restricted to a tailless configuration to maintain simplicity, but to also exhibit body freedom flutter.

J.1.1 Aims and Objectives

The aim was to construct a free flight tailless aircraft model of an aft swept configuration for flutter and dynamic stability analysis. This model was specifically designed to

perform body freedom flutter within the maximum airflow speed of the T3 wind Tunnel at City University. The objectives were as follows:

i) Using the current program FLUSTAR, design and construct a tailless aeroelastic model to perform body freedom flutter in a wind tunnel and subsequently compare with theoretical predictions.

ii) To evaluate the subcritical response, namely the short period damping and frequency. To observe the effects of flexibility and unsteady aerodynamics on this mode for this particular configuration. To then compare these experimental quantities with those from two methods. The first using the classical approach[17,38] assuming just rigid body modes and then secondly, the current stability analysis in FLUSTAR incorporating full flexibility and unsteady aerodynamics employing Theodorsen's function C(k) for convergent motion.

J.2 Wind Tunnel Model Construction

In prior investigations[17,38,39] concerning body freedom flutter of an ASW tailless aircraft, it has been the aircraft pitching moment of inertia that the flutter speed has been most sensitive too. Bearing this in mind a light but sturdy plywood base was designed as a fuselage to hold the wing and minimise its contribution to the total pitching moment of inertia. The initial geometry of the model was restricted by the dimensions of the working section of the (0.8m X 0.7m) T3 wind tunnel.

A parametric study was carried out on a particular geometry using initial estimates of the aircraft inertia and mass. A further parametric analysis was carried out by assuming the wings as aluminium and the sweep varied from 5° to 25° in steps of 5°. This initial analysis established that 20° sweep produced the lowest flutter speed for this particular configuration. Once the wing sweep was established the positioning of these wings on the ply wood base was fixed so that the aircraft c.g. was located as close as possible to wing elastic axis, carried through on to the base. This criterion simplifies the model and ensures that the c.g. is well ahead of the wing aerodynamic centre to ensure static stability.

The pitching moment of inertia of the fuselage proved to be difficult to control within the constraints required, Therefore the next parameter that was seen to be sensitive to this phenomenon, was the wing bending stiffness EI. It is found that generally lowering this quantity lowers the flutter speed. However a compromise needs to be established as reducing EI too much will substantially increase the wing deflection due to the static aerodynamic loads. The greatest opportunity comes in aeroelastic tailoring these wings, by using composite structures such as carbon fibres as in Ref.(84). However the current finite element program in FLUSTAR caters only for isotropic materials.

A joint investigation was initiated with J.Z. Khan, to establish the limitations of the current code in predicting frequencies and flutter speeds for graphite plates with varying amounts of cross coupling. The results of this investigation are presented in Appendix C. It is found that as long the ply arrangements have low flexural coupling ratios , the program will predict within engineering accuracy the fundamental frequencies and flutter speeds. As a result of this analysis it was decided to keep the current analysis as simple as possible by using thinner sheets of aluminium to provide the minimum allowable bending stiffness.

It is noted that with certain ply lay ups the resulting torsional stiffness GJ was reduced to such an extent that flutter analysis, suggested classical bending/torsion flutter as the main mode of instability, rather than body freedom flutter. Therefore subsequent analyses concentrated on establishing the cantilever flutter speed. For body freedom the role of the rigid body modes were confirmed by printing the flutter modes. Initial flutter calculations were carried out assuming the rigid body frequencies as zero and neglecting the low frequencies introduced via the support system.

Another significant parameter in this particular case was the influence of the mass of the fuselage. Although not an important factor for the Ricochet the mass was seen to have a marked influence on the wing first bending frequency of the model. As the fuselage mass increases the bending frequency falls, lowering the

flutter speed. However increasing the mass will increase the pitching moment of inertia producing a stabilising influence. Therefore once the aircraft c.g. was located Brass blocks were screwed onto the support system coincident with the aircraft c.g.. The advantage of using brass, is its high density, enabling large concentrations of mass to be concentrated over small areas, hence minimising any further increase in fuselage pitching inertia.

The layout for the final model is shown in Fig. J1 with the stiffness mass and inertia details shown in Table J1. Polystyrene fairings were placed around the plate wings to introduce camber and on the plywood base to create the fuselage shape. Slits were made in the wing to minimise the effect of these fairings on the wing stiffnesses. It is seen from Table J1 that comparing these experimental stiffnesses with the experimental values quoted for the uncovered plates in Appendix C, the effect of fairings , within experimental accuracy, does not significantly modify the stiffnesses.

J.3 Evaluation of Flutter Speed of Model Wing

As a means of establishing the experimental wing flutter speed, the wing was cantilevered and swept back to its 20^0 configuration in the working section of T3. The subsequent results are compared with CALFUN as in Appendix C, using both the cosine theory and the velocity component theory.[33] The experimental flutter speed and frequency is shown in Table J2a and J2b along with those quantities obtained theoretically. During the experiment, frequencies were monitored using a transducer on the plate, linked to a GENRAD facility (as outlined in Appendix C). At the flutter condition the flutter frequency was taken as the value at which the monitored aeroelastic frequencies coalesced. This proved to be a lot more reliable than measuring the frequencies using a stroboscope.

Referring to these tables it is seen that both theories give comparable results, to a large degree, part of the discrepancy in flutter speed was probably due to overestimating the sectional I_p/l. The initial estimate of this quantity relies on the assumption that the mass of the plate and fairings are

281

concentrated along the thickness of the plate. In reality there is a sectional contribution from the fairings, which will redistribute and decrease the effective value of I_p and thus raise the torsional frequency.

Table J3 shows the fundamental frequencies for the complete aircraft and Table J4 shows the subsequent theoretical body freedom flutter. As it can be seen this speed is well within the speed range of T3 (U < 50 m/s). Modal elimination confirms that the instability is rigid body coupling with the fundamental wing bending. The modes are numbered sequentially from the 1 to 5, where 1 and 2 are the rigid body modes and 3 to 5 are the remaining elastic modes. The flutter frequency also shows the low frequency nature of this instability. As an indication of the sensitivity of this flutter to the fuselage inertia, Fig. J2 shows the variation in flutter speed for various percentage decreases and increases in fuselage mass and pitching inertia. This assumes a fixed model c.g. location. Comparing Fig. J2 with the equivalent figure for the Ricochet, (see Fig. 3.16), the suggested effects of pitching inertia are more critical for this model especially for higher inertias.

J.4 Determination of Wing Stiffnesses
J.4.1 Flexural Rigidity

For the determination of these critical parameters a test rig was specially constructed as shown in Fig. J3. For determination of the Flexural rigidity, the plate is clamped securely at one end and a series of vertical loads applied at the other end. A point was selected along the plate, not too near the end, and the vertical displacements recorded with applied loading, for both the loading and unloading case. From the readings obtained, the slope P/δ was calculated using Eq.(J.1), from Engineers theory of bending, the flexural rigidity EI deduced. The loading was applied at the mid chord, which is the assumed position of the shear centre. Although this assumption is valid for isotropic plates, for composite plates with significant coupling ratios , applied bending is followed by small amounts of twist. Therefore the mean vertical displacement taken from the scales at both sides of the

plate was taken as the displacement of the mid chord or shear centre.

$$EI = \frac{x^2}{6} (x - 3L) \frac{P}{\delta} \qquad (J.1)$$
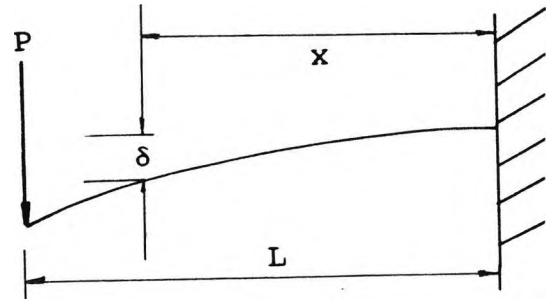
J.4.2 Torsional Rigidity

The determination of the torsional rigidity, the end loading was replaced by a pure torque applied about the plate section. This is achieved by the pulley arrangement shown in Fig. J4. This arrangement also cancels out the the effects of bending introduced by the application of this loading. The displacements recorded by both scales on either side is converted into angular displacements for the unloading and loading case. From this data the slope of TL/θ was calculated and using Eq.(J.2) the value of GJ deduced. The reason for taking readings from both sides was to monitor the nature of the rotation and to counteract any discrepancies arising from loading offset from the shear centre. This is important especially considering the nature of composites where the position of the shear centre is not so certain.

$$\theta = \frac{\delta}{d}$$

$$GJ = \frac{T L}{\theta} \qquad (J.2)$$
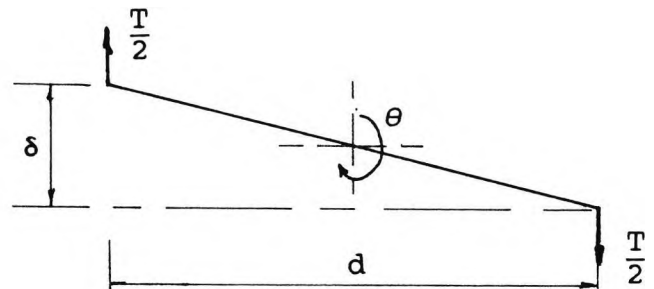
J.5 Evaluation of Model Pitching Moment of Inertia

As I_{yy} is a very sensitive parameter it is important to measure this correctly. The first technique relied on hanging the model via fish wires and measuring the period of oscillation. From these times and assuming the structure as a compound pendulum the pitching moment of inertia can be obtained from Eq.(J.3). However aligning both the wires to straighten the model proved difficult. Also as the model swung it carried out small oscillations about

283

its longitudinal axis and these had to die down before any measurements could be made.

$$I_{yy} = \frac{Mg\ r}{4\pi^2 f^2} \qquad (J.3)$$

where   Mg   weight of model
            f   frequency of motion
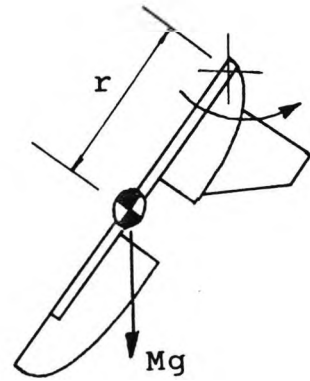
An alternative method of suspending the model was established. This arrangement consists of inserting small blades along the arms that suspended the model in the first method. This arrangement is seen in Fig. J1. These blades each rest on the edge of two plates clamped to a support. The arrangement sees the model hang and oscillate between the two plates, as seen in Fig. J5. This provides a sturdy platform to measure the oscillations and minimise the effects of friction at the supports.

J.6 Wind Tunnel Model Support System

As in ref.(84) because of the model weight, the preselected wing planform was not able to fly the model completely. Therefore a vertical rod support system is selected as in Ref.(84) to test the model. This system consists of a 0.8 m long, vertically installed, case hardened steel rod with a 10 mm diameter. A Thompson super ball bushing slides along the rod and attached to the fuselage through a pitch bearing mount located at the model centre of gravity. The pitch bearing or pitch gimbal along with the linear bearing is shown in Fig. J6. This gimbal allows only vertical heave and pitch freedoms, this is adequate for the current stability analyses which neglects forward changes in speed. a potentiometer is located on the pitch bearing to record pitching displacement.

As in Ref.(84) springs were to be located at the linear bearing and the pitch gimbals to provide the required support stiffnesses. In Ref.(84) a dynamic support instability was observed at certain speeds, this was due to interaction of the

pitch and plunge modes of the rigid aircraft. This was cured by making the still air model pitch frequency greater than the model plunge frequency. Spring stiffnesses were calculated bearing this instability in mind and avoiding possible interaction with the predicted body freedom flutter frequency of 2-4 Hz. However due to the small size of the T3 working section, springs of the necessary stiffnesses could not be obtained.

Alternative support systems were visualised before the program was terminated due to lack of time. The most promising set up is one in which the model is supported via a set of wires that loop outside the tunnel along miniature pulleys and return to the model to form a closed circuit. A mass is introduced into the circuit to counteract the weight of the model. The model is then free to plunge up and down, the wires running along the pulleys. The advantage of this system is that reliance is not placed so much on spring stiffness and with this arrangement a potentiometer can be inserted into the network to measure the model vertical displacement.

J.7 Experimental Procedure

If this work had been completed the following experiments would have been carried out.

1) A ground resonance test to determine the fundamental frequencies of the model and compare them with those from the finite element analysis.

2) Carry out wind tunnel tests on a static rig to evaluate the model lift curve slope and the trim condition from the $\partial C_m/\partial \alpha$ curve. If necessary small flaps might have to placed along the wing to attain the right trim condition. This test would also establish the static margin stick fixed from which the location of the aircraft c.g. could be refined. The new aerodynamic parameters above could be inserted into a modified flutter and stability analysis, provided by FLUSTAR.

3) Carry out in the wind tunnel body freedom flutter tests. However before the onset of flutter the subcritical response would be evaluated at fixed speeds. This would be achieved by knocking the model and measuring the subsequent trace in pitch from which

the damping and frequency of the short period mode could be ascertained.

Total Mass	0.764 kg
Pitch inertia of fuselage	0.0036 kgm^2
Wing mass	0.0585 kg
Wing span	0.68 m
Wing sweep angle	20^0
Gross wing area	0.0589 m^2
Wing aspect ratio	8.52

Wing stiffnesses			
	EI	0.1614	N/m^2
	GJ	0.2777	N/m^2
	M/l	0.1834	kg/m
	I_α/l	8.599×10^{-5}	kgm

Table J1 Aircraft model properties

Flutter speed (m/s)			% Difference	
Cosine theory	Vel-comp theory	Exp	Cosine theory	Vel-comp theory
32.90	31.28	38.39	-16.69	-22.73

Table J2a Comparison of theoretical and experimental flutter speeds for cantilevered model wing

Flutter frequency (Hz)			% Difference	
Cosine theory	Vel-comp theory	Exp	Cosine theory	Vel-comp theory
21.80	22.14	21.88	-0.37	1.17

Table J2b   Comparison of theoretical and experimental flutter
frequencies for cantilevered model wing

Frequencies (Hz)		
1st bending	2nd bending	1st torsion
5.16	32.37	44.64

Table J3   Theoretical fundamental frequencies for model wing

Modes used	Flutter Speed (m/s)	Flutter Frequency (Hz)
1,2,3,4,5	13.0	3.18
1,2,3	14.8	3.08

Table J4   Effect of normal modes on the model flutter

Fig. J1. Layout of flutter model

467mm

135mm

50mm

75mm

31.9mm

Scale 5:1

20°

80mm

210mm
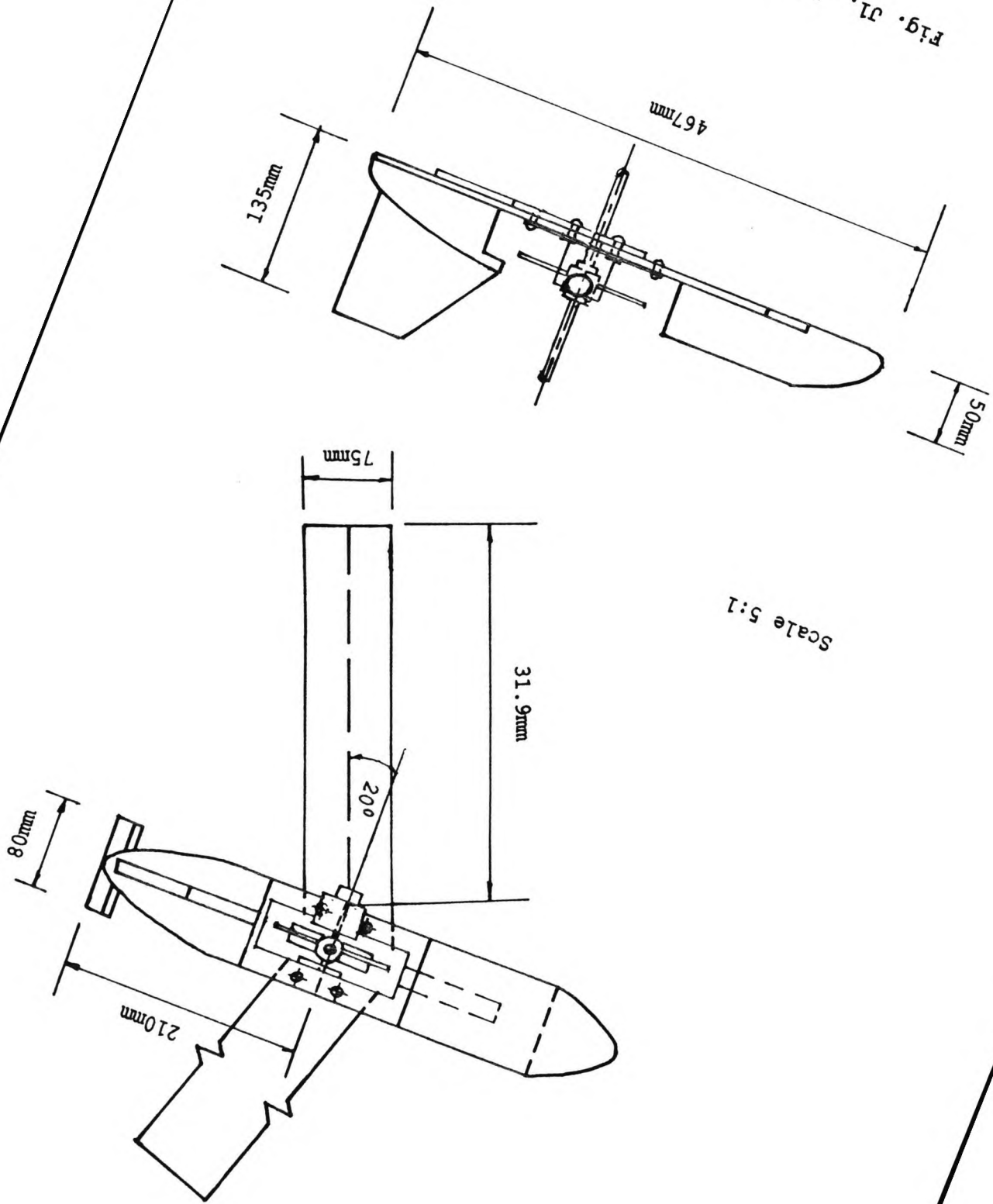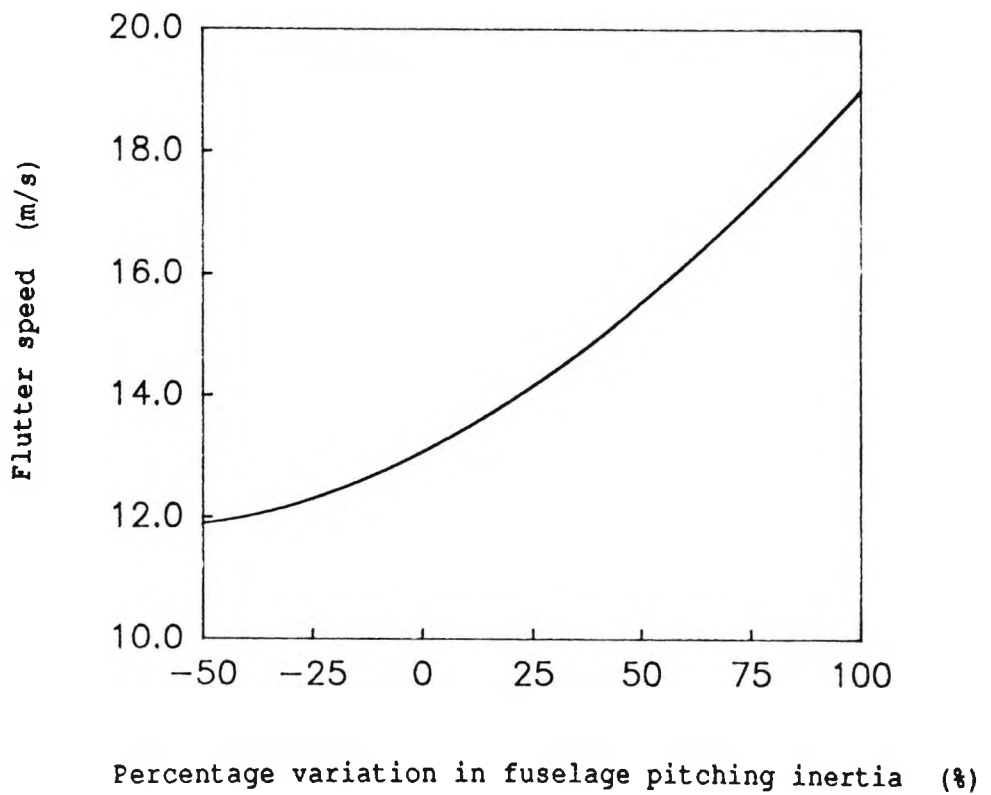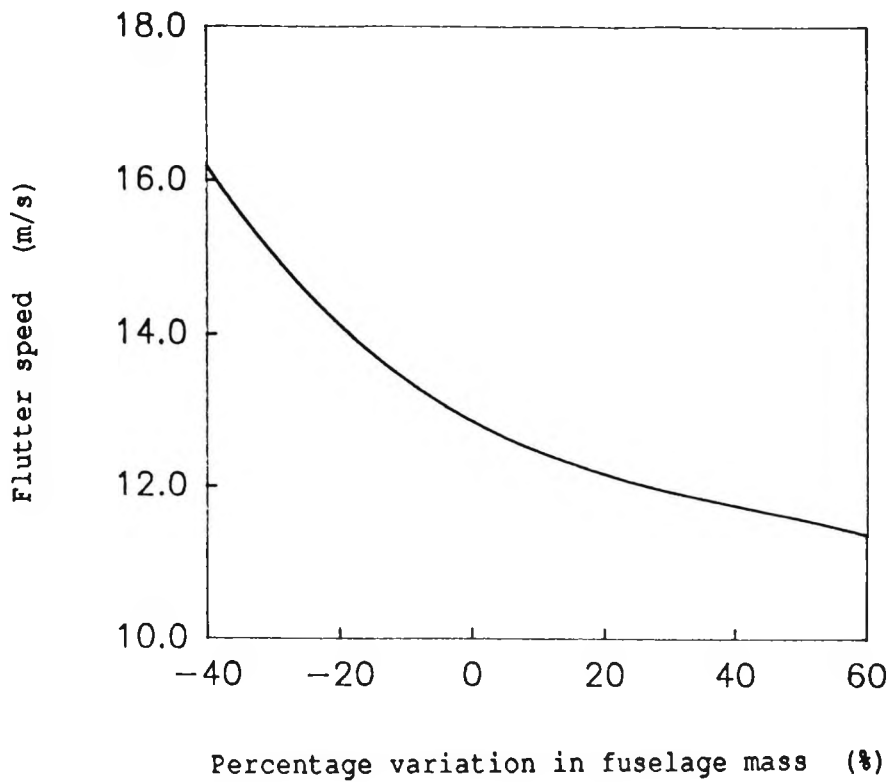
Fig. J2. Effect of variation in fuselage pitching moment of
inertia and mass on flutter speed of model
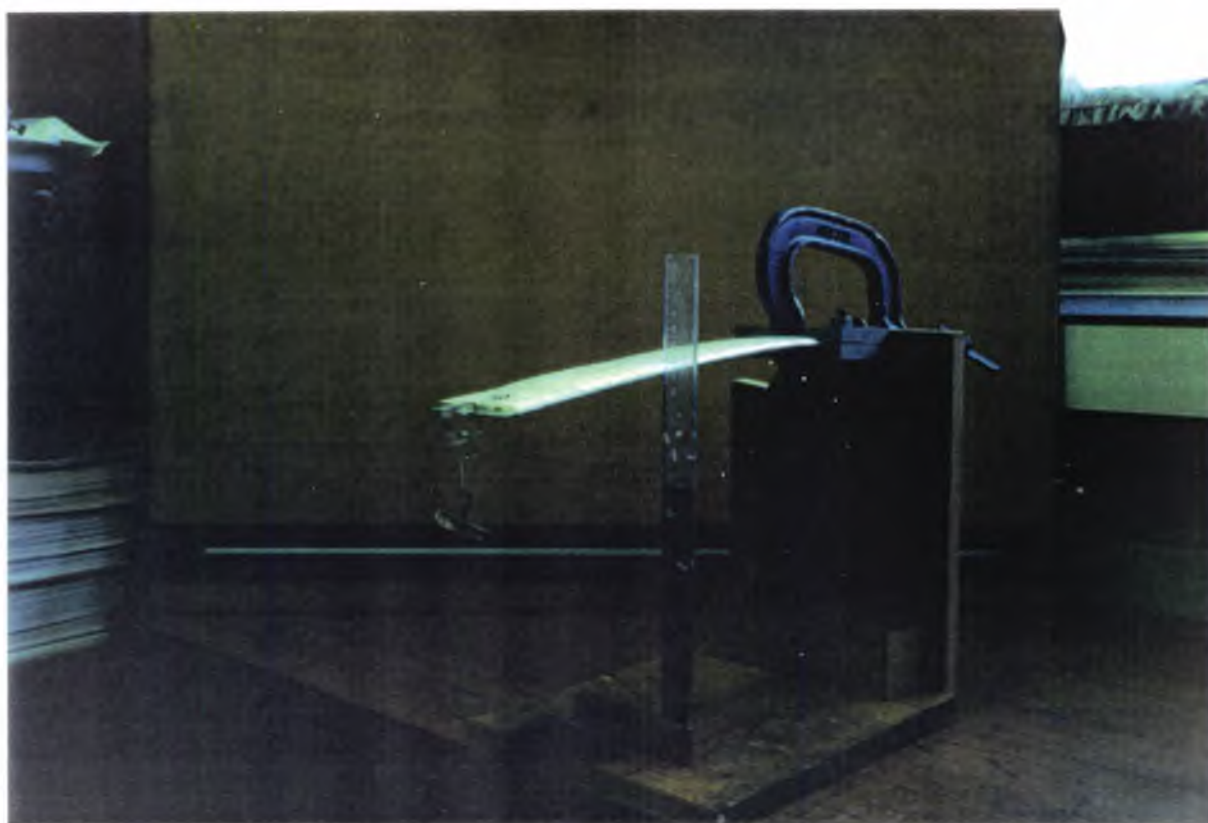
Fig. J3   Flexural rigidity test rig
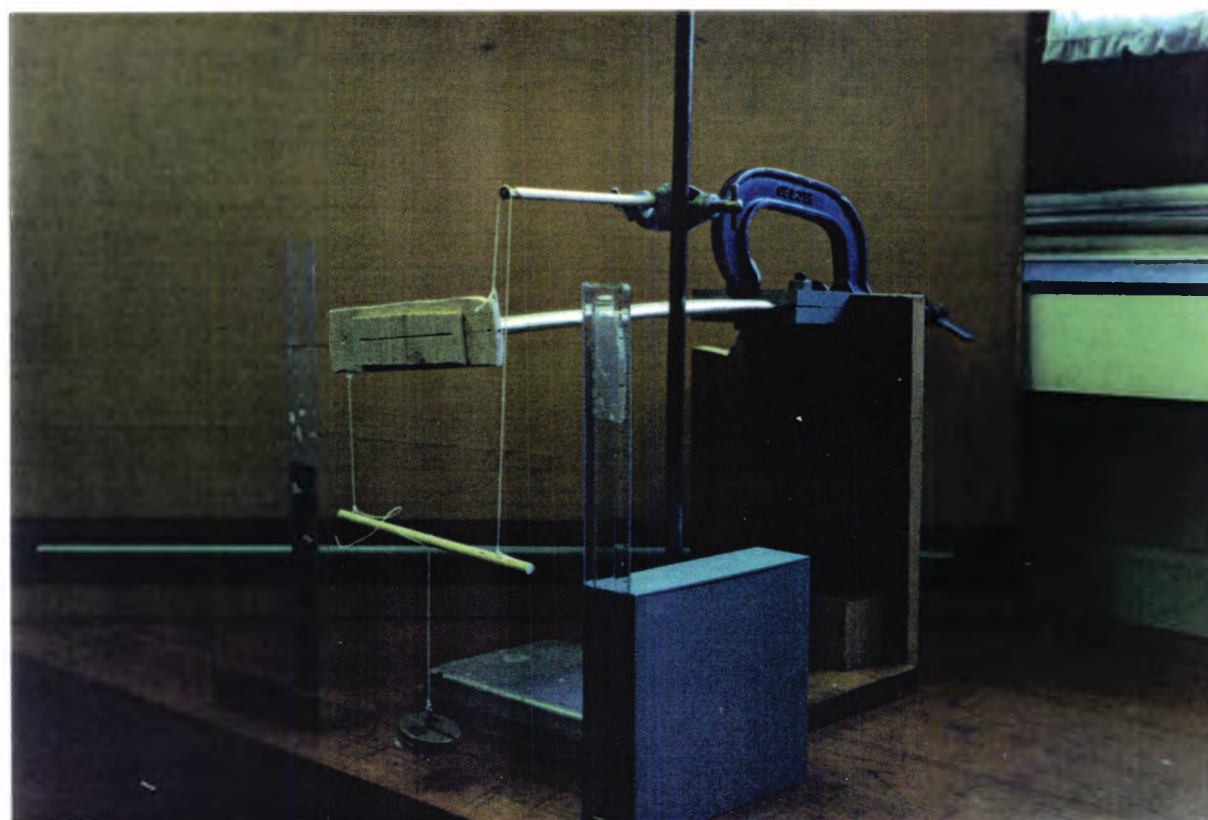
Fig. J4   Torsional rigidity test rig
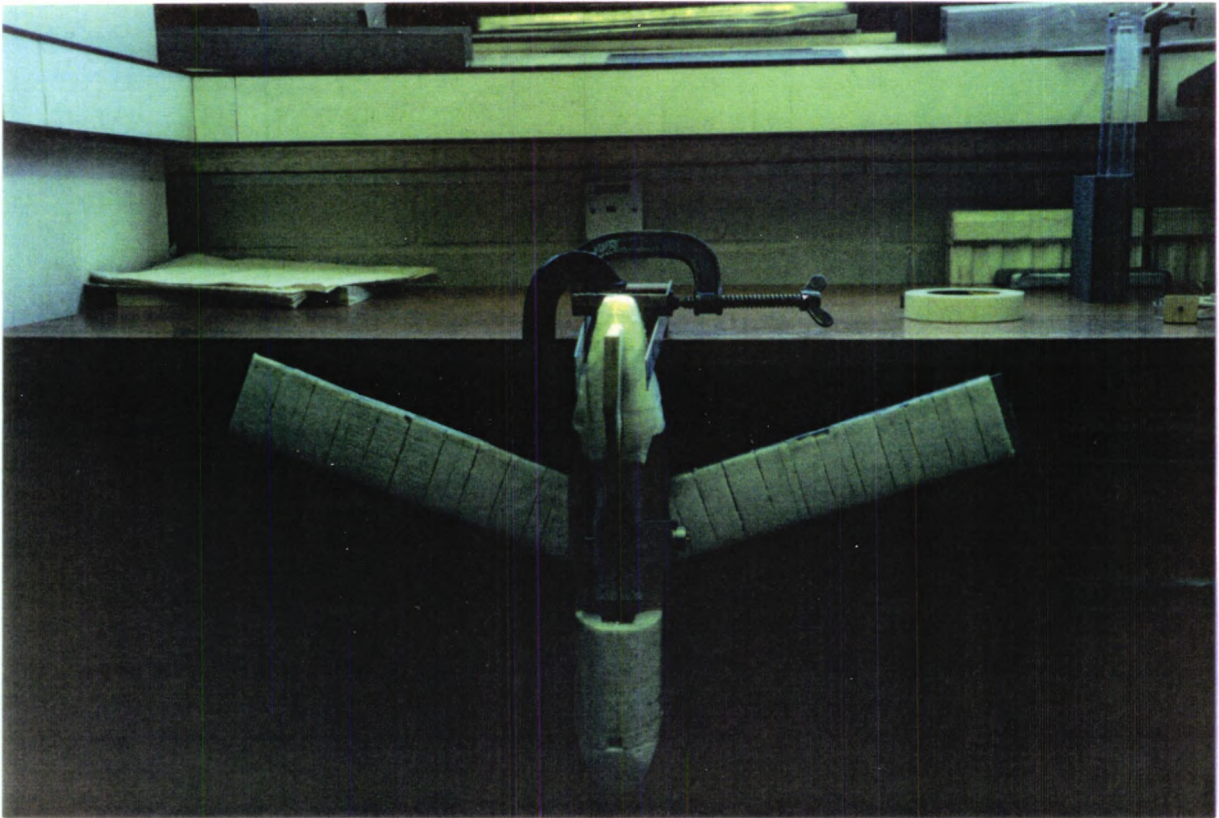
Fig. J5 Model pitching moment of inertia test rig
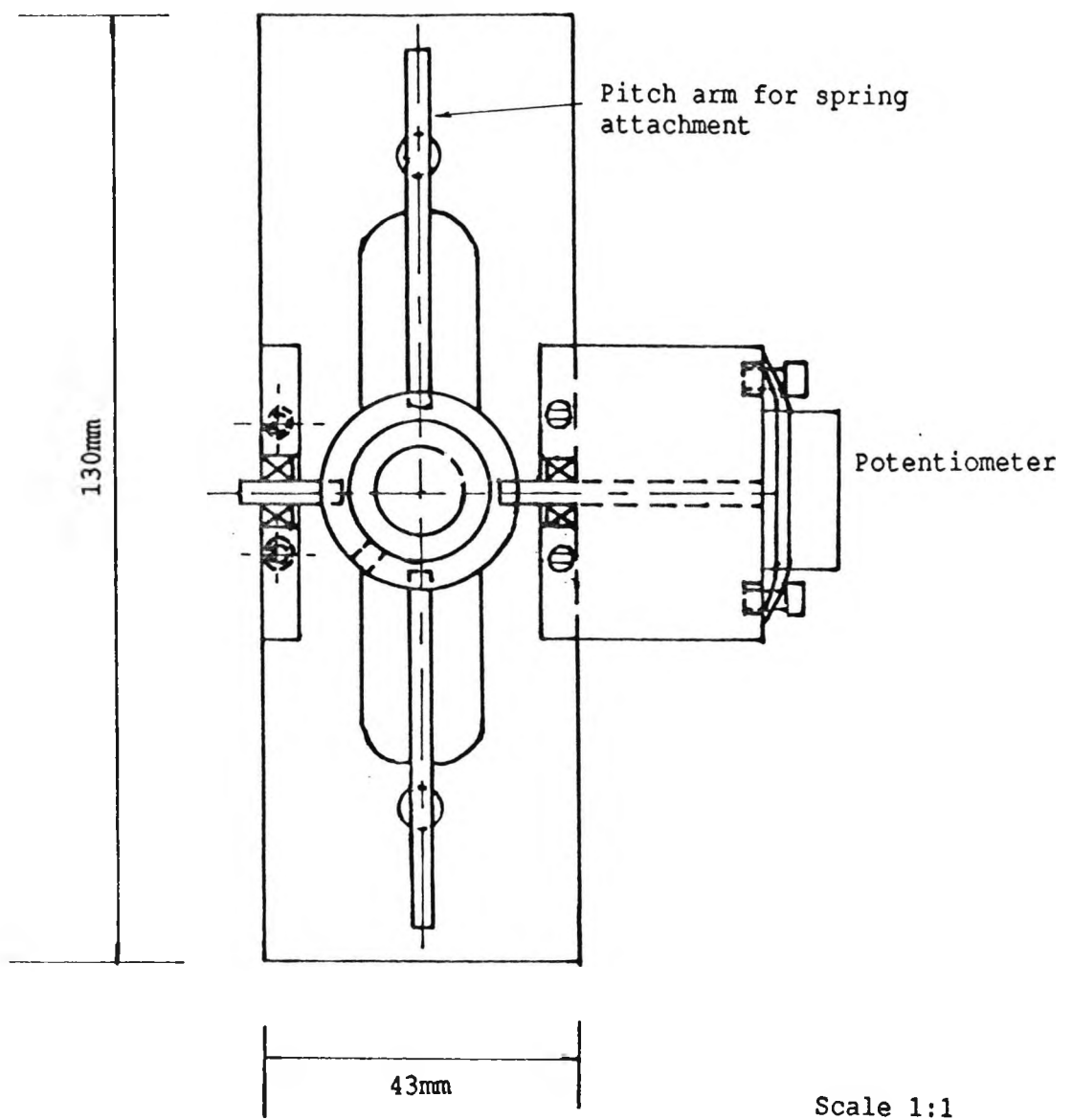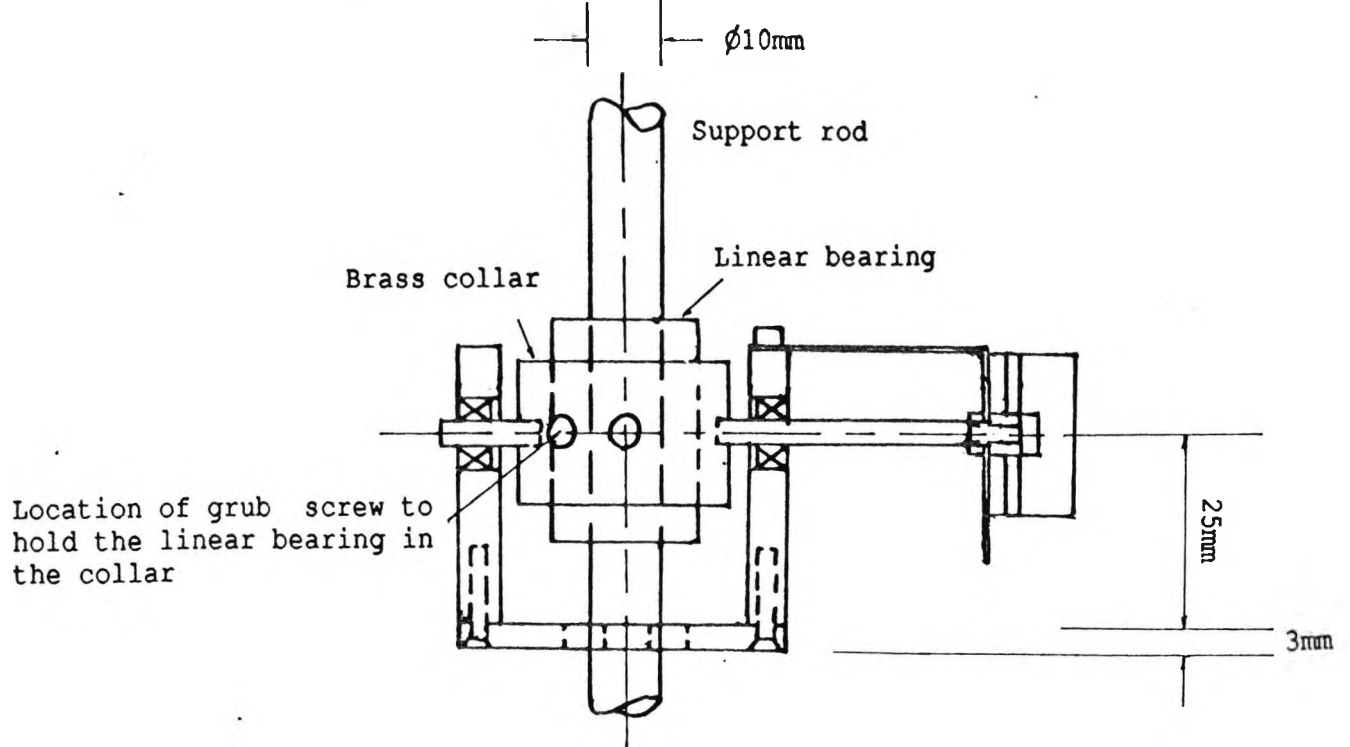
Fig. J6 Arrangement of pitch gimbal

APPENDIX K

K.0 Background to the Computer Program FLUSTAR

K.1 Introduction

A unified theory of aeroelastic analysis has been developed during the course of the investigation. The theory and implementation has been discussed within the main text of this thesis.

This section provides guidlines for prepering data for the FORTRAN computer program FLUSTAR. This program will accomplish the following tasks using a combination of the finite element theory and aerodynamic strip theory.

1) Evaluation of flutter speed and aeroelastic modes at flutter speed of an aircraft using normal modes.

2) Investigation of the short period oscillation characteristics of an aircraft.

3i) Calculation of both the linear and angular acceleration responses to continous random atmospheric turbulence using the frequency response function and the power spectral density (PSD) method.

3ii) Determination of the acceleration response of a flexible aircraft to a unit step gust velocity. Evaluation of the statistical discrete gust (SDG) method and identification of the worst response to a pair of gusts.

For tasks (1) and (2) the option of introducing an unsteady wake at the tailplane is provided.

K.2 Structural and Aerodynamic Idealisation

The structural idealisation is common to all three types of the above of analyses. The aircraft structure is idealised as a framework, with beam elements located along the elastic axis. Member types and method of solution is identical to that implemented in BUNVIS[71] and is used to obtain the natural frequencies, mode shapes and the generalised mass and stiffness matrices.

Using two-dimensional unsteady aerodynamics[5] and strip theory the mode shapes are incorporated to yield the generalised aerodynamic forces. The option of including modified

aerodynamics[30] is incorporated to take into partial account the effects of finite span and compressibility.

K.3 Additional Features

As in BUNVIS the main consideration when writing the program was to reduce the array space needed. Nearly all the storage is in two-dimensional arrays, one real (RA) and one integer (IA), which, are used for very compact storage of data and working space. The dimensions of these two arrays can be altered to match the size of the problem. Now in addition to quantities particular to the structural analysis, parameters for the aerodynamics are also stored in the same real array.

The original BUNVIS relied on a linear and rotational spring at the c.g. node, to provide the respective rigid body freedoms. In this program the springs are retained but there is the added facility of reading in zero frequency modes directly. This option is installed in cases of severe ill conditioning. In symmetric flutter and dynamic stability analysis, the two rigid body modes, namely heave (δ_{zR}) and rotational pitch (θ_{yR}) are required (these freedoms are defined in Fig. 3.4.), whereas in antisymmetric analysis only rigid body roll (θ_{xR}) is required.

K.4 Input Data Preparation

Card Group No.1

CF	Convergence factor. Solutions are obtained to an accuaracy of at least 1 part in CF.
FQ	Positive trial value of first required eigenvalue. Any positive number can be used (but excessive values must be avoided for vibration problems).
NN	No. of structural nodes.
NC	No. of connections.

NR	No. of numbers in list of real numbers.
NM	No. of eigenvalue frequencies incorporated in analysis.
ND	No. of triplets in list of affected degrees of freedom.
LR	Use 1 if rotary inertia is to be allowed for in analysis.
LS	Use 1 if shear deflection is to be allowed for, otherwise 0.
SF	Shape factor, use any dummy value if LS=0 above.
PR	Poisson's ratio, use any dummy value if LS=0.
IFGTO	Use 0 if tailplane aerodynamics are to be incorporated in analysis, otherwise 1.

Card Group No.2

IA	NM integers forming the list of required natural frequencies. The integers in this list must be in ascending order and must be prefixed by a negative sign to obtain the mode shape.

Card Group No.3

IA	Connection list in triplets. Each triplet defines one connection. The three integers in each triplet are the node

numbers of the connected nodes, which must be given in ascending order, followed by the member number. Such triplets must be given in the order of their i values, where i is the first integer of the triplet, i.e. the lower numbered of the two connected nodes. Triplets with the same i value can be given in any order.

Card Group No.4

NMR   No. of rigid body modes implemented.

Card Group No.5   Section properties of each member.

EI   Flexural stiffness
EA   Axial stiffness
GJ   Torsional stiffness
M/L   Mass per unit length
IP   Polar moment of inertia
AF   Axial force

Card Group No.6

RA   List of real numbers: NR real numbers used to define coordinates and values of lumped masses, lumped (rotatory) inertias and elastic support stiffnesses.

Card Group No.7

IA   Node coordinate list in triplets. The coordinates can be related to any right-hand cartesian axis system xyz. The node coordinate list references the list of real numbers to enable the program to deduce the three coordinate values (x, y, and z) of

each structure node. The i th triplet corresponds to node i and the three integers respectively give the locations in the list of real numbers of the nodes x, y and z coordinates. The sign of a coordinate can be changed by a prefixing the integer which locates it in the list of real numbers by a minus sign. Thus negative integers can be used, with positive numbers in the list of real numbers, to give negative coordinates. Thus two coordinates which are equal and opposite can be obtained from a single number in the list of real numbers.

Card Group No.8

IA   List of affected degrees of freedom. The list is in triplets and the number of triplets must be read as ND in card 1 data. Each of the triplets comprises three integers of which the first two must be postive and the third can be negative. These three integers must give, respectively:

i)   Node Number

ii) Degree of freedom reference number

iii) Indicator to effect suppression or elastic support of the freedom, or to add lumped mass or inertia at the node.

1,2 or 3 at (ii) denote δ_x δ_y and δ_z respectively, and 4, 5 and 6 denote θ_x θ_y and θ_z respectively. If a zero is used at (ii) all the translational freedoms (i.e. the displacement in the x, y and z directions) are affected simultaneously.

For suppression, (iii) is set to zero and the computer suppresses the freedom (ii) of node (i). If (iii) is set greater than zero its value gives the location in the list of real numbers of a lumped mass ((ii)=0) or inertia ((ii)>3) which the program will associate with θ_x θ_y and θ_z at node (i) if (ii)=0, or with rotation (ii) at node (i) if (ii) > 3.

If (iii) is negative, =-j say, then there is an elastic support at the node which constrains the translation (or rotation) (ii) at node (i) with a linear (or rotational) stiffness given as the j th number in the list of real numbers.

The triplets must be given in ascending order of their node

numbers (i.e. the numbers at (i)) but the order in which the stiffnesses or masses/inertias associated with any one node are altered is immaterial.

Card Group No.9

IFGRM	Use 1 if rigid body modes in card 10 are going to be read in, otherwise 0.
IFGMT	Use 1 if aeroelastic analysis involves symmetric modes. Otherwise -1 for antisymmetric analysis.

Card Group No.10

RA	NMR x NN data items describing the rigid body modes of the aircraft.
	If IFGMT = 1 The vertical displacement δ_z of each node starting sequentially from 1 to NN followed by the corresponding rigid pitch rotation θ_y for each mode.
	If IFGMT = -1 the vertical displacement of each node starting sequentially from 1 to NN followed by the corresponding rigid roll θ_x.

Card Group No.11

NWN	No. of wing nodes, not including the undercarriage node.
NIP	No of wing integration points for the evaluation of the aerodynamic forces.
NRB	No. of rigid body modes disregarded in analysis.

NCS	Maximum number of crossing points for real and imaginary determinant.
SWP	Sweep angle of the wing elastic axis (deg).
RO	Atmospheric density
G	Structural damping
NUC	Node number of undercarriage, otherwise 0
Card Group No.12	If IFGTO = 1 (i.e tailless configuration) use 0 for the parameters below.
NTPN	No. of tailplane nodes
NNTT	Node number of tailplane tip.
NNTR	Node number of tailplane root
NIPT	No. of integration points in evaluation of tailplane aerodynamic forces.
Card Group No.13	If IFGTO = 1 (i.e tailless configuration) use 0 for the parameters below.
SWPT	Tailplane sweep angle (deg)
SMC	Standard mean chord of wing
XLT	Distance of wing aerodynamic centre from tailplane aerodynamic centre.
ZT	Vertical height of tailplane from horizontal datumn. (positive upwards).

Card Group No.14

      Y   Spanwise distance of wing node from fusealge intersection.

      B   Wing section semi-chord

      AH   The distance of the elastic axis (shear centre) from mid-chord point expressed as a fraction of the semi-chord (B). Taken positive rearward.

      CLA   Wing lift curve slope of spanwise strip (/rad).

If IFGTO = 0, card Group No.14 is repeated for the tailplane

Card Group No.15   Offset mass

      OM   Use 0.0 if offset mass is not to be considered, otherwise use the magnitude of this mass.

      XI   Moment of inertia of offset mass about y axis.

      R   Distance offset from node

      KL   Node number of offset connection

Card Group No.16

      IFGAA   Single integer which indicates the type of analysis, from the menu below:
                                                1. Flutter Analysis
                                                2. Dynamic Stability Analysis
                                              3. Response Analysis

IFGM	Use 1 to find aeroealstic modes in flutter analysis, otherwise use 0.
IFGUW	Use 1 to introduce the effects of an unsteady wake at the tailplane, otherwise use 0.
NZI	No. of integration points taken to represent a single wake vortex cell.

Flutter Analysis (IFGAA = 1)

For this analysis the next card groups inserted are as follows:

Card Group No.17	This card contains the frequency range for flutter analysis in (rad/s).
WFI	Starting frequency
DWF	Increment in frequency
WFMAX	Maximum value of frequency
Card Group No.18	This card indicates the airspeed range in (m/s).
UI	Starting airspeed
DU	Increment in airspeed
UMAX	Maximum value

Dynamic Stability Analysis (IFGAA = 2)

For this analysis the next card groups are as follows where ρ in this card group is taken as the modulus of the complex argument k, where $k = \dfrac{\omega b}{U} - \dfrac{i\mu b}{U} = \rho e^{i\theta}$

Card Group No.17

    U   Airspeed taken for dynamic stability analysis.

Card Group No.18

    RHO   Starting ρ value

    DRHO   Increment in ρ value

    RHOMAX   Maximum value of ρ

Card Group No.19

    THETA   Starting θ value

    DTHETA   Increment of θ value

    THETAM   Maximum Value of θ

Response Analysis (IFGAA = 3)
For this analysis the next card groups are as follows:

Card Group No.17   This contains items for the Power Spectral Analysis (PSD).

    DW   Increment in frequency for frequency response function.

    U   Airpeed taken for response analysis

    N   Number of frequency points taken for integration of the output power spectrum.

Card Group No.18   This contains items for the Statistical Discrete Gust analysis (SDG) and are fully discussed in Ref.(31).

NT	No. of time intervals
DT	Time Interval at which the straight ramp response is to be calculated.
TMAX	Time of the last point in the step response.

Card Group No.19

NH	No. of trial values of $\bar{H}$ supplied (NH $\geq$ 3).

Card Group No.20

H(I)	I = 1, NH trial gust lengths. $\bar{H}$ to be bracketed; $t_{MAX} \geq H/V \geq \Delta t$ preferably.

Card Group No.21

HLTOL	Accuracy required, $\Delta H/\bar{H}$

Card Group No.22

IPR	Print control parameter giving different levels of output.
IPR = -1	Data summary; γ and t_γ for trial H(I) and $\bar{H}$; λ ; λ_w ; worst gust pair:
= 0	as IPR = -1 plus γ and t_γ for all extra gust lengths investigated including $\frac{1}{2}\bar{H}$ and $2\bar{H}$. Also the integrals in (9) or (10) (ref.31) are output at intervals of Δt for H = $\bar{H}$ and $\frac{1}{2}\bar{H}$.
= 1	as IPR = 0 plus the tabulated spline fit to the step response.

= 2	as IPR = 0 plus ramp responses for each H(I) supplied by the user. The multiplying factor $vH^{-2/3}$ is also output for converting the integrals to $\phi(H,t)$.
= 3	as IPR = 1 and IPR = 2 combined.
IANAL	Set to zero if subroutine ANALYTIC to evaluate $\phi(H,t)$ analytically is either not provided or not being used. Otherwise, input any non-zero integer value.

```
 1.0000D+06   2.00 21   20   38   6 75  0   0   0.67   0.3   0
-1 -2 -3 -4 -5 -7
    1    2    1    2    3    2    3    4    3    4    5    4    5    6    5
    6    7    6    7    8    7    8    9    8    9   10    9   10   11   10
   11   12   11   12   13   20   12   14   12   14   15   13   15   16   14
   16   17   15   17   18   16   18   19   17   19   20   18   20   21   19
2
    8.8200D+04   1.000D+07   1.3400D+04   4.5710   0.02917   0.0
    1.0950D+05   1.000D+07   1.7500D+04   5.7910   0.05364   0.0
    1.4450D+05   1.000D+07   2.0900D+04   7.1000   0.09364   0.0
    1.8350D+05   1.000D+07   2.3800D+04   8.0820   0.1236   0.0
    2.6240D+05   1.000D+07   2.9300D+04   20.459   0.4419   0.0
    3.4380D+05   1.000D+07   3.6800D+04   9.9270   0.2276   0.0
    4.6410D+05   1.000D+07   5.2100D+04   10.927   0.2718   0.0
    6.3230D+05   1.000D+07   7.9300D+04   11.954   0.3180   0.0
    8.6120D+05   1.000D+07   1.2360D+05   12.954   0.3718   0.0
    1.1633D+06   1.000D+07   1.8930D+05   13.945   0.4300   0.0
    1.4552D+06   1.000D+07   2.5180D+05   14.945   0.4927   0.0
    2.253D+06    1.000D+07   9.4350D+04   4.878    0.4182   0.0
    1.3488D+06   1.000D+07   8.3200D+04   3.775    0.1377   0.0
    7.605D+05    1.000D+07   6.6700D+04   3.000    0.06714 0.0
    3.155D+05    1.000D+07   4.6250D+04   1.986    0.02465   0.0
    1.1910D+04   1.000D+07   1.4060D+04   6.0520   0.01155   0.0
    6.1700D+03   1.000D+07   1.0620D+04   5.0236   0.0056335 0.0
    4.0180D+03   1.000D+07   7.8920D+03   4.2016   0.0036617   0.0
    2.7260D+03   1.000D+07   5.3090D+03   3.1512   0.002535   0.0
    1.0000D+07   1.000D+06   1.000D+06   1.000D-02   1.000D-04 0.0
   11.000    10.175    9.0757    7.9746    6.8746    6.3246    4.9496    3.8496
    2.7496    1.6496    5.4965    0.0    -5.4965    -1.6496 -2.7496 -3.8496
   -4.9496   -6.3246   -6.8746   -7.9746   -9.0757   -1.0175   -11.000   -1.025
   -2.0250   -3.0250   -4.5410    3.5000    7.0000    1.0500    1.4250    0.7380
    0.60    0.55    112.09    35.70    5.70    2.20
   12    1   12   12    2   12   12    3   12   12    4   12   12    5   12
   12    6   12   12    7   12   12    8   12   12    9   12   12   10   12
   12   11   12   12   12   12   32   12   12   24   12   12   25   12   12
   26   12   12   27   12   12   27   28   12   27   29   12   27   30   12
   27   31   12
    1    1    0    1    2    0    1    6    0    2    1    0    2    2    0
    2    6    0    3    1    0    3    2    0    3    6    0    4    1    0
    4    2    0    4    6    0    5    1    0    5    2    0    5    6    0
    6    1    0    6    2    0    6    6    0    7    1    0    7    2    0
    7    6    0    8    1    0    8    2    0    8    6    0    9    1    0
    9    2    0    9    6    0   10    1    0   10    2    0   10    6    0
   11    1    0   11    2    0   11    6    0   12    1    0   12    2    0
   12    3  -33   12    4    0   12    5  -34   12    6    0   13    1    0
   13    2    0   13    3   35   13    4    0   13    5   36   13    6    0
   14    1    0   14    2    0   14    4    0   14    6    0   15    1    0
   15    2    0   15    4    0   15    6    0   16    1    0   16    2    0
   16    4    0   16    6    0   17    1    0   17    2    0   17    3   37
   17    4    0   17    5   38   17    6    0   18    1    0   18    2    0
   18    6    0   19    1    0   19    2    0   19    6    0   20    1    0
   20    2    0   20    6    0   21    1    0   21    2    0   21    6    0
1 1
0.0 0.0 0.0 0.0 0.0 0.0 0.0 0.0 0.0 0.0 0.0 0.0 -0.162519 0.225721
```

```
0.44593 0.66615 1.0 1.0 1.0 1.0 1.0
0.220216 0.220216 0.220216 0.220216 0.220216 0.220216 0.220216
0.220216 0.220216 0.220216 0.220216 0.220216 0.220216 0.220216
0.220216 0.220216 0.220216 0.220216 0.220216 0.220216 0.220216
1.0 1.0 1.0 1.0 1.0 1.0 1.0 1.0 1.0 1.0 1.0 1.0 1.0 1.0 1.0 1.0
1.0 1.0 1.0 1.0 1.0
0.0 0.0 0.0 0.0 0.0 0.0 0.0 0.0 0.0 0.0 0.0 0.0 0.0 0.0 0.0 0.0
0.0 0.0 0.0 0.0 0.0
 12 11 0 10 0.00 1.225 0.0 0
 5 21 17 7
 0.0 0.69 4.815 1.5
11.0 0.180 -0.012  6.283185 -0.5
10.175 0.214 -0.023 6.283185 -0.5
9.075 0.258 -0.038 6.283185 -0.5
7.975 0.304 -0.046 6.283185 -0.5
6.875 0.349 -0.068 6.283185 -0.5
6.325 0.363 -0.072  6.283185 -0.5
4.949 0.382 -0.072  6.283185 -0.5
3.849 0.397 -0.072  6.283185 -0.5
2.749 0.411 -0.072 6.283185 -0.5
1.649 0.427 -0.072 6.283185 -0.5
0.549 0.442 -0.072 6.283185 -0.5
0.000 0.449 -0.072 6.283185 -0.5
1.425 0.177 0.00 4.70 -0.5
1.050 0.2022 0.00 4.70 -0.5
0.70 0.2275 0.00 4.70 -0.5
0.350 0.2530 0.00 4.70 -0.5
0.00 0.2785 0.00 4.70 -0.5
0.0 0.0 0.0 1
1 0 1 30
48.0 1.0 51.0
72.0 0.1 73.0
```

K.5(B) Data file for longitudinal stability analysis of A1 with
Downwash

```
   0.10000D+06 2.00  20  19  38   4 72   0 0 0.670 0.30 0
 -1 -2 -3 -8
    1   2   1   2   3   2   3   4   3   4   5   4   5   6   5
    6   7   6   7   8   7   8   9   8   9  10   9   9  11  10
   11  12  11  12  13  12  13  14  13  14  15  14  14  16  15
   16  17  16  17  18  17  18  19  18  19  20  19
 2
   2.6100D+05 9.1250D+07 2.4000D+05 6.940 0.3764 0.0
   3.2400D+05 1.1682D+08 3.4000D+05 9.772 0.5030 0.00
   4.3200D+05 1.4240D+08 4.5000D+05 11.360 0.7450 0.0
   5.7600D+05 1.6940D+08 6.2000D+05 12.821 1.0370 0.0
   9.0900D+05 1.9500D+08 9.0000D+05 14.251 1.5190 0.0
   1.2780D+06 2.1900D+08 1.2600D+06 20.170 1.9766 0.0
   1.7550D+06 3.3600D+08 1.7800D+06 19.520 2.4500 0.0
   2.2230D+06 4.5210D+08 2.2600D+06 26.323 3.9030 0.0
   1.0D09 1.0D09 1.0D09 1.0D-03 1.0D-03 0.0
   2.6370D+06 4.7216D+08 2.5900D+06 27.850 4.2020 0.0
   3.0060D+06 4.9010D+08 2.8700D+06 28.946 4.4430 0.0
   3.3750D+06 5.1450D+08 3.1600D+06 34.496 4.6820 0.0
   1.0D09 1.0D09 1.0D09 1.0D-03 1.0D-04 0.0
   1.0D09 1.0D09 1.0D09 1.0D-03 1.0D-04 0.0
   1.0D09 1.0D09 1.0D09 1.0D-03 1.0D-04 0.0
   7.29065D06 1.0D+10 2.9342D+05 22.7985 13.460 0.0
   7.29065D06 1.0D+10 2.9342D+05 6.1265 5.0400 0.0
   1.4600D+05 1.0D+11 1.0D+07 10.770 1.0D-03 0.0
   7.9100D+04 1.0D+10 1.0D+07 8.6442 1.0D-03 0.0
 -0.49670 5.00 -0.43180 4.558 -0.3810 4.048 -0.30480 3.546 -0.2286
   3.038 -0.15240 2.528 -0.076200 1.9668 1.618 1.318 1.008 0.758
   0.428 0.0 0.45584 0.78144 1.44718 -0.02332 -1.03332 -4.48932
   0.7775   1.555 -1.5850 0.80 0.35 20.0 182.0 116.31 85.442 10.0
   2.3945 6.735
    1   2  20   3   4  20   5   6  20   7   8  20   9  10  20
   11  12  20  13  14  20  20  15  20  20  16  20  21  16  22
   20  17  20  20  18  20  20  19  20  20  20  20  23  20  20
   24  20  20  25  20  20  26  20  20  26  27  20  26  28  20
    1   1   0   1   2   0   1   6   0   2   1   0   2   2   0
    2   6   0   3   1   0   3   2   0   3   6   0   4   1   0
    4   2   0   4   6   0   5   1   0   5   2   0   5   6   0
    6   1   0   6   2   0   6   6   0   7   1   0   7   2   0
    7   6   0   8   1   0   8   2   0   8   6   0   9   1   0
    9   2   0   9   6   0  10   3  32  10   6   0  11   1   0
   11   2   0  11   6   0  12   1   0  12   2   0  12   6   0
   13   1   0  13   2   0  13   6   0  14   1   0  14   2   0
   14   4   0  14   6   0  15   1   0  15   2   0  15   3  33
   15   4   0  15   5  34  15   6   0  16   1   0  16   2   0
   16   3 -30  16   4   0  16   5 -31  16   6   0  17   1   0
   17   2   0  17   3  35  17   4   0  17   5   3  17   6   0
   18   1   0  18   2   0  18   3  36  18   4   0  18   5  37
   18   6   0  19   1   0  19   2   0  19   6   0  20   1   0
   20   2   0  20   6   0
 1 1
   0.105996 0.09146 0.08008 0.06302 0.04596 0.02890 0.01184
```

```
-5.2217D-03 -5.2217D-03 -0.10729 -5.2217D-03 -5.2217D-03
-5.2217D-03 -5.2217D-03 -0.329266 0.0 0.226153 1.0 1.0 1.0
0.22391 0.22391 0.22391 0.22391 0.22391 0.22391 0.22391 0.22391
0.22391 0.22391 0.22391 0.22391 0.22391 0.22391 0.22391 0.22391
0.22391 0.22391 0.22391 0.22391
1.0 1.0 1.0 1.0 1.0 1.0 1.0 1.0 1.0 1.0 1.0 1.0 1.0 1.0 1.0 1.0
1.0 1.0 1.0 1.0
1.0D-05 1.0D-05 1.0D-05 1.0D-05 1.0D-05 1.0D-05 1.0D-05 1.0D-05
1.0D-05 1.0D-05 1.0D-05 1.0D-05 1.0D-05 1.0D-05 1.0D-05 1.0D-05
1.0D-05 1.0D-05 1.0D-05 1.0D-05
13 13 0 10 9.58 1.055 0.0 10
3 20 18 5
0.0 1.5 4.355 0.0
5.00 0.4572 -0.462 4.221 -0.5
4.558 0.505 -0.459 4.221 -0.5
4.048 0.565 -0.438 4.221 -0.5
3.546 0.624 -0.425 4.221 -0.5
3.038 0.683 -0.413 4.221 -0.5
2.528 0.743 -0.402 4.221 -0.5
1.9668 0.808 -0.383 4.221 -0.5
1.618 0.850 -0.404 4.221 -0.5
1.318 0.885 -0.349 4.221 -0.5
1.008 0.921 -0.296 4.221 -0.5
0.758 0.950 -0.257 4.221 -0.5
0.428 0.989 -0.207 4.221 -0.5
0.00  1.04 -0.1452 4.221 -0.5
1.555 0.335 0.0 3.52 -0.5
0.7775 0.435 0.0 3.52 -0.5
0.0 0.535 0.0 3.52 -0.5
0.0 0.0 0.0 1
2 0 1 30
5.0 1.0 9.0
61.68
55.0 1.0 62.0
```

STABILITY OF AIRCRAFT

STRUCTURAL DETAILS:

CF	FQ	NN	NC	NR	NM	ND	LR	LS	SF	PR
1.0000E+06	2.0000E+00	21	20	38	6	75	0	0	6.700	3.0000 0

LIST OF NORMAL MODES REQUIRED FOR FLUTTER ANALYSIS:

-1 -2 -3 -4 -5 -7

CONNECTION LIST: 20 CONNECTIONS IN ALL(LOWER NODE,HIGHER NODE,MEMBER)

1	2	1	2	3	2	3	4	3	4	5	4	5	6	5
6	7	6	7	8	7	8	9	8	9	10	9	10	11	10
11	12	11	12	13	20	12	14	12	14	15	13	15	16	14
16	17	15	17	18	16	18	19	17	19	20	18	20	21	19

LIST OF MEMBER PROPERTIES:

EI	EA	GJ	MASS/L	MASS M.I/L	AXIAL FORCE
8.8200E+04	1.0000E+07	1.3400E+04	4.5710E+00	2.9170E-02	0.0000E+00
1.0950E+05	1.0000E+07	1.7500E+04	5.7910E+00	5.3640E-02	0.0000E+00
1.4450E+05	1.0000E+07	2.0900E+04	7.1000E+00	9.3640E-02	0.0000E+00
1.8350E+05	1.0000E+07	2.3800E+04	8.0820E+00	1.2360E-01	0.0000E+00
2.6240E+05	1.0000E+07	2.9300E+04	2.0459E+01	4.4190E-01	0.0000E+00
3.4380E+05	1.0000E+07	3.6800E+04	9.9270E+00	2.2760E-01	0.0000E+00
4.6410E+05	1.0000E+07	5.2100E+04	1.0927E+01	2.7180E-01	0.0000E+00
6.3230E+05	1.0000E+07	7.9300E+04	1.1954E+01	3.1800E-01	0.0000E+00
8.6120E+05	1.0000E+07	1.2360E+05	1.2954E+01	3.7180E-01	0.0000E+00
1.1633E+06	1.0000E+07	1.8930E+05	1.3945E+01	4.3000E-01	0.0000E+00
1.4552E+06	1.0000E+07	2.5180E+05	1.4945E+01	4.9270E-01	0.0000E+00
2.2530E+06	1.0000E+07	9.4350E+04	4.8780E+00	4.1820E-01	0.0000E+00
1.3488E+06	1.0000E+07	8.3200E+04	3.7750E+00	1.3770E-01	0.0000E+00
7.6050E+05	1.0000E+07	6.6700E+04	3.0000E+00	6.7140E-02	0.0000E+00
3.1550E+05	1.0000E+07	4.6250E+04	1.9860E+00	2.4650E-02	0.0000E+00
1.1910E+04	1.0000E+07	1.4060E+04	6.0520E+00	1.1550E-02	0.0000E+00
6.1700E+03	1.0000E+07	1.0620E+04	5.0236E+00	5.6335E-03	0.0000E+00
4.0180E+03	1.0000E+07	7.8920E+03	4.2016E+00	3.6617E-03	0.0000E+00
2.7260E+03	1.0000E+07	5.3090E+03	3.1512E+00	2.5350E-03	0.0000E+00
1.0000E+07	1.0000E+06	1.0000E+06	1.0000E-02	1.0000E-04	0.0000E+00

LIST OF NR REAL NUMBERS:

1.1000E+01	1.0175E+01	9.0757E+00	7.9746E+00	6.8746E+00	6.3246E+00
4.9496E+00	3.8496E+00	2.7496E+00	1.6496E+00	5.4965E-01	0.0000E+00
-5.4965E-01	-1.6496E+00	-2.7496E+00	-3.8496E+00	-4.9496E+00	-6.3246E+00
-6.8746E+00	-7.9746E+00	-9.0757E+00	-1.0175E+01	-1.1000E+01	-1.0250E+00
-2.0250E+00	-3.0250E+00	-4.5410E+00	3.5000E-01	7.0000E-01	1.0500E+00
1.4250E+00	7.3800E-01	6.0000E-01	5.5000E-01	1.1209E+02	3.5700E+01
5.7000E+00	2.2000E+00				

305

NODE CO-ORDINATE LIST:CO-ORDINATES OF 21 NODES(X,Y,Z:RIGHT HANDED SET)

12	1	12	12	2	12	12	3	12	12	4	12	12	5	12
12	6	12	12	7	12	12	8	12	12	9	12	12	10	12
12	11	12	12	12	12	32	12	12	24	12	12	25	12	12
26	12	12	27	12	12	27	28	12	27	29	12	27	30	12
27	31	12												

LIST OF ND AFFECTED DEGREES OF FREEDOM:

1	1	0	1	2	0	1	6	0	2	1	0	2	2	0
2	6	0	3	1	0	3	2	0	3	6	0	4	1	0
4	2	0	4	6	0	5	1	0	5	2	0	5	6	0
6	1	0	6	2	0	6	6	0	7	1	0	7	2	0
7	6	0	8	1	0	8	2	0	8	6	0	9	1	0
9	2	0	9	6	0	10	1	0	10	2	0	10	6	0
11	1	0	11	2	0	11	6	0	12	1	0	12	2	0
12	3	-33	12	4	0	12	5	-34	12	6	0	13	1	0
13	2	0	13	3	35	13	4	0	13	5	36	13	6	0
14	1	0	14	2	0	14	4	0	14	6	0	15	1	0
15	2	0	15	4	0	15	6	0	16	1	0	16	2	0
16	4	0	16	6	0	17	1	0	17	2	0	17	3	37
17	4	0	17	5	38	17	6	0	18	1	0	18	2	0
18	6	0	19	1	0	19	2	0	19	6	0	20	1	0
20	2	0	20	6	0	21	1	0	21	2	0	21	6	0

AERODYNAMIC DETAILS:

NWN	NIP	NRB	NCS	SWP	RO	G	NUC
12	11	0	10	0.00	1.2250	0.000	0

NTPN	NNTT	NNTR	NIPT
5	21	17	7

SWPT	SMC	XLT	ZT
0.00	0.6900	4.8150	1.5000

WING DETAILS

Y	B	AH	CLA	A
11.000	0.180	-0.012	6.283	-0.500
10.175	0.214	-0.023	6.283	-0.500
9.075	0.258	-0.038	6.283	-0.500
7.975	0.304	-0.046	6.283	-0.500
6.875	0.349	-0.068	6.283	-0.500
6.325	0.363	-0.072	6.283	-0.500
4.949	0.382	-0.072	6.283	-0.500
3.849	0.397	-0.072	6.283	-0.500
2.749	0.411	-0.072	6.283	-0.500
1.649	0.427	-0.072	6.283	-0.500
0.549	0.442	-0.072	6.283	-0.500
0.000	0.449	-0.072	6.283	-0.500

TAILPLANE DETAILS

YT	BT	AHT	CLAT	AT
1.425	0.177	0.000	4.700	-0.500
1.050	0.202	0.000	4.700	-0.500
0.700	0.228	0.000	4.700	-0.500
0.350	0.253	0.000	4.700	-0.500
0.000	0.279	0.000	4.700	-0.500

GENERALISED MASS AND STIFFNESS MATRICES

```
2.07407E+01   1.97260E-02  -7.11608E-03   2.97650E-05  -7.50745E-05   1.17457E-03
1.97260E-02   2.53831E+02  -1.00913E-02  -1.60321E-03  -9.40659E-05  -1.95952E-04
7.11608E-03  -1.00913E-02   1.51171E+01   6.38208E-05   5.32505E-05   1.67970E-04
2.97650E-05  -1.60321E-03   6.38208E-05   1.07028E+01  -5.84754E-06   8.16098E-06
7.50745E-05  -9.40659E-05   5.32505E-05  -5.84754E-06   1.14744E+00   1.64361E-03
1.17457E-03  -1.95952E-04   1.67970E-04   8.16098E-06   1.64361E-03   6.14780E-01
```

```
2.76722E-02   3.38391E-06   1.61170E-04   8.84054E-04  -1.85212E-02  -4.61597E-03
3.38701E-06   6.00609E-01  -7.65242E-02  -4.45904E-02   1.34589E-02  -2.08196E-03
1.61170E-04  -7.65242E-02   1.85462E+03  -5.02267E-02  -8.45034E-01   2.54470E-01
8.84053E-04  -4.45904E-02  -5.02267E-02   1.86141E+04  -7.62200E-03  -9.43817E-03
1.85212E-02   1.34589E-02  -8.45034E-01  -7.62200E-03   9.66617E+03   7.89295E+00
4.61597E-03  -2.08196E-03   2.54470E-01  -9.43817E-03   7.89295E+00   6.83841E+03
```

FREQUENCIES IN RAD/SEC:

```
3.58909E-02 4.86185E-02 1.10762E+01 4.17013E+01 9.17635E+01 1.05194E+02
```

INTERPOLATED VALUES OF HH,AA,BB,AHH,CLA,A

WING DETAILS

ERTICAL DISPLACEMENT

```
0.00000E+00   1.00000E+00   1.00000E+00  -1.00000E+00   1.03705E-01   6.37637E-02
0.00000E+00   1.00000E+00   8.06252E-01  -5.05935E-01   2.40119E-02   1.12170E-02
0.00000E+00   1.00000E+00   6.18716E-01  -7.66579E-02  -3.32472E-02  -2.46785E-02
0.00000E+00   1.00000E+00   4.41127E-01   2.41688E-01  -4.95252E-02  -3.01154E-02
0.00000E+00   1.00000E+00   2.84325E-01   3.86742E-01  -2.59780E-02  -1.03250E-02
0.00000E+00   1.00000E+00   1.51233E-01   3.84885E-01   1.28213E-02   1.48394E-02
0.00000E+00   1.00000E+00   4.38366E-02   2.94241E-01   4.13973E-02   2.82891E-02
0.00000E+00   1.00000E+00  -3.53048E-02   1.61295E-01   4.97114E-02   2.57984E-02
0.00000E+00   1.00000E+00  -8.89359E-02   4.04970E-02   4.10132E-02   1.33470E-02
0.00000E+00   1.00000E+00  -1.17778E-01  -5.00028E-02   2.75636E-02   6.18344E-04
0.00000E+00   1.00000E+00  -1.27773E-01  -7.58578E-02   2.02409E-02  -4.88049E-03
```

ITCHING ROTATION

```
2.20216E-01   0.00000E+00   7.21713E-04   1.28195E-02   2.77909E-01  -1.00000E+00
2.20216E-01   0.00000E+00   7.82857E-04   1.27852E-02   2.74367E-01  -9.83300E-01
2.20216E-01   0.00000E+00   8.39604E-04   1.26978E-02   2.65292E-01  -9.40554E-01
2.20216E-01   0.00000E+00   8.91878E-04   1.25162E-02   2.46725E-01  -8.53616E-01
2.20216E-01   0.00000E+00   9.18593E-04   1.22256E-02   2.18156E-01  -7.21977E-01
2.20216E-01   0.00000E+00   9.28598E-04   1.17948E-02   1.78470E-01  -5.44025E-01
2.20216E-01   0.00000E+00   9.41762E-04   1.13138E-02   1.36809E-01  -3.62097E-01
2.20216E-01   0.00000E+00   9.47013E-04   1.08919E-02   1.03052E-01  -2.19811E-01
2.20216E-01   0.00000E+00   9.43209E-04   1.05378E-02   7.71724E-02  -1.15361E-01
2.20216E-01   0.00000E+00   9.33271E-04   1.02717E-02   5.99604E-02  -5.02825E-02
```

```
.20216E-01   0.00000E+00   9.25515E-04   1.00360E-02   4.57764E-02   1.22236E-03
ALUES OF AHH:

1.20000E-02-3.64528E-02-3.63699E-02-5.23490E-02-7.06160E-02-7.22665E-02

7.20609E-02-7.18099E-02-7.24639E-02-7.05701E-02-7.20000E-02

ALUES OF CLA:

6.28318E+00  6.28318E+00  6.28318E+00  6.28318E+00  6.28319E+00  6.28319E+00

6.28319E+00  6.28318E+00  6.28319E+00  6.28318E+00  6.28318E+00

ALUES OF A:

-5.00000E-01-5.00000E-01-5.00000E-01-5.00000E-01-5.00000E-01-5.00000E-01

-5.00000E-01-5.00000E-01-5.00000E-01-5.00000E-01-5.00000E-01

AILPLANE DETAILS


ERTICAL DISPLACEMENT

1.00000E+00   1.00000E+00  -1.32743E-01  -1.32266E-01  -8.56961E-01  -1.01179E-01
1.00000E+00   1.00000E+00  -1.31908E-01  -1.21438E-01  -6.21900E-01  -6.86104E-02
1.00000E+00   1.00000E+00  -1.31095E-01  -1.10899E-01  -3.96130E-01  -3.74944E-02
1.00000E+00   1.00000E+00  -1.30377E-01  -1.01677E-01  -2.04890E-01  -1.14742E-02
1.00000E+00   1.00000E+00  -1.29815E-01  -9.45566E-02  -6.43321E-02   7.26050E-03
1.00000E+00   1.00000E+00  -1.29454E-01  -9.00741E-02   1.84790E-02   1.79737E-02
1.00000E+00   1.00000E+00  -1.29328E-01  -8.85205E-02   4.55677E-02   2.13831E-02

ITCHING ROTATION

2.20216E-01   0.00000E+00  -1.53322E-03  -1.49460E-02  -4.31204E-02   1.05855E-02
2.20216E-01   0.00000E+00  -1.53145E-03  -1.49454E-02  -4.31145E-02   1.05841E-02
2.20216E-01   0.00000E+00  -1.52382E-03  -1.49444E-02  -4.31016E-02   1.05806E-02
2.20216E-01   0.00000E+00  -1.51410E-03  -1.49430E-02  -4.30829E-02   1.05752E-02
2.20216E-01   0.00000E+00  -1.50531E-03  -1.49411E-02  -4.30583E-02   1.05678E-02
2.20216E-01   0.00000E+00  -1.49979E-03  -1.49387E-02  -4.30268E-02   1.05580E-02
2.20216E-01   0.00000E+00  -1.49915E-03  -1.49356E-02  -4.29863E-02   1.05449E-02

VALUES OF AHH:

 0.00000E+00  0.00000E+00  0.00000E+00  0.00000E+00  0.00000E+00  0.00000E+00

 0.00000E+00

VALUES OF CLA:

 4.70000E+00  4.70000E+00  4.70000E+00  4.70000E+00  4.70000E+00  4.70000E+00

 4.70000E+00

VALUES OF A:

-5.00000E-01-5.00000E-01-5.00000E-01-5.00000E-01-5.00000E-01-5.00000E-01

-5.00000E-01

EFFECTS OF DOWNWASH INCLUDED WITH NZI = 30

UTTER ANALYSIS
```

IAL FREQUENCY: INITIAL VALUE   INCREMENT   FINAL VALUE
                 48.000   1.000   51.000

IAL VELOCITY: INITIAL VALUE   INCREMENT   FINAL VALUE
                 72.000   0.100   73.000

        ********** ALL DATA ABOVE THIS LINE **********

        ********** RESULTS FOLLOW THIS LINE **********

AROW	THETA	U	MU	OMEGA	REAL PT	IMAG PT
48.000	0.00	72.000	0.000	48.000	-0.3701E+25	-0.8430E+25
49.000	0.00	72.000	0.000	49.000	-0.6868E+24	-0.5045E+25
50.000	0.00	72.000	0.000	50.000	0.2344E+25	0.6657E+24

RHO VALUE WHEN REAL DET ZERO= 49.22660

RHO VALUE WHEN IMAGINARY DET ZERO= 49.88344

51.000	0.00	72.000	0.000	51.000	0.5122E+25	0.9257E+25
48.000	0.00	72.100	0.000	48.000	-0.4113E+25	-0.7659E+25
49.000	0.00	72.100	0.000	49.000	-0.1253E+25	-0.4149E+25
50.000	0.00	72.100	0.000	50.000	0.1586E+25	0.1701E+25

RHO VALUE WHEN REAL DET ZERO= 49.44119

RHO VALUE WHEN IMAGINARY DET ZERO= 49.70923

51.000	0.00	72.100	0.000	51.000	0.4144E+25	0.1045E+26
48.000	0.00	72.200	0.000	48.000	-0.4535E+25	-0.6885E+25
49.000	0.00	72.200	0.000	49.000	-0.1829E+25	-0.3251E+25
50.000	0.00	72.200	0.000	50.000	0.8323E+24	0.2742E+25

RHO VALUE WHEN REAL DET ZERO= 49.68726

RHO VALUE WHEN IMAGINARY DET ZERO= 49.54243

51.000	0.00	72.200	0.000	51.000	0.3171E+25	0.1165E+26
48.000	0.00	72.300	0.000	48.000	-0.4955E+25	-0.6108E+25
49.000	0.00	72.300	0.000	49.000	-0.2403E+25	-0.2347E+25
50.000	0.00	72.300	0.000	50.000	0.7370E+23	0.3787E+25

RHO VALUE WHEN REAL DET ZERO= 49.97024

RHO VALUE WHEN IMAGINARY DET ZERO= 49.38264

51.000	0.00	72.300	0.000	51.000	0.2192E+25	0.1285E+26
48.000	0.00	72.400	0.000	48.000	-0.5376E+25	-0.5326E+25
49.000	0.00	72.400	0.000	49.000	-0.2983E+25	-0.1440E+25
50.000	0.00	72.400	0.000	50.000	-0.6980E+24	0.4834E+25

RHO VALUE WHEN IMAGINARY DET ZERO= 49.22956

51.000	0.00	72.400	0.000	51.000	0.1199E+25	0.1406E+26

RHO VALUE WHEN REAL DET ZERO= 50.36800

48.000	0.00	72.500	0.000	48.000	-0.5806E+25	-0.4542E+25
49.000	0.00	72.500	0.000	49.000	-0.3565E+25	-0.5296E+24

309

50.000	0.00	72.500	0.000	50.000	-0.1461E+25	0.5888E+25

RHO VALUE WHEN IMAGINARY DET ZERO= 49.08253

51.000	0.00	72.500	0.000	51.000	0.2150E+24	0.1527E+26

RHO VALUE WHEN REAL DET ZERO= 50.87173

48.000	0.00	72.600	0.000	48.000	-0.6229E+25	-0.3753E+25
49.000	0.00	72.600	0.000	49.000	-0.4147E+25	0.3852E+24

RHO VALUE WHEN IMAGINARY DET ZERO= 48.90692

50.000	0.00	72.600	0.000	50.000	-0.2230E+25	0.6945E+25
51.000	0.00	72.600	0.000	51.000	-0.7802E+24	0.1649E+26
48.000	0.00	72.700	0.000	48.000	-0.6659E+25	-0.2962E+25
49.000	0.00	72.700	0.000	49.000	-0.4732E+25	0.1304E+25

RHO VALUE WHEN IMAGINARY DET ZERO= 48.69435

50.000	0.00	72.700	0.000	50.000	-0.3003E+25	0.8006E+25
51.000	0.00	72.700	0.000	51.000	-0.1772E+25	0.1771E+26
48.000	0.00	72.800	0.000	48.000	-0.7085E+25	-0.2166E+25
49.000	0.00	72.800	0.000	49.000	-0.5312E+25	0.2227E+25

RHO VALUE WHEN IMAGINARY DET ZERO= 48.49306

50.000	0.00	72.800	0.000	50.000	-0.3773E+25	0.9073E+25
51.000	0.00	72.800	0.000	51.000	-0.2764E+25	0.1894E+26
48.000	0.00	72.900	0.000	48.000	-0.7512E+25	-0.1367E+25
49.000	0.00	72.900	0.000	49.000	-0.5898E+25	0.3154E+25

RHO VALUE WHEN IMAGINARY DET ZERO= 48.30239

50.000	0.00	72.900	0.000	50.000	-0.4543E+25	0.1014E+26
51.000	0.00	72.900	0.000	51.000	-0.3757E+25	0.2017E+26
48.000	0.00	73.000	0.000	48.000	-0.7941E+25	-0.5645E+24
49.000	0.00	73.000	0.000	49.000	-0.6483E+25	0.4085E+25

RHO VALUE WHEN IMAGINARY DET ZERO= 48.12142

Output file for example K.5(B)

STABILITY OF AIRCRAFT

STRUCTURAL DETAILS:

CF	FQ	NN	NC	NR	NM	ND	LR	LS	SF	PR
1.0000E+05	2.0000E+00	20	19	38	4	72	0	0	6.700	3.0000 0

LIST OF NORMAL MODES REQUIRED FOR FLUTTER ANALYSIS:

-1 -2 -3 -8

CONNECTION LIST: 19 CONNECTIONS IN ALL(LOWER NODE,HIGHER NODE,MEMBER)

1	2	1	2	3	2	3	4	3	4	5	4	5	6	5
6	7	6	7	8	7	8	9	8	9	10	9	9	11	10
11	12	11	12	13	12	13	14	13	14	15	14	14	16	15
16	17	16	17	18	17	18	19	18	19	20	19			

LIST OF MEMBER PROPERTIES:

EI	EA	GJ	MASS/L	MASS M.I/L	AXIAL FORCE
2.6100E+05	9.1250E+07	2.4000E+05	6.9400E+00	3.7640E-01	0.0000E+00
3.2400E+05	1.1682E+08	3.4000E+05	9.7720E+00	5.0300E-01	0.0000E+00
4.3200E+05	1.4240E+08	4.5000E+05	1.1360E+01	7.4500E-01	0.0000E+00
5.7600E+05	1.6940E+08	6.2000E+05	1.2821E+01	1.0370E+00	0.0000E+00
9.0900E+05	1.9500E+08	9.0000E+05	1.4251E+01	1.5190E+00	0.0000E+00
1.2780E+06	2.1900E+08	1.2600E+06	2.0170E+01	1.9766E+00	0.0000E+00
1.7550E+06	3.3600E+08	1.7800E+06	1.9520E+01	2.4500E+00	0.0000E+00
2.2230E+06	4.5210E+08	2.2600E+06	2.6323E+01	3.9030E+00	0.0000E+00
1.0000E+09	1.0000E+09	1.0000E+09	1.0000E-03	1.0000E-03	0.0000E+00
2.6370E+06	4.7216E+08	2.5900E+06	2.7850E+01	4.2020E+00	0.0000E+00
3.0060E+06	4.9010E+08	2.8700E+06	2.8946E+01	4.4430E+00	0.0000E+00
3.3750E+06	5.1450E+08	3.1600E+06	3.4496E+01	4.6820E+00	0.0000E+00
1.0000E+09	1.0000E+09	1.0000E+09	1.0000E-03	1.0000E-04	0.0000E+00
1.0000E+09	1.0000E+09	1.0000E+09	1.0000E-03	1.0000E-04	0.0000E+00
1.0000E+09	1.0000E+09	1.0000E+09	1.0000E-03	1.0000E-04	0.0000E+00
7.2906E+06	1.0000E+10	2.9342E+05	2.2799E+01	1.3460E+01	0.0000E+00
7.2906E+06	1.0000E+10	2.9342E+05	6.1265E+00	5.0400E+00	0.0000E+00
1.4600E+05	1.0000E+11	1.0000E+07	1.0770E+01	1.0000E-03	0.0000E+00
7.9100E+04	1.0000E+10	1.0000E+07	8.6442E+00	1.0000E-03	0.0000E+00

LIST OF NR REAL NUMBERS:

-4.9670E-01	5.0000E+00	-4.3180E-01	4.5580E+00	-3.8100E-01	4.0480E+00
-3.0480E-01	3.5460E+00	-2.2860E-01	3.0380E+00	-1.5240E-01	2.5280E+00
-7.6200E-02	1.9668E+00	1.6180E+00	1.3180E+00	1.0080E+00	7.5800E-01
4.2800E-01	0.0000E+00	4.5584E-01	7.8144E-01	1.4472E+00	-2.3320E-02
-1.0333E+00	-4.4893E+00	7.7750E-01	1.5550E+00	-1.5850E+00	8.0000E-01
3.5000E-01	2.0000E+01	1.8200E+02	1.1631E+02	8.5442E+01	1.0000E+01
2.3945E+00	6.7350E+00				

NODE CO-ORDINATE LIST:CO-ORDINATES OF 20 NODES(X,Y,Z:RIGHT HANDED SET)

1	2	20	3	4	20	5	6	20	7	8	20	9	10	20
11	12	20	13	14	20	20	15	20	20	16	20	21	16	22
20	17	20	20	18	20	20	19	20	20	20	20	23	20	20
24	20	20	25	20	20	26	20	20	26	27	20	26	28	20

LIST OF ND AFFECTED DEGREES OF FREEDOM:

1	1	0	1	2	0	1	6	0	2	1	0	2	2	0
2	6	0	3	1	0	3	2	0	3	6	0	4	1	0
4	2	0	4	6	0	5	1	0	5	2	0	5	6	0
6	1	0	6	2	0	6	6	0	7	1	0	7	2	0
7	6	0	8	1	0	8	2	0	8	6	0	9	1	0
9	2	0	9	6	0	10	3	32	10	6	0	11	1	0
11	2	0	11	6	0	12	1	0	12	2	0	12	6	0
13	1	0	13	2	0	13	6	0	14	1	0	14	2	0
14	4	0	14	6	0	15	1	0	15	2	0	15	3	33
15	4	0	15	5	34	15	6	0	16	1	0	16	2	0
16	3	-30	16	4	0	16	5	-31	16	6	0	17	1	0
17	2	0	17	3	35	17	4	0	17	5	38	17	6	0
18	1	0	18	2	0	18	3	36	18	4	0	18	5	37
18	6	0	19	1	0	19	2	0	19	6	0	20	1	0
20	2	0	20	6	0									

AERODYNAMIC DETAILS:

NWN	NIP	NRB	NCS	SWP	RO	G	NUC
13	13	0	10	9.58	1.0550	0.000	10

NTPN	NNTT	NNTR	NIPT
3	20	18	5

SWPT	SMC	XLT	ZT
0.00	1.5000	4.3550	0.0000

WING DETAILS

Y	B	AH	CLA	A
5.000	0.457	-0.462	4.221	-0.500
4.558	0.505	-0.459	4.221	-0.500
4.048	0.565	-0.438	4.221	-0.500
3.546	0.624	-0.425	4.221	-0.500
3.038	0.683	-0.413	4.221	-0.500
2.528	0.743	-0.402	4.221	-0.500
1.967	0.808	-0.383	4.221	-0.500
1.618	0.850	-0.404	4.221	-0.500
1.318	0.885	-0.349	4.221	-0.500
1.008	0.921	-0.296	4.221	-0.500
0.758	0.950	-0.257	4.221	-0.500
0.428	0.989	-0.207	4.221	-0.500
0.000	1.040	-0.145	4.221	-0.500

TAILPLANE DETAILS

YT	BT	AHT	CLAT	AT
1.555	0.335	0.000	3.520	-0.500
0.777	0.435	0.000	3.520	-0.500
0.000	0.535	0.000	3.520	-0.500

GENERALISED MASS AND STIFFNESS MATRICES

6.57411E+01	-2.51052E-01	3.06713E-02	-8.83192E-02
-2.51052E-01	4.38011E+02	5.46200E-02	-9.17167E-02
3.06713E-02	5.46200E-02	9.52119E+00	1.56152E-04
-8.83192E-02	-9.17167E-02	1.56152E-04	2.04690E+00

8.21562E+08	4.27684E+07	1.77489E+02	-1.63148E+04
4.27684E+07	9.92033E+06	3.23066E+02	-1.60337E+04
1.77489E+02	3.23066E+02	5.80515E+04	5.32990E+00
-1.63148E+04	-1.60337E+04	5.32989E+00	3.70539E+05

FREQUENCIES IN RAD/SEC:

5.02659E+01 5.02659E+01 7.80835E+01 4.24443E+02

INTERPOLATED VALUES OF HH,AA,BB,AHH,CLA,A

WING DETAILS

VERTICAL DISPLACEMENT

1.05996E-01	1.00000E+00	1.00000E+00	1.16528E-01
5.48795E-02	1.00000E+00	8.36648E-01	1.12165E-01
1.25514E-01	1.00000E+00	6.87007E-01	-6.90704E-02
4.86111E-02	1.00000E+00	5.31391E-01	-1.63198E-02
6.66424E-02	1.00000E+00	3.96728E-01	-6.98771E-02
3.70110E-02	1.00000E+00	2.75985E-01	-3.97697E-02
2.90129E-02	1.00000E+00	1.76592E-01	-2.84135E-02
1.90924E-02	1.00000E+00	9.68634E-02	-1.31409E-02
-3.99139E-03	1.00000E+00	3.62373E-02	1.62845E-02
-4.64755E-03	1.00000E+00	-3.67009E-03	1.01813E-02
-6.05535E-03	1.00000E+00	-2.71100E-02	2.95409E-03
-6.38634E-03	1.00000E+00	-3.46472E-02	-9.46166E-04
-5.22170E-03	1.00000E+00	-3.45478E-02	-2.53072E-03

PITCHING ROTATION

2.23910E-01	1.00000E-05	5.76223E-02	-1.00000E+00
2.23910E-01	1.00000E-05	5.67461E-02	-9.30830E-01
2.23910E-01	1.00000E-05	5.66091E-02	-9.67113E-01
2.23910E-01	1.00000E-05	5.27523E-02	-8.11772E-01
2.23910E-01	1.00000E-05	4.79896E-02	-7.43954E-01
2.23910E-01	1.00000E-05	4.13118E-02	-6.16470E-01
2.23910E-01	1.00000E-05	3.49032E-02	-5.08790E-01
2.23910E-01	1.00000E-05	2.81876E-02	-3.97521E-01
2.23910E-01	1.00000E-05	2.12724E-02	-2.92328E-01
2.23910E-01	1.00000E-05	1.54900E-02	-2.03675E-01
2.23910E-01	1.00000E-05	1.05593E-02	-8.89632E-02
2.23910E-01	1.00000E-05	6.28595E-03	1.08517E-02
2.23910E-01	1.00000E-05	6.39655E-03	6.19248E-03

VALUES OF AHH:

```
-4.62000E-01-6.46490E-01-2.30487E-01-5.38195E-01-3.65283E-01-4.34988E-01

-3.96140E-01-3.68130E-01-4.06861E-01-3.34044E-01-2.72680E-01-2.11118E-01

-1.45200E-01
```

VALUES OF CLA:

```
  4.22100E+00 4.22100E+00 4.22100E+00 4.22100E+00 4.22100E+00 4.22100E+00

  4.22100E+00 4.22100E+00 4.22100E+00 4.22100E+00 4.22100E+00 4.22100E+00

  4.22100E+00
```

VALUES OF A:

```
-5.00000E-01-5.00000E-01-5.00000E-01-5.00000E-01-5.00000E-01-5.00000E-01

-5.00000E-01-5.00000E-01-5.00000E-01-5.00000E-01-5.00000E-01-5.00000E-01

-5.00000E-01
```

TAILPLANE DETAILS

VERTICAL DISPLACEMENT

```
1.00000E+00    1.00000E+00    -1.16308E-01     6.93649E-03
1.00000E+00    1.00000E+00    -1.05014E-01     1.10501E-03
1.00000E+00    1.00000E+00    -9.62054E-02    -2.94481E-03
1.00000E+00    1.00000E+00    -8.98822E-02    -5.21297E-03
1.00000E+00    1.00000E+00    -8.60444E-02    -5.69948E-03
```

PITCHING ROTATION

```
2.23910E-01    1.00000E-05    -1.95358E-02    -8.27717E-03
2.23910E-01    1.00000E-05    -1.95358E-02    -8.27705E-03
2.23910E-01    1.00000E-05    -1.95358E-02    -8.27658E-03
2.23910E-01    1.00000E-05    -1.95359E-02    -8.27574E-03
2.23910E-01    1.00000E-05    -1.95360E-02    -8.27454E-03
```

VALUES OF AHH:

```
  0.00000E+00 0.00000E+00 0.00000E+00 0.00000E+00 0.00000E+00
```

VALUES OF CLA:

```
  3.52000E+00 3.52000E+00 3.52000E+00 3.52000E+00 3.52000E+00
```

VALUES OF A:

```
-5.00000E-01-5.00000E-01-5.00000E-01-5.00000E-01-5.00000E-01
```

EFFECTS OF DOWNWASH INCLUDED WITH NZI = 30

DYNAMIC STABILITY ANALYSIS

```
        VELOCITY=    61.680
```

```
TRIAL RHO: INITIAL VALUE      INCREMENT      FINAL VALUE
              5.000             1.000           9.000
```

AL THETA: INITIAL VALUE   INCREMENT   FINAL   VALUE
             55.000   1.000   62.000

          ********** ALL DATA ABOVE THIS LINE **********

          ********** RESULTS FOLLOW THIS LINE **********

AROW	THETA	U	MU	OMEGA	REAL PT	IMAG PT
5.000	55.00	61.680	-4.096	2.868	0.1104E+18	0.3400E+18
6.000	55.00	61.680	-4.915	3.441	0.1099E+18	0.3673E+18
7.000	55.00	61.680	-5.734	4.015	0.2303E+17	0.2698E+18
8.000	55.00	61.680	-6.553	4.589	-0.2215E+18	-0.1210E+17

RHO VALUE WHEN REAL DET ZERO=   7.09419

RHO VALUE WHEN IMAGINARY DET ZERO=   7.95709

AROW	THETA	U	MU	OMEGA	REAL PT	IMAG PT
9.000	55.00	61.680	-7.372	5.162	-0.7106E+18	-0.5471E+18
5.000	56.00	61.680	-4.145	2.796	0.1101E+18	0.3373E+18
6.000	56.00	61.680	-4.974	3.355	0.1174E+18	0.3558E+18
7.000	56.00	61.680	-5.803	3.914	0.4935E+17	0.2416E+18
8.000	56.00	61.680	-6.632	4.474	-0.1629E+18	-0.6881E+17

RHO VALUE WHEN REAL DET ZERO=   7.23249

RHO VALUE WHEN IMAGINARY DET ZERO=   7.77832

AROW	THETA	U	MU	OMEGA	REAL PT	IMAG PT
9.000	56.00	61.680	-7.461	5.033	-0.6008E+18	-0.6520E+18
5.000	57.00	61.680	-4.193	2.723	0.1078E+18	0.3358E+18
6.000	57.00	61.680	-5.032	3.268	0.1249E+18	0.3467E+18
7.000	57.00	61.680	-5.871	3.812	0.7661E+17	0.2185E+18
8.000	57.00	61.680	-6.709	4.357	-0.1010E+18	-0.1173E+18

RHO VALUE WHEN REAL DET ZERO=   7.43138

RHO VALUE WHEN IMAGINARY DET ZERO=   7.65063

AROW	THETA	U	MU	OMEGA	REAL PT	IMAG PT
9.000	57.00	61.680	-7.548	4.902	-0.4850E+18	-0.7451E+18
5.000	58.00	61.680	-4.240	2.650	0.1038E+18	0.3357E+18
6.000	58.00	61.680	-5.088	3.180	0.1324E+18	0.3399E+18
7.000	58.00	61.680	-5.936	3.709	0.1048E+18	0.2003E+18
8.000	58.00	61.680	-6.784	4.239	-0.3578E+17	-0.1579E+18

RHO VALUE WHEN REAL DET ZERO=   7.74550

RHO VALUE WHEN IMAGINARY DET ZERO=   7.55912

AROW	THETA	U	MU	OMEGA	REAL PT	IMAG PT
9.000	58.00	61.680	-7.632	4.769	-0.3582E+18	-0.8256E+18
5.000	59.00	61.680	-4.286	2.575	0.1021E+18	0.3348E+18
6.000	59.00	61.680	-5.143	3.090	0.1412E+18	0.3346E+18
7.000	59.00	61.680	-6.000	3.605	0.1354E+18	0.1863E+18
8.000	59.00	61.680	-6.857	4.120	0.3372E+17	-0.1904E+18

RHO VALUE WHEN IMAGINARY DET ZERO=   7.49453

AROW	THETA	U	MU	OMEGA	REAL PT	IMAG PT
9.000	59.00	61.680	-7.715	4.635	-0.2250E+18	-0.8939E+18

RHO VALUE WHEN REAL DET ZERO=   8.13030

315

5.000	60.00	61.680	-4.330	2.500	0.9988E+17	0.3348E+18
6.000	60.00	61.680	-5.196	3.000	0.1495E+18	0.3321E+18
7.000	60.00	61.680	-6.062	3.500	0.1661E+18	0.1775E+18
8.000	60.00	61.680	-6.928	4.000	0.1054E+18	-0.2149E+18

RHO VALUE WHEN IMAGINARY DET ZERO=   7.45233

9.000	60.00	61.680	-7.794	4.500	-0.8579E+17	-0.9498E+18

RHO VALUE WHEN REAL DET ZERO=   8.55137

5.000	61.00	61.680	-4.373	2.424	0.9710E+17	0.3357E+18

316